Department of Mechanical and Aerospace Engineering

Doctoral Thesis
in Aeronautics and Space Engineering

GRAVITY GRADIOMETERS FOR PLANETARY GEODESY: REQUIREMENTS AND CONCEPT FOR A SPACE INSTRUMENT

Candidate:
Marco Lucente

Advisors:
Prof. Luciano Iess (University of Rome "La Sapienza")
Dr. David M. Lucchesi (IAPS/INAF)
Dr. Ing. Francesco Santoli (IAPS/INAF)

XXXII cycle - *Academic Year 2018-2019*

Table of contents

List of Figures

First researches to date on MEMS-based gravity gradiometers, potentially to be used in future space missions, began at the University of Twente in the Netherlands [180]. They studied a micro-gradiometer which would have in principle a level noise of $0.1 - 1\ EHz$ and a weight below 1 kg. In particular, range into which design parameters of such a MEMS-based gradiometer should fall was investigated by the research group. Apart the natural constraint on the (limited) size and mass, analysis was focused on temperature, spring constant and quality factor. They found out that to have a bandwith within the range $10 - 3 - 1\ Hz$ for the measurements, a device with resonance frequency higher than $1\ Hz$ would be necessary and a low spring constant would needs, at least in the order of $1\ Nm$. However, this makes very difficult to manufacture and to test a weak constant spring. Simulations proved that such a spring would not be strong enough to tolerate gravity on-ground and hence additive masses (gold) should be added. Concerning the other parameters, a quality factor of 105 was assumed to reach a good sensitivity and a temperature of $77\ K$ was

1. Introduction

The measurement of the gravitational field of Solar System bodies is becoming ever and ever crucial in the physical description of their composition, state and evolution. Indeed, many planetary processes at large scale are ruled by their internal structure, where surface and tectonic features are mainly the result of heat exchanges from the interior to the surface [30]. Gravity field measurements are one of the observational methods to investigate those processes and to place constraints on the structure of the planetary interiors and on the formation and geologic evolution of a planet ([40], [30]). The retrieval of the spherical harmonic coefficients used to describe the gravitational field of a body gives insights into e.g. its polar oblateness, moment of inertia and deviations from hydrostatic equilibrium. With geologic assumptions and other remote sensing data, significant geophysical parameters, related e.g. to crust and mantle density and thickness, core size and structure, mantle/core coupling can be obtained ([30]). These parameters are used in planetary models to address topics such as planets differentiation, thermal evolution, characteristics and composition of the interiors. Moreover, the internal structure can be further investigated (wherever possible) through seismometers on the surface, exploiting the analysis of seismic waves travelling through the interior (as performed by Apollo missions EASEP and ALSEP packages and currently by Mars Insight) [1][2].

Until now, the Radio-Tracking technique (RT), part of the Radio Science (RS) observations, jointly with POD (Precise Orbit Determination), has been *de-facto* the main technique for gathering this type of information. It has been implemented in several deep-space missions, such as Magellan (Venus), MRO (Mars), Cassini (Saturn), Messenger (Mercury), Juno (Jupiter), and, in the forthcoming future, BepiColombo (Mercury) and JUICE (Jupiter and its moons).

Concerning scientific targets of interest, it needs to be highlighted that gravity field models are available (section 2), besides the Earth and the Moon, just for few planetary bodies such as the terrestrial planets Mercury, Venus and Mars. However, often such models are restricted only to large spatial resolutions, about one or more hundreds of kilometers, not enough to understand the geophysical processes that have driven formation and evolution of those bodies [32]. The accuracy of these models is good enough as well but just for the lower part of the gravity field spectra, where a sufficient signal-to-noise ratio is achieved. Moreover, there is much more lack of data for the external planets, where only few gravity field parameters have been derived for some of the gaseous planets and their main moons ([34], [90], [91]).

Any improvement on those targets, with a special attention to Venus, Mars and Galilean moons, would be very helpful in understanding their interior and the geophysical and geological processes that operated on them.

To answer the need for higher space resolution and accuracy in planetary gravity fields, two different approaches can be pursued:

1. to improve the measurement performance of the instrumentation used for RS; in these experiments the gravity field to be studied is inferred by the orbit of a spacecraft (that can be considered a ‘proof mass’ falling in the overall external gravity field) and an accelerometer is used to measure the Non-Gravitational Perturbations (NGP) perturbing the spacecraft free-fall, i.e. its motion from a pure (in principle) geodesic of space-time. An improvement of the accelerometer performance and its integration within an enhanced tracking system used to measure the spacecraft position and velocity, are needed conditions to improve the performance of gravity field reconstruction.
2. to introduce innovative measurement concepts, allowing to overcome some of the bottlenecks of the current methods (non-continuous monitoring, field attenuation with the

altitude, disturbances mitigation, etc., [18]). In a roadmap definition, one of the more promising is the gravity gradiometry technique, which would allow to directly sense the gravity field by measuring the gravity gradients, and not just indirectly, as for RT, through monitoring the spacecraft gravitational perturbations. Unlike the radio-tracking, space-based gravity gradiometry has still to unfold its potentialities; indeed, the ESA's GOCE mission is the first and unique till now that has flown a gravity gradiometer to explore Earth's gravity in 2009-13 [136]. The planetary gradiometry still awaits achievements outside the Earth System.

Satellite gradiometry refers to the measurement of acceleration differences, ideally in all three spatial directions, between the test-masses of an ensemble of accelerometers inside one satellite [18]. The differentiation of gravity accelerations allows to highlight small-scale surface and sub-surface features, making such a technique, differently wrt RT, inherently sensitive to medium and large degrees (i.e. high resolutions) of the spherical harmonic representation of the gravity field. Therefore, the use of gradiometry would allow to improve the gravity field knowledge by measuring medium and large degrees, filling the gap above depicted and fostering the investigation on the structure and evolution of the planets.

The activity of this PhD Thesis starts from the definition of the planetary gravity field state of the art and the identification of the needs of the scientific community to improve the planetary bodies knowledge. Based on this result, a selection of targets of interest will be operated. A review of the gravity field measurement techniques will be carried out, identifying advantages and drawbacks, pointing out innovative techniques such as gradiometry. On the basis of these activities, a series of numerical simulations will be implemented to produce the time series of gradiometric signals foreseen in a set of case studies. The choice of the case studies will be based on the preliminary studies about the science needs. The main outcome will be a set of requirements to be matched by a typical gradiometric instrument/mission, aiming at fulfilling the scientific needs. An important requirement would be, for instance, the typical instrument sensitivity and spectral band, as well as the expected acceleration or gravity gradient amplitude of a signal sensed with a reasonable signal-to-noise ratio. Different scenarios will be simulated on the basis of the science needs.

In chapter 2 the gravity field is faced from the theoretical point of view and a snapshot of the current understanding of gravity field of planetary bodies is carried out. At last, science needs are identified and planetary bodies of interest are selected.

In chapter 3 measurement techniques of the gravity field are described, focusing the attention on the gravitational gradiometry. Advantages and drawbacks are considered. Moreover, spaceborne, airborne and groundborne gradiometric instruments have been identified and analysed to identify the current state of the art.

In chapter 4 gravity mission needs are identified in terms of science and mission requirements. Afterwards, a matlab code developed to compute the gravity gradient signal expected in some case studies is described and evaluated. At last, analysis of ways to increase the sensitivity of gradiometers is carried out.

In chapter 5, based on analysis of previous chapters, an instrument concept is introduced and analysed to match the requirements identified. The basic performance are derived, discussed and compared to the signal that is expected to be measured according to the computation carried out with the matlab code. Future work foresees to further develop the concept and to further deep the analysis of the identified gradiometer configurations.

2. The Gravity Field of Planetary Bodies

2.1 Scientific motivations

The study of the origin and the evolution of the Solar System is a relatively recent domain in the modern science investigation. After the first studies in 1500-1600 with Tycho Brahe, Johannes Kepler and Galileo Galilei, followed by the discovery of the gravitational law by Isaac Newton, Solar system bodies were intensively studied by astronomers and physicists. A fundamental breakthrough in this direction was the beginning of the space era on the 4th of October 1957. That day, a small round-shaped object launched by the URSS, Sputnik 1, become the first artificial satellite orbiting the Earth. Since then, the run to conquer the space environment around Earth is increased, powerfully pushed by the struggle between USA and URSS during the Cold War. Moreover, the extraordinary technological developments achieved in the previous decades allowed to make conceivable the exploration of space well beyond the Earth's closeness. The rush to space was extended to Moon at first, followed by Venus, Mars, Mercury. Each mission pushed some steps forward in the technological capability of sending an artificial probe to specific targets, routing it on the right path, and communicating and commanding it following the desiderata. At the same time, the capability of hosting on-board sensing instruments working at different wavelengths and able to study multiple aspects of the bodies increased more and more. Such probes allowed to study different aspects of planetary bodies such as atmosphere, surface and interiors through the use of on-board payloads devoted to sound with cameras, spectrometers, altimeters, radar at several wavelengths of the electromagnetic spectrum. At last, the spectacular achievement of landing human beings on the Moon in 1967, proved that the Solar System was not so far from us as before.
The coming of space era on the 4th October 1957 with the launch of Sputnik gave a strong push to the study of the Solar System with the use of spacecrafts launched very close to their object of investigation. However, besides this wondering possibility, since from the first Sputnik was clear that the spacecraft itself could bring valuable science benefits simply observing its orbital motion. Actually, the orbit followed by a spacecraft around a central body (Earth or other) is ruled out by the Kepler laws which are loosely related to the Newton's Law of Gravitation. The gravitational force affects the behaviour of the spacecraft which acts as a test mass plunged into the field generated by the central body. The characteristics of the orbit reflect peculiarities of the body mass distribution. The Kepler laws are exactly satisfied when we deal with bodies of spherical shape and homogeneous mass distribution. When the shape starts differing from it, deviations arise as much as the shape become more complex and variable. The capability of identifying those peculiarities are tightly loose to the ability to accurately follow the trajectory of the spacecraft.
It needs to highlight that in this chapter just satellite methods to determine the gravity field will be addressed, whereas groundborne, shipborne and airborne techniques, essentially based on absolute and relative gravimetry, are not dealt with.
Therefore, precise and detailed knowledge of the gravity filed of celestial bodies is essential for revealing and understanding their internal structure and composition, and also for applications such as mission operations.
In this field, generally named planetary sciences, the science approach is necessarily interdisciplinary, involving knowledge of geology, geophysics, astronomy, astrophysics, science of atmosphere, biology, chemistry and a lot of other disciplines. Due to its natural pervasiveness and to the capability of attraction and modelling of macroscopic mass objects, the research and study of the gravity field is an integral part of planetary sciences. Indeed, origin, development and evolution of Solar System, both as whole and as its main

components such as Sun, planets, asteroids and comets, are deeply related to the gravity field interactions. Gravity field information constitute powerful constraints and indications for the reconstruction of planets history and evolution, from the formation till to the current imagine.
It needs to highlight that in this thesis just satellite methods to determine the gravity field will be addressed, whereas groundborne, shipborne and airborne techniques, essentially based on absolute and relative gravimetry are not dealt with.

Table 2-1 Milestones in the measurement of gravity field through satellite geodesy (adapted and elaborated from [48])

Year	Event	Implications
1958	Determination of the oblateness from tracking of Sputnik	• Definitive determination of the Earth's oblateness
1959	Determination of the "pear shape" of the Earth (odd zonal harmonic)	• First determination of a gravity term not associated with rotation • Showed that Earth has major density variations not associated with isostaic topographic compensation
1963	Longitudinal variations from camera tracking included in gravity field determination	• confirmed the "$10^{-5}/l^2$" rule for the decrease in magnitude of variations in gravity with degree l; $\pm 27\,m$ rms error in the geoid
1965	Doppler tracking from US Navy TRANET network included in gravity filed determination	• significantly improved gravity filed accuracy to $\pm 12\,m$ rms error in the geoid
1968	Effetcive satellite-to-satellite tracking, i.e. Earth to lunar satellite	• Mapped the front-side field of the Moon to better accuracy than contemporary measurements of the Earth
1975	The first altimetric satellite Geodetic Satellite Mission (GEOS-3)	• Measured sea-level height at the 1 m-level, an order of magnitude improvement in the ocean geoid
1979	Incorporation of laser ranging data into gravity field solutions	• Significantly reduced systematic error and improved accuracy of the geopotential field
1979	Gravity field of Mars determined from Mariner orbiters	• Showed a gravity field twice as great in its irregularities as predicted from Earth's field
1981	Gravity field of Venus determined from Pioneer orbiter	• Showed a gravity field of much greater geoid:topography ratio that the Earth's, implying depths of compensation greater than 100 km
1983	Generation of marine gravity field from Seasat data	• Revealed major uncharted tectonic features of the ocean floor
1983	Detection fo the change in Earth's oblateness from high LAGEOS spacecraft	• Implied an increasing spin rate consistent with the long-term post-glacial motion of matter toward the rotation axis

1987	Incorporation of tidal variations in gravity field determination	• Provided important constraints on ocean-tide solutions
1987	Analysis of monthly gravity data from LAGEOS and complementary atmospheric pressure data	• Linked seasonal variations of the geopotential with atmospheric pressure variations
1993	Comprehensive solution incorporating altimetry, surface gravimetry, an GPS tracking (Joint Gravity Model – JGM3)	• Determined the gravity field to the 70th degree, plus tides, to an estimated geoid accuracy of $\pm 0.5\ m$
1995	Mass of asteroid 243 Ida determined from Galileo spacecraft Doppler tracking	• Bulk desity consistent with “rubble-pile” model of asteroids
1995	Inference of tidal Love number of Venus from Magellan Doppler Tracking	• The high value (0.27) indicated that Venus has a completely fluid core, consistent with the absence of an energy source for a Venusian magnetic field
1995	Geodesy satellite altimetry (ERS-1 acquired; Geosat declassified)	• Led to a global map of the oceanic gravity field with a resolution of 20 km
1996	Measurement of the ellipsoidal fields of the Galilean satellites	• Moment of inertia indicated big irone cores in Ganymede and Europa, a modest core in Io, and no core in Callisto
2000	First satellite-to-satellite mission around Earth, in the high-low mode (CHAMP)	• global magnetic and gravity fields mapping
2002	First satellite-to-satellite mission around Earth, in the low-low mode (GRACE)	• First systematic and continouos measure of the time-variable gravity field (monthly)
2009	First space gradiometer mission around the Earth (GOCE)	• measurement of the geoid with an accuracy 1-2 cm and gravity anomaly 1-2 mGal, till to degree and order l ~200 (~ 100 km)
2011	First satellite-to-satellite mission around Moon (GRAIL)	• measurement of the lunar gravity field to degree and order $l\ = 1800$
2018	Extension of GRACE mission (GRACE-FO), added inter-satellite laser link	• continuity of the GRACE measures, improvement in the inter-satellite ranging

2.2 Theoretical foundation

2.2.1 Gravitation and orbits

The gravitation is a physical phenomenon so remarkably widespread and ubiquitous for the humankind that since the ancient ages it has been generally considered for granted and accepted without other significant speculations. Ancient populations, at first Chaldeans and Babylonians, conducted widespread observations and understanding of astronomical phenomena such as Moon, Sun and stars motion exploiting them especially for agriculture and religion concerns. Several Greek astronomers and mathematicians, among them

Eratosthenes, Hypparchus, Pytagoras and Ptolemaeus, faced many problems concerning geometry, mathematics along with Earth shape, stars motion and at last the ancient cosmogony, summarised in the "*Almagest"* by Ptolemaeus [11]. Ptolemaeus, also on the basis of previous speculations from Hipparchus, developed his theory for an Earth-centred Solar System, which allowed to explain the observed motion of Sun and planets, although with an increasing complexity. However, the time to face the physical cause of observed motions was far to come. The Greek philosopher Aristotle asserted that gravitation is a natural property of material things, causing them to fall or rise (in case of some gases), and the more material the greater this tendency [6]. Till to the arrival of the scientific method, no further explanation was needed.

A first attempt to bridge the gap between ancient times and modern epoch was realised by Nicholas Copernicus (1473-1543). His work emerged in a period of significant transformations and innovations such as the discovery of the New World by Cristoforo Colombo, the invention of the telescope, with its reconstruction and the consequent applications by Galileo, and the development of the printing press by Johann Gutenberg. Copernicus devoted more than 31 years to understand the fundamental motions of the Solar System and summarised his work in the "*De Revolutionibus Orbium Coelestium*". He proposed a planetary system Sun-centred, changing radically the traditional view by Ptolomaeus. Indeed, the theory of Copernicus showed off three differences with respect to Ptolemaic theory: the Sun at the centre, new numbers and data, details of planetary motion [1].

In between 1500 and 1600 Galileo Galilei (1564-1642), the father of the experimental method, was the first one to face in depth the nature of gravitation through observations and investigations. His experiments on the falling bodies allowed to change the Aristotelian view and to separate the action of the gravitation from the mass of the falling object. Indeed, he proved the "Universality of Free-Fall" (UFF), i.e. different bodies fall with the same acceleration, disregarding the mass of the body. Galileo was the first to test the UFF, using two pendula of different composition to an accuracy of about 10^{-3} [7][8][9]. Today this has been verified with very high accuracy and it constitutes the bulk of Einstein Equivalence Principle in the weak version (Weak Equivalence Principle). Although this was a giant step from the philosophical speculation to the scientific evidence, Galileo experiments faced just locally the behaviour of bodies under the gravitation influence.

A further step towards the understanding of gravitation happened at the beginning of 1600. Johannes Kepler (1571-1630), capitalising on the availability of several years of accurate observations of planets that Tycho Brahe had carried out to develop his model of the planetary system, tried fitting different geometrical curves to those data, in particular related to the position of Mars. After almost a year he found out the ellipse as possible fitting solution. After this first result, in 1609 Kepler published the first two laws of planetary motion, whereas the third one followed in 1919. The famous Kepler's laws marked an historical breakthrough in astronomical and physical science because they explained for the first time the planets motion in a simpler manner with respect to Ptolemaeus theory. Such an extraordinary result needed to reject the hypothesis of Earth at the center and circular orbits:

1. First Law: the orbit of each planet is an ellipse with the sun at one of its foci
2. Second Law: each planet revolves so that the line joining the planet to the Sun sweeps out equal areas in equal time (*Law of areas*)
3. Third Law: the square of the period of a planet (T) is proportional to the cube of its mean distance from the Sun

The third law in the generalised form (i.e. m not negligible with respect to M) is formulated often as in the following:

$$\frac{a^3}{T^2} = \frac{G(M+m)}{4\pi^2}$$

where a is the semi-major axis, T is the orbital period, M and m are the masses of two orbiting bodies. For the Solar System, the condition $M \gg m$ is well satisfied with M mass of the Sun and m mass of the planet, hence the ratio a^3/T^2 can be considered a constant.
However, these laws were just a cinematic description of the motion whereas an explanation of causes, of the dynamics, remained unsolved till to Newton.

Isaac Newton (1642-1727) in 1665 was a student at the University of Cambridge when an outbreak of plague forced the University to close till the spring of 1667 [1][25]. The obligated "holidays" were the most creative period of Newton since he was able to produce the law of gravitation, the three laws of motion and developed the fundamentals of differential calculus [25]. However, the complex personality of the man prevented the publication of most of those results for more than twenty years. Edmund Halley (1656-1742), the discoverer of the comet, was the most important supporter of Newton work. At last Halley convinced Newton to complete and to publish all his work on planetary motion. Two years occurred to complete all the process in 1686. The publication, paid by Halley and published in 1687, is the famous and monumental "Philosophiae Naturalis Principia Mathematica" where, besides the laws of motion, the law of Universal Gravitation was stated by Newton. With his studies and on the basis of results of his pioneers Newton concluded that the motion of Moon and planets obeys the same law of falling objects on the Earth (the famous "apple"). Figure 2-1 shows the link between the two phenomena apparently disconnected. This intuition allowed to him to formulate the law of Universal Gravitation: both the fall of objects on the Earth and the motion of planets is attributed to an attractive force, the gravitation, and the law states that two bodies are attracted each other with a force F proportional to the product of their masses, M and m, and to the universal gravitational constant, G, inversely proportional to the square of their relative distance r and which acts along the line joining the body centres:

$$\vec{F} = -G\frac{Mm}{r^2}\hat{r}$$

Newton concluded with his studies on the basis of Kepler observations and the three laws.
The standard and known value of the gravity acceleration $\vec{g}$ is $9.8\,m/s^2$. This value for the gravitational acceleration was for a long time assumed to be constant for the entire planet. However, the use of more and more sensitive tools allowed to verify that the force of gravity actually varies from place to place on the surface of the planet. The standard value refers to Earth as a homogeneous sphere, but actually this value ranges from a minimum of $9.78\,m/s^2$ at the Equator to a maximum of $9.83\,m/s^2$ at the poles.

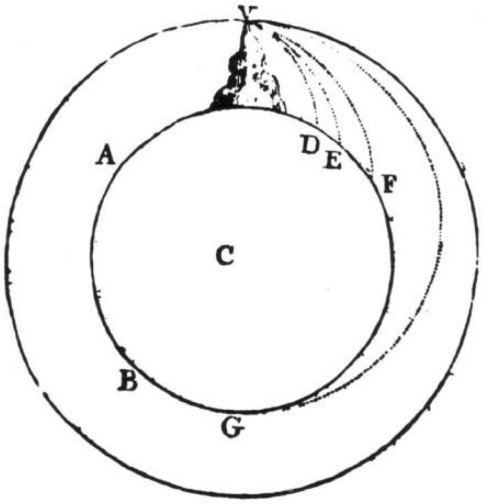

Figure 2-1: Figure extract from “De mundi systemate” by Isaac Newton (1715), Vol. 3 of “Philosophiae Naturalis Principia Mathematica”, which depicts as the free-fall of objects and the planets orbit have the same origin

Indeed, the global gravity field of a planet is the result of the superposition of several contributions whose signals decrease as much as the spatial scale reduces. Figure 2-2 shows different ssources of signal and the related order of magnitude with respect to the global signal $\vec{g}$. Effects of first order come from the spherical shape. For instance, considering the Earth, the contributions to the gravity acceleration $\vec{g}$ are the effects of a spherical Earth at order one. The most significant deviation from the standard value of g is a result of Earth’s rotation. As Earth spins, its shape is slightly flattened into an ellipsoid, followed by the flattening due to rotation. Effetcs due to rotation and equatorial bulge are of order $10^{-3}g$, mountains and ocean trenches are of order $10^{-4}g$ and so on.

Type	Signal size vs g (m/s^2)	Contribution
Static	10^{0}	Earth as homogeneous sphere
	10^{-3}	Oblateness and centrifugal acceleration
	10^{-4}	Mountains, valleys, ocean ridges, subduction zones
	10^{-5}	Density variations in lithosphere and upper mantle
	10^{-6}	Sediments, salt domes, ores
Dynamic	10^{-7}	Solid earth and ocean tides
	10^{-8}	Loading effects, atmospheric pressure, groundwater variations
	10^{-9}	Polar motion, ocean topography (sea level)
	10^{-10}	General Relativity

Figure 2-2: components of the gravitational acceleration in terms of sources and related order of magnitude (rielaboration from [136])

2.2.2 Spherical harmonics

The gravitational force is described by the Newton's law which states that the force is proportional to the masses of the involved bodies and to a universal constant G, the universal gravitation constant (the first constant of physics), whereas at the same time scales as inverse of the squared distance between the bodies:

$$\vec{F} = -G\frac{Mm}{r^2}\hat{r}$$

According to the classical theory, the gravitational field is a vector field which is generated by a mass M following the expression:

$$\vec{g} = -G\frac{M}{r^2}\hat{r}$$

derived from the previous equation and in which $\vec{g}$ is the usual gravitational acceleration. Being the gravitational force a conservative field, it can be expressed through a potential:

$$V = -G\frac{M}{r}$$

i.e. for an extended body:

$$V(\vec{x}) = G\int\frac{\rho(\overrightarrow{x'})}{|\vec{x}-\overrightarrow{x'}|}d\overrightarrow{x'}$$

where ρ is the mass density of the body located at $\overrightarrow{x'}$, $\vec{x}$ is the position where the potential is evaluated on all the volume supporting the mass distribution, such that:

$$M = \int\rho(\overrightarrow{x'})\,d\overrightarrow{x'}$$

and the gravitational acceleration can be obtained from:

$$\vec{g}(\vec{x}) = -\nabla V(\vec{x})$$

The gravitational acceleration satisfies the Laplace equation:

$$\nabla\cdot\vec{g} = -4\pi G\rho$$

Combining the previous equations, we get:

$$\nabla^2 V = -4\pi G\rho$$

which is the well-known *Poisson's equation* [10][11]. If we apply the equation outside the attracting body, in empty space, the density is zero and the Poisson equation is reduced to the *Laplace's equation*:

$$\nabla^2 V = 0$$

or explicitly:

$$\frac{\partial^2 V}{\partial x^2} + \frac{\partial^2 V}{\partial y^2} + \frac{\partial^2 V}{\partial z^2} = 0$$

In general, any function $V(x, y, z)$ which is solution of the Laplace's equation is a *harmonic function*. Moreover, it can be proved that every harmonic function is analytic, i.e. it is continuous and has continuous derivatives of any order [10]. Hence, the gravitational potential generated by an extended body is harmonic at all points where there are no attracting masses and hence also the outer potential of a planetary body. This result is very important since it opens the possibility to represent in advantageous way the gravitational potential of a body in space (hence the gravity field). To do this, it occurs to look for solutions of the Laplace's equation.
Solutions of the Laplace's equation can be better determined by using spherical geocentric coordinates $V = V(r,\ \varphi,\ \lambda)$ (Figure 2-3), where r is the distance from the center, φ is the latitude $[-\pi/2\,, +\pi/2]$ and λ is the longitude $[0, 2\pi]$.

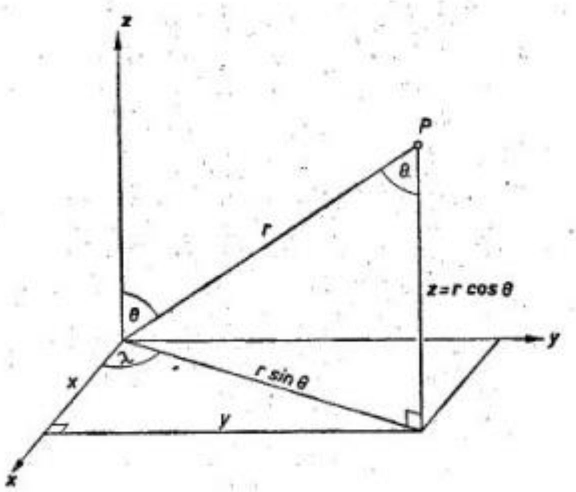

Figure 2-3: spherical and rectangular coordinates (from 10)

Considering the transformations which relate spherical and cartesian coordinates:

$$\begin{cases} x = r\cos\theta\cos\lambda \\ y = r\cos\theta\sin\lambda \\ \quad z = r\sin\varphi \end{cases}$$

the Laplace's equation in spherical coordinates [11].
In general, the equation is not easy to solve, apart considering simple boundaries [6] [11]. This is the case when the gravitational potential has spherical symmetry around the origin, that is $V(r,\ \varphi,\ \lambda) = R(r)$. In this condition, all the possible spherically symmetric harmonic functions are as the following [11]:

$$R(r) = \frac{k}{r} + const$$

Choosing the constant equals to zero, it derives that the solution coincides with the gravitational potential of a point mass in the origin and with mass $M = k/G$. This implies that

the gravity field generated by two spherically symmetric planets with equal mass is the same outside both planets. In general, the same harmonic function can be generated by many different mass distributions [10]. It is therefore not possible to determine uniquely the mass distribution from the external potential; the *inverse problem of the potential theory,* i.e. the determination of the internal mass distribution of a planetary body from the measure of the gravitational field on or outside its surface, has no unique solution. Additional information is needed to determine uniquely the mass distribution, for instance, through the planet rotation, seismology, or magnetic field. In general, the problem of computing the harmonic function inside or outside a surface S (not necessarily a sphere) from its boundary values on S is known as *Dirichlet's problem* [10].
The most important harmonic functions are the *spherical harmonics*. Considering spherical shapes (approximation for the planet surface) and adopting spherical coordinates, we look for solutions by separating the variables in the shape $V(r,\theta,\lambda) = f(r)Y(\theta,\lambda)$. It can be proved [10][11] that solutions of the Laplace equation are the following functions:

$$V(r,\varphi,\lambda) = r^l\, Y(\varphi,\lambda)$$

$$V(r,\varphi,\lambda) = \frac{Y(\varphi,\lambda)}{r^{l+1}}$$

with l a suitable integer constant. These functions are known as *solid spherical harmonics*, whereas the angular parts are known as *surface spherical harmonics* [10]. The solutions with r^l describe the gravity field inside a cavity surrounded by a mass distribution: they are *internal harmonics*. Those with $1/r^{l+1}$ describe the gravity field outside the cavity including the mass distribution: they are *external harmonics* and are of interest for the gravity field representation.
Approaching in the same way for functions $Y(\theta,\lambda)$ and looking for solutions in the shape $Y(\theta,\lambda) = g(\theta)h(\lambda)$, it can be proved that solutions are as follows [10]:

$$Y_l(\theta,\lambda) = P_{lm}(\sin\varphi)\cos m\lambda$$

$$Y_l(\theta,\lambda) = P_{lm}(\sin\varphi)\sin m\lambda$$

where l and m are integers, $P_{lm}(\sin\theta)$ are the so-called Legendre functions which are used to derive these solutions [11]:

$$P_{lm}(\sin\varphi) = (1-\sin\varphi^2)^{m/2}\sum_{j=0}^{L} T_{lmj}\sin\varphi^{l-m-2j}$$

where L is the integer part of $l - m/2$ and:

$$T_{lmj} = -\frac{(l-m-2j+1)(l-m-2j+2)}{2j(2l-2j+1)}T_{lmj-1}$$

The general solution of the Laplace's equation will be a linear combination of all those solutions, i.e., limiting just to external harmonics, as in the following [11][12]:

$$V(r,\lambda,\varphi) = \frac{GM}{r}\sum_{l=0}^{+\infty}\sum_{m=0}^{l}\left(\frac{R}{r}\right)^l P_{lm}(\sin\varphi)(C_{lm}\cos m\lambda + S_{lm}\sin m\lambda) \tag{2-1}$$

or, equivalently:

$$V(r,\lambda,\varphi) = \frac{GM}{R}\sum_{l=0}^{+\infty}\sum_{m=0}^{l}\left(\frac{R}{r}\right)^{l+1} P_{lm}(\sin\varphi)(C_{lm}\cos m\lambda + S_{lm}\sin m\lambda) \tag{2-2}$$

where R is a reference radius (the equatorial radius, in general), P_{lm} are the fully normalised Legendre functions, l and m are respectively degree and order of spherical harmonics, C_{lm} and S_{lm} are the coefficients of the spherical harmonics or Stokes'. This expression is provided in geocentric spherical coordinates r, λ, φ, respectively radius, longitude and latitude (see Appendix for a definition).
The consequence is that the gravitational potential V of a planetary body is a harmonic function in free space and at the same time every harmonic function can be represented as a Newtonian potential of a mass distribution. This result is very important and allows to represent the gravitational field in terms of potential V generated by a body at any point $P(r, \lambda, \varphi)$ on and above its surface by summing up over degree and order of a spherical harmonic expansion.
The harmonic coefficients (C_{lm}, S_{lm}) constitute the spectrum of the harmonic expansion and are therefore sometimes named *spectral coefficients*. Known such coefficients of a specific degree l over orders m ($m = 0,1,2 \ldots l$), the *power spectrum of the field* σ_l^2 (or $\boldsymbol{c_l}$), also named *signal degree variance*, can be computed as [15][16][17][125]:

$$\sigma_l^2 = \sum_{m=0}^{l}(C_{lm}^2 + S_{lm}^2) \tag{2-3}$$

The degree variance can be interpreted as the power spectral density of a function and it indicates the energy content of the signal per frequency l.
Often, the square root of the power spectrum, the Root-Mean-Square value (RMS) per degree, also known as *signal degree amplitude* and somewhere indicated as σ_l, is used in place of the power spectrum to evaluate the gravity signal amplitude:

$$\sigma_l \equiv \sqrt{c_l} = \sqrt{\sum_{m=0}^{l}(C_{lm}^2 + S_{lm}^2)} \tag{2-4}$$

Moreover, the *signal degree-order variances* σ_{lm}^2 can be computed as well from the previous power spectrum when the power spectrum is averaged over all the m degrees:

$$\sigma_{lm}^2 = \frac{\sigma_l^2}{2l+1} \tag{2-5}$$

More often, the square root of the signal degree-order variances, σ_{lm}, is used. They are referred to as RMS power per coefficient per degree and represent the expected average (RMS) signal content per l, m:

$$\sigma_{lm} \equiv \frac{\sigma_l}{\sqrt{2l+1}} = \sqrt{\frac{\sigma_l^2}{2l+1}} \tag{2-6}$$

The degree and degree-order variances σ_l^2, σ_{lm}^2can be computed, beside in terms of unitless coefficients (i.e. by using the normalised spherical harmonic coefficients), also for a given gravity functional, such as geoid heights (N, unit m, coefficient R), in terms of gravity anomalies (Δg, unit m/s^2, coefficient $(l-1)GM/R^2$), and in terms of vertical gravitational gradient (double spatial derivative of radial gravitational potential Γ_{rr}, unit s^{-2}, coefficient $(l+1)(l+2)GM/R^3$).
The signal degree amplitude in terms of geoid height, gravity anomaly and vertical gravitational gradient are the following ones:

$$\sigma_l(N) = R\,\sigma_l$$

$$\sigma_l(\Delta g) = \left(\frac{GM}{R^2}\right)\left(\frac{R}{r}\right)^{l+2}(l-1)\,\sigma_l \tag{2-7}$$

$$\sigma_l(\Gamma_{rr}) = \left(\frac{GM}{R^3}\right)\left(\frac{R}{r}\right)^{l+3}(l+1)(l+2)\,\sigma_l$$

Typically, an estimate on the RMS of the gravity coefficients per degree is achieved by using a rule established by Kaula [13] in 1963. Kaula's rule states that the RMS of Stokes coefficients follows a power law according to:

$$\sigma_{lm} = \frac{\sigma_l}{\sqrt{2l+1}} = \sqrt{\frac{\sum_{m=0}^{l}(C_{lm}^2 + S_{lm}^2)}{2l+1}} = \frac{k}{l^2} \tag{2-8}$$

where l is the degree of the coefficient and k is a constant whose value depends upon the planet: $\mathrm{k} \cong 9\ 10^{-6}$ for Earth [53], $\mathrm{k} \cong 1.2\ 10^{-5}$ for Venus [64], $\mathrm{k} \cong\ 8.5\ 10^{-5}$ for Mars [80], $\mathrm{k} \cong 3.6\ 10^{-4}$ for the Moon [131], $\mathrm{c} \cong 4\ 10^{-5}$ for Mercury [54].
This rule has been used as an a priori information bound on the gravity coefficients of other planetary bodies before their gravity fields are measured by spacecraft.
In planetary geodesy, the science of the measurement and representation of the planets, the gravity field of a planet is analysed in terms of a "gravity field model", i.e. a mathematical representation of the gravity field in the three-dimensional space through a spherical harmonic expansion [14]. The gravity field model is used to approximate the real gravity field. However, in order to model the real gravity field exactly, we would need infinite coefficients perfectly determined. This is not possible and just a limited number of coefficients can be determined and used to approximate the real field as accurately as possible. In this frame, a gravity field model foresees a maximum degree l_{max} and includes $(l_{max}+1)^2$ coefficients [12]. The model represents the planet's gravity field with a spatial resolution depending on the maximum degree l_{max}. Its accuracy is established by two errors, namely omission and commission error [15].
The omission is referred to the error occurring because of the truncation of the spherical harmonic series expansion at some degree (l_{max}); indeed, the terms above the maximum degree (shorter wavelength than the resolution limit of the model) are omitted.
The commission is related to the errors existing in the potential coefficients themselves, i.e. the accuracy of the Stokes coefficients (C_{lm} and S_{lm}). Since the coefficients cannot be determined perfectly, every single coefficient has an error component (formal or calibrated). Moreover, higher degree coefficients are subjected to larger errors. Indeed, the accuracy refers to a certain wavelength interval and it is different for different wavelength intervals. At

last, the commission error increases as the maximum degree, l_{max}, of the spherical harmonic expansion increases, whereas the omission error decreases.
The representation of the gravity field through equation (2-1) with a maximum degree l_{max} corresponds to a low-pass filtering, where l_{max} refers to the spatial resolution at the Earth surface [12]. An estimate of the smallest gravity field feature represented by the gravity model (the shortest half-wavelength ψ_{min}) is as follows [12]:

$$\psi_{min} = \frac{\pi R}{l_{max}} \tag{2-9}$$

Where R is the equatorial radius of the planet; such an estimate follows from the number of possible zeros along the equator.
However, it can be proved that a more precise evaluation of the resolution is carried out by the following equation (in radians) [12]:

$$\psi_{min} = 4\sin^{-1}\left(\frac{1}{l_{max}+1}\right) \tag{2-10}$$

The corresponding value in metric unit for the resolution is:

$$\Delta s = \psi_{min} R \tag{2-11}$$

This value characterises the size of the smallest feature, half-wavelength, which can be produced by the $(l_{max}+1)^2$parameters.
Three different spherical harmonics coefficients are identified (), according to the terms:

$$P_{lm}(\sin\varphi)(\cos m\lambda)$$

$$P_{lm}(\sin\varphi)(\sin m\lambda)$$

the zonal coefficients ($l \neq 0, m = 0$), the sectorial coefficients ($l = m \neq 0$) and the tesseral coefficients ($l \neq 0, l \neq m \neq 0$). Each one corresponds to a different mass distribution, as shown in Figure 2-4, along with a scheme of the coefficients structure [17].
In these developments, the coefficients of the spherical harmonics have to be determined by the particular mass distribution for any given planet or body. If these coefficients can be inferred from some method, the expansion in spherical harmonics can be “inverted”, in principle, to find out the mass distribution inside the planet required to produce these coefficients. Indeed, the characteristics of the gravitational field outside a planet are completely established by its internal mass distribution. However, gravity information alone is not enough, as highlight above, to determine the internal mass distribution of a planet [11].

The physical quantities that can be derived from the gravity field are typically named gravity field functionals [20][15]. For some of them, additionally, the knowledge of a reference system is necessary. There are functionals which are 3-D functions in the space outside the Earth, and there are functionals which are only dependent on latitude and longitude, therefore they are 2D functions.
Such gravity functionals are introduced in order to translate the “raw” gravitational information derived from the measurement of spherical harmonics coefficients into geophysical and geodetic quantities useful to be processed and interpreted by the scientific community. Such functionals are typically used in geophysics, geodesy and geology to infer

information about the surface and internal structures observed on a planet. It is worth here to mind that the geodesy is the discipline that deals with the measurement and representation of the Earth, the gravity field and geodynamic phenomena such as polar motion, Earth tides and crustal motion. On the other hand, geophysics uses gravity to learn about the density variations of the Earth's interior, whereas classical geodesy uses gravity to define the geoid.

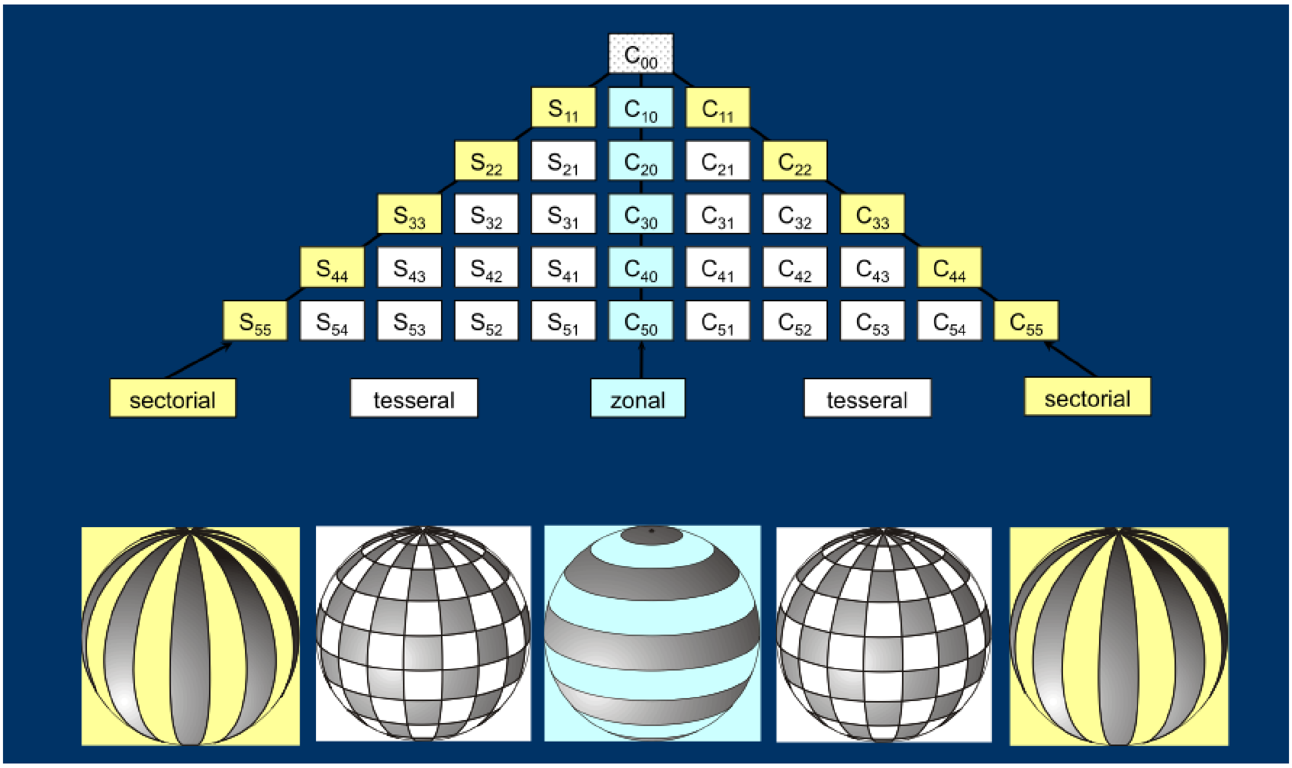

Figure 2-4: Representation of the different types of spherical harmonic coefficients [17]

Four main observables are typically used: geoid height (known also as geoid undulation or anomalies), gravity disturbances, gravity anomalies and gravity-gradients. The origin of these functionals is well understood considering that gravity of a planet is closely associated to three different surfaces: the topographic surface (the real planet surface), the ellipsoidal surface (geometrical model), i.e. a mathematical model of the surface, and the geoid (physical model), i.e. a surface as defined by the planet's gravity. Figure 2-5 helps us to understand the differences between those surfaces.

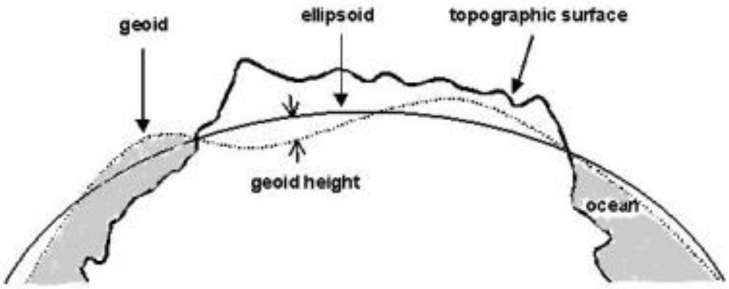

Figure 2-5: Difference between geoid, ellipsoid and topography

The equipotential surface of the Earth's gravity field that coincides with the Mean Sea Level (MSL) in the absence of currents, air pressure variation, etc., is called the geoid.
Most of the efforts in physical geodesy are concentrated on the geoid determination with steadily increasing accuracy (10). The geoid is important for understanding more about ocean currents and is also used as a reference for traditional height systems and monitoring sea-level change. However, as in the case of any other equipotential surface of the Earth's gravity field, the geoidal surface is also an irregular surface and too complicated to serve as the computational surface.
The mathematical surface that best fits the geoid is the reference ellipsoid. The relation between the geoid and the ellipsoid is shown in Figure 2-5. The ellipsoid lies below the geoidal surface in elevated regions and above the MSL over the oceans. The geometrical separation between the geoid and the reference ellipsoid is called the geoidal undulation, N, which generally varies globally between 110 m and 30 m (21).
On a planet the gravity is the result of combining the gravitational acceleration and the centrifugal rotation due to the rotation. In geodesy, such a term is used to distinguish form gravitation, which is referred just to the gravitational field alone.
Each one of these surfaces can be used as vertical datum, i.e. as zero surface to which heigths or elevations can be referred. Hence, different "heigth" can be considered, depending on the envisaged application. The height of a point of the topographic surface can be referred to the ellipsoid and defined as the vertical wrt the ellipsoid surface: h ellipsoid height. Alternatively, the height can be considered as the vertical wrt the geoid, i.e. the surface as defined Points on or near the Earth's surface (the subject is the same for other terrestrial planets) are described through three coordinates, latitude, longitude and height.

2.3 Planetary Interiors

There are different ways through which is possible to study the surface and the interior of a planet [29], basically identified by four approaches: seismology, magnetic field studies, investigation of planetary rotation, gravity analysis.
As well known for the Earth, one of the most powerful and direct methods to investigate the internal structure of a planet is the analysis of seismic waves travelling through the different layers of the body interior. However, the transfer, sic et simpliciter, of such a methodology to a planet or satellite different from Earth, poses several problems. The deployment of a network of seismometers, for instance, on the surface of Mars or Venus, or some galileian or saturnian satellite (in order to study the extremely interesting interior), would be costly, on long-term timing and very challenging from the technological point of view. Nonetheless, beside the first seismometers deployed on the Moon with Apollo missions, followed by Viking 1 and 2 on Mars, a new small step in this direction is on-going through the InSight lander, launched towards Mars on Mid 2018 and landed on November 2018. The unique on-board SEIS seismometer (Seismic Experiment for Interior Structure) collecting waves from marsquakes, thumps of meteorites or magma churning in depth, will provide some insights on the planet interior.
Magnetic field studies investigating the magnetic induction response to time-variable magnetic files can help in determining how the body's electrical conductivity (related to the composition) changes with depth [30].
The measurement of the gravity field of a planet allows to infer fundamental information about its internal structure and its surface. Typically, gravity field models are recovered through a reconstruction of the coefficients of the spherical harmonics. Depending on the technique applied and its characteristics (see section 3), just a limited number of coefficients

are determined, on the basis of the maximum degree l to which is possible to measure with sufficient accuracy. Such coefficients provide information on the contribution to the gravity physical information at different spatial scales depending on the consider degree l. Moreover, those coefficients are related to geodetic and geophysical properties of the body. Indeed, it is possible to prove ([1], [23]) that the Stokes coefficients are the normalised multipoles of the planet's mass density distribution $\rho(\vec{r})$ ([1], [27]). In particular, the degrees two harmonic coefficients of the gravity field ($C_{20}, C_{21}, S_{21}, C_{22}, S_{22}$) are related to the inertia matrix of the planet ([1], [23]) and hence depends on the distribution of the mass in the interiors. They can be expressed in terms of the moments of inertia:

$$C_{20} = -J_2 = \frac{1}{MR^2}\left(\frac{A\ +\ B}{2} - C\right)$$

$$C_{21} = -\frac{1}{MR^2} I_{13}$$

$$C_{22} = \frac{1}{4MR^2}(B - A)$$

$$S_{22} = -\frac{I_{12}}{2MR^2}$$

$$S_{21} = -\frac{I_{23}}{MR^2}$$

where M and R are the mass and the mean radius of the body, respectively, $C > B > A$ are the principle moments of inertia of the body (C is the axial moment of inertia), and the other terms are the products of inertia, following the inertia matrix I:

$$I = \begin{pmatrix} A & I_{12} & I_{13} \\ I_{12} & B & I_{23} \\ I_{13} & I_{23} & C \end{pmatrix}$$

Indeed, measurements of the degree two harmonic coefficients of a planet allow to infer information about interior structure through the estimates of its moments of inertia. From these data, different geophysical models of the interiors can be compared and constraints can be derived to explain the observations.

However, since there are five Stokes coefficients versus six independent components of I, the determination of moments of inertia from the measurements of the harmonic coefficients is not unique [27]. Additional information need to be gathered, for instance through the monitoring of the rotation state of the body [27], or altimeter data.

Actually, this is a more general issue in gravity field determination. As pointed out by the Gauss theorem, the flow of the gravitational field $\vec{g}$ generated by a point mass M across an oriented (from inside to outside) surface S (including M into the volume V) is the following:

$$\Phi(\vec{g}) = \int_S \vec{g} \cdot \overrightarrow{dS} = \int_S -\frac{GM}{r^2} dS \cos\theta =$$

$$-GM \int_S \frac{1}{r^2} dS_n = -GM \int_S d\Omega = -4\pi GM$$

$$\Phi(\vec{g}) = -4\pi GM$$

i.e. the flow of $\vec{g}$ is not depending on the position of the mass M inside the closed surface S but just on the M value. Moreover, the flow is null if M is outside the surface.
The application of Gauss theorem to compute the gravitational field flow of an extended mass M, enclosed in a sphere of radius R and with the constraint of spherical symmetry (i.e. the value of $\vec{g}$ depends just on the distance from the centre of mass, $\vec{g} = \vec{g}\ (r)$), across a sphere of radius r allows to derive the following result:

$$\vec{g}\ (\vec{r}) = -\frac{GM}{r^2}\hat{r}$$

i.e. a spherically symmetric extended body generates outside the body the same gravity field as a point mass placed at the centre of mass. The result shows up the well-known and general inverse gravitational problem: an exact knowledge of the gravitational field outside a body does not allow to infer the mass distribution inside the body interior [1],[27]. In spite of this, the gravity investigation approach is unique in collecting direct information on the mass density field, even if the knowledge is integrated and it cannot be unequivocally inverted [29].
Indeed, although additional information needs to be collected to determine uniquely the moments of inertia, gravity measurements are fundamental to put constraints on their values and hence helpful to constrain the geophysical models used to describe the observations.
In general, moments of inertia of planets are derived combining measurements of the second-degree harmonic coefficients of the gravity field and of the precession of the spin axis due to external torques. However, the measurement of the spin axis precession is not an easy task [23] [50], indeed other information on the rotation state can be inferred through quantities such as the obliquity (i.e. the inclination of the rotation axis with respect to the normal to the orbit plane) and the librations in longitude (i.e. small periodic oscillations from a uniform rotation state).
Another important effect to be considered in the understanding of planetary interiors is the tidal influence on the gravitational field of the planet. Indeed, the intrinsic gravity field is modified with respect to the pure spherical symmetry field because of the several irregularities that a planet owns at different size scales. The most relevant deviations are typically shown up by the second-order term J_2 of the spherical harmonics expansion (quadrupole moment). To this term contributes both the planetary rotation and the tidal deformation exerted by an external body (Sun, satellite, other).

2.4 The Gravity Field: State of the Art and Missions

The study of the Solar System starts on its main constituents: Sun, planets/moons and minor bodies, such as dwarf planets, asteroids, comets, Kuiper belt objects. Apart our star, the study of all these components aims at achieving a deeper understanding of the Solar System, its birth, its history, its characteristics features and its evolution. At the same time, the study of planets, through the investigation of similarities and differences and by comparison with the Earth, helps in better understanding our planet too. This approach is useful as well in the relatively new field of exoplanets researches.
Planets of Solar System are typically divided in terrestrial planets and giant planets, depending on their characteristics. Jupiter, Saturn, Uranus and Neptune are named giant planets; they include (Sun apart) most of the mass of Solar System and are characterised,

for comparison with the other class, by large distances from the Sun, large sizes and volumes, low density, extended atmospheres, low surface temperatures and a complex and rich moons system. Mercury, Venus, Earth and Mars constitute the terrestrial planets; they are much closer to the Sun, have small diameters and volumes, high density, thin atmosphere, solid surfaces, few moons or none.

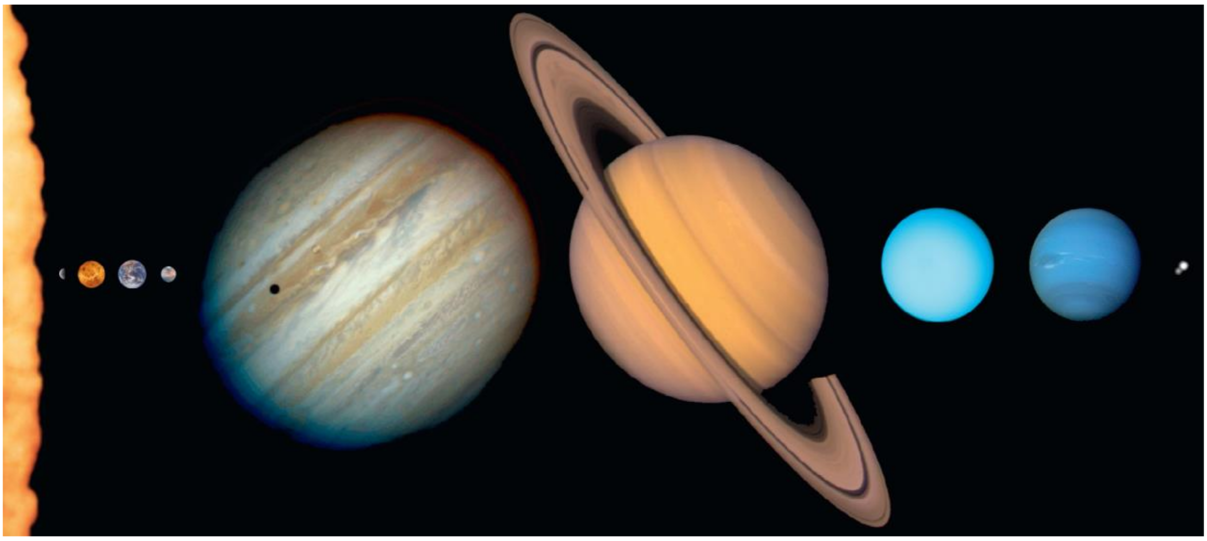

Figure 2-6: The Solar System planets Mercury, Venus, Earth, Mars, Jupiter, Saturn, Uranus, and Neptune and the dwarf planet Pluto [31]. They are shown with their correct relative sizes and ordered according to their distance from the Sun.

The terrestrial planets [32] show off similarities in many aspects, although the different evolution produced significant differences as well. They have been formed from mass accretion in the solar nebula. The Earth seems the only planet to be characterised by active plate tectonics and large height difference between the old continental crust and the young oceanic crust. Mercury and the Moon have a lithosphere characterised by widespread volcanism and impact craters. A similar snapshot foresees Mars with a characteristic separation between a Northern hemisphere filled by plains and a Southern hemisphere densely cratered. The surface seems to have been modified in its early history by atmospheric influences and by flows of a liquid fluid, likely water. Venus, the most similar to the Earth as size and mass, underwent a very different evolution that covered it by a dense and aggressive atmosphere, increasing significantly the surface temperature (due to an impressive greenhouse effect), and produced an extended volcanism.
The giant planets [34], because of their huge masses, played a crucial role in the formation of the Solar System, affecting significantly the motion of many objects in the system, hindering the grouping of small bodies to form a planet in the asteroid belt, contributing to the Kuiper belt and Oort cloud formation, preserving part of the gases (mostly hydrogen and helium) that were existing at the time of Sun and planets formation. All the giant planets show off a large flattening due to a rapid rotation and a composition dominated by hydrogen and helium that make them fluid envelopes with no liquid or solid surface. They possess extended atmospheric systems with large and long-lasting clouds, crossed by zonal wind patterns and with compositions dominated by ammonia for Jupiter/Saturn and by methane for Uranus/Neptune. Apart the dominant and common composition based on hydrogen and helium elements, Uranus and Neptune, smaller with respect to the other two, present a relatively different interior structure enriched by the so called planetary “ices”, a mixture of

compounds such as ammonia (NH_3), methane (CH_4) and water (H_2O), so named because of their occurrence on the surfaces of the major planets' icy satellites [34][31].
The study of planets is based on manifold sources of information [32]: imaging and spectrometry of the surface, atmosphere sounding, magnetic field measurements, neutral and charged particles detection, orbit analysis from planetary fly-bys, as in the case of the outer planets (Uranus and Neptune) and of a number of planetary moons or asteroids or comets, or from orbits of planetary orbiters. The latter one allows to retrieve information on the gravity field and on the rotation parameters of the body. For some planets, detailed topographic information exists, based on measurements of altimeters. For some bodies, such as Mars and Moon, rock samples can be analysed in-situ or after being returned to the Earth, respectively. Gravity field information combined with images showing the characteristic surface features allow to correlate the gravity variations observed from the orbit with the topography associated to the reliefs.
In the last two decades, significant advances have been achieved in the measurement, modelling and interpretation of the gravity field of several planetary bodies in the Solar System. Such an advancement has been motivated because gravity information allows to derive information and place constraints on the formation, interior structure and geologic evolution of a planet. The characteristics of the gravitational field outside a planet are completely established by its internal mass distribution. Combining gravity field data, topographic data and some geologic assumptions [30], the gravitational inverse problem can be faced more effectively and important geodetic and geophysical parameters can be estimated. They are used to formulate planetary models and to help in addressing questions concerning planetary differentiation, crust formation, thermal evolution, and magmatic processes.
However, there is a great variability among the achieved gravity knowledge, although to collect gravity data has become central to understand planetary bodies. Obviously, a great and extraordinary effort was directed to the Earth gravity field, through a fleet of dedicated satellites which started to monitor the spatial variation of the gravity field with very high resolution and accuracy. Moreover, the GRACE mission [79] started to measure systematically the time variation of the gravity field, i.e. the possibility of tracking mass displacements and flows, mass redistribution associated to glacier sheets, etc. A significant effort has been pursued for the Moon as well, especially with the GRAIL mission [101] that allowed to improve considerably its gravity knowledge.
Concerning other Solar System bodies, gravity field models are available, besides Earth and the Moon, just for few planetary bodies such as the terrestrial planets Mercury, Venus and Mars. However, such models are restricted only to large spatial resolutions, about one or few hundreds of kilometres, not enough to understand the geophysical processes who have driven formation and evolution of those bodies. Moreover, such models are affected in the solution by the spatial variations of the Earth-orbiter tracking geometry and by the limited range of orbit parameters of orbiters [32]. Indeed, the quality of gravity field varies significantly, since it depends on different items, such as the accuracy and type of observations, spacecraft orbital parameters, the space environment [44].
There is much more lack of data for the external planets, where only few gravity field parameters have been derived for some of the gaseous planets (Jupiter and Saturn) and their main moons. Any improvement on those targets would be very helpful in understanding their interior and the geophysical and geological processes explaining the observations. Indeed, models of the interior structure of all planets can be constructed from a sufficiently detailed knowledge of their figures and their gravity fields.
Gravity information from all the remaining planets and moons are derived just from fly-bys or orbit perturbations; they provide just the most elementary gravity-related information.

Concerning minor bodies in the Solar System such as asteroids and comets, since the beginning of 2000 the gravity models, and just for low degrees, have been determined for few bodies. In 2000, the radio-tracking of the NEAR (Near Earth Asteroid Rendez-vous) spacecraft around the Eros asteroid allowed to produce a gravity model till to degree and order $l = 10$ [104]. In 2011-2012 the Dawn spacecraft, orbiting around Vesta asteroid in the main belt between Earth and Mars, has been tracked by ground stations allowing to recover the gravity field, till degree and order $l = 20$, and the main orientation parameters [105]. In 2014-2016 the Rosetta spacecraft during the orbit around the comet Churyumov-Gerasimenko was tracked by ground stations but just a degree and order 2 was derived. Indeed, the radio-tracking technique has an accuracy decreasing with the mass of the tracked body (section 3.2.1), therefore where the involved masses are very reduced, as expected for the smaller asteroids, the technique is adequate just for the main lower degrees ($l = 2$ or little more).
A list of the missions who contributed the most to the measurement of the gravity field of targeted planets/moons/minor bodies has been reported in Table 2-2. In the following sections some details about the most significant missions in the Solar System for gravity field retrieval have been addressed.
Some clarifications need to correctly understand the following sections in this chapter.
As explained in section 2.2.2, the gravity field of a planet is represented in terms of a gravity field model, i.e. a mathematical representation based on a spherical harmonic expansion. The gravity field model is used to approximate the real gravity field, in terms of spherical harmonic coefficients till to a maximum degree l_{max}.
From such an approximating gravity potential all related gravity field functionals can be computed, such as geoid height, gravity anomaly and gravity disturbance. The determination of a planet's global gravity field is one of the main tasks of planetary geodesy. It is a reference for geodesy and it provides important information about planets, their interiors and their atmospheres for all the geosciences.
One of the terms used in the following sections is the concept of degree strength or global resolution [64][84], intended as the degree of the gravity field model for which the signal-to-noise ratio is 1 and hence it is considered the minimum gravity signal achievable for that model. Graphically, it is identified by the point where the RMS power per coefficient per degree of the gravity field, representing the expected average signal, intercepts the corresponding error curve. The degree strength achieved can be higher than this minimum value over specific areas of a planet due to the orbit characteristics of the spacecraft that carried out measurements.
In the following the gravity field models of planetary bodies will be reported. Given the fully normalised Stokes coefficients of a specific degree l over orders m, the behaviour of the gravity field model is represented in terms of RMS power per coefficient per degree l, i.e. the expected average signal content per l, m, according to the formula (as explained in section 2.2.2):

$$\sigma_{lm} = \sqrt{\frac{\sum_{m=0}^{l}\left({C_{lm}}^2 + {S_{lm}}^2\right)}{2l+1}}$$

Table 2-2 Gravity field measurements in the Solar System

Body	Mission	Type	Technique	Band	Year
Mercury	Mariner 10	fly-by	RT	S, X	1974-75
	MESSENGER	orbiter	RT	X	2011-15
	BepiColombo	orbiter	RT	X, Ka	2025
Venus	Mariner 5	fly-by	RT	S	1967
	Mariner 10	fly-by	RT	S, X	1974
	Venera 9-10	orbiter	RT	S	1975-77
	Pioneer VO	orbiter	RT	S	1978-92
	Magellan	orbiter	RT	S, X	1990-94
Earth	CHAMP	orbiter	SST-HL	L	2000-10
	GRACE	orbiter	SST-LL	Ka	2002-17
	GOCE	orbiter	GG	Laser/ GPS	2009-13
Moon	Clementine	orbiter	RT	S	1994
	Lunar Prospector	orbiter	RT	S	1998-99
	Kaguya	orbiter, subsat	RT/SST-LL	S, X	2007-2009
	GRAIL	orbiter	SST-LL	Ka (inter), S, X	2012
Mars	Mariner 9	orbiter	RT	S	1971-72
	Viking	orbiter	RT	S	1976-80
	Mars Express	orbiter	RT	X	2003-on going
	Mars Global Surveyor	orbiter	RT	X	v
	Mars Reconnaissance Orbiter	orbiter	RT	X	2005-on going
Jupiter	Pioneer 10 & 11	fly-by	RT	S	1973-
	Voyager 1 & 2	fly-by	RT	S, X	1979-80
	Galileo	orbiter	RT	S, X	1995-2003
	Juno	orbiter	RT	X, Ka	2016-on-going
Saturn	Pioneer 10 & 11	fly-by	RT	S	1973/76
	Voyager 1 & 2	fly-by	RT	S, X	1980-81
	Cassini	orbiter		X, Ka	2004-2017
Uranus	Voyager 2	fly-by	RT	S, X	1986
Neptune	Voyager 2	fly-by	RT	S, X	1989
Asteroids/Comets					
Eros	NEAR	orbiter	RT	X	2000
Vesta	Dawn	orbiter	RT	X	2011-2012
Churyumov-Gerasimenko	Rosetta	orbiter	RT	S, X	2014-2016

2.4.1 Mercury

Figure 2-7: An enhanced-color view of Mercury, assembling images at various wavelengths captured by the MESSENGER spacecraft. The circular area on the center-top part is Caloris Basin (courtesy NASA / Johns Hopkins University Applied Physics Laboratory / Carnegie Institution of Washington)

2.4.1.1 Characteristics

At present, Mercury is one the planet less explored since the beginning of the space era because of its proximity to the Sun and the harsh environment that envelopes its surrounding. Mercury is also the smallest and the less explored planet among the terrestrial planets. Mercury is the inner representative of the terrestrial planets class in the Solar System. Small, rocky, very close to the Sun, Mercury has always represented a challenge in the knowledge of the planets due to its excessive proximity to our star.

Few information was available until the arrival of Messenger mission in 2011. The spacecraft completed its primary year long mission (2012), having taken nearly 100.000 images of the surface of Mercury.

Among its initial discoveries was finding high concentrations of magnesium and calcium on Mercury's night side, identifying a significant northward offset of Mercury's magnetic field from the planet's center, finding large amounts of water in Mercury's exosphere, and revealing evidence of past volcanic activity on the surface. It was also during this first extended mission that the spacecraft found evidence of water ice at Mercury's poles, frozen at locations that never see the sunlight (made possible by the fact that the tilt of Mercury's rotational axis is almost zero).

2.4.1.2 Missions

Mercury has been observed by Mariner 10 [51] in March 1974 and March 1975 trhough three fly-bys and the pictures have revealed a geological surface covered by impacts, with an aspect similar to our Moon. In addition, ground-based radar measurements were collected to gather information on Mercury's gravity and structure. After that, NASA's MESSENGER mission reached the planet in 2011 and entered into orbit for the first time. The result was a four year mission with allowed to collect a first snapshot of this elusive planet.

Mercury is going to be observed by ESA/JAXA mission BepiColombo, currently on the cruise phase towards the planet, through six flybys before the final arrival to orbit the planet in 2025.

2.4.1.2.1 Mariner 10

NASA's Mariner 10 [51] was the first spacecraft sent to study Mercury and the seventh successful launch in the Mariner series. It was also the first spacecraft to use the gravitational pull of one planet (Venus) to reach another (Mercury), a technique largely used today to reach planets saving fuel known as gravity assist, and the first spacecraft mission to visit two planets. Indeed, an important contribution in this direction was from the Italian mathematician Giuseppe "Bepi" Colombo [58], whose studies were focused on Mercury as well. He was the first one to highlight that though suitable changes in the Mariner 10 trajectory, the spacecraft could fly by Mercury three times, rather just one as foreseen in the original mission. Indeed, the spacecraft flew by Mercury three times in a retrograde heliocentric orbit and returned images and data on the planet. The Mariner 10 returned the first-ever close-up images of Venus and Mercury. Also for this reason, ESA decided to devote its first mission to Mercury to him: BepiColombo (section 2.4.1.2.3). The primary scientific objectives of the mission were to measure Mercury's environment, atmosphere, surface, and body characteristics and to make similar investigations of Venus. Secondary objectives were to perform experiments in the interplanetary medium and to obtain experience with a dual-planet gravity-assist mission.
During three flybys of Mercury, Mariner 10 took images of almost half the planet's moon-like surface and transmitted several data indicating an unexpected magnetic field, a metallic core comprising about 80 percent of the planet's mass, and temperatures ranging from 187 degrees Celsius on the dayside to -183 degrees Celsius on the nightside.

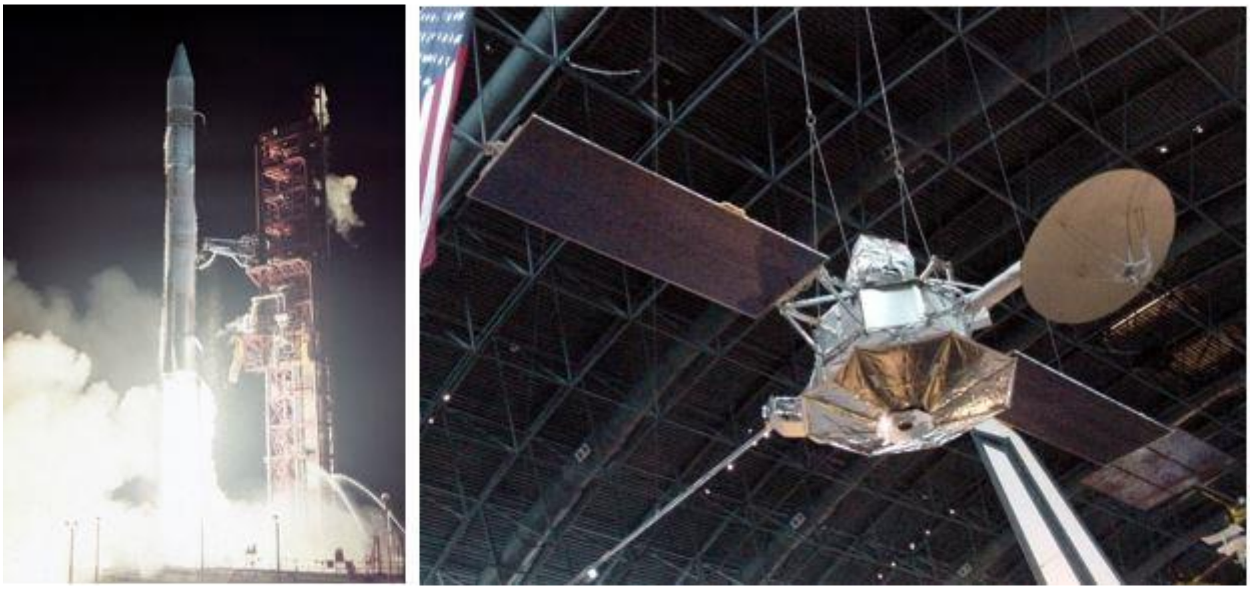

Figure 2-8: Launch of Mariner 10 on its Atlas-Centaur rocket on the left and flight spare of Mariner 10 at the National Air and Space Museum on the right (NASA courtesy).

2.4.1.2.2 MESSENGER

MESSENGER (Mercury Surface, Space Environment, Geochemistry and Ranging) [54] was the seventh Discovery-class mission by NASA and the first spacecraft to orbit Mercury. Its primary goal was to study the geology, magnetic field, and chemical composition of the planet. It was the first mission to Mercury after Mariner 10, more than 30 years before.
Launched in 2004, the MESSENGER spacecraft reached Mercury after six-and-a-half-year cruise characterised by several gravity-assist maneuvers through the inner solar system, including one flyby of Earth (2005), two flybys of Venus (2006 and 2007), and three flybys of Mercury itself (January and October, 2008, 2009).
MESSENGER finally entered orbit around Mercury on March 2011, on an orbit highly elliptical (9.300 × 200 km) with a 12-hour orbital period.
By Christmas Day 2014, it was clear that the spacecraft's propellants were running out and that MESSENGER would impact the planet in late March 2015. The spacecraft impacted the surface of Mercury by April 30, 2015, after it ran out of propellant. As expected, MESSENGER hit the planet's surface at about 14.080 km/hour, creating a new crater on Mercury.

2.4.1.2.3 BepiColombo

ESA (European Space Agency) jointly with JAXA (Japan Aerospace Exploration Agency) developed BepiColombo, a cornerstone mission of the Cosmic Vision Programme, with the aim of a deeper and widespread investigation of the planet and of its surrounding environment [57][59]. Named after the Italian scientist Giuseppe "Bepi" Colombo, for his contribution to the study and to the exploration of Mercury, the mission foresees two orbiters, the MPO (Mercury Planet Orbiter) and the MMO (Mercury Magnetosferic Orbiter), to be placed in complementary low polar orbits around Mercury, after about a 7 years-journey and 9 gravity-assists (one at Earth, two at Venus, six at Mercury). On the 19th of October 2018 BepiColombo was successfully launched from the European spaceport in Kourou (French Guiana) and is currently on the cruise phase.
The MPO hosts on-board a suite of advanced eleven scientific instruments to carry out several investigations such as imaging, IR-spectroscopy/radiometry, laser altimetry, UV/X-ray/gamma-ray/neutron spectroscopy, radio-science experiments, magnetic field and particle measurements [57][59]. One of the main objective of the mission is the realization of Radio-Science Experiments (RSE). The RSE are a set of intertwined experiments aimed at 1) determining the gravity field of Mercury, 2) evaluating the rotation state of Mercury, 3) carrying out some Einstein's General Relativity tests at Mercury, in order to determine with improved accuracy different post-Newtonian parameters, such as the Eddington parameters γ and β, related, respectively, to the space-time curvature generated by a mass and to the degree of non-linearity in the gravitational field, the Nordtvedt parameter η, related to possible violations of the Strong Equivalence Principle, and the parameters α_1 and α_2 related to preferred frame effects [60][61][62].

2.4.1.3 Gravity models

The gravity field of Mercury has been measured very recently, in the period 2011-2015, through the mission MESSENGER (see section 2.4.1.2.2), which orbited the planet for the first time. Before MESSENGER, just three fly-bys were accomplished in the 1974-75 by

Mariner 10 which provided the first measurements of its gravity field, allowing to collect just basic information on the mass of the planet and on the coefficients related to the quadrupole field. Improvement of the current data from MESSENGER are expected from the BepiColombo mission, currently on the cruise phase towards Mercury and planned to arrive on 2025.

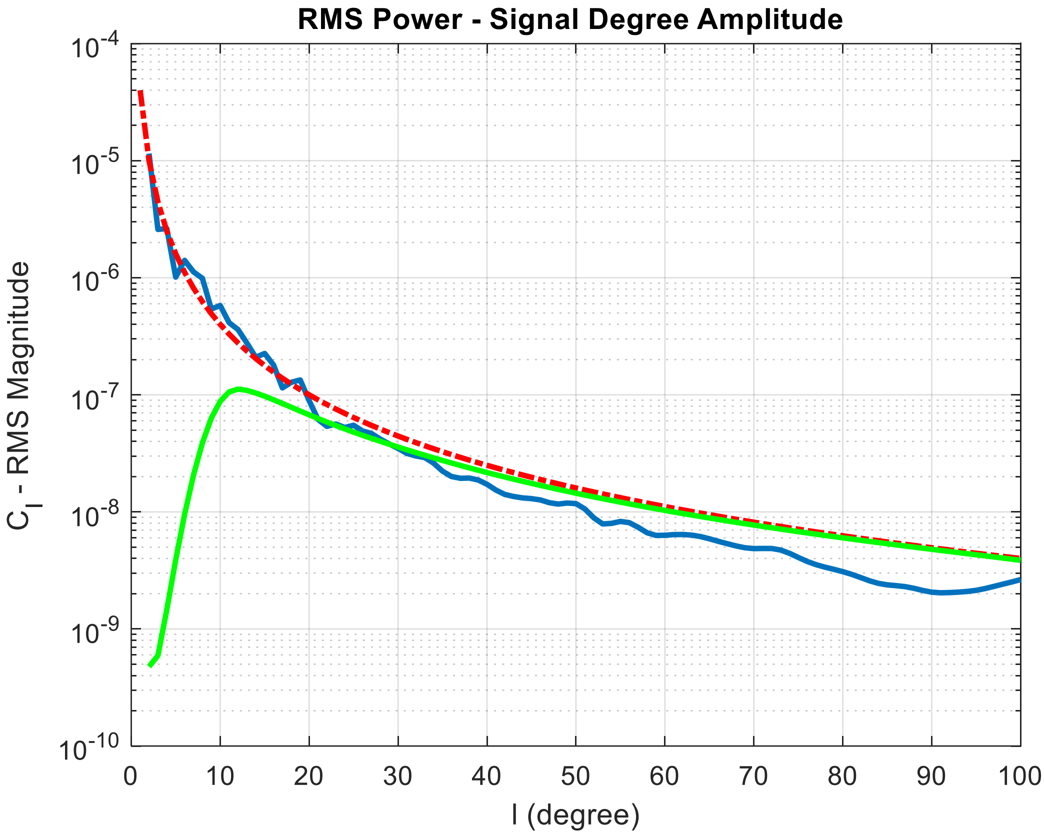

Figure 2-9: The Mercury gravity spectrum as derived from HgM008 ([55], computed with data from [86]): gravity field, gravity field error and Kaula rule are shown respectively in blue, green and red colours

The last gravity model of Mercury is named HgM008 [55] and updates previous models such as the HgM005 derived from Mazarico et al. [54]. Such a model is based on the whole MESSENGER dataset and shows effective improvements in the reconstruction of the Mercury's gravity field. The model is based on an innovative technique for orbit determination in which simultaneous numerical integration of both the spacecraft and planet equations of motion has been carried out in order to determine parameters related to MESSENGER and Mercury orbital dynamics [55]. Previous solutions were retrieved by adopting pre-converged ephemeris of the planet.

The HgM008 gravity field model allowed to achieve a spherical harmonic solution till to degree and order 100. Figure 2-9 depicts the gravity spectrum of Mercury derived from this solution. The maximum resolution achieved over the planet corresponds to the degree $l \sim 35$, where the averaged (over the planet) S/N = 1.

This solution includes an accurate estimation of the gravitational tides Love number k_2 and of the pole orientation as well. The gravitational potential Love number k_2 in the HgM008 solution is 0.5690±0.025, a value larger than previous estimates [54], indicating a warm and weak mantle or the presence of a solid FeS layer at the top of the core. The accurate

measurement of pole's orientation enabled a more accurate computation of Mercury's polar moment of inertia that supports the presence of a large solid inner core.
However, the degree strength averaged over the planet, where the signal-to-noise ratio equals to 1, is achieved around $l = 35$ at global level. Moreover, such a model shows off a better resolution for the northern hemisphere due to the lower altitude reached by MESSENGER spacecraft in that region. However, the physical significance is lower, till to $l = 10 - 15$, where the signal-to-noise ratio achieves a good value of 5-10.

2.4.2 Venus

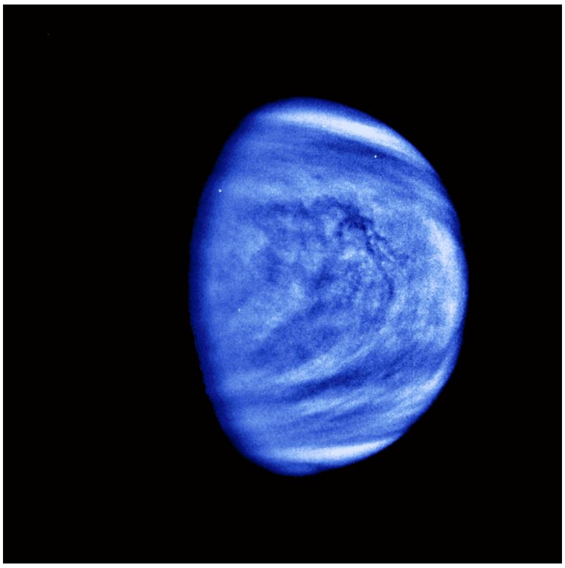

Figure 2-10: An image of Venus taken from Galileo spacecraft at a distance of about $3 \cdot 10^6$ km

2.4.2.1 Characteristics

Venus is the planet which mostly features characteristics similar to Earth in terms of size, mass and density. Its radius (6052 km) is only 320 km smaller than that of Earth. Its density is equal to 5.25 g/cm^3 (vs 5.52 g/cm^3 for the Earth) and can be explained by the lower pressures inside the planet if one takes the same elementary composition. Indeed, it is often considered the twin of our planet but indeed, apart those elements, Venus shows characteristics enough far from Earth. A very thick atmosphere CO_2 – based, which produces a pressure of about 90 atm at the surface and a widespread clouds system, hides permanently the planet and induces a great greenhouse effect whose consequence is to increase the surface temperature till to 480°C [32][45]. Indeed, the two planets have followed significantly different geological and climate evolutions, probably started very early in their history. These differences likely reflect substantial diversities in the interior composition and in the rheology [65]. Gravity anomalies are smaller than those of Moon and Mars and they correlate better with topography than on Earth. This suggests at least partial isostatic compensation.
Venus has no intrinsic magnetic field as found by Mariner and Pioneer Venus Orbiter missions [41]. Although the planet has a molten metallic core similar in size to Earth's core, the absence of a magnetic field is not completely understood. A possible explanation is that Venus has not cooled sufficiently for an inner core to have yet formed but enough that a

purely thermally-driven dynamo cannot operate [41]. This is consistent with Venus' slightly smaller size compared with Earth. Schubert suggest that the planet had a magnetic field in the past until 1.5 billion of years ago [32].
Radar observations allowed to go through the dense atmosphere and to observe the surface [36][32][180]. Its surface is covered with volcanoes but no mission revealed signs of activity. Venus' topography is dominated by two mountains named Aphrodite Terra (equator) and Ishtar Terra (northern latitudes). The topographic features are compensated and the gravity signal is very weak over these areas. The lack of features such as rift and trench typical on the Earth oceans allowed to conclude that Venus does not show signs of active plate tectonics: it is a one-plate planet [36]. However, there are features resembling major tectonic structures on the Earth such as rift valleys and plateaus (Beta Regio, Alta, Eistla and Bell Regiones [36]). Very characteristic features of Venus are coronae. These are quasi-circular topographic features with 100–2.600 km diameter. They consist of concentric ridges and interior plains, either topographic lows or highs. Coronae are often flanked by troughs [36]. McKenzie et al. (1992) and Schubert et al. (1994) argue that they resemble subduction zones [32]. Data from Venus Express (ESA), the last mission to visit the planet till now, has provided evidence of geologically recent volcanism [36]. Indeed, analysing the radiation emitted from the surface in the near-infrared and filtered by the atmosphere, Venus Express mapped the distribution of thermal emissivity over the surface, finding out anomalously high values of emissivity at three hotspots (Imdr, Themis, and Dione Regiones). Such anomalies have been interpreted to be associated with geologically young lava flows (younger than 2.5 million years and probably much younger, about 250000 years or less) that have experienced relatively little surface weathering.

2.4.2.2 Missions

As highlighted above, Venus is the planet which is the most similar to the Earth and it is one of the terrestrial planets most targeted by space missions. Radar images allowed to go through the dense atmosphere and to observe the surface. First images were obtained by the Soviet Venera 15 and 16 and by Pioneer Venus Orbiter in the 80s. At last, the NASA Magellan mission between 1990 and 1994 carried out the most accurate survey of the Venus planet. Venus Express by ESA (2006-2014) was mainly dedicated to the planet's atmosphere
Concerning the future, at present no mission to Venus is planned. However, some proposals/studies are on-going.
Within the frame of ESA Cosmic Vision Plan, as candidate for a medium-class opportunity, EnVision [42] mission (possible launch 2030s) would determine the nature and current state of geological activity on Venus and its relationship with the atmosphere, to better understand the different evolutionary pathways of the two planets. Among its objectives, the measurement of the gravity field is foreseen as well.
The Indian Space Agency ISRO (Indian Space Research Organisation) recently issued a call for international proposals to participate in its mission to Venus to be launched in 2023 [43]. The science goals of the mission include investigating Venus' surface and subsurface, atmosphere, ionosphere, plasma environment, and the Sun-Venus interaction.
The Russian Space Agency Roscosmos with NASA have recently published a Phase II report to define the science and architecture of a comprehensive mission to Venus, named Venera-D [43]. The baseline mission architecture would consist of an orbiter and a VEGA-type lander with an attached Long-Lived, In-Situ Solar System Explorer with the aim of understanding Venus as a system, from the top of the atmosphere to the surface and interior.

2.4.2.2.1 Venera

Venus was a major target of the Soviet Union’s planetary exploration program during the 1960s, ’70s, and ’80s, which achieved several spectacular successes.
Venera was a series of 16 flyby, orbital, and landed missions to Venus conducted by the Soviet Union from 1961 to 1983. After an early sequence of failed missions, in 1967 Soviet scientists launched Venera 4, comprising a flyby spacecraft as well as a probe that entered the planet’s atmosphere. Highlights of subsequent missions included the first successful soft landing on another planet (Venera 7 in 1970), the first images returned from the surface of another planet (Venera 9 and 10 landers in 1975), and the first spacecraft placed in orbit around Venus (Venera 9 and 10 orbiters).
In terms of the advances they provided in the global understanding of Venus, the most important Soviet missions were Veneras 15 and 16 in 1983. The twin orbiters carried the first radar systems flown to another planet that were capable of producing high-quality images of the surface. They produced a map of the northern quarter of Venus with a resolution of 1–2 km (0.6–1.2 miles), and many types of geologic features now known to exist on the planet were either discovered or first observed in detail in the Venera 15 and 16 data. Late the following year the Soviet Union launched two more spacecraft to Venus, Vegas 1 and 2. These delivered Venera-style landers and dropped off two balloons in the Venusian atmosphere, each of which survived for about two days and transmitted data from their float altitudes in the middle cloud layer. The Vega spacecraft themselves continued past Venus to conduct successful flybys of Halley’s Comet in 1986.

2.4.2.2.2 Pioneer Venus Orbiter

The Pioneer Venus mission by NASA consisted of two spacecraft to study Venus: the Orbiter and the Multiprobe. The latter separated into 5 separate vehicles near Venus. The Orbiter was launched on the 20 May 1978 from the Kennedy Space Center aboard an Atlas-Centaur rocket. It went into orbit around Venus on 4 December 1978. The main objective was to investigate the solar wind in the Venusian environment, map Venus' surface through a radar imaging system, and study the characteristics of the upper atmosphere and ionosphere. The Orbiter carried twelve instruments, most of them dedicated to plasma investigations of the Venusian upper atmosphere, as well as instruments for observing reflected sunlight from the cloud layers at a variety of wavelengths, and a surface radar mapper. There was, however, a gamma-ray burst detector experiment added on the satellite. The mission ended when the spacecraft entered the atmosphere on 8 October 1992.
The Pioneer Venus Multiprobe was launched on 8 August 1978. It encountered Venus on 9 December 1978. It consisted of 5 separate probes: the probe transporter (referred to as the Bus), a large atmospheric entry probe (called Sounder), and 3 identical small probes (called North, Day, and Night). The Sounder released from the Bus on 15 November 1978; the 3 small probes released on 19 November 1978. All probes entered the Venusian atmosphere within 11 minutes of each other, and descended towards the surface over approximately an hour long period sending back data to the Earth.

2.4.2.2.3 Magellan

The NASA Magellan spacecraft, named after the sixteenth-century Portuguese explorer whose expedition first circumnavigated the Earth, was launched May 4, 1989, and arrived at Venus on August 10, 1990. During the first 8-month mapping cycle around Venus, Magellan collected radar images of 84 percent of the planet's surface, with resolution 10 times better than that of the earlier Soviet Venera 15 and 16 missions. Altimetry and radiometry data also measured the surface topography and electrical characteristics. During the extended mission, two further mapping cycles from May 15, 1991 to September 14, 1992 brought mapping coverage to 98% of the planet, with a resolution of approximately 100 m. Precision radio tracking of the spacecraft measured Venus' gravitational field to show the planet's internal mass distribution and the forces that have created the surface features. Magellan's data permitted the first global geological understanding of Venus, the planet most like Earth in our solar system.

2.4.2.3 Gravity models

The first gravity information about Venus are dated to the first spacecrafts who visited the planet in the 60-70s years. In that period investigations were possible through the Mariner 5 fly-by in 1967, the Mariner 10 fly-by in 1974 and at last with Venera 9 and 10 in 1975-77, the first orbiters around Venus [63]. Data from those missions allowed to establish upper limits for the low degree and order terms of the spherical harmonic expansion of Venus gravity field. In particular, very low values of the zonal term J_2, about three order of magnitudes less with respect to Earth, were estimated, the main difference being driven by the very slow rotation of Venus on its axis (243 days vs 1). Indeed, Venus is the planet that is characterised by the longest sidereal rotation around its own axis, and in the opposite direction with respect to all the planets except for Uranus.
In the following years, two other missions, Pioneer Venus Orbiter and Magellan, provided a nearly global gravity dataset for Venus. The first gravity models of this period were able to provide solutions till to degree and order 10-20, based on low-altitude data from Pioneer Venus Orbiter. Following combinations of low and high-altitude data allowed to push the gravity field solutions to degree and order 50 [64].
The arrival of Magellan spacecraft in 1990 provided further data in X- and S-band that allowed to increase significantly the resolution achieved. The Magellan Doppler tracking data provide the best precision for spacecraft-based gravity measurements allowing to reach spherical harmonic degree and order 180 in specific equatorial regions [64]. The latest model for Venus is the MGNP180U [64], available at NASA's Planetary Data System [46]. It is based on two-way Doppler tracking data of Pioneer Venus Orbiter (S-band) and Magellan (S- and X-band) collected from the Deep Space Network (DSN) at Goldstone (California), Madrid (Spain) and Canberra (Australia). The gravity model is depicted in Figure 2-11 in terms of RMS power per coefficient per degree, that represents the expected average signal. As shown, the model is valid till to degree and order 180. However, the degree strength (the global resolution), i.e. the degree for which the signal-to-noise ratio is 1, is achieved at about $l = 70$ (as shown in Figure 2-11). This means that a resolution of about 270 km is achieved at the surface, although regionally this can reach about 100 km ($l = 180$).

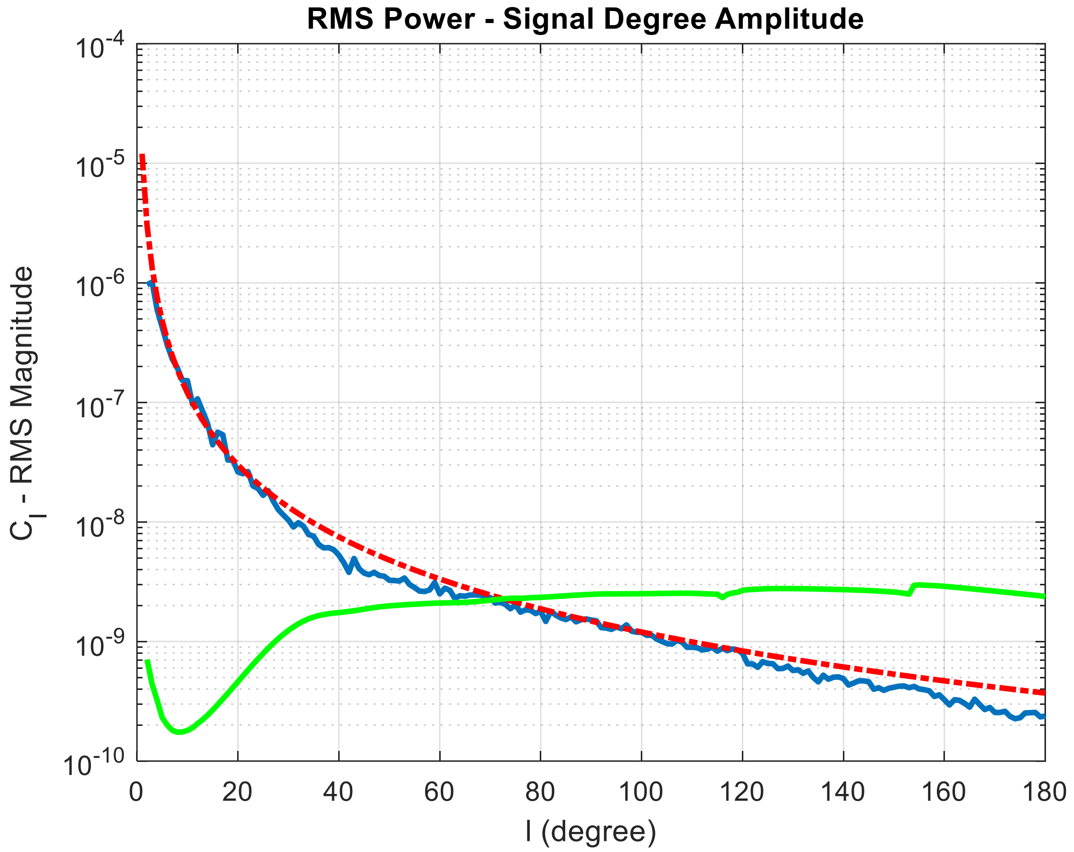

Figure 2-11: The Venus gravity spectrum from MGNP180U (computed with data from [85]): gravity field, gravity field error and Kaula rule are shown respectively in blue, green and red

Such a model shows important improvements with respect to previous solutions, with particular significance for degree and order higher of 80. However, in order to relax the computational effort, the MGNP180U was determined in three separate steps [64]. A first solution was established till to degree and order 120 with a complete unconstrained covariance matrix and a spatial a priori constraint based on the gravitational acceleration strength. In a second step this model was considered as nominal solution with the same a priori constraint and the solution for the coefficients from degrees 116 to 155 was derived. In a third and last step the coefficients were determined for degrees from 155 to 180 by constraining them through the Kaula's rule. Due to the spatial constraint, the spatial resolution of MGNP180U depends strongly on the position on the surface. Figure 2-12 shows the degree strength determined from the unconstrained degree and order 120 covariance in the first step. Values close to contours are the harmonic degrees for which the sign-to-noise ratio is 1. This means that higher spectral resolutions can be achieved close to equatorial regions, whereas lower values are found in other regions (around 40 for instance in the picture) [30].
From these data it follows that the current gravity field model of Venus, although seemingly is pushed to high spherical harmonic resolutions, the maximum resolution averaged over the planet does not exceed the degree and order 70 averaged and the equatorial regions are better covered.

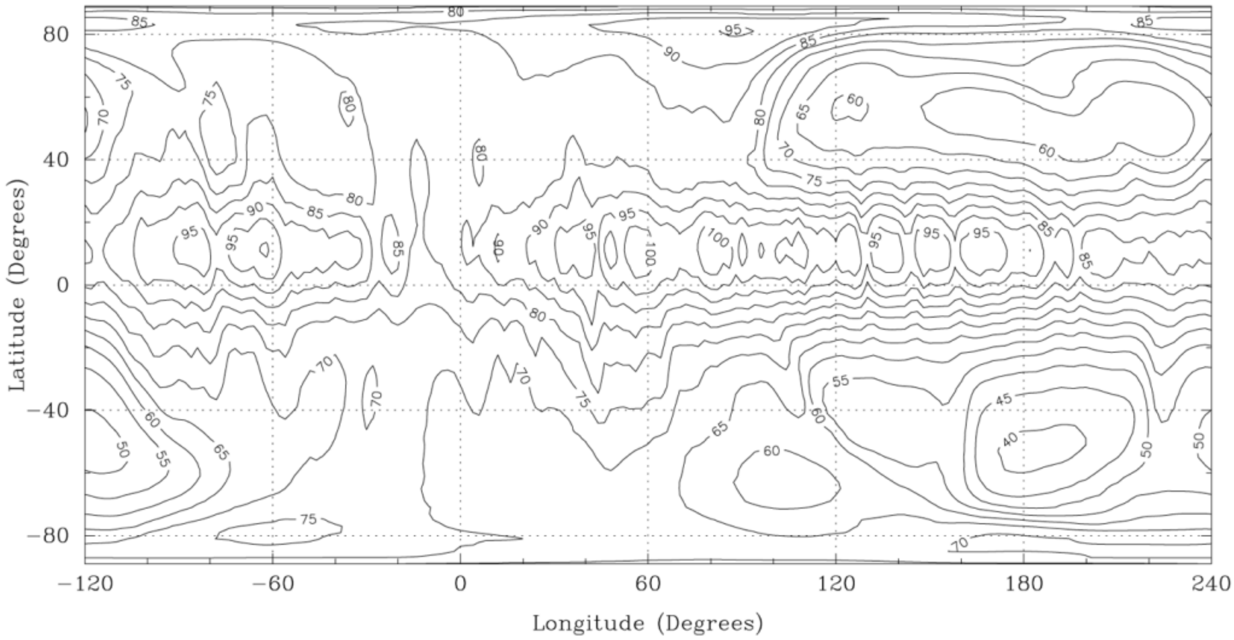

Figure 2-12: Spatial distribution of the degree strength on Venus as determined for the gravity model MGNP180U [64]: the contours are in harmonic degree and represent the degree for which the signal-to-noise ratio is 1

The degree two is very small because the Venus' rotation is very small. Therefore, a significant value of the moment of inertia cannot be determined. It would be very interesting to get higher degree variations to study the compensation of the numerous volcanoes that are present on Venus. However, the dense atmosphere prevents any spacecraft to orbit the planet at less than 300 km for long periods.

2.4.3 Earth

2.4.3.1 Missions

The gravity field of the Earth has been studied significantlhy both from space and ground. In particular, from space the major improvement has been achieved in the last twenty years due to the development of three dedicated missions: CHAMP, GRACE and GOCE.
Moreover, important improvements have been provided by LAGEOS satellite.

2.4.3.1.1 LAGEOS

LAGEOS (LAser GEOdynamics Satellite) is one of the first artificial satellites developed exclusively for geodynamic measurements using laser-ranging techniques [69]. LAGEOS was launched by NASA from the Western Test Range in California on May 4, 1976. The satellite is a sphere, 60 cm in diameter, having a mass of about 407 kg. The spherical aluminium outer portion of the satellite has a mass of 117 kg. Embedded within it are 422 cube corner reflectors made of fused silica and four made of germanium. A cylindrical brass inner core of the satellite is 27.5 cm long and 31.76 cm in diameter and has a mass of 175 kg. LAGEOS was launched into a nearly circular orbit at high enough altitude (about 6000 km) to reduce the effects of atmospheric drag and uncertainties in the orbit due to unmodeled short-wavelength gravity signals yet at low enough altitude to assure good signal

return to the tracking systems. Its spherical shape and high density minimise the sensitivity of the orbit to radiation pressure.
When LAGEOS was first launched, the existing laser tracking systems and data analysis techniques permitted station coordinates to be derived at about the meter level of precision. Using special analyses for removing common biases on obser-vations at two sites separated by several hundred kilometers, it was possible to reduce the uncertainty in baseline distance changes to better than a decimeter and in some cases to a few centimeters. Advances over the years in laser tracking technology, modelling techniques, and computer procedures have improved the accuracy of site determinations to a few centimeters in all coordinates. Contemporary measurements then are in the range where important geodynamic and geodetic observations can be made.

2.4.3.1.2 CHAMP

The German CHAMP mission (CHAllenging Micro-satellite Payload for geophysical research and application) [70] was dedicated to Earth's observation: global magnetic and gravity fields mapping. The satellite has been launched on July 15th, 2000 from the cosmodrome Plesetsk by a Russian COSMOS rocket at an altitude of 454 km in a circular orbit with an inclination of 87.3°. CHAMP performed for the first time the combination of uninterrupted three dimensional high low tracking of its low orbit perturbations by the satellites of the GPS constellation and a high-precision three-axes measurement of the satellite surface forces: residual drag, solar and Earth radiation pressures and attitude manoeuvre thrusts are measured by the STAR (Space Three-axis Accelerometer for Research) accelerometer integrated at the centre of mass of the satellite. A by-product of the accelerometer measurements is the determination of the atmospheric density variations during the decade of the mission.
STAR is a six-axis accelerometer providing the three linear accelerations along the instrument sensitive axes and the three angular accelerations about these axes. STAR presents a measurement range of $\pm 10^{-4}\, m/s^2$ and exhibits a resolution of better than $3 \cdot 10^{-9}\, m/s^2$ for the y and z axes and $3 \cdot 10^{-8}\, m/s^2$ for the x axis within the measurement bandwidth from $10^{-4} - 10^{-1}\, Hz$.
The measurements are integrated over 1 s before delivery to the satellite data bus. The configuration of the instrument is compatible with ground tests which demand specific characteristics of the less accurate x-axis for the operation under 1 g gravity field.

2.4.3.1.3 GRACE

Jointly implemented by NASA and DLR under the NASA Earth System Science Pathfinder Program, in March 2002 the Gravity Recovery and Climate Experiment (GRACE) mission, was successfully launched as the pioneering mission with the Satellite-To-Satellite Tracking approach in the Low-Low mode (SST-ll) configuration. The SST-ll mode was applied for the first time [71] in order to highlight the effect of small-scale features. Basically, in this approach two spacecrafts on the same orbit follows each other over a distance of some hundreds of kilometers (typically between 100-400 km). Since the greater an object's mass, the greater its gravitational pull, during the orbit spacecrafts accelerate very slightly as they approach an underlying massive feature and slow down as they move away. By monitoring with very high accuracy the inter-satellite range between spacecrafts, the velocity difference can be recovered. The gravity field can be reconstructed from that velocity difference which is directly proportional to the gravitational potential differences at the satellite locations. The bulk of the Earth's gravitational field is mostly generated by the mass of Earth's interior. However, a small part is due to water on or near Earth's surface. The ocean, rivers, glaciers and underground water change much more rapidly than the Earth's interior does, reacting to changing seasons and to storms, droughts and other weather and climate effects. Due to its configuration, GRACE allowed to observe these changes from space through a dedicated gravity mission.

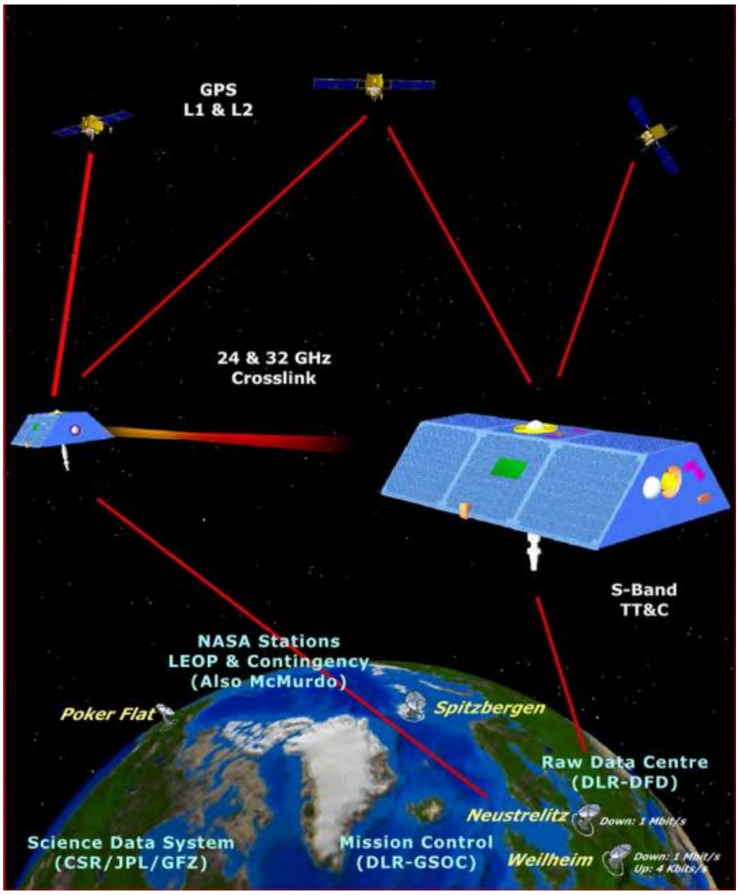

Figure 2-13: Schematic view of the flight configuration and ground support for the GRACE mission [130]

The primary science objective of the GRACE mission was to provide global gravity field of the Earth and its temporal variations with a spatial resolution in the range 400 km to 40.000 km every thirty days.

GRACE mission [71][72] consisted of two identical satellites that followed each other in the same near-circular orbits at ~500 km altitude and 89.5º inclination, at a distance of about 220 ± 50 km. The relative motion between the two satellites and its temporal variations were measured with very high precision by a K-band Ranging System (KBR), with an accuracy better than 10 μm and 1 μm/s. Furthermore, each GRACE satellite was equipped with a high precision three-axis accelerometer at its centre of mass. Such sensors were employed to measure the effect of non-gravitational forces on the two spacecrafts, to be taken into account in the evaluation of the inter-satellite distance.

In addition to the inter-satellite ranging system, each satellite also hosted on-board Global Positioning System (GPS) receivers and attitude sensors. The use of GPS allowed to create a SST-hl configuration (high-low), as in the CHAMP mission, in which the positioning provided by the GPS helped in the orbit determination. The satellite altitude decays naturally

(~30 m/day) so that the ground track does not have a fixed repeat pattern. The satellites are nominally held in a 3-axis stabilised, nearly Earth-pointed orientation, such that the K-Band antennas are pointed precisely at each other. Except for the K-Band ranging system, there was a considerable heritage in the satellite design from the CHAMP mission. Moreover, it hosts as well corner-cube reflectors.
At last, the combination of SST-ll and SST-hl allowed to reach much higher accuracy in the determination of the relative position, velocity and acceleration of the geometrical configuration of the spacecraft. The fundamental observable is the line-of-sight (LOS) acceleration difference between a satellite pair. The SST-hl provides invaluable information for resolving the long and medium wavelengths (spherical harmonic degree $l < 70$) of the gravity field, whereas in the low–low configuration (SST-ll) short-wavelengths ($l < 200$) of the field can also be recovered. Moreover, such a configuration can be viewed as a huge synthetic one-component gradiometer with an arm length of 200-250 km, whose measurement precision is inversely proportional to the baseline length, i.e. the inter-satellite distance. From this point of view, GRACE can be considered potentially a precise one-dimensional virtual gradiometer.

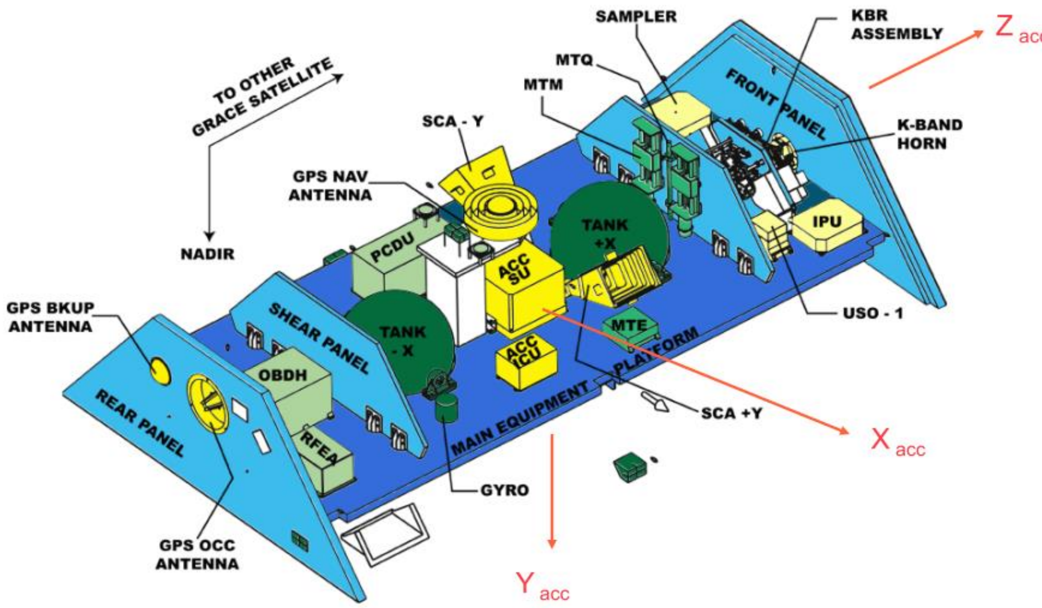

Figure 2-14: layout of the components of one of the GRACE satellites [129]

Figure 2-14 depicts the layout of a single GRACE satellite (both have the same design) [129]. Each satellite has a trapezoidal cross section, based on the FLEXBUS design of Astrium (length = 3122 mm, height = 720 mm, bottom width = 1942 mm, top width = 693 mm), made of CFRP (Carbon Fiber Reinforced Plastic). Due to a very low coefficient of thermal expansion, CFRP provides the dimensional stability necessary for precise range change measurements between the two spacecrafts.
Each Earth-pointing spacecraft is three-axis stabilised by AOCS (Attitude and Orbit Control System). Specifically, sensors are constituted by a Coarse Earth Sun Sensor (CESS) for omni-directional, coarse attitude measurement in the initial acquisition, survival and stand-by modes of the satellite, a boom-mounted magnetometer used jointly with the CESS in safe mode and for the commanding of the torque rods in fine pointing mode, a high precision star

camera and GPS flight receiver, an IMU (Inertial Measurement Unit) and optical gyro providing 3-axis rate information in survival modes.
The actuators include a cold gas system (with 12 attitude control thrusters and two orbit control thrusters, each rated at 40 mN) and three magnetorquers.
The mass of each spacecraft is 432 kg (science payload = 40 kg, fuel = 34 kg), with a power of 150-210 W (science payload = 75 W). Solar panels are mounted on top and sides of each spacecraft.

2.4.3.1.4 GRACE Follow-On

Launched on May 2018, the GRACE Follow-On mission (Gravity Recovery and Climate Experiment-Follow-On/GRACE-FO), is a joint NASA-GFZ project to continue the objectives of the original GRACE (2002-2017) mission and provide continuity for the GRACE data set [132].
The main objective of GRACE-FO is to obtain precise global and high-resolution models for the static and the time variable components of the Earth's gravity field. By using the same approach pursued in GRACE, this objective is achieved by making accurate measurements of the inter-satellite range between two twin satellites flying on a low altitude polar orbit; the measurement is accomplished by using a K/Ka-Band microwave tracking system. Moreover, each satellite carries geodetic quality Global Navigation Satellite System (GNSS) receivers for precise positioning, a Laser Retro-Reflector (LRR) for independent ranging from ground, and high accuracy accelerometers to precisely measure the non-gravitational accelerations acting on the satellite.
In addition, an experimental payload, the Laser Ranging Interferometer (LRI), is hosted on-board as complementary instrument with respect to the microwave system to provide inter-satellite range laser-based with much higher accuracy.

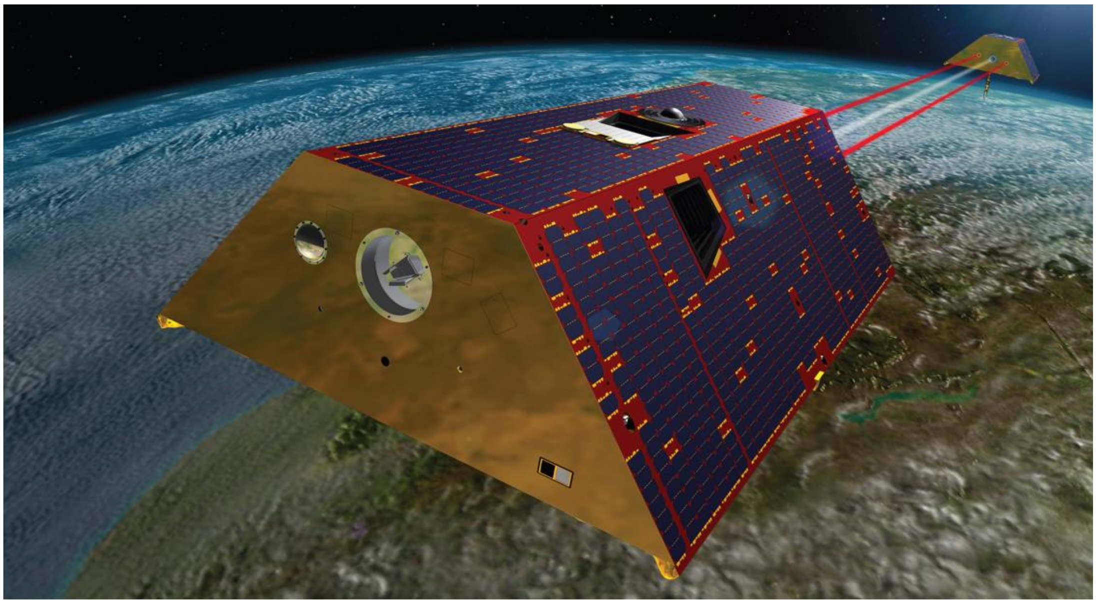

Figure 2-15: GRACE-FO artistic image (from [TBW])

2.4.3.1.5 GOCE

GOCE, acronym for Gravity field and steady-state Ocean Circulation Explorer mission, is the first and currently alone gravity mission employing an on-board gradiometer. Successfully launched on the 17^{th} of March 2009 from Plesetsk cosmodrome in Northern Russia, it was the first mission of Earth exploration in the frame of the Living Planet Program by ESA [133] [136]. Its primary objective was to determine the Earth's gravitational field with high accuracy and spatial resolution: better than $1-2\ mGal$ ($10^{-5}\ m/s^2$) in terms of gravity anomaly and around $1-2\,cm$ in terms of geoid radial accuracy, both at a spatial scale of $100\,km$, i.e. at degree and order $l=200$ [136][134]. The mission ended on the 11th of November 2013 after a planned destructive re-entry into the atmosphere.

Table 2-3 GOCE mission highlights

GOCE	
Launch date	17 March 2009
Launcher/location	Rockot/Plesetsk cosmodrome
Launch mass	1050 kg
Orbit	Sun-synchronous, dawn-dusk, 250-280 km
Duration	March 2009-November 2013

In order to reach its ambitious objectives, design and development of mission and spacecraft were driven by the need of a very low orbit and an extremely quiet environment, free as much as possible from non-gravitational forces.
As trade-off a dawn-dusk Sun-synchronous orbit ($i = 96.7°$) was chosen with altitudes in the range 250-280 km, allowing optimal Sun illumination and minimising thermal gradients. However, to accomplish the measure and to maintain such a low orbit, several advanced and novel technologies were implemented, making GOCE a "technological masterpiece". These technologies include drag-free-control, electric propulsion, electrostatic gravity gradiometry, triple junction Gallium-Arsenide (GaAs) solar cells and the manufacturing of large, 3D carbon-carbon honeycomb structures [133].

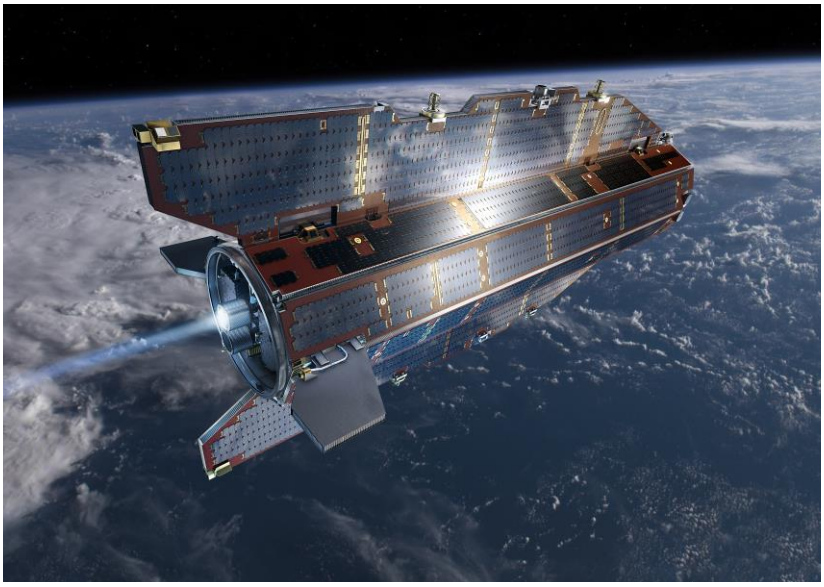

Figure 2-16: artistic view of GOCE spacecraft in orbit (from [133])

Very low orbits imply the need to minimise atmospheric drag forces and torques, reducing as much as possible mechanical disturbances. As result, the futuristic spacecraft structure shown in Figure 2-16 is adopted. Indeed, the satellite is very slim with a cross-sectional area of $1.1\ m^2$, a length of $5.3\ m$ and a launch mass of about $1050\ kg$. Such a shape is chosen to minimise the cross-section in the flight direction and hence to reduce the drag. The gradiometer is hosted in the centre of the structure, close as much as possible to the spacecraft centre of mass in order to minimise the angular accelerations and the non-inertial accelerations induced by lateral drag forces on the sensors [138].
The main structure is an octagonal cylinder, made mostly by carbon-fibre reinforced plastic sandwich panels, divided in several compartments, hosting equipment and electronic units, as shown in Figure 2-17. Such a material guarantees lightness, robustness and stable thermal conditions. This “missile” configuration guarantees symmetry around the flight direction, whereas two winglets provide aerodynamic stability. The spacecraft is kept Sun and nadir-pointed through magneto-torquers; one side of the satellite faces ever the Sun and the other one is used as radiator. As depicted in Figure 2-16, two wing-mounted and four body-mounted solar panels allow to collect solar radiation. On each wing, one upwards (zenith) and one downwards (nadir), is mounted a S band antenna for communications. The upper part hosts two GPS antennas as well. Attitude measures are gathered through three star-trackers and by the gradiometer as well.
The need to achieve high performance for the gradiometer established very stringent thermal stability requirements in the range of few milli-degrees Kelvin. To this respect, the thermal decoupling between gradiometer and spacecraft is achieved. Two layers can be identified: an external actively thermal controlled area is kept at a very stable temperature through heaters, whereas an internal passive area, hosting the accelerometers in a homogeneous environment, is separated by blankets. The temperature must be stable to within 10 milli-degrees Kelvin for a period of 200 seconds [138].

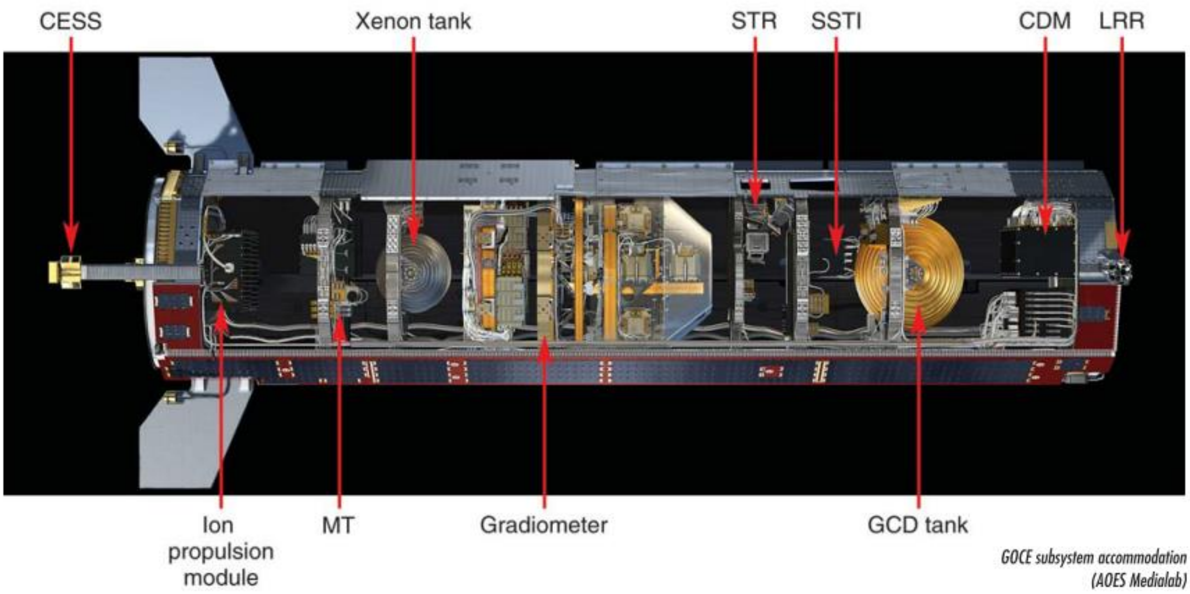

Figure 2-17: Top-down view of GOCE spacecraft showing instruments location. From the left: Coarse Earth-Sun Sensor (CESS), ion propulsion, magneto-torquers (MT), Xenon tank for the ion propulsion, gradiometer, star-tracker, Satellite-to-Satellite Tracking Instrument i.e. GPS (SSTI), nitrogen tank for cold-gas thrusters, command data management unit (CDM), laser retro-reflector (LRR) ([135][141])

Because of the advanced performance achieved by GOCE, there is no neat division between payload and platform but all the spacecraft is built as one whole gravity instrument, in which all the components work together to accomplish an accurate measure of the gravity gradient.
The real core of the payload is represented by the Electrostatic Gravity Gradiometer (EGG), which is devoted to measure the components of the gravity gradient in the three-dimensional space. Although the gradiometer itself is very accurate in the measure, it is more sensitive to the medium and short spatial scales. Therefore, to map the gravity field on all the spatial scales, a second payload is added, a state-of-the-art GPS receiver, which is part of the Satellite-to-Satellite Tracking Instrument (SSTI). It allows to recover the spacecraft positioning through the tracking of up to 12 GPS satellite signals, received by a pair of hemispherical antennas located on the zenithal spacecraft wing. Precise orbit determination is based on data from SSTI and provides information on the long wavelengths of the gravity field spectrum, (i.e. the low degree harmonics). SSTI data are used also for real-time on-board navigation and attitude-reference- frame determination [136].
A further secondary payload enriches the overall GOCE capability, the Laser Retro-Reflector (LRR). The LRR provides supplementary data for Satellite Laser Ranging (SLR) observations to be used as backup for precise orbit determination. It consists of an array of corner-cubes, mounted on a hemispherical frame, able to reflect laser pulses sent by a SLR ground network back along the incident light path [136].
A detailed description of the gradiometer is provided in section 3.3.2.2 related to instruments state of the art.
The gravity gradients, the observable to be measured, are recovered through the principle of the differential accelerometry (see section 3.3). Measurements from two accelerometers belonging to the same arm and separated by $50\ cm$ are subtracted. Neither moving parts, nor liquid fuel were foreseen in the spacecraft to minimise internal disturbances and vibrations to the accelerometers.
In order to take away the (however small) non-gravitational accelerations acting on the spacecraft body, a drag-free system has been employed.

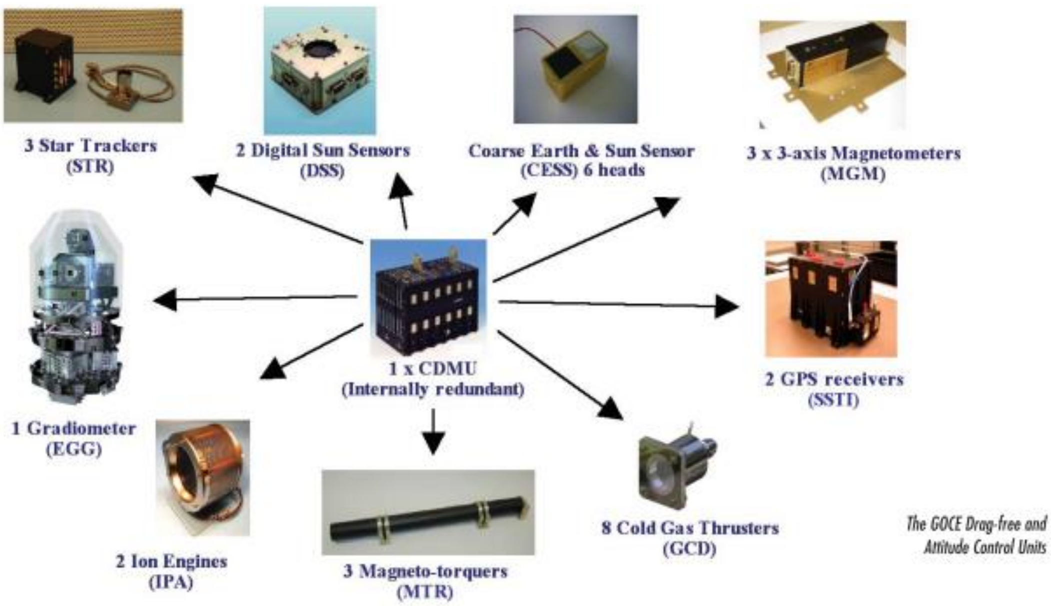

Figure 2-18: view of the drag-free and attitude control units in GOCE spacecraft ([135])

Fundamental to accomplish the measurements is the Drag-Free and Attitude Control (DFAC) [139] [136], by using an ion engine for compensating the along track non-gravitational forces and a set of magnetic torquers for attitude control [140]. The drag-free control system aims at realising a virtual environment reducing the non-gravit ational linear accelerations below a threshold compatible with the accelerometer dynamic range and with the gradiometric performance. For the same reason, the attitude control must constrain the angular accelerations and the angular rates [140].
Due to the intrinsic nature of the gradiometer, able to recover also attitude information through angular accelerations, the gradiometer operates as main sensor in the DFAC.
GOCE was built by an all-European industrial consortium. The GOCE prime contractor was Thales Alenia Space Italy, whereas Astrium Friedrichshafen was responsible for the platform and Thales Alenia Space France along with ONERA for the gradiometer. About 40 other contractors were involved, as depicted in Figure 2-19.

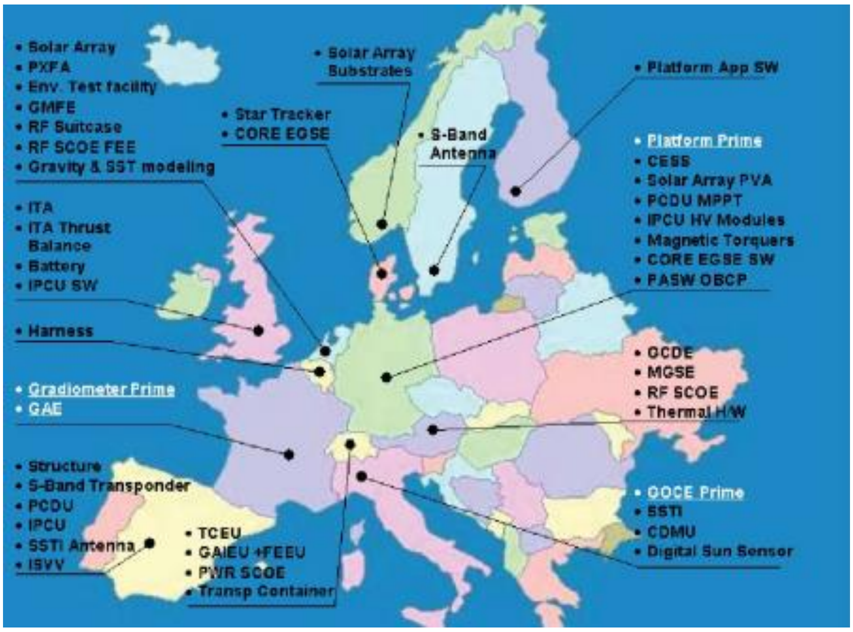

Figure 2-19: Consortium of industries participating in GOCE ([135])

It should be highlighted that GOCE objectives are complementary to those of GRACE mission. While GOCE aims at achieving a maximum spatial resolution in the determination of the Earth’s static gravity field, providing a detailed map of spatial gravity and geoid variations, GRACE is mostly devoted to sense its temporal variations, caused by the transport and redistribution of masses in the Earth system [133].

2.4.4 Moon

Figure 2-20: The near side of Earth's Moon from Lunar Reconnaissance Orbiter spacecraft (Nasa courtesy).

2.4.4.1 Missions

The Moon after the Apollo spacecrafts has started again to be a target of interest at the beginning of nineties. Hereafter only missions that allowed to obtain relevant gravity field data are reported.

2.4.4.1.1 Lunar Prospector

The mission Lunar Prospector (LP) is the first lunar mission NASA-supported after the Apollo fleet. It was launched on January 1998 and placed in a near circular orbit at an altitude of 100 km.

2.4.4.1.2 Kaguya

The SELenological and ENgineering Explorer (SELENE), nicknamed Kaguya before the launch as the namesake of the princess of a famous Japanese tale following the Japanese tradition, was launched by the H-IIA rocket on September 14, 2007, being the Japan's first large lunar mission after the technological demonstrator Hiten [73]. The major objectives of the mission were to understand the Moon's origin and evolution, and to observe the moon in different ways in order to utilise it in the future.
Kaguya investigated the Moon in order to obtain information on its elemental and mineralogical composition, its geography, its surface and sub-surface structure, the remnant of its magnetic field, and its gravity field. At the same time, the observation equipment installed on the orbiting satellite observed plasma, the electromagnetic field and high-energy particles.
Kaguya was constituted by three spacecrafts: a three-axis stabilised main orbiter and two spin-stabilised subsatellites, one named "Okina" (Rstar), used as relay satellite, and a second one named "Ouna" (Vrad), used as satellite in the Very-Long Baseline Interferometry (VLBI). The main orbiter was injected into a peripolar orbit of the Moon at an altitude of 100 km. Okina was placed in an elliptic orbit at an apolune altitude of 2400 km to relay communications between the main orbiter and the ground station for measuring, first time directly, the gravity field of the farside of the Moon. The Ouna satellite, which was in an

elliptic orbit at an apolune altitude of 800 km, played a role of measuring the gravity field around the Moon by sending radio waves.
When Main is orbiting over the farside of the Moon, a tracking signal in the S-band frequency, transmitted from Usuda Deep Space Center (UDSC) of the Japan Aerospace Exploration Agency (JAXA), is relayed by Rstar to Main keeping the phase coherence. Then Main returns the coherent tracking signal to Rstar, and Rstar converts the S-band (2.2 GHz) signal into X-band (8.5 GHz) to downlink a coherent Doppler signal to UDSC, thus establishing tracking data of Main over the farside (four-way Doppler measurement) (12) (fig. S1). At the same time, conventional range and range rate measurements are carried out between Rstar and UDSC (two-way Doppler and range measurements) (fig. S1).
The Kaguya was maneuvered to be dropped around 80.5 degrees east longitude and 65.5 degrees south latitude onto the Moon on June 11, 2009.

2.4.4.1.3 GRAIL

Launched on September 2011 from Cape Canaveral, the GRAIL mission (Gravity Recovery And Interior Laboratory) by NASA was constituted by a couple of twin spacecrafts aimed at mapping the gravity field of the Moon with unprecedented accuracy and spatial resolution [101]. The twin orbiters, named Ebb and Flow, were placed into a polar orbit at the end of 2011, and through a series of manoeuvres were settled into a precise formation to carry out two science phases: a primary mission (March-May 2012) at an average altitude of 55 km and an extended mission (August-December 2012) from a mean altitude of 23 km. Each orbiter hosts a Lunar Gravity Ranging System (LGRS) instrument that carries out dual-one-way ranging to precisely measure the relative motion between the spacecrafts. These distance changes, related especially to the underlying mass distribution variation, are used to develop the lunar gravity field map. The science payload is a GRACE-heritage lunar gravity ranging system (LGRS, it is a modified version of an instrument used on the same spacecraft) that transmits and receives an inter-orbiter Ka-band signal to measure the relative velocity of the two orbiters and an S-band inter-orbiter signal for time correlation between the two orbiters. The science payload includes an Ultra-Stable Oscillator (USO) that provides a steady reference signal for all data, and a Radio Science Beacon to provide one-way X-band signal to the ground for precision orbit determination. The launch mass of each orbiter was 306 kg, including 106 kg of propellant.

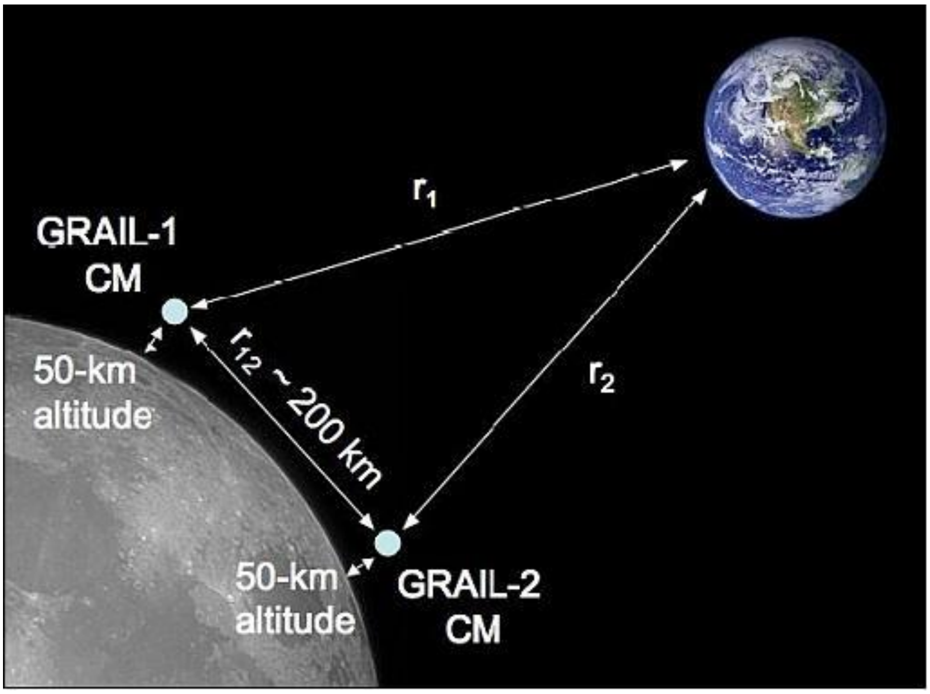

Figure 2-21: Top view of GRAIL spacecraft (NASA courtesy)

The mission configuration is equivalent to the GRACE mission around the Earth. The GRAIL mission was led by the Massachusetts Institute of Technology. The project was managed by the Jet Propulsion Laboratory (JPL), with Lockheed-Martin Space Systems Corporation (LMSSC) contracted to provide the spacecraft. GRAIL's science instrument was developed by JPL. The Science Team contains representation from 15 academic institutions and NASA Centers. GRAIL's twin spacecraft have heritage derived from an experimental U.S. Air Force satellite (XSS-11) and the Mars Reconnaissance Orbiter (MRO) mission, both developed by LMSSC.
GRAIL is a satellite-to-satellite tracking mission that was developed to map the structure of the lunar interior by producing a detailed map of the gravity field. Actually, GRAIL was developed to map the structure of the lunar interior from crust to core. This objective was accomplished by producing detailed maps of the lunar gravity field at unprecedented resolution. These gravity maps will be interpreted in the context of other observations of the Moon's interior and surface obtained by orbital remote sensing and surface samples, as well as experimental measurements of planetary materials. The resulting improved knowledge of the interior was used to understand the Moon's thermal evolution, and by comparative planetological analysis, the evolution of other terrestrial planets. The GRAIL-A (GR-A) and GRAIL-B (GR-B) orbiters, renamed Ebb and Flow after insertion into the lunar orbit, are nearly identical with heritage from past spacecraft built by Lockeed Martin.

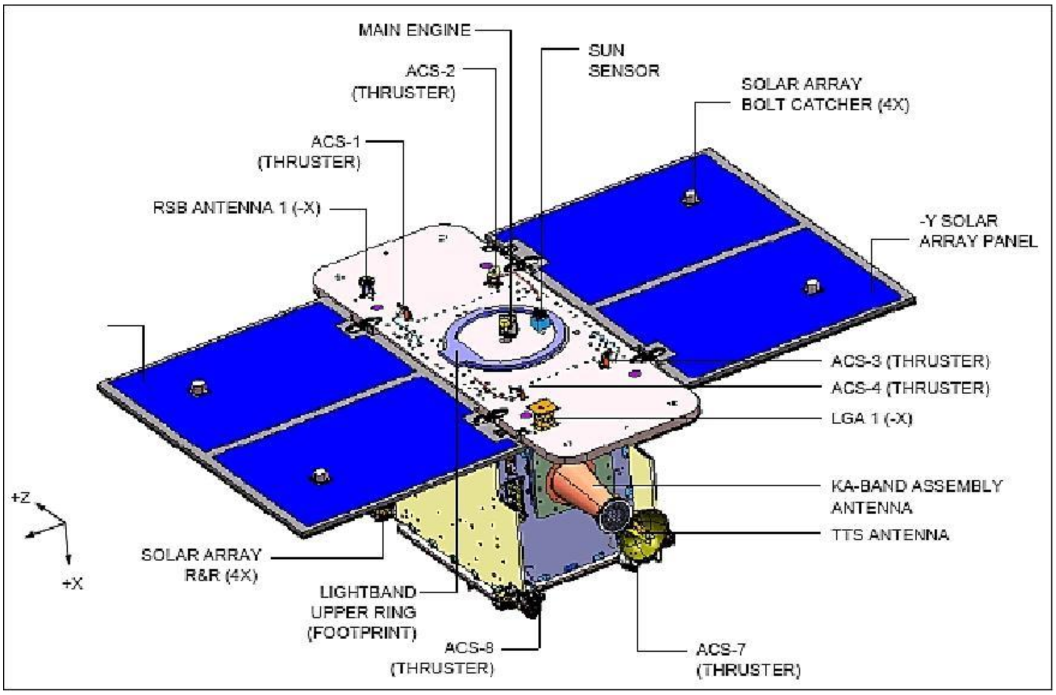

Figure 2-22: Top view of GRAIL spacecraft (from https://earth.esa.int/web/eoportal/satellite-missions/g/grail)

The orbiters are three-axis stabilised with reaction wheels and hydrazine warm-gas thrusters for attitude control, and a star tracker and an inertial measurement unit (IMU) for attitude determination. The IMU propagates the attitude when the star tracker is off-line. Sun sensors provide attitude information in safe mode. A 22-N hydrazine main engine operating in blow-down mode provides the thrust for all manoeuvres except the small orbit trim manoeuvres that are performed with the 1-N ACS thrusters.
Accelerometers in the IMU are used for main engine burn cutoff and manoeuvre reconstruction. There are two low gain antennas (LGA), for communication to the ground.

2.4.4.2 Gravity models

Surprisingly, the global gravity of the Moon is presently known better than any other body in the Solar System, including our Earth [30]. Such a level of knowledge has been achieved in the last twenty-five years through the collection of large and ever and ever accurate gravity data in different missions, such as Lunar Prospector, Kaguya/Selene and, most of all, GRAIL. Especially the latter one allowed to greatly increase the details of the lunar gravitational field.
The measurement of the Moon gravity field started since the dawn of the space programs. Luna 10 mission from URSS in 1966 allowed an accurate estimate of J_2 spherical harmonic coefficient, whereas in 1966-1968 the five Lunar Orbiter from the US provided Doppler tracking data to map the gravity field from equatorial to polar orbital inclinations [67]. Moreover, subsatellites released from Apollo 15 and 16 in 1971 and 1972 were tracked at S-band by the Deep Space Network (DSN). However, although first analyses on this historical data reached at most degree 16 based on data from Apollo 8, 12, 15, 16 and Lunar Orbiter [66], new advances were provided through the use of faster computers, allowing to produce high resolution gravity fields to degree 60 [68]. Further improvements for the low spherical harmonic degrees were introduced through the Clementine mission in 1994 [68].

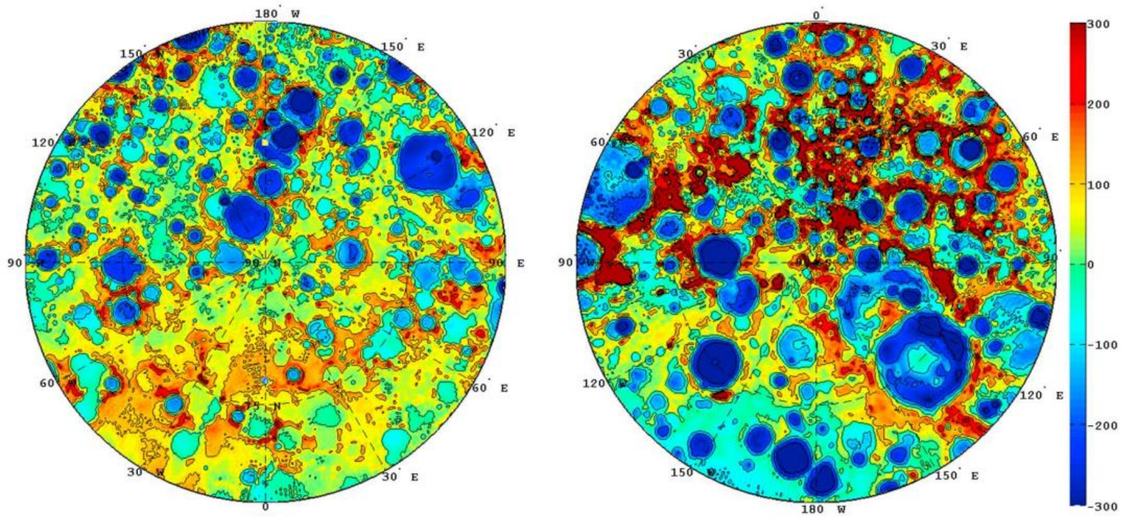

Figure 2-23: High-resolution images of the northern (left) and southern (right) Moon polar regions ([76])

New significant advancements were added with Lunar Prospector (LP), which arrived to the Moon in 1998. Several models were derived from LP tracking data, which were collected at S-band for 1 year, 1 month and 6 months, respectively, on a 100 km, 40 km and 30 km altitude polar orbit [67]. A first model, LP75G, was completed to degree and order 75 and it was followed by higher-resolution models at degree 100 (LP100J) and 150 (LP150Q). The latter one revealed new mascons and increased the knowledge of not yet sampled nearside regions. Moreover, LP150Q was also used as nominal gravity field for following lunar missions, including GRAIL.
A weakness of lunar gravity field models of those times was the lack of observations of the Moon farside, because the Earth-Moon spin-orbit resonance 1:1 hampered its direct observation through the direct tracking from Earth to a spacecraft. The Japanese mission Selenological and Engineering Explorer (SELENE, later Kaguya), launched in 2007, filled in this gap through the first direct measurement of the farside lunar gravity, allowing to produce a gravity model till to degree and order 100 (SGM100h) and to retrieve gravity information on the farside to about harmonic degree 70 [67].
However, the arrival of the GRAIL mission in 2012 has completely overcome this weakness through a direct observation of the gravity field also on the dark side of the Moon.

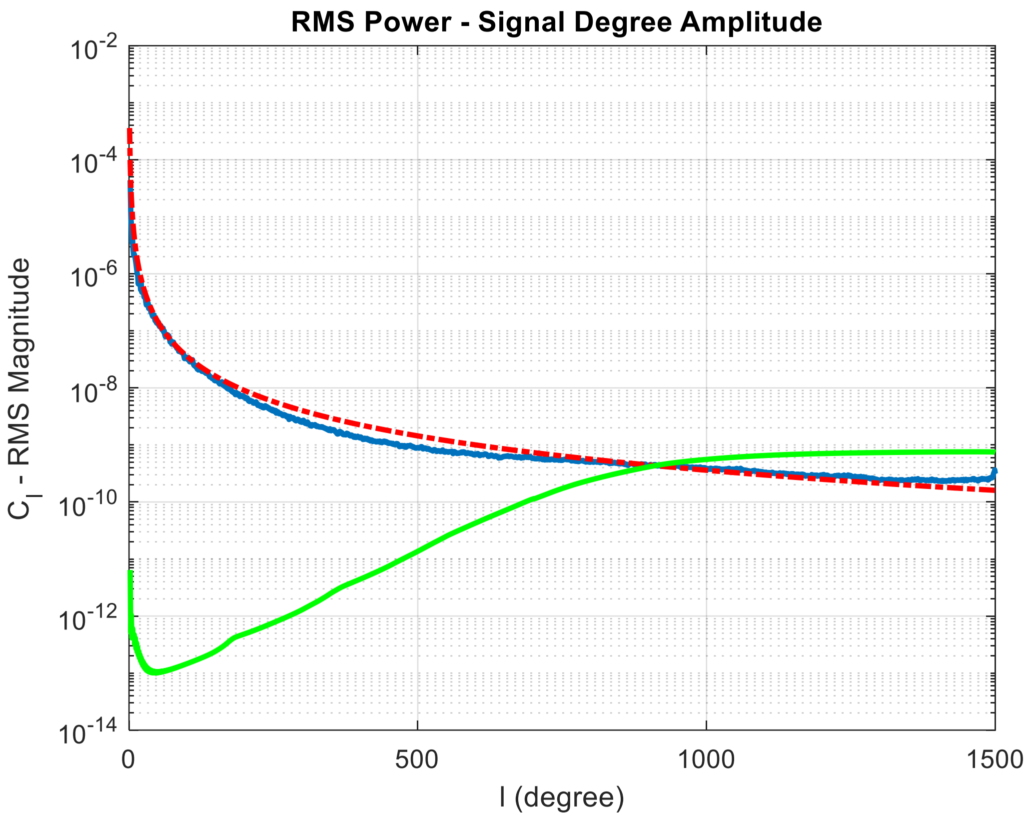

Figure 2-24: The gravity spectrum of Moon from GL1500E (computed with data from [85]): gravity field, gravity field error and Kaula rule are shown respectively in blue, green and red colours

2.4.5 Mars

Figure 2-25: An image of Mars taken from Hubble Space Telescope near the opposition of the red planet (NASA courtesy)

2.4.5.1 Characteristics

Mars is the archetype of the Solar System planets since ancient times. Due to its high brightness, after the Venus and Jupiter couple, and its fascinating red colour, Mars received a lot of attention by ancient cultures, including Greeks and Romans. The latter ones associated it to the god of war with the names Ares and Mars, respectively.
Due to all these reasons, Mars is one of the planet most targeted by space missions.
The surface of Mars is characterised by a wide variety of volcanic and tectonic structures [32]. Differently from the Earth, there are no indications of active plate tectonics, but crustal magnetisation indicates that plate tectonics may have occurred in early Mars evolution. The most evident characteristic of Mars is the hemispheric division of its surface between much younger lowland plains with relatively sparsely craters in the north and heavily cratered and rough highlands, formed in its early history in the south [32]. The boundary between emispheres is dominated by outflow channels and chaotic terrain extending along broad gradual slopes [36]. The Tharsis regions is situated close to the near-equatorial boundary between the northern and southern hemispheres and represents a giant volcanic dome established early in the planet’s history. Major volcanoes such as Olympus Mons and the Tharsis Montes were emplaced on top of the Tharsis area [36].
The Martian thermal history can be divided into a very active early phase with accretional eating, core formation, strong mantle convection, and high surface fluxes of heat and magma and a second phase – the last 3.5 billions of years – marked by slow cooling. Mantle plumes play a major role in heat exchange. Very likely its core is completely fluid and non-convecting [32].

2.4.5.2 Missions

Mars is one of the most explored planets in the Solar System. More missions have been attempted to Mars than to any other place in the Solar System except the Moon, and about half of the attempts have failed. Table 2-4 shows off a list of the successful missions to the Red Planet.
Starting with Mariner 4, US and USSR dominated the rush to Mars starting with the Mariner series (Mariner 4, on 1964).
From the point of view of gravity field data, the most important missions devoted to begin from 1996 on with the Mars Global Surveyor (MGS), Mars Odyssey (MO) and the Mars Reconnaissance Orbiter (MRO).

Table 2-4 List of the successful missions to Mars (from [83])

#	Launch	Name	Country	Reason
1	1964	Mariner 4	US (flyby)	Returned 21 images
2	1969	Mariner 6	US (flyby)	Returned 75 images
3	1969	Mariner 7	US (flyby)	Returned 126 images
4	1971	Mars 3 Orbiter/Lander	USSR	Orbiter obtained approximately 8 months of data and lander landed safely, but only 20 seconds of data
5	1971	Mariner 9	US	Returned 7,329 images
6	1973	Mars 5	USSR	Returned 60 images; only lasted 9 days
7	1973	Mars 6 Orbiter/Lander	USSR	Occultation experiment produced data and Lander failure on descent
8	1975	Viking 1 Orbiter/Lander	US	Located landing site for Lander and first successful landing on Mars

9	1975	Viking 2 Orbiter/Lander	US	Returned 16,000 images and extensive atmospheric data and soil experiments
10	1996	Mars Global Surveyor	US	More images than all Mars Missions
11	1996	Mars Pathfinder	US	Technology experiment lasting 5 times longer than warranty
12	2001	Mars Odyssey	US	High resolution images of Mars
13	2003	Mars Express Orbiter/Beagle 2 Lander	ESA	Orbiter imaging Mars in detail and lander lost on arrival
14	2003	Mars Exploration Rover - Spirit	US	Operating lifetime of more than 15 times original warranty
15	2003	Mars Exploration Rover - Opportunity	US	Operating lifetime of more than 15 times original warranty
16	2005	Mars Reconnaissance Orbiter	US	Returned more than 26 terabits of data (more than all other Mars missions combined)
17	2007	Phoenix Mars Lander	US	Returned more than 25 gigabits of data
18	2011	Mars Science Laboratory	US	Exploring Mars' habitability
19	2013	Mars Atmosphere and Volatile Evolution	US	Studying the Martian atmosphere
20	2013	Mars Orbiter Mission (MOM)	India	Develop interplanetary technologies and explore Mars' surface features, mineralogy and atmosphere.
21	2016	ExoMars Orbiter/Schiaparelli EDL Demo Lander	ESA/Russia	Orbiter studying Martian atmosphere and EDL demo lander lost on arrival
22	2018	Mars InSight Lander	US	Spacecraft is now on its way to Mars and is scheduled to land on Mars around 3 p.m. EST (noon PST) Nov. 26, 2018.

2.4.5.2.1 Mars Reconnaissance Orbiter (MRO)

NASA's Mars Reconnaissance Orbiter was launched from Cape Canaveral in 2005, on a search for evidence that water persisted on the surface of Mars for a long periods of time. While other Mars missions have shown that water flowed across the surface in Mars' history, it remains a mystery whether water was ever around long enough to provide a habitat for life.

2.4.5.3 Gravity models

Mars is one of the most explored planet in the Solar System and hence a lot of data are available from the several missions which orbited and currently orbit the red planet. A list of the successful missions to the red planet [83] is shown in Table 2-4. First gravity models of Mars were developed through the data of Mariner 9 in 1971-72 and later with Viking orbiters in 1975-1982 [76]. The best model was a complete gravity field to degree and order 50, Mars 50c [81], based on a previous nominal field GMM-1 (Goddard Mars Model 1) developed by Smith et al. [82]. These previous models suffered from a not uniform resolution due to high

elliptical orbits and from the use of low frequency radio-tracking at S band (2-4 GHz, Figure 3-3).
The following missions to Mars allowed to build new and improved gravity field solutions. The use of higher frequency range (X-band, 8-12 GHz) and lower orbits (about 400 km for the periapse) started with Mars Global Surveyor (MGS) [76] and allowed to produce the first completely uniform gravity field model. The MGS95J is the last model of this mission and includes data from Mars Odyssey as well: the solutions were determined at degree and order 95 but the global resolution (or degree strength), i.e. the degree where the average coefficient magnitude equals the uncertainty [65], was limited to degree 70, corresponding to a spatial resolution of 152 km [84].

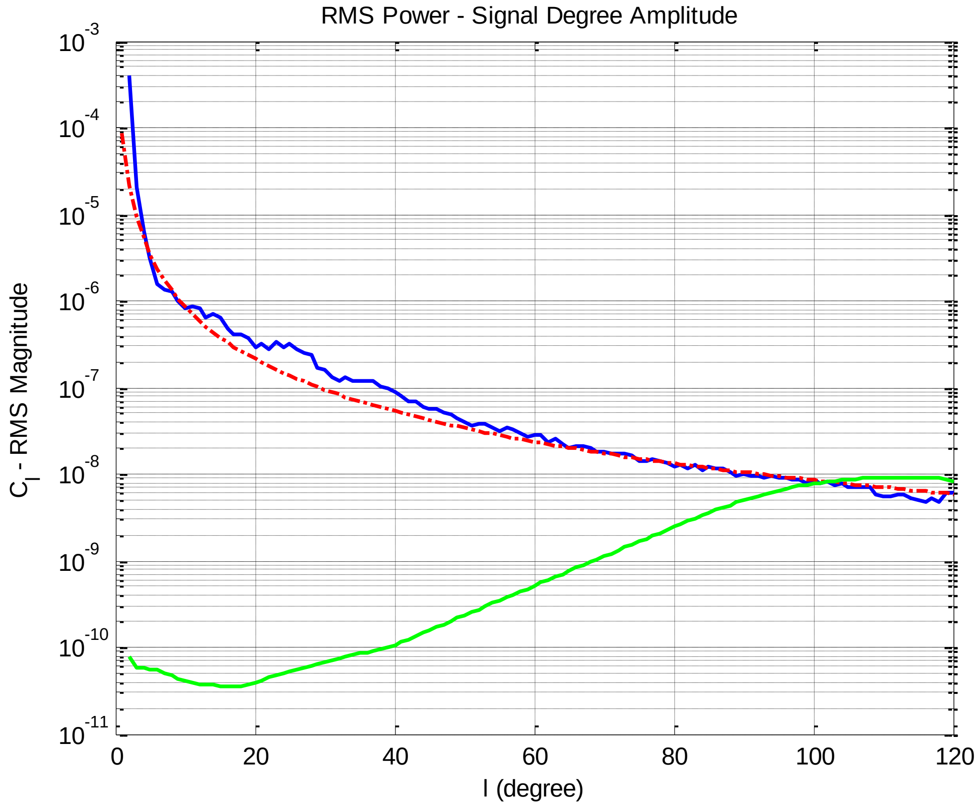

Figure 2-26: The gravity spectrum for MRO120D (computed with data from [85]): gravity field, gravity field error and behaviour of the field according to Kaula rule are shown, respectively, in blue, green and red

With the arrival of Mars Reconnaissance Orbiter (MRO) in 2005 on a low polar orbit with periapse of 255 km, a significant improvement in the global resolution was achieved, increasing from harmonic degree 70 to 90. These data gave birth to the series of gravity solutions named MRO95A and following [76].
The latest gravity model to date is the MRO120D developed by the group of Alex Konopliv at JPL [65]. This model combines radio-tracking data coming from several years of observations collected by different orbiters and landers, respectively: Mars Reconnaissance Orbiter (MRO), Mars Odyssey (MO), Mars Global Surveyor (MGS) and Mars Pathfinder, Viking lander, Mars Exploration Rover Opportunity (MER). This combination of different dataset provides information on gravity, tides and orientation.
With respect to previous models, MRO120D improves the higher degree gravity coefficients (due to more MRO tracking data) and reduces the uncertainty in the Mars orientation parameters up to a factor of two with respect to previous models. The new field extends the

maximum spherical harmonic degree to 120 with a degree strength close to degree 95/100. Figure 2-26 shows off the gravity solution of MRO120D along with the corresponding error and the behaviour of the gravity field according to Kaula rule for Mars (Mars constant $c = 8.5 \cdot 10^{-5}$ from [76]). For MRO120D a Kaula power constraint is applied to harmonic degrees higher than 80.

A picture of the spherical harmonic resolution of the gravity field distributed in space is shown in Figure 2-27. Such an image shows off the spatial distribution of the degree strength over the Mars surface [80]. For each longitude and latitude, the gravity error spectrum is computed and compared to the expected gravity coefficient magnitude versus degree. The point where the error in the spectrum equals the signal gives the resolution or degree strength. From this picture derives that a minimum global resolution is achieved at harmonic degree 90, whereas improvements till 120 are achieved over the south pole due to the lower MRO altitude.

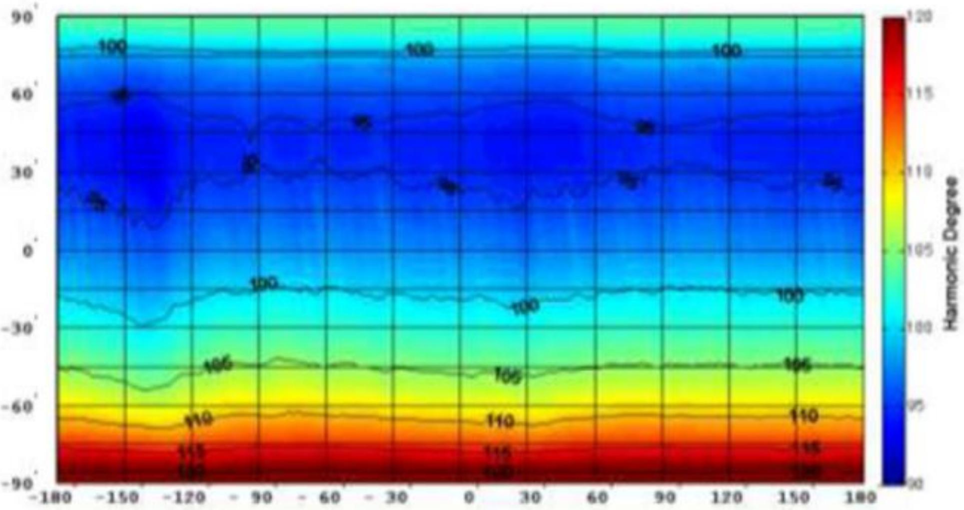

Figure 2-27: The resolution of the Mars gravity field MRO120D from the covariance matrix of the solution [80].

Concerning information about the planet, Doppler radio-tracking data have provided basic information about the planet's mass, spin-axis precession rate, degree-2 tidal potential Love number k2, and static and seasonal gravitational field [80]. The interior structure of Mars was initially modelled but these models suffered from poorly known values of its radius and Moment of Inertia (MoI). Improved measurements of the planet's mass M, radius R, gravitational potential, and rotation rate by the Mariner, Viking, and Pathfinder spacecraft provided geodetic constraints required for models of the interior structure. The polar Moment of Inertia of Mars was derived from a combined analysis of low-degree gravitational field data and spin-axis precession estimates from MGS tracking and Mars Pathfinder and Viking Lander range and Doppler data. The values of the MoI factor of Mars are consistent with the model of a mostly hydrostatic planet with a non-hydrostatic contribution to the MoI factor entirely related to the axi-symmetric distribution of topographic loads about [36].

2.4.6 Outer planets characteristics and gravity models

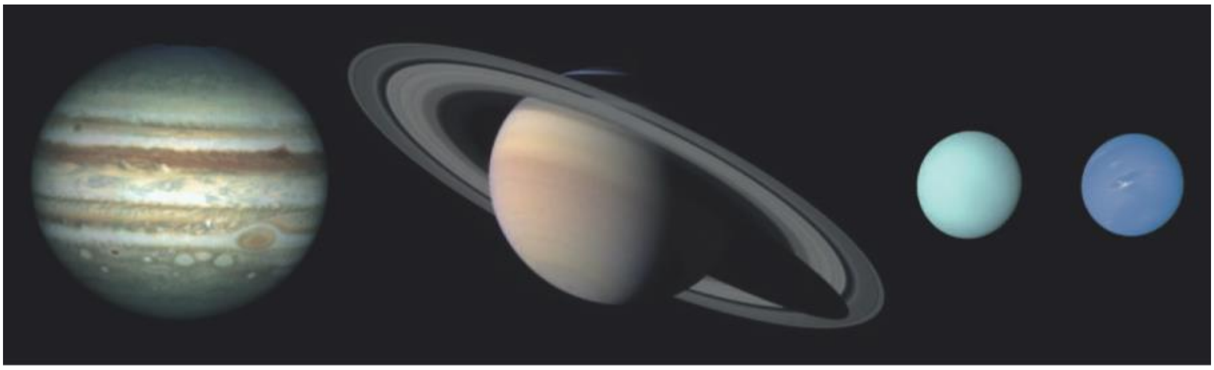

Figure 2-28: A group picture of the external planets Jupiter, Uranus and Neptune (from Voyager 2) and Saturn (Cassini), from [34]

All the four outer planets are characterised by large masses, which produce strong and extended gravity fields, and fast rotations, which induce evident pole flattening. Indeed, the gravitational field measured by the spacecrafts departs from a purely spherical function due to the planets' rapid rotation. Because the giant planets are very close to hydrostatic equilibrium the coefficients of even order in the spherical harmonic expansion are the only ones that are not negligible [34]. Table 2-5 and Table 2-6 report some parameters of the external giant planets, such as mass, density, polar and equatorial radius, gravity harmonics coefficients (unnormalised) for Jupiter and Saturn, as obtained from the last measures of Juno (Jupiter) and Cassini (Saturn) missions [90][91], and spherical harmonic coefficients (normalised to the reference radius R_{ref}) for Uranus and Neptune [34].

Table 2-5 Characteristics of the giant planets gravity field (adapted from [90][91] and from [34])

Data	Jupiter		Saturn		References
	Value	Uncertainty	Value	Uncertainty	
$M\ x\ 10^{-26}(kg)$	18.986112	5.68463036			[34]
$R_{eq}\ x\ 10^{-7}(m)$	7.1492	-	6.0268	-	[34]
$R_{pol}\ x\ 10^{-7}(m)$	6.6854	-	5.4364	-	[34]
$\bar{R}\ x\ 10^{-7}(m)$	6.9894	-	5.8210	-	[34]
$\bar{\rho}\ x\ 10^{-3}(kg\ m^{-3})$	1.3275	-	0.6880	-	[34]
$R_{ref}\ x\ 10^{-7}(m)$	7.1492	-	6.0330	-	[34]
$J_2\ x\ 10^{-6}$	14696.572	0.014	16290.573	0.028	[90][91]
$C_{21}\ x\ 10^{-6}$	− 0.013	0.015	-	-	[90][91]
$S_{21}\ x\ 10^{-6}$	− 0.003	0.026	-	-	[90][91]
$C_{22}\ x\ 10^{-6}$	0.000	0.008	-	-	[90][91]
$S_{22}\ x\ 10^{-6}$	0.000	0.011	-	-	[90][91]
$J_3\ x\ 10^{-6}$	− 0.042	0.010	0.059	0.023	[90][91]
$J_4\ x\ 10^{-6}$	− 586.609	0.004	-935.314	0.037	[90][91]
$J_5\ x\ 10^{-6}$	− 0.069	0.008	-0.224	0.054	[90][91]
$J_6\ x\ 10^{-6}$	34.198	0.009	86.340	0.087	[90][91]
$J_7\ x\ 10^{-6}$	0.124	0.017	0.108	0.122	[90][91]
$J_8\ x\ 10^{-6}$	− 2.426	0.025	-14.624	0.205	[90][91]
$J_9\ x\ 10^{-6}$	− 0.106	0.044	0.369	0.260	[90][91]
$J_{10}\ x\ 10^{-6}$	0.172	0.069	4.672	0.420	[90][91]

$J_{11}\ x\ 10^{-6}$	0.033	0.112	-0.317	0.458	[90][91]
$J_{12}\ x\ 10^{-6}$	0.047	0.178	-0.997	0.672	[90][91]

Table 2-6 Characteristics of the icy giant planets gravity field (adapted from [34])

Data	Uranus	Neptune
$M\ x\ 10^{-26}(kg)$	0.8683205	1.0243548
$R_{eq}\ x\ 10^{-7}(m)$	2.5559	2.4766
$R_{pol}\ x\ 10^{-7}(m)$	2.4973	2.4342
$\bar{R}\ x\ 10^{-7}(m)$	2.5364	2.4625
$\bar{\rho}\ x\ 10^{-3}(kg\ m^{-3})$	1.2704	1.6377
$R_{ref}\ x\ 10^{-7}(m)$	2.5559	2.5225
$J_2\ x\ 10^2$	0.35160	0.34084
$J_4\ x\ 10^2$	−0.354	−0.334
$P_\omega\ x\ 10^{-4}(s)$	6.206	5.800
q	0.02951	0.02609
C/MR_{eq}^2	0.230	0.241

From these data derive that these planets have low densities, from 0.688 g/cm^3 for Saturn to 1.64 g/cm^3 for Neptune, to be compared with densities of 3.9 to 5.5 g/cm^3 for the terrestrial planets in the Solar System. Since the internal compression strongly increases with mass, the conclusion is that these planets contain an important proportion of light materials, including hydrogen and helium. At the same time, it implies that Uranus and Neptune, which are less massive, must contain a relatively larger proportion of heavy elements than Jupiter and Saturn. Indeed, Jupiter and Saturn are likely dominated in the composition by hydrogen and helium at 90 %, whereas in Uranus and Neptune the composition achieves no more than 15-20 % [35]. Therefore, outer planets are furtherly subdivided between gas giant planets Jupiter and Saturn, dominated by hydrogen-helium, and the “ice giants” or “sub giants” Uranus and Neptune. The latter name “ice giants” refers to the so named planetary ices, a mixture of condensed compounds constituted mainly by H_2O, CH_4, NH_3, characteristic elements found on the surface of the icy satellites (Europa, Ganymede, Callisto, Titan, Triton), and likely included in the Uranus and Neptune bulk interiors at high-pressure [34].
All the planets, with deviations more or less pronounced, show large flattening witnessed by the flattened poles, extended atmospheres characterised by zonal winds, large cyclonic formations and vortexes, variegate colours due to different minor species in the high atmosphere, widespread clouds with different compositions, ammonia for Jupiter and Saturn whereas methane for Uranus and Neptune.
The planets are also relatively fast rotators, with periods of about 10 hours for Jupiter and Saturn, and about 17 hours for Uranus and Neptune [34]. This aspect is witnessed by the visual observation of the pole flattening and by the significant difference between the polar and equatorial radii. Moreover, this is also proved by the gravitational moments represented by the harmonic coefficients that differ significantly from a null value. However, the fluid nature of these planets implies that there is no unique rotation frame: atmospheric zonal winds imply that different latitudes rotate at different velocities, and the magnetic field provides another rotation period. Because the magnetic field is tied to the deeper levels of the planet, it is believed to be more relevant when interpreting the gravitational moments.
The Jovian system has been studied deeply for the first time by the NASA mission Galileo between 1995 and 2000. One of the most important achievements is that the Galilean

satellites (Io, Europa, Ganymede and Callisto) are differentiated [180]. Models of the internal structure of these satellites have been developed in the last years based on interpretation of tectonics, magnetic field, and moment of inertia (J_2). One of the main questions that forthcoming missions (the future JUICE and Europa Clipper) would have to address is the presence of an ocean within Europa and the determination of its depth thickness and may be composition.
Other issues include the characteristics of the core and the existence of volcanism in the silicate core. Europa has an eccentricity which is maintained thanks to the 1,2,4 Lagrange resonance between Io, Europa and Ganymede. The H_2O/silicate ratio of Europa is much smaller (density much larger) than that of the larger satellites Ganymede and Callisto. Also, Europa is quite close to Jupiter and models of tidal heating suggest that this is a major source of internal heating which may prevent the satellite from a complete freezing. Because Europa has an induced magnetic field and an active tectonics, it is supposed that it hides a deep ocean, whose depth is debated. Measures of Love numbers kS and k2, whose values are related to the presence of an ocean, to the thickness of the ocean, and to the viscosity of the ice shell, could help in solving this element [180].
The most recent measurements of the Jupiter gravity field have been acquired by the on-going Juno mission [90]. Data allowed to reconstruct the gravitational field till to degree 24 with a degree strength of $l = 12$; results are reported in Figure 2-29 [90].

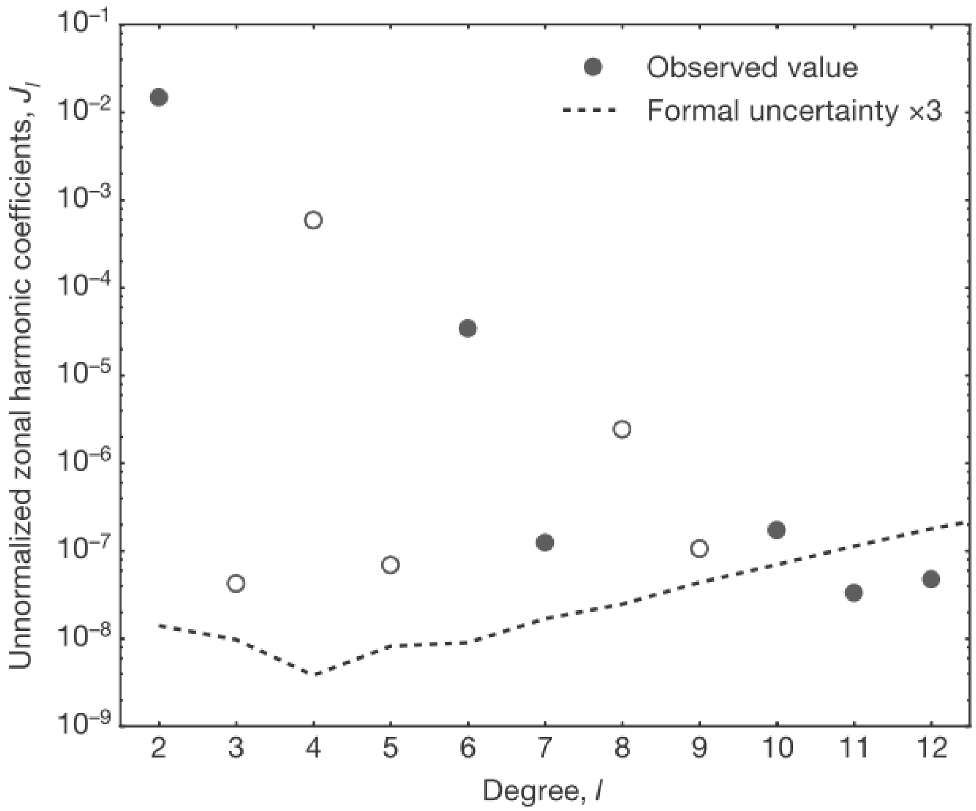

Figure 2-29: Plot of the unnormalised harmonic zonal coefficients as derived from Juno measurements at Jupiter; circles show the measured values (solid for positive and empty for negative), while dashed line depicts the uncertainty (from [90]).

Indeed, as depicted in [90] and [91], the mass distribution in a fluid and fastly rotating planet would imply a spherical expansion of the gravitational field with only even zonal harmonics. Any internal dynamics due to winds in the deep atmosphere would introduce signatures in

the ideal gravitational field as deviations in the uniform rotation on the even zonal harmonics and north-south asymmetries through non-zero values of the odd zonal harmonics. This expected behaviour has been confirmed at Jupiter with Juno measures, depicted in Figure 2-29, where even harmonics are the dominant elements in the gravitational field, whereas the odd harmonics smaller although non-zero show an interior dynamics likely associated to zonal winds till to 2000-3000 km deep in the atmosphere.
Saturn's system has been deeply studied by the NASA/ESA Cassini-Huygens mission from October 2004 to September 2017.
The measurements of last mission phase [91], collected through repeated passes closer and closer to the cloud tops, allowed to determine the gravitational field till to degree and order 20, with a degree strength of $l = 12$ (twice the previous known values) (Figure 2-30).

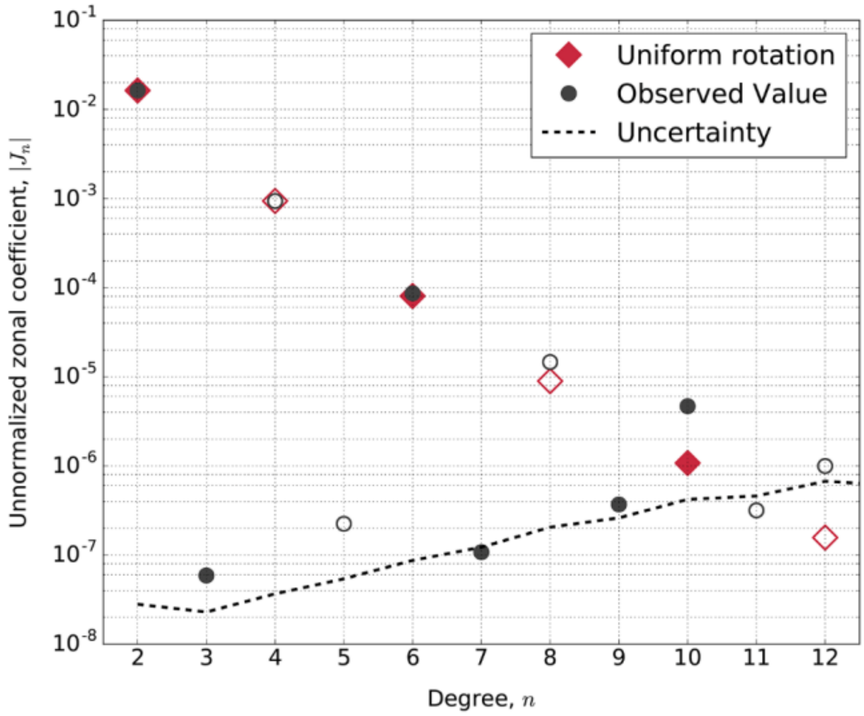

Figure 2-30: Plot of the unnormalised harmonic zonal coefficients as derived from Cassini measurements during the "Grand Finale"; red diamonds (solid for positive e and empty for negative) depict the model of uniform rotation, while circles show the measured values (from [91]).

A comparison between the expected values for a uniform rotation of a fluid body and the observed values provided evidence of a differential rotation of the atmosphere extending in depth (about 9000 km). Such a behaviour derives from the rise of the observed values of J_6, J_8, J_{10} with respect to the uniform rotation, as depicted from results in Figure 2-30.
Concerning its large satellite Titan, the gravity field has been reconstructed till to degree and order 5 in terms of degree strength [92]. Such data were based on the analysis of 9 fly-bys dedicated to gravity measurements, in addition to a high-altitude pass (not previously sampled) during the last phase of Cassini mission. Such data allowed to confirm that Titan is differentiated and its interior state is compatible with hydrostatic equilibrium. Moreover, the moon is subjected to large tidal variations driven by the orbit eccentricity around Saturn.

2.4.6.1 Missions

The external Solar System was explored for the first time by the Pioneers probes that flew by Jupiter (Pioneers 10 and 11) and Saturn (Pioneer 11) and later by the very successful Voyager I and II missions [31]. The latter ones took advantage of a rare geometric arrangement of the outer planets that occurs only once every 176 years. This configuration allowed a single spacecraft to swing by all four gas giants without the need for large on-board propulsion systems; without these gravity assists, the flight time to Neptune would have been 30 years. Moreover, the Voyagers discovered rings at Jupiter and Uranus and explored the rich satellite systems and found the Galilean Io moon to be the most volcanically active body in the Solar System. The Voyagers for the first time allowed a detailed view of the rich phenomenology of icy satellite surfaces. The next step was the Galileo mission which put the first orbiter around Jupiter and after several years plunged into Jupiter’s crushing atmosphere in September 2003. The spacecraft was deliberately destroyed to protect the Jovian system, in particular Europa, from being polluted. Galileo made several discoveries, including the magnetic field of Ganymede and evidence for oceans underneath the ice crusts of the Galilean moons Europa, Ganymede, and Callisto. Moreover, on its route to Jupiter, Galileo discovered for the first time a moon (Dactyl) that is orbiting an asteroid (Ida) and observed comet Shoemaker–Levy crashing into Jupiter. Galileo observed the Jovian satellites at much improved resolution and discovered several new ones. Comparison with Voyager images of volcanic features on Io showed significant modifications that had occurred in the roughly 20 years between the two missions.

An instrumented descent probe released from the Galileo orbiter entered the Jovian atmosphere in December 1995 and provided the first in situ measurements of the state and the chemistry of a giant planet atmosphere shroud.

More recently, the NASA Juno mission has arrived to Jupiter (July 2016) and it is studying the planet’s gravity and magnetic fields, its atmosphere dynamics, and its composition.

Moreover, the Jovian satellites Callisto and Europa will be the prime target of ESA’s JUICE (JUpiter ICy moons Explorer) mission in the 2022-23, with a special focus on Ganymede around which the spacecraft will enter into orbit for the first time (2033).

The Saturn system shared with the Jupiter’s one the history of exploration by automatic probes with Pioneer 11 and Voyager 1 and 2. The first orbiter around Saturn was the successful and extraordinary NASA/ESA mission Cassini, launched in 1997 and arrived to Saturn in 2004. It is the longest mission after the Voyager era and the longest for an orbiter around a planet, lasting till the 15th of September 2017, when the probe was plunged into the planet to ensure the safety and the conservation of the Saturn's moons for future exploration—in particular, the ice-covered, ocean-bearing moon Enceladus, and also Titan, with its intriguing pre-biotic chemistry.

The Cassini key discoveries included the global ocean with indications of hydrothermal activity within Enceladus, and liquid methane seas on Titan.

2.4.7 Small bodies gravity

Future missions to asteroids and outer planets will address the question of the internal structure of these bodies. Between Mars and Jupiter, several asteroids orbit around the Sun. Among those, Ceres and Vesta have been studied by the Dawn mission. Vesta is a dense asteroid and several meteorites (HED meteorites) are thought to come from this asteroid. Their study shows that they are differentiated. But this must be checked by future missions.

2.4.7.1 Missions

Apart mission Dawn to Ceres and Vesta asteroid, or Hayabusa to Ryuku, or similar, hereafter the attention is directed to a new mission currently envisaged and in definition. Indeed, an interesting mission in the domain of small bodies is *Hera*. It is a candidate for an ESA small mission of opportunity within the Asteroid Impact & Deflection Assessment mission (AIDA), whose second component is the Double Asteroid Redirection Test (DART) by NASA [101]. The objective of the mission belongs basically to a planetary defence initiative, focused on the Near-Earth Asteroid (NEA) constituted by the binary system Didymos and Didymoon. It is constituted by two very small bodies, a 780 meter diameter primary and a 160 meter diameter secondary. Indeed, the NASA mission aims at performing a kinetic impact on Didymoon, whereas Hera will follow up with a detailed investigation of the modification induced on the moon after the crash. A timeline of the events is depicted in Figure 2-31.

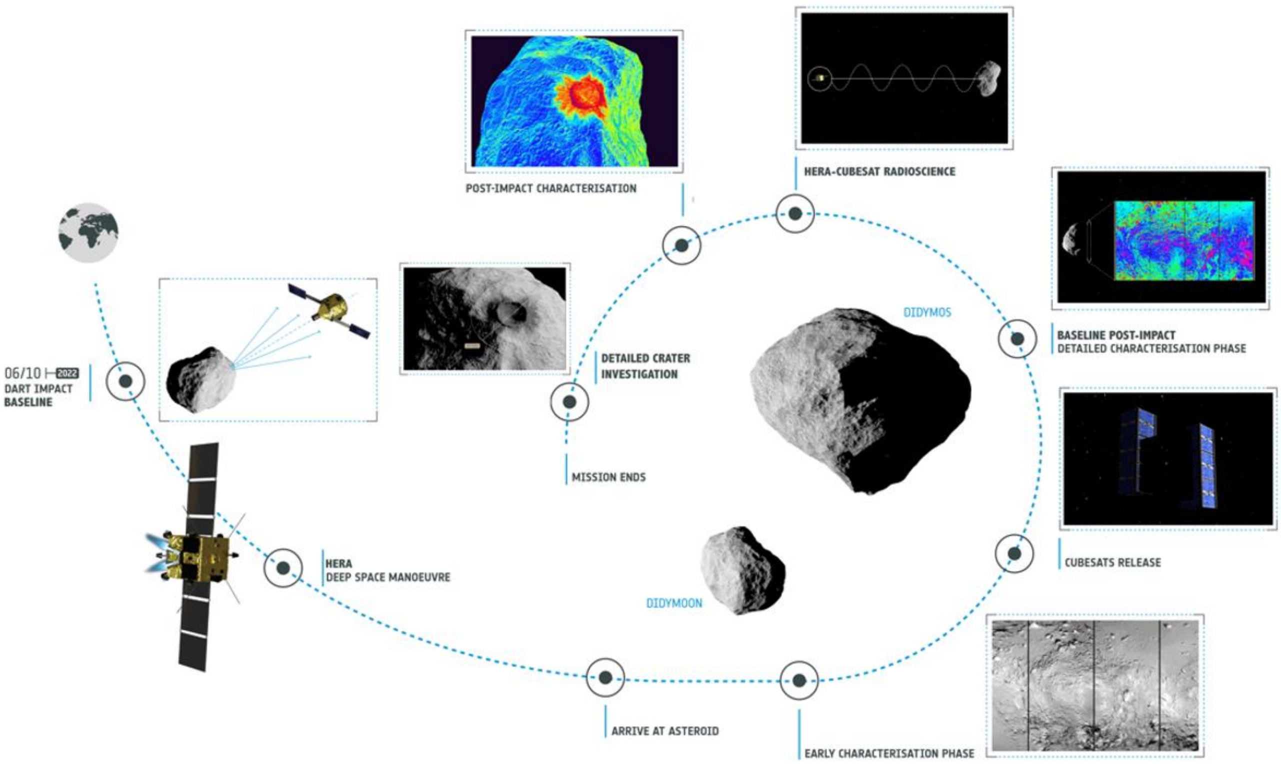

Figure 2-31: Timeline of the DART and Hera missions to be sent to the Didymos binary asteroid system (picture from ESA website)

However, in addition to the main objective, manifold benefits can be derived in terms of science return and technology demonstration. The mission is underdefinition, however some elements have been already established.

After the collision of DART with the small moon in 2022, the Didymoon orbit and orbital period will change. However, those changes will not be measured accurately by ground observatories and consequently the transferred momentum will not be measured directly because of the unknown Didymoon mass. Hera mission, to be launched in 2023 and to arrive in 2026, will perform such a measure along with a detailed investigation of the moon through a high-resolution visual and laser mapping, detailed observations of the produced crater and of the surface properties, radio-science measurements to reconstruct mass, dynamics and gravity field to infer information on the internal structure. The latter one will be

fostered through the use of JUVENTAS cubesat to establish an intersatellite link with Hera mothercraft. JUVENTAS will use also low frequency radar, three axis gravimeter, visible camera for interior and surface characterisation. A second cubesat APEX will characterise the crater and its surroundings through imager, spectrometer, ion mass analyse and magnetometer. At the end of the mission both cubesats will try to land on Didymoon and to accomplish further in-situ analyses for the following days.
The relevant part of this mission is the capability of measuring the gravity filed of the small moon. Moreover,

2.5 Science needs

The retrieval of gravity field information is crucial to investigate scientific issues of interest and to answer to questions related to the formation, evolution and structure of planetary bodies. Planetary interiors maintain information on the processes at large scale that have driven the thermal and tectonic evolution; indeed, surface and tectonic features are mainly the result of heat exchanges from the interior to the surface. Gravity field measurements are one of the observational methods to investigate those processes and to place constraints on the structure of the planetary interiors, the formation and geologic evolution of a planet [40][30]. The retrieval of the spherical harmonic coefficients used to describe the gravitational field of a body gives insights into e.g. its polar oblateness, moment of inertia and deviations from hydrostatic equilibrium. With geologic assumptions and other remote sensing data, significant geophysical parameters, related e.g. to crust and mantle density and thickness, core size and structure, mantle/core coupling can be obtained [30]. These parameters are used in planetary models to address topics such as planets differentiation, thermal evolution, characteristics and composition of the interiors.
The information collected in the previous sections offers an extremely diversified scenario on the current knowledge of the gravity field. As multiple fleet of spacecrafts have visited some planetary bodies for a deep exploration, such as Mars, Venus and obviously the Earth and the Moon, very few satellites or none have reached other bodies. In the latter case, just few satellites entered the orbit's body, whereas others carried out single or multiple fly-bys. Moreover, apart the Earth and the Moon, the spatial resolution is limited to the major structures and features, achieving hundreds of kilometers, also for the most explored planets, Mars and Venus. The result is that the gravity field knowledge is very good for some objectives and very poor or lacking for others.
A summary of the latest gravity field models of planets and moons (when available) is shown in Table 2-7. Some clarifications about the meaning of the items used in the table. The global resolution is the degree where the average coefficient magnitude equals the uncertainty (S/N = 1), hence the error in the spectrum equals the signal; it is also known as degree strength averaged over the whole planet [65][84]. The spectral resolution is the highest achievable harmonic degree l of the spherical harmonic expansion, although just on particular areas. The spatial resolution is derived from the known formula $\Delta_{res}= \pi R/l$, where l is the maximum harmonics degree and R is the equatorial radius of the body (see section 2.2.2).
On the basis of the previous gravity field state of the art the following considerations in terms of scientific requirements can be drawn.
Future missions for Earth and Moon should focus on higher accuracy and higher resolution in space and time. Gravity field models of Earth and Moon nowadays are well known up to very high degrees and orders. In the years several models for Earth gravity have been produced depending on the employed data and on the application to be used. Indeed, the combination of data of different origins allowed to reach very high degrees/spatial resolutions. One of the last models (as obtained from [47]) is the SGG-UGM-1 [77] which is

based on the model EGM2008 and on GOCE data. Such a global gravity model allows to compute the harmonics till to degree and order 2159, with a degree strength averaged over the planet of about 200 corresponding to a spatial resolution of about 9 km. The EGM2008 is a spherical harmonic model of the Earth's gravitational potential, obtained by merging terrestrial, altimetry-derived, and airborne gravity data, which first provided a very accurate and global gravity model for the Earth for a wide range of applications [78]. Time resolution is a characteristic introduced in some of the last models (when needed) since the arrival of GRACE mission; with this mission a systematic study of time variable Earth's gravity field over a monthly range has started, previously limited to J_2 and few other degrees. In this case, one of the first model produced is the GGM05S [79] estimated till to spherical harmonic degree 180 by using roughly ten years (2003-2013) of GRACE K-band range-rate, attitude, accelerometer and GPS tracking data. This dynamic field allows to reach a degree strength around 160, corresponding to a spatial resolution of about 125 km.

Table 2-7 Latest gravity field models of planets and moons in Solar System

Body	Mission	Model	Resolution			Reference
			Spectral ($max\ l$)	Global ($max\ l$, $S/N = 1$)	Spatial ($\pi R/l$, km)	
Mercury	Messenger	HgM008[a]	50	41	~190	[54]
Venus	Magellan/Pioneer	MGNP180U [b]	180	70	~270	[64]
Earth	several space/ground-borne	SGG-UGM-1 [c] (static field)	2159	~200	~9	[77]
	GRACE	GGM05S [c]	180	~160	~125	[79]
Moon	GRAIL	GL1500E [b]	1500	~900	~6	[75][76]
Mars	MGS, Mars Odyssey, MRO	MRO110D[b]	120	95/100	~100	[82]
Jupiter	Juno/Galileo/Pioneer/ Voyager	-	12	~10	~22000	[90]
Io	Galileo		2-3	-	-	[93]
Europa	Galileo		2-3	-	-	[93]
Ganymede	Galileo		2-3	-	-	[93]
Callisto	Galileo		2	-	-	[94]
Saturn	Cassini/Huygens	-	12	~10	~20000	[91]
Titan	Cassini/Huygens		5	5	~1600	[92]
Uranus	Voyager 2	-	4	-	-	[34]
Neptune	Voyager 2	-	4	-	-	[34]
Ceres	Dawn	-	18	16	8	[107]
Vesta	Dawn	-	-	20	42	[105]
Eros	NEAR	-	15	10	5	[104]
Churyumov-Gerasimenko	Rosetta	-	-	2	3	[106]

[a] https://pgda.gsfc.nasa.gov/products/71
[b] available at NASA's Planetary Data System (PDS Geosciences Node, http://pds-geosciences.wustl.edu/)
[c] available at International Centre for Global Earth Models (ICGEM) (http://icgem.gfz-potsdam.de/home)

For the Moon, the knowledge is very accurate, better than for the Earth, and it is extended till very high degrees, especially through the contribution of GRAIL, which is a spin-off of GRACE mission, in terms of employed technique and payload-heritage, applied to the Moon. Gravity models allowed to arrive to a degree 1500 (GL1500E, [46]), whereas the degree strength achieved is the degree 900, corresponding to a spatial resolution of about 6 km. This was achieved also due the possibility to fly over the surface at very low altitudes, due to the lack of atmosphere.

The approach is different for the Solar System planets. Indeed, the knowledge of the gravity field is good just for some bodies, such as Mars and Venus, which were most intensively studied in the past decades with several fleet of spacecrafts. Other planetary bodies have data limited to few degrees of the spherical harmonic expansion or are lacking measurements.

The Mercury gravity knowledge, very poor and based on three fly-bys by Mariner 10 on 1974-75, was increased drastically with the Messenger mission at the beginning of 2011. Although the developed gravity model allows to determine the field till to $l = 50$ (section 2.4.1.3, spatial resolution of $\sim 150\ km$), the real significance in terms of signal-to-noise ratio (from 5 to 10) is for $l = 10 - 15$ ($\sim 500\ km$). The highly eccentric orbit of Messenger fostered the gravitational mapping at maximum resolution in the northern hemisphere with respect to the southern one [171]. The ESA/JAXA BepiColombo mission aims at increasing such a knowledge, extending it also at southern regions and at least till to $l = 25$ with a signal-to-noise ~ 10, when the mission will enter its nominal phase in 2026-2027 [53].

The best gravity model for Venus is represented by the MGNP180U (section 2.4.2.3), valid till to degree and order 180. However, the physical significance is limited to the major structures not exceeding the degree $l = 70$, corresponding to a spatial resolution of $\sim 270\ km$, although for specific regions of the surface can reach a degree $l = 180$ (100 km). At present no planned mission to Venus is foreseen, just studies such as EnVision mission [110] or VERITAS [112], one of the candidates as medium-class mission in the ESA Cosmic Vision plan.

The latest gravity model of Mars is the MRO120D (section 2.4.5.3) which combines observations carried out by several orbiters and landers. MRO120D achieves the spherical harmonic degree $l = 120$ (locally, corresponding to a spatial resolution of about 100 km) but the global significance is limited to a degree $l = 95/100$, equals to the major structures not exceeding about 100 km in terms of spatial resolution.

The Jupiter system is being explored by Juno mission. Collected data provided the last gravity field model of the planet till to $l_{max} = 24$ with a maximum resolution averaged over the planet at $l = 12$ [90]. Current results show that even harmonics are dominant, whereas the non-zero odd harmonics are related to an interior dynamics likely associated to zonal winds till to 2000-3000 km deep in the atmosphere.

JUICE mission aims at shedding light on Ganymede by measuring gravity field up to $l = 30$ in the first half of 2030. At the same time, the Europa Clipper mission estimates to reconstruct the gravity field of the Jovian moon till to $l = 20$ [95].

The Saturnian system benefits from data collected mainly by the outstanding Cassini mission, which operated continuously at Saturn and its moons for fourteen years till to 2017, and the Voyagers' swing-bys. The last phase of Cassini mission allowed to infer the gravitational field of Saturn till to degree and order 20, with a degree strength of $l = 12$ [91]; such data provided evidence of a differential rotation deep in the atmosphere extending till 9000 km from the cloud tops. An increased knowledge of the gravity of the most large moon Titan has been achieved ($l = 5$).

Concerning the remaining outer planets, no spacecraft has been put in orbit around the icy giants till now and no clear plan to explore such planets is identified for the next years. Some

studies and proposals were carried out, such as the ODINUS mission concept [36], aimed at placing a set of twin spacecrafts, each one in orbit around one of the two ice giant planets, the Uranus Pathfinder [37], proposed to the European Space Agency's M3 call for medium-class missions in 2010 for the study of Uranus and its system, and the OSS [38], a proposal for an M-class mission ESA-NASA to explore the Neptune system along with Triton. In this frame, the gravity field of Uranus and Neptune is almost unknown apart the basic gravitational moments [34], as witnessed by the Table 2-7, and the determination of the gravity field would be one of the fundamental objectives of a future mission to these planets. Such an interest is also strictly related to the study of exoplanets in terms of formation and evolution, since most of the bodies till now identified out of the Solar System have a size intermediate between the Earth and Neptune [39].
A different issue concerns the small bodies in the Solar System, which have drawn an increasing interest in the last years from the scientific community and the space agencies all over the world. The great success achieved by the Rosetta mission that reached the comet Churyumov-Gerasimenko in 2014, entered in orbit and followed it for one year and a half, followed by the Dawn mission to Vesta main belt asteroid in 2011-2012 and to Ceres dwarf planet in 2015-2018, has woken up a rush to explore asteroids and comets. Indeed, such objects maintain much of the pristine materials from which the Solar System was originated and hence their deep study would be very helpful in understanding the origin and the evolution of planetary bodies. Indeed, the recent selection (2017) by NASA Discovery program of Lucy, mission aimed at exploring six Trojans satellites of Jupiter, and Psyche, aimed at the namesake metallic asteroid of the main belt, depicts the current trend of Solar System exploration [109][110].
Table 2-7 reports the gravity field models determined till now for some small bodies, such as Ceres, Vesta and Eros [107][105][104]. For the Churyumov-Gerasimenko comet just the basic gravitational parameters were determined [106]. From the above considerations, it derives that, from the point of view of the scientific community, the study of the gravity field of small bodies assumes a significant relevance in the frame of structures and evolution understanding. However, the scant masses in play for these bodies reduce the level of expected gravity signals and consequently requires very small orbiting distances and /or the use of techniques different with respect to the traditional radio-tracking (section 2.4).

On the basis of the previous gravity fields state of the art it is possible to derive the following considerations:

- The knowledge of the gravity fields of planetary bodies in the Solar System is extremely diversified, with a neat separation between terrestrial planets, the most explored by space missions, and giant/ice giants planets, little or not explored;
- Within this frame, the gravity information in terms of degree strength averaged over the planet is more detailed for Mars ($l \sim 100$) and Venus ($l \sim 70$), whereas the Mercury knowledge has started very recently ($l \sim 40$);
- Obviously, the Earth ($l \sim$ 200) and especially the Moon ($l \sim 900$) are known at the best, due to the relatively "easiness" of being targeted (both) and the possibility to fly very close to the surface (the Moon), because of the lack of atmosphere;
- Among the outer planets, the gravity field is very poorly characterised, achieving, in terms of degree strength averaged over the planet, just to $l = 10$ both for Jupiter and Saturn, since the first one has been visited till now by two orbiters alone (Galileo, in the past, and Juno, orbiting at present) while the second one just by one orbiter (Cassini). Uranus and Neptune are almost completely unknown, from this point of

view, since the only information available, limited to the fundamental gravitational moments ($l = 4$), has been gathered by the Voyager 2 fly-bys;

- In terms of spatial resolutions (as degree strength averaged over the planet), apart Earth and Moon for which the knowledge is very high, the current limits range from $l \sim$ 10 (Jupiter) to $l \sim$ 100 (Mars), corresponding to average resolutions within $\psi \sim 20.000 - 100\ km$, altough locally, such values can increase due to a better gravity characterisation.

Table 2-8 resumes the status of knowledge of gravity for the bodies investigated, dividing in four ranges the achieved level: poor ($l \leq 10$), low ($l \leq 50$), medium ($50 < l \leq 150$), high ($l > 150$).

Table 2-8 Gravity field state of knowledge in terms of degree strength

Body	**Current gravity knowledge (max resolution)**			
	Poor ($l \leq 10$)	**Low ($l \leq 50$)**	**Medium ($50 < l \leq 150$)**	**High ($l > 150$)**
Mercury		X		
Venus			X	
Earth				X
Moon				X
Mars			X	
Jupiter	X			
Ganymede	X			
Europa	X			
Titan	X			
Saturn	X			
Uranus	X			
Neptune	X			

We focus our attention on the "medium" interval because, as we will show clearly later (section 3.3), the satellite gravity gradiometry is inherently sensitive to medium and large degrees (i.e. high resolutions) of the gravity field. As depicted in the table, the medium interval is covered by Venus and Mars. Such an approach obviously is valid also for the Earth and the Moon. However, in this thesis the focus is on the use of the gradiometry technique for planetary bodies outer to our system, hence Earth and Moon are not considered.

As explained in the most recent National Research Council (NRC) Planetary Decadal Survey, "Visions and Voyages for Planetary Science in the Decade 2013–2022", in which priority science questions to be addressed by NASA are reported [96] [97], understanding the formation and evolution of the inner planets within our solar system is critical to understanding how and why Earth evolved the way it did and for interpreting information about newly discovered exo-solar planets. Considering the inner planets, three science goals have been identified: 1. Understand the origin and diversity of terrestrial planets, 2. Understand how the evolution of terrestrial planets enables and limits the origin and evolution of life, and 3. Understand the processes that control climate on Earth-like planets. Within this frame, a list of science priorities at the same level has been identified by the Venus Exploration Analysis Group (VEXAG, 2016): (1) Understand atmospheric formation, evolution, and climate history on Venus, (2) Determine the evolution of the surface and

interior of Venus, and (3) Understand the nature of interior-surface-atmosphere interactions over time, including whether liquid water was ever present. The second objective has been further delved into assessing the evolution of volcanism, tectonism, and other geologic processes that construct and modify the crust [97].
Similarly, within the frame of inner planets, science topics with priority for the science com munity can be identified for Mars as well [98].
The Galilean moons in the last years are attracting a lot of attention, as witnessed by the future missions JUICE (in development, science phase in 2030-2033) and Europa Clipper (in development), because they reply a small Solar system around the central Jupiter.
Ganymede and Europa are the moons more intriguing for the scientists because they are effectively planets (Ganymede is the largest moon in the Solar System and it is bigger than Mercury) and because several clues support the presence of oceans beneath their surfaces. Moreover, Ganymede is the only moon in the Solar System generating a magnetic field.
Limiting the unsolved science questions to those related to the gravity knowledge, a summary of them is reported in Table 2-9.

Table 2-9 Science topics in Solar System planetary bodies

Science Target	Science Theme	Science Questions	Objective	Note
Venus	Surface and interior	How does Venus lose its heat?	Gravity – topography on a global scale Surface geology	[96] [97]
		How volcanically and tectonically active has Venus been over the last billion years	Surface geology, topography, and gravity, Seismicity	-
		Has Venus always been in a stagnant lid regime or was a plate tectonics regime present in the past?	Surface geology, topography, and gravity	-
Mars	Interior	What is the size of the core and what are the rheological properties of the mantle?	Tides	[98]
	Surface, Crust and Mantle	How did local geological regions form?	Gravity – topography on a global scale	-
		What is the elastic thickness, and how does it correlate with the flexural signal?		-
	Polar caps	What is the amount of CO2 that is	Mass (gravity), thickness (altimetry),	-

		exchanged between the polar caps and the atmosphere?	and extent (imaging) of seasonal deposits	
Ganymede		Has Ganymede a subsurface ocean?	Gravity, subsurface ocean, magnetic field	
Europa		Has Europa a subsurface ocean?	Gravity, subsurface ocean	
Titan		How are distributed the liquid hydrocarbon on the surface and sub-surface?	Gravity, subsurface ocean	
Mercury		How is the interior mass distribution at Mercury?	Gravity, magnetic field, interior structure	

From the point of view of the science needs from the international community and from the current knowlegde depicted in the previous sections, it is possible to state that:

- Primary interests are demonstrated for Venus, which was explored last from Venus Express (2006-2014) and whose main focus was the atmosphere. Several studies have been and are being carried out for it (as EnVision and VERITAS). Interests are related to the different thermal, geological and atmospheric evolution, although Venus is the planet more similar to Earth as size. The lack of magnetic field and plate tectonics along with the unknown Moment of Inertia of the planet (difficult to measure because of the very slow rotation) makes difficult to infer deeper information on the interior structure, leaving many parameters free in the models
- At the same time, Mars keeps alive the interest in it, being the planet most targeted in terms of dedicated missions till now and for the future as well. The first seismometer out of the Earth and Moon (Apollo missions) is currently operating on Mars with Mars Insight. However, several questions related to the interior structure are still open.
- Comparison of the planetary bodies gravity field state of the art with the scientific needs allows to infer that the most interesting objectives, especially from the point of view of a gradiometric mission, are represented by Venus and Mars, in addition to specific targets among the Galilean and Saturnian moons, such as Ganymede, Europa, Titan.

3. Measurement Techniques

3.1 Introduction

This chapter is devoted to depict the different techniques employed to measure the gravitational field of planetary bodies with focus on planets other than Earth. Techniques are limited to space-borne techniques.
The simplest method to measure the gravity field of a body is to measure the orbital period and the semi-major axis of a small natural moon or a small satellite orbiting it; from the Kepler's third law the mass of the central body can be determined (section 2.2.1). In case of spherically symmetric mass distribution this allows to have a complete gravity field knowledge. However, this is a not so realistic condition and can be applied just for specific cases, such for instance for mass estimates in binary stars. In general, the gravity field will be described in terms of a spherical harmonics expansion because the mass distribution will have variations more or less pronounced with respect to the spherical symmetry. In this case, the orbit followed by the natural moon or by the satellite will not be pure Keplerian but will show off deviations reflecting the mass distributions on the primary body. Such deviations can be monitored establishing a radio-link with the satellite which allows to measure position and velocity, to determine the real orbit and from that to infer information on the gravity field determining that orbit.
Such satellite-based methods to study the gravity field date to the early space era.
It is worth to highlight that some measurement techniques are not considered in the following sections because they are currently not applicable for planetary bodies different from Earth, which are the focus of this thesis. However, a general overview is provided hereafter.

Laser-ranging
Laser ranging in space began with ranging to retroreflectors on the Moon placed by the Apollo [Faller et al., 1969] and Luna missions. Pulses fired by a powerful, earthbased laser are reflected back to the transmitting site, where time-of-flight measurements are made using standardised clocks, timers and detectors. Such measurements routinely achieve decimeter precision using very short pulses and single-photon detectors. Laser ranges require only small corrections for atmospheric transmission and provide precise constraints on the dynamics of the Earth-Moon system. With retroreflectors, the number of photons available for timing decreases with the fourth power of the distance, making distances much beyond the Moon's orbit impractical. A transponder, on the other hand, receives pulses and sends pulses back in a coherent fashion so that the photon counting decreases only by the square of distance in both directions, making ranging possible at far greater distances.
Satellite laser ranging fundamentally relies on the (rate)(time) = distance relationship to ultimately estimate tracking site positions which can then be used to monitor changes in a variety of Earth processes (e.g., tectonic motion, polar motion, earth rotation, tidal and gravitational forces). The raw SLR "range" is a time interval measurement. The actual range is defined as one half the product of the speed of light and the elapsed time between the emission of a laser pulse and its reception at the same tracking site after having been reflected by the satellite. These are known as full-rate data. Conversely, their average on a suitable time span (120 s in the case of LAGEOS) is called Normal Points. Normal points have a precision (RMS) down to 1 mm. When a large number of these temporally and geographically distributed range measurements are ordered by time and location, each range can be considered a constraint in the solution of the numerically integrated equations of motion describing the satellite trajectory. The misclosures between the a priori predicted and observed ranges are used to form the linear least squares equations which best satisfy

all of the range information simultaneously. The resulting system of equations is then solved to yield the time-averaged three-dimensional coordinates of the tracking stations.

3.2 The classical concept

Apart the Earth and the Moon, the classical technique used to gather gravity field data of planetary bodies is the radio-tracking of a spacecraft. Indeed, this technique is the more common approach to acquire gravity field information by exploiting the several spacecrafts spread over the Solar System flying by or orbiting planets, asteroids or comets. The reason is that any spacecraft needs to be tracked from the ground-stations on the Earth (when in the window visibility) to establish a communication link [117]. Moreover, such a tracking allows to carry out navigation in space by measuring position and velocity of the spacecraft while orbiting a planetary body or on the cruise towards some destination. Being the spacecraft in free-fall in the gravitational field of the central body (a planetary body or the Sun in general), it acts as a “proof mass” able to sense the field along the orbit. Indeed, the followed orbit is the result of the characteristics of the field, apart any non-gravitational effect. In the following the radio-tracking concept will be analysed according to two configurations: radio-tracking between a ground-station and a spacecraft, and radio-tracking between spacecrafts.

3.2.1 Radio-tracking

The basic technique used to retrieve information on the gravitational field of a planetary body is the monitoring of a spacecraft orbiting the body through the radio-tracking. By measuring accurately position and velocity of the spacecraft which is sensitive to the gravitational field along its path it is possible to reconstruct the followed orbit and at the same time to estimate the gravitational field. This approach relies on the establishment of a radio-link between an observer on the Earth (ground-station) and a spacecraft on its path, i.e. an exchange of electromagnetic waves belonging to the radio spectrum. The uplink aims at controlling the spacecraft and/or the on-board instruments through telecommands, whereas the downlink retrieves the telemetry to monitor the general health status and science data during the mission. However, such a link allows two other functionalities: navigation capability, to determine spacecraft position and velocity in space, and radio-science, i.e. the capitalisation of the radio-link to afford experiments with a science return.

The radio-science is a topic covering different research areas [117][118], including determination of planetary masses and mass distributions, planetary geodesy, study of planetary atmospheres and ionospheres, planetary rings, solar plasma and magnetic fields, tests of Fundamental Physics and hence test of General Relativity as well. The determination of the gravitational field of a planetary body by radio-tracking belongs to the radio-science investigations.

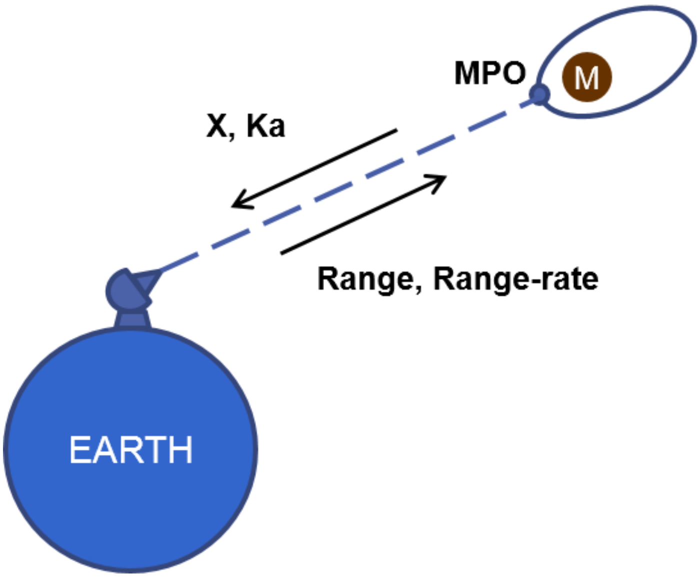

Figure 3-1: radio-tracking scheme (example for the Bepicolombo mission)

Depending on the investigated phenomenon, radio-science observations rely on the measurement and study of specific observables such as amplitude, phase and polarisation of the electromagnetic waves exchanged between spacecraft and Earth over various timescales. Typically, these observables are used to infer other quantities more directly referred to the problem.
In the gravitational field measurement, relative distances and velocities between a spacecraft and the Earth constitute those observables, often indicated as range and range-rate (or Doppler). They are used as input in the so-called Precise Orbit Determination process (POD) [22]. Orbit determination for celestial bodies has been a topic faced by astronomers and mathematicians since ancient times, although just since the beginning of scientific method in between 1500-1600 several scientists have devoted to find out and develop much of the fundamental mathematics and physics in use today.
The classical orbit determination problem, characterised by the assumption that the bodies move under the influence of a central (or point mass) force, faces the process by which it is possible to obtain the knowledge of a spacecraft's motion relative to the center of mass of a central celestial body in a specified coordinate system [22].
The general orbit determination problem states that if at a certain time t_0 the state of a spacecraft is known and the motion equations are known as well, then they can be integrated to determine the state of the spacecraft at any time. However, since the initial state is never known exactly and since some constants and some forces are difficult to model or to estimate in the problem, then the derived state of the spacecraft is ever affected by errors and there will be a deviation between the predicted and the actual motion. By using observations of the spacecraft motion is possible to determine a better estimate of the state and hence of the motion, deriving at the same time an estimate of the orbit.
The observations are the measurements carried out by the ground-stations, i.e. the observables range and range-rate or other data (azimuth, elevation, etc.). The state variables of the spacecraft are constituted by a set of parameters used to predict the motion; it includes at least position and velocity of the spacecraft. However, the state vector can be expanded to include also parameters of the dynamical model, i.e. related to the equations of motion, and parameters of the observation model, i.e. related to the observation-state relationship, which establishes the link between observables and state vector. Indeed, any

observable which affects directly the spacecraft motion or the observation-state relationship can be introduced in the general state vector of the spacecraft in order to be estimated through the observations.
This is the case when a measure of the gravitational field of planetary body needs to be carried out. The state vector is increased to include, beside position and velocity of the spacecraft, also the coefficients of the spherical harmonic expansion C_{lm} and S_{lm} (section 2.2.2), which can be estimated in the orbit determination process.
The orbit determination process is a problem of state estimation, i.e. determine the best estimate of the state of a spacecraft, whose initial state is unknown, from observations influenced by random and systematic errors, using a mathematical model that is not exact.
When an estimate of the state vector has been made (trajectory, harmonic coefficients, etc.), the corresponding motion and observations can be predicted. However, the predicted values will differ from the true values due to several effects, such as approximations involved in the method of orbit improvement and in the mathematical model, errors in the observations, errors in the computational procedure, errors in the numerical integration procedure. For this reason, the overall process of observation and estimation must be repeated as much as possible, compatible with the mission constraints, while the motion goes on.
In the general orbit determination problem, both the dynamics and the measurements involve significant non-linear relationships. For the general case, such relations are described by the non-linear expressions [22]:

$$\begin{gathered}\dot{\boldsymbol{X}} = F(\boldsymbol{X}, t) \\ \boldsymbol{X}(t_k) = \boldsymbol{X}_k \\ \boldsymbol{Y}_i = G(\boldsymbol{X}_i, t_i) + \boldsymbol{\epsilon}_i \qquad i = 1, \dots, l\end{gathered} \tag{3-1}$$

where $\boldsymbol{X}_k$ is the unknown n-dimensional state vector at the time t_k, and $\boldsymbol{Y_i}$ for $i = 1, \dots, l$, is a p-dimensional set of observations that are to be used to obtain a best estimate of the unknown value of $\boldsymbol{X}_k$. Such relations are typically affected by a number of observations (p) lower than the state vector components (n), non-linear behaviour, errors in the observations ($\boldsymbol{\epsilon}_i$). To simplify the problem, both the dynamical and observation equations are linearised in terms of a Taylor's series around a reference solution $\boldsymbol{X}^*$ and suppressing higher order terms. Such an approach allows to obtain a set of linear differential equations with time-dependent coefficients for the state deviations, $\delta\boldsymbol{x} = \boldsymbol{X} - \boldsymbol{X}^*$, translating the non-linear orbit determination problem aimed at determining the complete state vector into a linear orbit determination problem in which the deviation from a reference solution is to be determined:

$$\begin{gathered}\delta\dot{\boldsymbol{x}}(t) = A(t)\,\delta\boldsymbol{x}(t) \\ \boldsymbol{y}_i = \widetilde{H}_i\,\boldsymbol{x_i} + \boldsymbol{\epsilon}_i \qquad i = 1, \dots, l\end{gathered} \tag{3-2}$$

with:

$$\begin{gathered}A(t) = \left[\frac{\partial F(t)}{\partial \boldsymbol{X}(t)}\right]^* \qquad \widetilde{H}_i = \left[\frac{\partial G}{\partial \boldsymbol{X}}\right]_i^* \\ \delta\boldsymbol{x} = \boldsymbol{X}(\boldsymbol{t}) - \boldsymbol{X}^*(t)\end{gathered} \tag{3-3}$$

$$\delta \boldsymbol{x}_i = \boldsymbol{X}(t_i) - \boldsymbol{X}^*(t_i)$$

$$y_i = \boldsymbol{Y}_i - G(\boldsymbol{X}_i^*, t_i) \qquad\qquad i = 1, \ldots, l$$

The general solution can be expressed through a state transition matrix $\Phi(t, t_k)$ as:

$$\delta \boldsymbol{x}(t) = \Phi(t, t_k)\delta \boldsymbol{x}_k \tag{3-4}$$

At last, the orbit determination procedure through the radio-tracking of a spacecraft provides a mean to estimate the gravitational field of the orbited body. It is worth to highlight that such a technique works well for large bodies, whereas its accuracy decreases as much as smaller the body mass, because of a smaller tracking signal, effects due to typical irregular body shapes and uncertainty due to the solar radiation pressure [26] (section 2.4).

The process is depicted in Figure 3-2. The observed observables collected at the ground station are compared with the computed observables, which provide a reference solution.

The computed observables are derived by integrating numerically the equation of motion and by using the observation model which relates observations with the state variables. Residuals resulting from the comparison between computed and observed observables are evaluated with a least-squares fit. Such residuals are computed iteratively and differential corrections to the parameters to be estimated, i.e. the spacecraft state (position and velocity) and the chosen model parameters (spherical harmonic coefficients), are implemented progressively in a loop (Figure 3-2) till to achieve a minimum in the residuals. Since both the dynamic model and the observation-state relationship are typically non-linear functions, the estimate of the parameters is based on a non-linear least squares approach.

At last, the accurate tracking of a spacecraft orbiting a planetary body allows to reconstruct its orbit and at the same time to derive precious information on the gravitational field through procedures of orbit determination (POD, Precise Orbit Determination).

The range-rate observable constitutes the rate of change of distance separating transmitter and receiver and it is proportional to the Doppler shift of the microwave link. Conceptually it measures the relative velocity of a spacecraft with respect to the Earth comparing the frequency between the transmitted and received signal, showing a frequency shift due to the relative motion. Three types of configurations are currently envisaged for the tracking with radio-links [117][22], depending on the source of the reference signal and on the number of the involved ground-stations. The measurement is said “one-way” when the signal is transmitted by the spacecraft to the ground-station (downlink) and it is generated by an on-board oscillator. The measurement “two-way” refers to a signal generated by the ground-station, using a local frequency reference, transmitted to the spacecraft and coherently retransmitted back to ground (same reference in Tx/Rx). At last, “three-way” is the two-way approach with two different ground stations for uplink and downlink.

Quality of Doppler observables depends on the frequency stability achievable by the master reference frequency. With two-way Doppler links the frequency reference is located at the ground-station and allows to reach very high stability, with Allen deviations in the order of $10^{-14} - 10^{-15}$ for integration times till to $1000\ s$ [119].

Apart this condition, the quality is limited also by thermal noise or plasma noise. Whereas Ultra-Stable Oscillators (USO) are able to reach high degree of stability in frequency, the quality of Doppler data is limited by plasma noise or thermal noise. This happens when the radio-signals cross plasma regions such as solar corona, interplanetary medium and ionosphere. A way to circumvent this phenomenon is to establish a multi-frequency link with the spacecraft [120][121]. Exploiting the different effect of plasma on the radio-propagation according to the frequency, multiple frequency links allow to remove almost completely the plasma noise. This approach was firstly successfully validated with Cassini's tracking data during the cruise phase radio-science experiments [122] and it will be used also in the BepiColombo mission to Mercury to reach very high performance [123]. Moreover, multifrequency measurements are widely used in GNSS (Global Navigation Satellite Systems) for removing the ionospheric range delay affecting pseudorange and phase observables [121].

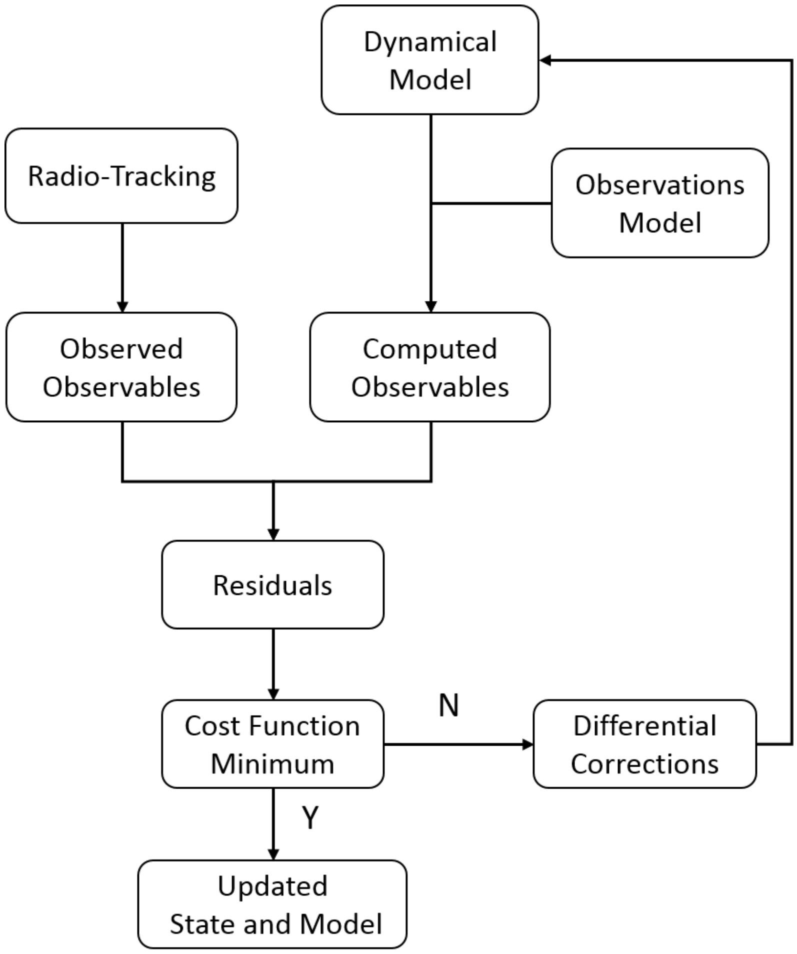

Figure 3-2: Scheme of the precise orbit determination process (POD) to estimate the spacecraft orbit and a set of model parameters, i.e. the spherical harmonic coefficients.

Typically, electromagnetic waves employed for communication/navigation belong to the radio spectrum, specifically to the microwave region which covers the range from 1 GHz to 300 GHz formally (EHF, Extremely High Frequency). Within this region different bands are identified with names often inherited from radar domain: L, S, C, X, Ku, K, Ka, Q, V, W.
Historically, radio-links with spacecrafts has seen the use of microwave frequencies progressively increasing due to on one side to the technological progress in microwave equipment and Tx/Rx transponders and on the other side for the progress in counteract and/or to measure the disturbances introduced by the atmosphere, rain and clouds which rises with the use of higher and higher frequencies.
Figure 3-3 depicts a spectrum of the main frequency ranges employed for satellite communications.

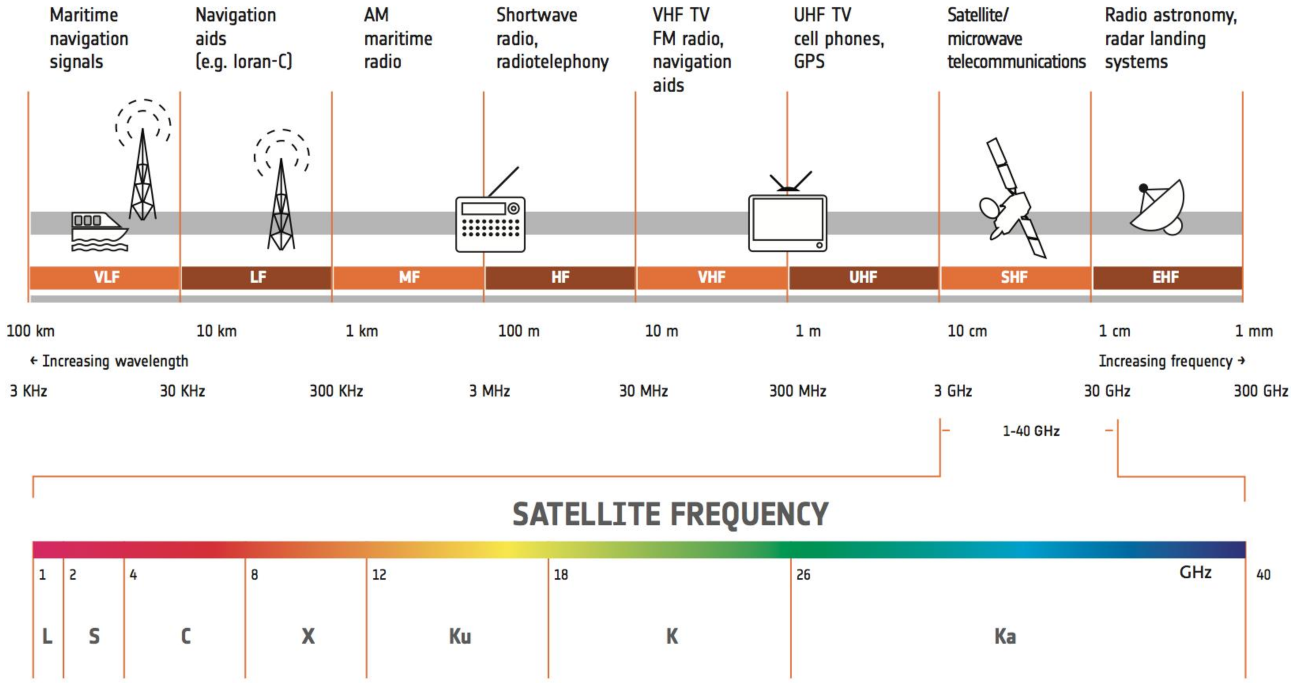

Figure 3-3: Spectrum of frequency bands typically used for satellite communications and radio-tracking (ESA courtesy)

Next to these observables different elements complement and enrich the radio-tracking process: radiometers, water vapour gauges, igrometers.

3.2.2 SST/ll (low-low)

The classical concept of radio-tracking between a ground-station and a spacecraft can be adapted to establish a radio-link between two spacecrafts following each other on the same orbit and separated by a proper distance, typically hundreds of kilometers. This type of configuration is known as Satellite-To-Satellite Tracking approach (SST) in the low-low mode (SST-ll) [6][17][18]. A further configuration, named high-low mode (SST-hl), is identified when spacecrafts belong to orbits at different altitudes. This is the case of the CHAMP mission in which the main spacecraft, in LEO orbit, receives signals from the MEO orbit of GPS constellation.

The principle of SST/ll concept is to measure as accurately as possible the relative motion of two spacecrafts by measuring the inter-satellite distance and velocity through a radio-link. The change of this distance is directly referred mainly to the gravitational field beneath the spacecrafts orbit. Such a differential measure allows to highlight the effect of small-scale features. Hence, a precise measurement of the distance variation allows to infer information on the gravitational field producing that change. However, effects not related to the gravitational field and introduced by non-gravitational forces on the two spacecrafts need to be compensated for or be measured. The observable of interest is the relative motion of the centres of mass of the two satellites, which has to be derived from the inter-satellite link together with the measured acceleration and attitude data. The first approach of this type has been pursued by the US-German mission GRACE [72][71].

3.3 Gravitational Gradiometry

Classical techniques, essentially radio-tracking based, derive information on the gravitational field of planetary bodies through a precise tracking of a test mass in free fall, constituted by a spacecraft in orbital motion. From these data a carefully reconstruction of the orbit based on POD procedures is achieved. Once non-gravitational perturbations of different origin (if any) are taken into account in this process, deviations in the obtained orbit from the pure Keplerian orbit are interpreted as irregularities in the mass distribution at the planet surface and in its interior. Indeed, the gravitational field is recovered indirectly through the observation of deviations to the orbit of the satellite as Keplerian orbit.

Radio-tracking techniques require ever and ever more challenging accuracies in the measurement of range and range-rate observables in order to improve the orbit determination and at last to improve the estimate of the spherical harmonic coefficients. Currently [116], typical precisions of radio tracking data are at the level of 0.02–0.1 mm/s at 60-s integration time for range-rate measurements (X-band) and 0.5–5 m for range measurements; for Doppler measurements, the systematic errors are typically close to negligible. Conversely, systematic errors in range measurements can achieve large values, at the 1 m level (similar to the random noise). Propagation effects in the interplanetary medium affect mainly the radio tracking noise and depend strongly on the solar elongation angle. As previously anticipated (section 3.2.1), the combination of observations at multiple wavelengths provide a mean to remove the majority of these errors. X- and Ka-band combination was used for Cassini and is currently employed for Juno; the same will happen on the BepiColombo mission, currently on cruise, and JUICE. For those missions, the quality requirements of tracking data are 0.01 mm/s at 60-s integration time and $3\ \mu m/s$ at 1000-s integration time. An additional advanced radio ranging system allows two-way range measurements with an accuracy around $20\ cm$ [116].

Although tracking techniques are nowadays a fundamental instrument to map the gravity field of several planets and satellite and even although improvement margins are possible [178], alternative and/or complementary techniques are mandatory to be considered to achieve increased spatial resolution and accuracy of the gravity models in the medium/long term future. Such approaches have to counteract and/or overcome (even partially) some of the limitations faced by tracking techniques.

At first, satellites can be tracked from ground stations just for selected time windows, depending on the visibility conditions and on the number of engaged stations. Being the gravitational perturbations to the orbit due to the mass distribution at the surface and within the body, especially that lying under the spacecraft orbit, gravity is sensed more accurately when the planetary surface is visible in the line of sight of the ground-station as the planet rotates under the spacecraft [101]. While for the Earth such a condition is less demanding, a different scenario is found for planets or satellites around the Solar System. For instance, the Moon, being in synchronous rotation with the Earth due to the spin-orbit resonance $1:1$, shows up the same face to us, hence the far-side is never directly visible: gravity is sensed more accurately on the nearside than on the far-side by radio-tracking. Indeed, far-side lunar gravity was not directly measured till to 2008 with Kaguya mission (section 2.4.4.1.2). Later the GRAIL mission (section 2.4.4.2) allowed to improve the gravity measurements with a different approach. In the Kaguya mission, a sub-satellite, tracked by the main orbiter and not in line-of-sight with the Earth, was used to monitor the gravitational perturbations on the far-side. A similar condition, although depending on the visibility from the Earth, applies for several natural satellites around the Solar System that are tidally-locked with the respective planet, i.e. one side is always facing towards the planet.

A further shortcoming to be considered is that the satellite motion is affected by non-gravitational perturbations during its orbit as well. These effects introduce disturbances to

the tracking observables not generated by the gravitational field and impact negatively on the correct orbit determination process and hence on the estimate of the Stokes coefficients. Just measurements through an on-board high-sensitivity accelerometer or accurate modelling of these effects allow to reduce this error term.
Another disadvantage is related to the accuracy achievable into the tracking observables which affects the model parameters estimate and hence the spherical harmonic coefficients. In a typical two-way Doppler link, the quality of data is related to the stability of the frequency reference, to the thermal noise generated by the on-board instruments involved in the tracking and to the plasma noise, as already explained in section 3.2.1.
The state of the art performance for range and range-rate measurements are expected for the BepiColombo mission which foresees an accuracy of $3\ \mu m/s$ at $1000\ s$ integration time for range-rate and $20\ cm$ for range [123].
Another important limitation is related to the intrinsic characteristics of the gravitational field: the strength of the field decreases with the increase of the distance from the planet's centre, as stated from the inverse squared Newton's law. That means low orbits are preferred because they support stronger gravity signals with respect to higher ones. Such an attenuation is better understood looking at the spherical harmonic expansion, where the contribution to the global field by a term of degree l decreases as much as increases l, as showed up by the factor $(R/r)^l$: for a specific orbit height, the signal contribution lowers as much as the degree l is higher. In other terms, for a specific orbit height, the shorter wavelengths, related to structures of smaller size and hence higher spatial resolution, are attenuated more than longer wavelengths. This is very neat in the expression of the gravity field spherical harmonic expansion.
A completely different approach with respect to the previous techniques is pursued through the gravitational gradiometry. In spite of observing indirect effects on the spacecraft orbit due to gravity, the gradiometry approach aims at investigating the characteristics of the gravitational field through the direct observation of the spatial variation of gravitational field. Indeed, the gravitational acceleration $\vec{g}$ experienced by a test mass at $\vec{x}$ position is the spatial gradient of the gravitational potential generated by the planet mass located at $\overrightarrow{x'}$, i.e. are valid the following (section 2.2.2):

$$V(\vec{x}) = G \int \frac{\rho\left(\overrightarrow{x'}\right)}{\left|\vec{x} - \overrightarrow{x'}\right|} dW \tag{3-5}$$

$$\vec{g}(\vec{x}) = \nabla \mathrm{V}(\vec{x}) \tag{3-6}$$

where ρ is the mass density and W is the space volume, occupied by the density mass, to which the integral is extended. The spatial gradient of the components of the gravitational acceleration $\vec{g}$ constitutes the *gravitational gradient tensor*:

$$\Gamma(\vec{x}) = \nabla \vec{g}(\vec{x}) = \nabla(\nabla \mathrm{V}(\vec{x})) \tag{3-7}$$

i.e. the second derivatives of the gravitational potential V. The gravitational gradients constitute a second-order tensor field with 3 x 3 components, which is referred to as gravitational gradient tensor [137]. In an arbitray local Cartesian coordinates system the gravitational gradient is expressed as follows:

$$\Gamma_{ij} = \begin{pmatrix} \frac{\partial g_x}{\partial x} & \frac{\partial g_x}{\partial y} & \frac{\partial g_x}{\partial z} \\ \frac{\partial g_y}{\partial x} & \frac{\partial g_y}{\partial y} & \frac{\partial g_y}{\partial z} \\ \frac{\partial g_z}{\partial x} & \frac{\partial g_z}{\partial y} & \frac{\partial g_z}{\partial z} \end{pmatrix} = \begin{pmatrix} \frac{\partial^2 V}{\partial x^2} & \frac{\partial^2 V}{\partial x \partial y} & \frac{\partial^2 V}{\partial x \partial z} \\ \frac{\partial^2 V}{\partial y \partial x} & \frac{\partial^2 V}{\partial y^2} & \frac{\partial^2 V}{\partial y \partial z} \\ \frac{\partial^2 V}{\partial z \partial x} & \frac{\partial^2 V}{\partial z \partial y} & \frac{\partial^2 V}{\partial z^2} \end{pmatrix} = \begin{pmatrix} \Gamma_{xx} & \Gamma_{xy} & \Gamma_{xz} \\ \Gamma_{yx} & \Gamma_{yy} & \Gamma_{yz} \\ \Gamma_{zx} & \Gamma_{zy} & \Gamma_{zz} \end{pmatrix} \tag{3-8}$$

Among the nine components, just five are the independent ones. Indeed, due to the conservative nature of the field ($\nabla X \, \vec{g}(\vec{x}) = 0$ and hence $\vec{g}(\vec{x}) = \nabla \mathrm{V}(\vec{x})$) and to the Poisson equation (outer space), i.e. the Laplace equation:

$$\frac{\partial^2 V}{\partial x^2} + \frac{\partial^2 V}{\partial y^2} + \frac{\partial^2 V}{\partial z^2} = 0 \tag{3-9}$$

the tensor is symmetric and just 5 components are independent (ZZ, XX, XY, XZ, YZ). The diagonal components, Γ_{ii}, are known as inline-components, whereas the off-diagonal components, Γ_{ij} $(i \neq j)$, are named off-line components or cross-components.

The gravitational gradient can be interpreted in two other ways [167]. It constitutes the tidal field generated by a celestial body at the location of the gradiometer instrument. This field would be exactly zero at centre of mass of the spacecraft. Moving from that position, the tidal force increases, as much as the distance from the centre of mass increases (roughly 1 ppm of $\vec{g}$ at a distance of $1 \, m$) [167].

From the point of view of General Relativity, the gravitational gradient has a geometrical interpretation. Γ_{ij} components express, at any point, the curvature structure of the central body's gravitational field: the gravity gradient corresponds to the Riemann curvature tensor.

3.3.1 Principles of measurement

As stated by the Equivalence Principle of Einstein, it is not possible through a local measurement to discriminate the gravitational field from an acceleration of the reference frame [168]. To accomplish the measure and separate the two contributions it needs to resort to a second order measure, i.e. to the gravitational gradient [169]. In this case, a differential measurement between two proof masses allows (ideally) to remove the common underwent acceleration and to retrieve the gravity signal.

As seen in section 2.2.1, an object orbiting a planet undergoes a continuous free-fall in the gravitational field where it is moving. Such an object constitutes a "proof-mass" able to explore and to probe the gravity field in different spatial positions. Indeed, if two proof-masses are placed in different positions in a gravity field and on the same equipotential surface they will be subjected to different gravitational accelerations $\overrightarrow{g_A}$ and $\overrightarrow{g_B}$ (Figure 3-4). Each vector will be directed along the line of force going through the proof-mass and orthogonal to the equipotential surface to that point. If not fixed, the two masses A and B will begin falling towards the planet along the (converging) lines of force and the relative distance between them will decrease. The change in the relative distance is a measure of the difference in gravitational acceleration between the two points [125].

If the two proof masses are located at different heights on the same line of force they will undergo again different gravitational accelerations, $\overrightarrow{g_C}$ and $\overrightarrow{g_D}$. However, the proof-mass in the position D, being closer to the planet, will be attracted more than the mass located in C.

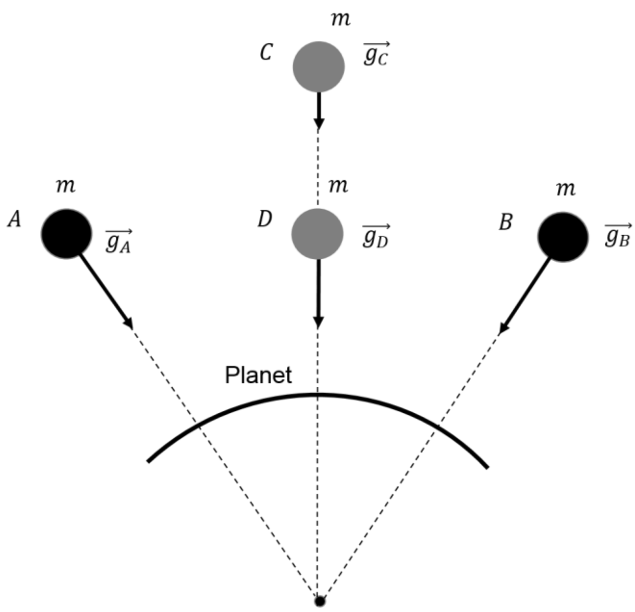

Figure 3-4: Ideal behaviour of proof-masses in a gravitational field

Consequently, if they were left free to move, they would begin falling and the relative distance between C and D would increase. Also in this case the change in the relative distance between the two proof-masses is a measure of the difference in gravitational acceleration between the two points.

In both examples, the relative movement is generated by a differential gravitational acceleration at the masses position, i.e. by the gravity gradient at the two positions, also known as tidal force. From these examples it derives that by monitoring the relative motion of proof-masses in a gravitational field it is possible to gather information on the gravity gradient between their position and at last on the gravitational field.

In a spacecraft orbiting a planet a proof-mass located into its centre of mass is effectively in free-fall in the gravity field along with all the spacecraft; they are at rest one to each other. If a second proof-mass is added within the spacecraft without any support, it will experience a relative movement with respect to the first one due to a difference of gravitational acceleration at the two locations, as previously explained. Such a difference reflects directly the mass distribution that generates the gravitational field of the body.

This happens also for two proof masses moved with respect to the centre of mass: they will experience a relative movement due to the different gravitational acceleration with respect to the centre of mass. If these proof masses are part of two accelerometers, they are kept fixed with respect to the satellite through a suspension of different type (mechanical, electrostatic, etc.). In this case they measure the difference of gravitational accelerations at the proof masses positions, i.e. a physical observable proportional to the gravity gradient.

The result is the technique known as *differential accelerometry* in which the gravity gradient Γ_{ij} is approximated by measuring the finite relative accelerations over the relative baseline. The approximation is equivalent to express as Taylor-series [167] the accelerations in two points A and B symmetric with respect to the centre of mass O:

$$a(A) = a(O) + \Gamma(O)(x_A - x_0) + o^2$$
$$a(B) = a(O) + \Gamma(O)(x_B - x_0) + o^2 \quad (3\text{-}10)$$

where higher terms contain higher derivatives of Γ. Subtracting the two terms we get:

$$a(B) - a(A) = \Gamma(O)(x_B - x_A) + o^3 \tag{3-11}$$

where even terms cancel due to the symmetry and odd terms can be considered negligible. At last, the measure of gradient is translated into:

$$\Gamma_{ij} = \begin{pmatrix} \frac{\partial^2 V}{\partial x^2} & \frac{\partial^2 V}{\partial x \partial y} & \frac{\partial^2 V}{\partial x \partial z} \\ \frac{\partial^2 V}{\partial y \partial x} & \frac{\partial^2 V}{\partial y^2} & \frac{\partial^2 V}{\partial y \partial z} \\ \frac{\partial^2 V}{\partial z \partial x} & \frac{\partial^2 V}{\partial z \partial y} & \frac{\partial^2 V}{\partial z^2} \end{pmatrix} = \begin{pmatrix} \frac{\Delta a_x}{\Delta x} & \frac{\Delta a_x}{\Delta \mathrm{y}} & \frac{\Delta a_x}{\Delta \mathrm{z}} \\ \frac{\Delta a_y}{\Delta x} & \frac{\Delta a_y}{\Delta \mathrm{y}} & \frac{\Delta a_y}{\Delta \mathrm{z}} \\ \frac{\Delta a_z}{\Delta x} & \frac{\Delta a_z}{\Delta \mathrm{y}} & \frac{\Delta a_z}{\Delta \mathrm{z}} \end{pmatrix} + o^3 \tag{3-12}$$

Whereas an accelerometer senses the inertia of a single test mass to an applied force, two coupled accelerometers sense the difference of inertia from two test masses in reply to a differential force. Such a coupling constitutes a *gravitational gradiometer*. In general terms, one may envisage a gradiometer as the juxtaposition of two accelerometers and the sensed gradient as the ratio of the acceleration difference to the baseline length between them. As such, the gradiometer measures only an approximation of the gradient at a point, which is adequate for sufficiently small baselines.
In general, instruments specifically devoted to measure the gravitational gradient are named gravitational gradiometers. The word “gradiometer” is in general referred to the measure of the second derivative of a physical observable, whatever it is, such as gravity, magnetic field, electromagnetic field. Moreover, following a distinction inherited from geodesy, the word “gravity” is referred to measurements carried out on the planet’s surface, where it is sum of the acceleration due to the mass attraction alone and the centrifugal acceleration due to planet’s rotation, whereas the word “gravitation” refers to the mass attraction effect alone. Hence, for a satellite mission, it is correct to say gravitational gradiometry.
Theoretically, at least 12 accelerometers are needed to have a full-tensor gradiometer, i.e. all the components [6]. However, just 5 components are not dependent, hence a minimum of 5 accelerometer pairs are needed to measure all the independent component of the gradiometer.

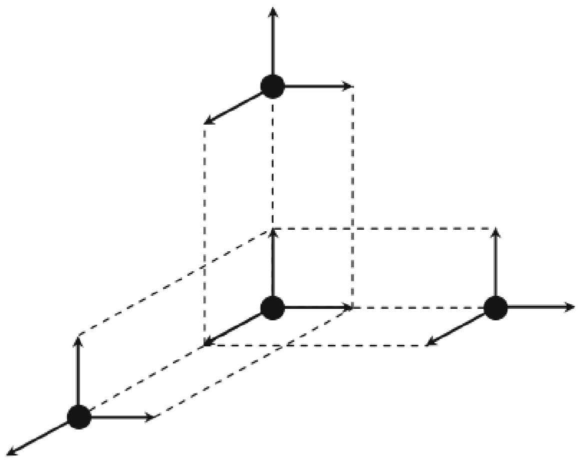

Figure 3-5: Configuration for a full-tensor gradiometer (from [6])

Gravitational gradient can be measured as well through another approach, in which angular accelerometers are employed and angular accelerations are the sensed observables.
In this case, the gradient at the position of two masses, separated by a certain baseline, generates a torque and hence a rotation (instead of a linear displacement). Such instruments are named torsion balance-based gradiometers and measure the differential torques exerted on two test masses over the related baseline; from a conceptual point of view the gradiometer is likely resembling a dumbbell.
At last, referring to Figure 3-6, an *in-line component (Γ_{ii}) gradiometer* can be realised by differencing signals between two linear accelerometers (proof-masses A-B or C-D) whose sensitive axes (arrows) are aligned along their separation, as shown in Figure 3-6.

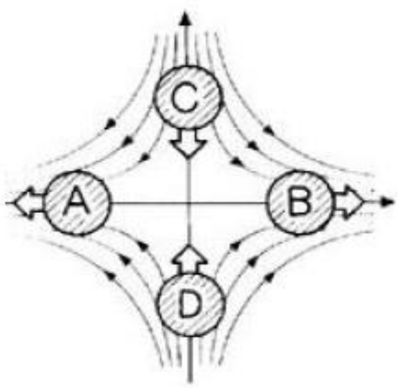

Figure 3-6: Concept of configuration for an in-line component gradiometer [170]

On the other hand, an *off-line (Γ_{ij} ($i \neq j$)) gradiometer (or cross-component)* can be realised by differencing angular accelerations (Figure 3-7) between two concentric arms A-B and C-D or by combining the linear accelerations on the four proof-masses.

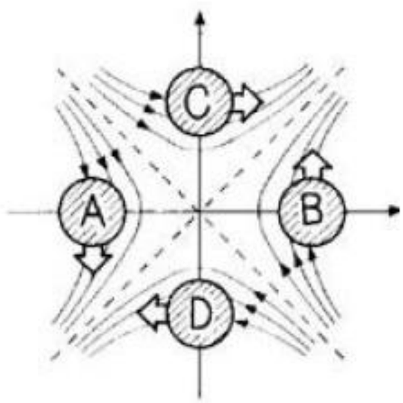

Figure 3-7: Concept of configuration for an off-line (or cross-component) component gradiometer [170]

At last, a *tensor gradiometer (Γ_{ij})* could be realised by combining 3 in-line gradiometers with 3 cross-component gradiometers.

The gradiometry approach allows to reduce some of the drawbacks experienced by radio-tracking techniques.

The issue of line-of-sight constraints required by radio-tracking can be counteracted with this approach. Gradiometers would allow to ease this condition providing the complete coverage of a planet faster than tracking, because they not suffer from the visibility problems and ground stations schedule constraints experienced through radio-tracking.

If, in an ideal case, all nine components of the symmetric gradient tensor were measured, it would be, in principle, possible to solve the attitude of the instrument from the measurements, at least if some additional information from star trackers is available.

3.3.2 Instruments State of the Art

Gravity gradiometry is a discipline over 120 years old, whose beginning can be identified with the introduction, by the Hungarian geophysicist Baron Lorand von Eötvös (1848 – 1919) [143][6], of the torsion balance, specifically designed to measure the gravity gradient for the first time (1890). Actually, the physical unit currently used for gravity gradients is named "Eötvös" (symbol "E" equals to $10^{-9}s^{-2}$, corresponding to measure an acceleration difference of $10^{-9}\,m/s^2$ over a $1\,m$ baseline) after his name, because of its pioneering studies about the gradient of Earth' gravity field carried out with this new instrument. Eötvös inherited the concept from the Coulomb's torsion balance (1784), which was used to sense electrostatic forces, and capitalised on the instrument adapting to measure the gravity gradients. The Eötvös's torsion balance is constituted by two test masses m located at the ends of a horizontal beam of length $2l$ and hung to a platinum-iridium (or, tungsten) wire. A vertical offset between masses was introduced to be sensitive to horizontal gradients as well. A differential gravity force acting on the two masses, i.e. a gravity gradient, induces a torque on the beam that twists about the vertical axis. The gradient is counterbalanced by a restoring torque created by the torsional force of the wire. The rotation of the beam is read on a scale through a telescope aiming at a mirror (Figure 3-8). This apparatus allowed Eötvös to achieve an accuracy of $10^{-9}s^{-2}$. He developed also another version of the torsion balance to study the equivalence of inertial and gravitational mass, as postulated by the Equivalence principle of Einstein.

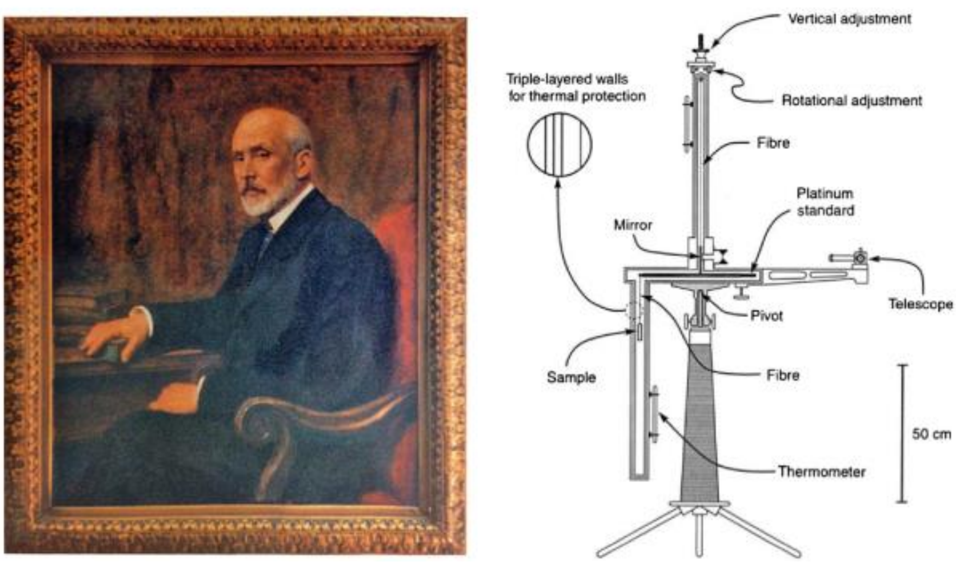

Figure 3-8: Left: a portrait of Baron Lorand von Eötvös by Gyula Eder (1941); Right: a scheme of the Eötvös's torsion balance (from [143])

The basic operation, reprocessed and adapted, is briefly described hereafter, as presented in [6]. Schematising the instrument as depicted in Figure 3-8, the beam is subjected to a torque M as (neglecting the mass beam):

$$\vec{M} = \overrightarrow{r_A} \times m\overrightarrow{g_A} + \overrightarrow{r_B} \times m\overrightarrow{g_B} \tag{3-13}$$

where $r_A = (-x, -y,\ 0)$ and $r_B = (x,\ y,\ h)$ are the position vectors of proof masses with origin at the instrument centre within the north-east-down coordinate system, g_A and g_B are the corresponding gravity vectors. The vertical component of the torque would be:

$$L_3 = mx\big(g_2(x, y, h) - \ g_2(-x, -y, 0)\big) + my(g_1(-x, -y, 0) - g_1(x, y, h)) \tag{3-14}$$

The gravity components (first-order) are composed by:

$$g_1 = \Gamma_{11}x + \Gamma_{12}y + \Gamma_{13}z$$
$$g_2 = \Gamma_{21}x + \Gamma_{22}y + \Gamma_{23}z \tag{3-15}$$

and hence:

$$L_3 = 2m(x^2 - \ y^2)\Gamma_{12} + 2mxy(\Gamma_{22} - \Gamma_{11}) + mh(x\Gamma_{23} - y\Gamma_{13}) \tag{3-16}$$

By using the azimuth with respect to the north and hence expressing $x = l\ \cos\alpha$ and $y = l\ \sin\alpha$, the equation (3-16 changes into:

$$-\tau(\theta_\alpha - \theta_0) = ml^2((\Gamma_{22} - \ \Gamma_{11})\sin 2\alpha + 2\Gamma_{12}\cos 2\alpha) + mlh(\Gamma_{23}\cos\alpha - \Gamma_{13}\sin\alpha) \tag{3-17}$$

where τ is the torsional coefficient of the wire, θ_0 is rest position of the beam, θ_α is the angle of the beam relative to the θ_0 when the instrument is at azimuth α. Repeating the measures at several azimuths allows to determine the unknown quantities: θ_0, $\Gamma_{22} - \Gamma_{11}$, Γ_{23}, Γ_{13}, Γ_{23}.

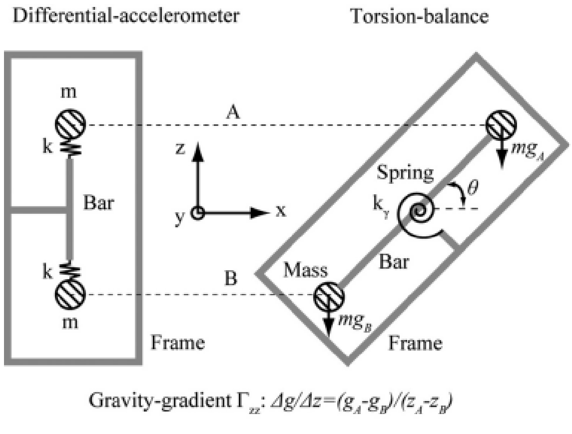

Figure 3-9: Schematic view of the operating principle of two basic types of gradiometer, founded on the approach used: differential-accelerometer and torsion-balance (adapted from [143])

In the early 1900s, the Eötvös instrument was largely used in Europe and in the US to help in the geophysical prospecting of oil and gas [6][148]. However, in 1930s the advent of gravimetry, for the measurement of the magnitude of the gravity, superseded gradiometry

instruments due to the greater efficiency and a similar accuracy. Just in 1970s gradiometry showed a new interest in military applications to measure the vertical deflection of the gravity vector. Indeed, different group at Hughes Aircraft Research Laboratories, Charles Stark Draper Laboratory of Cambridge and Bell Aerospace Laboratories developed gradiometers for ground and/or airborne applications, such as geophysics and geology through an intensive use in exploration and oilfield geophysics in search for mineral deposits.
Since the first Eötvös' torsion balance, several types of gradiometers have been proposed with different fields of application. Basically, gravity gradiometers can be grouped in two types, depending on the principle used to retrieve the gravity gradient (Figure 3-9): differential accelerometry and torsion-balance.
Gradiometers based on a differential-accelerometer approach found the retrieval of the gravitational gradient on the linear difference of gravitational acceleration between two test masses over the relative baseline of separation. In this case, the gradient is derived from a difference of specific forces acting on the test masses and the basic components are two linear accelerometers.
On the other hand, gradiometers based on a torsion-balance approach found their operating principle on the differential torques exerted on two test masses separated by a baseline. In this case, the different specific forces acting on the masses produce a net torque and induce a rotation; the basic components are two angular accelerometers and the gradiometer is likely resembling a dumbbell.
A schematic view of two approaches is reported in Figure 3-9.
Starting from these basic concepts, different types of gravity gradiometers can be envisaged, depending on, for instance, how the "elastic" element of the proof mass is realised, how the mass movement is detected, if by direct measure or by the feedback needed to keep fixed the mass, which technique is applied for sensing the linear or angular movement of test masses, etc.

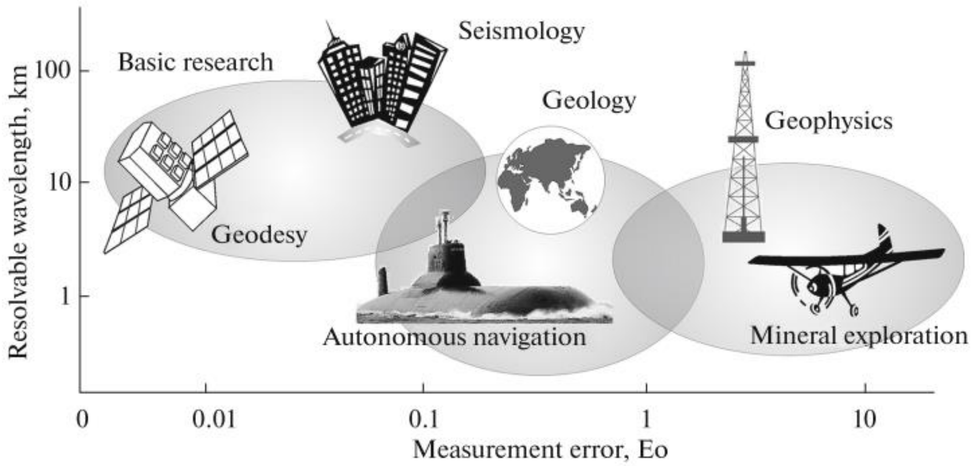

Figure 3-10: Gravity gradiometry applications versus the required sensitivity; on the y-axis the spatial resolution achievable is shown, whereas on the x-axis the accuracy in terms of gravity gradient (in Eötvös) is reported (from [142])

Since the first Eötvös' model to nowadays, the application field of gradiometers has been largely widespread, ranging from basic research devote to the verification of fundamental physics principles (inverse square of Newton's law, equivalence of inertial and gravitational mass) to geodesy (Earth's gravity mapping, ocean and climate studies), from geophysics and geology (mineral exploration, search for hydrocarbons) to autonomous navigation (underwater navigation, especially).

Figure 3-10 shows off a schematic view of main application fields in terms of spatial resolution and related needed accuracy [142].
In the following sections a review of the main gradiometers developed, in development or in study is presented. Different designs can be identified but all of them are led back to the approaches above depicted: differential accelerometry and torsion-balance-type.
Technologies employed as well are extremely diversified: mechanical superconducting, superconducting magnetically levitated, atom-interferometry, MEMS-type, etc.
The state of the art was focused on the main type of gradiometers developed till now:

- Airborne/terrestrial gradiometers
- Electrostatically suspended gradiometers
- Mechanically suspended gradiometers
- Superconducting gradiometers
- Atom-interferometry-based gradiometers
- MEMS-based gradiometers

Table 3-1 Stage of development (TRL, Technology Readiness Level) and performance (tested and/or expected) of main typologies of gravity gradiometers (DA: Differential Accelerometry, TB: Torsion Balance, F: with feedback)

Gravity Gradiometer	**Technology**	**Noise ($E/\sqrt{Hz}$)**	**Axes**	**Type**	**TRL**
GRADIO/ GOCE[1]	Electrostatic accelerometer	$2\ 10^{-2}$	Full	DA/F	9, flight-proven
GRACE[2]	SST-ll	-	single	DA	9, flight-proven
GRACE-FO[3]	SST-ll	-	single	DA	9 (7), in operation
GRAIL[4]	SST-ll	-	single	DA	9, flight-proven
SGG[5]	Superconducting mechanical	1	single	DA	3, prototype
SGG[5]	Superconducting mechanical spring and levitation	10^{-2} (tested)	three-components	TB& DA	4, prototype 3-components (diagonal)
SGG[5]	Superconducting levitated	$10^{-4}/\ 10^{-5}$ (potential)	two-components	TB& DA	4, prototype 2-components (diagonal and off-diagonal)
NA [6]	MEMS	$10^{-1}-1$ (potential)	single	TB	2, project/study
Seesaw-suspension[7]	MEMS	10	single	TB	2-3, partial prototype
Absolute GG[8]	Atom-interferometry	1-4	single	DA	4, on-ground tests
QGG/AIGG[9]	Atom-interferometry	30 (tested), 10^{-3}(potential)	single	DA	3-4, on-ground tests/project
RGG[10]	Rotating mechanical dumbbell	1-5	single	TB	4,

					tested breadboard model
GGI/FTG[11]	Rotating mechanical accelerometer	2-30	Full	DA/F	4-5, Airborne/ship/ on-ground operated
Draper[12]	Floated gradiometer	1	single/ three	TB	4, laboratory tested
ARKeX[13]	superconducting	2	single	DA	5, Airborne/on-ground operated
Gedex[14]	superconducting	1	single/ three	TB	5, Airborne/on-ground operated

[1]Alcatel/ONERA [137][136][139], [2]NASA/DLR [129], [3]NASA/DLR [REF], [4]NASA/JPL/MIT [131], [5]University of Maryland [173], [6]University of Twente (Netherlands), [7]Imperial College, [8]Yale University, [9]JPL/Caltech, [10]Hughes aircraft [6][143], [11]Bell Aerospace/Lockheed Martin [146][6][143, [12]Draper [143][6], [13]ARKeX [142][147], [14]Gedex [150][151]

Considering that most of the gradiometers have as core an accelerometer, a summary of the accelerometer performance state of the art has been carried out on the space qualified accelerometers currently available (flight proven, in operation and in development). Results are reported in Table 3-2.

Table 3-2 performance state of the art of space qualified accelerometers

Accelerometer	**Type**	**Mission**	**Sensitivity** $(m/s^2/\sqrt{Hz})$	**Bandwidth** (Hz)	**Stage**
STAR[1]	Electrostatic	CHAMP	$3\cdot10^{-9}$ (y, z), $3\cdot10^{-8}$ (x)	$10^{-4}-10^{-1}$	Flight-proven
SuperSTAR2[2]	Electrostatic	GRACE	10^{-10}	$10^{-4}-10^{-1}$	Flight-proven
MicroSTAR[3]	Electrostatic	GRACE-FO	$< 10^{-10}$		In operation
GRADIO[4]	Electrostatic	GOCE	$3\cdot10^{-12}$	$5\ \cdot10^{-3}-10^{-1}$	Flight-proven
T-SAGE[5]	Electrostatic	MICROSCOPE	$3\cdot10^{-10}$	$10^{-3}-2\ 10^{-2}$	In operation
ISA[6]	Electro-Mechanical	BepiColombo	10^{-8}	$3\ \cdot10^{-5}-10^{-1}$	In operation
HAA[7]	Electro-Mechanical	JUICE	10^{-8}	$10^{-4}-10^{-1}$	In development

[1]ONERA [153], [2]ONERA [153], [3]ONERA, [4]ONERA [152], [5]ONERA, [6]THALES ALENIA SPACE ITALY/INAF [154], [7] THALES ALENIA SPACE ITALY/INAF [158]

3.3.2.1 Airborne/terrestrial gradiometers

An interesting prospective can be envisaged for planetary bodies hosting a sufficiently thick atmosphere. For those targets, the possibility of using gradiometer on-board airplanes and/or balloons or in general flying mobile platforms can constitute an interesting alternative to gradiometer on-board an orbiter. Such an option is witnessed by different trends towards

the use of such flying platforms to explore and investigate closer aimed targets. Mars 2020 rover's mission, for instance, will include a small and autonomous helicopter to survey the planet and to access remote areas. A similar approach is considered for the mission Dragonfly, recently approved by NASA for the New Frontiers Program. This mission is based on a rotorcraft-lander to the largest Saturn's moon, Titan, as the next mission in its New Frontiers program. Expected to be launched in 2026 and to arrive in 2034, Dragonfly will explore several locations across Titan, sampling and measuring the composition of Titan's organic surface materials to characterise the habitability of Titan's environment and investigate the progression of prebiotic chemistry.
Apart this new trend in Solar System missions, whose effectiveness needs to be proved, several concepts have been developed and proved for terrestrial applications, especially in military applications and since seventies. Some of them have been also commercialised.

3.3.2.1.1 Hughes Aircraft gradiometer

The first prototype of a gravity gradiometer applied for moving platforms was invented by Robert Forward at the beginning of 1970s [143][144]. The Hughes Rotating Gravity Gradiometer (RGG) is depicted in Figure 3-11 [6]. Two dumbbells with identical test masses at their ends are coupled to the base in a cross-shaped structure through a central pivot, which is constituted by a torsional spring. A gravity gradient on the structure moves each dumbbell in opposite direction creating a relative torque which at the same time cancel the common mode disturbances. Moreover, dumbbells are rotated at a half the mechanical resonance frequency of the pivot (35 Hz); in this way, the gradient signal results at the double of the rotation frequency, due to the system symmetry, allowing at the same time a discrimination in frequency and an amplification of the output due to the resonance. A breadboard model was developed by Hughes with a diameter of 14 cm and an accuracy of 1 E for a 10 s of integration [6]. The development of the instrument was stopped in the early 1980s when the US Department of Defense chose the Lockheed Martin (ex Bell Aerospace) gravity gradiometer for long-term development [143].

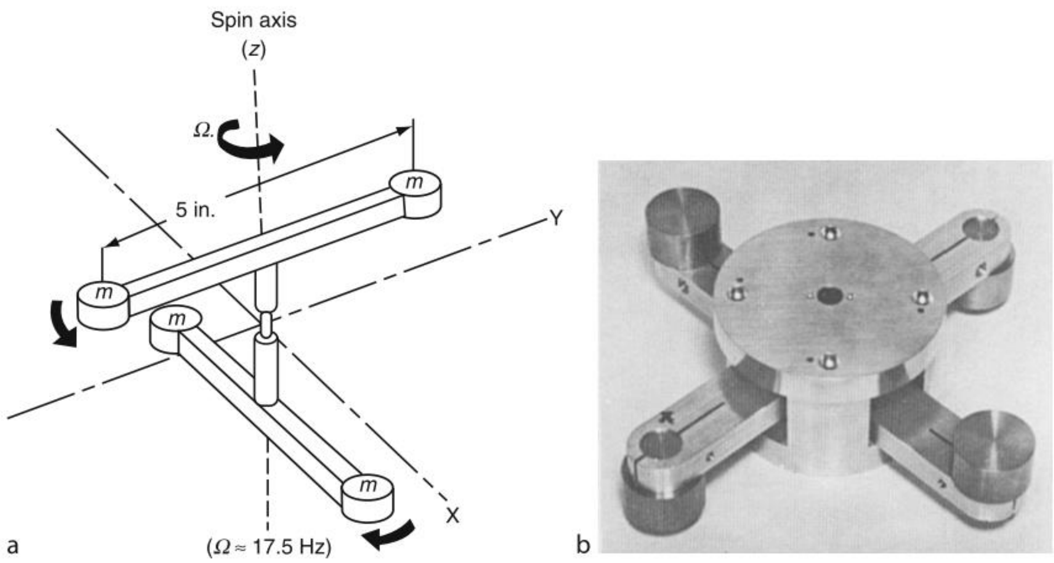

Figure 3-11: sketch of the Rotating Gravity Gradiometer (RGG) by Hughes Research Lab and related breadboard model [143][6]

The capability of rotation is often used in sensors to help in discriminating between signal and noise sources, especially in dynamic environments. Indeed, many of error and noises are modulated at the rotation frequency or not modulated, such as $1/f$ noise, whereas the gradient signal is modulated at doubled frequency due to the symmetry of the mass-baseline configuration.

3.3.2.1.2 Lockheed Martin gradiometer

The rotation is used also in the Gravity Gradient Instrument (GGI) which is the basic element of the Full-Tensor of Gravity Gradients (FTG), originally designed by Ernest Metzger at Bell Aerospace [143] [146]. A sketch of a single GGI is depicted in Figure 3-12. Two pairs of linear accelerometers are mounted on a disk in opposite positions within the same pair, with their sensing axes pointing in opposite directions and perpendiculars to the disk spin axis; the disk is rotated at angular velocity Ω. From equation (3-17) with $h = 0$, using $\alpha = \Omega t$ and $\alpha = \Omega t + \pi/2$ for a pair of accelerometers and $M = mr(a_1 + a_2)$ and $M = mr(a_3 + a_4)$ for the related torques, the measurement equation is [6]:

$$a_1(t) + a_2(t) - \left(a_3(t) + a_4(t) \right) = 2r(\Gamma_{22} - \Gamma_{11}) \sin 2\Omega t + 4r\Gamma_{12} \cos 2\Omega t \qquad (3\text{-}18)$$

The sum of signals from each pair yields the gravity gradient at the centre, nulling the common linear accelerations perpendicular to the spin axis; moreover, the difference of two sums from two orthogonally arranged accelerometers deletes also the rotational accelerations about the spin axis [146]. A single GGI allows to retrieve the difference of two diagonal elements and the related off-diagonal component (Γ_{12}, $\Gamma_{22} - \Gamma_{11}$ in the example). The rotation of the disk allows to modulate the gravity gradient at a doubled frequency with respect to the rotation Ω, because the same configuration repeats twice per rotation. Demodulation at the 2Ω frequency allows to recover the gravity gradient. However, other effects not inherent to the investigated signal and related to misalignments between accelerometers and/or mismatches between their scale factors are modulated at the same rotation frequency [146]. Indeed, demodulation of the unwanted signal at the rotation frequency provides information about those imperfections. Therefore, this output is used in feedback loop to move the proof mass in one of the accelerometers in each pair in order to null it.

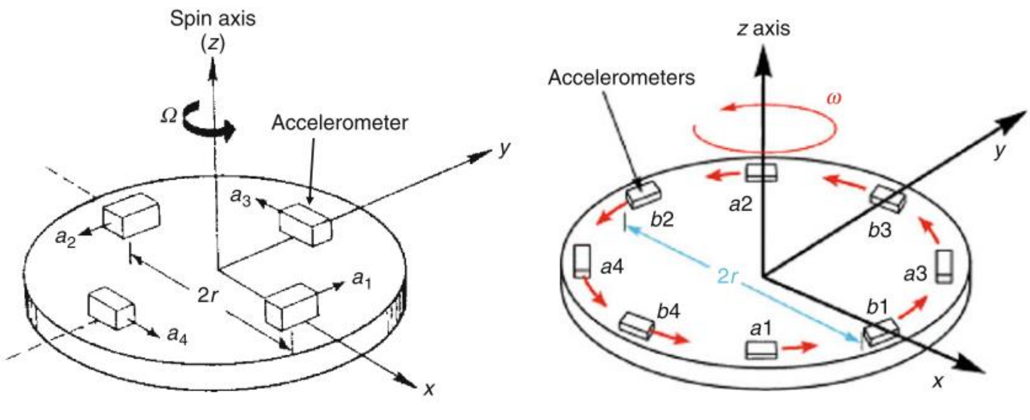

Figure 3-12: sketch of GGI by Bell Aerospace (left); the updated version of Lockheed Martin with doubled pairs of accelerometers (right) [6]

A complete instrument (FTG) is constituted by a set of three disks (GGI), orthogonally mounted, to obtain the full tensor gravity gradiometer. The adopted configuration is the so called “umbrella” mounting (Figure 3-13), which allows some advantages such as keeping the same orientation of each GGI with respect to the vertical, saving space in the arrangement and enhancing the gradiometers calibration since each disk senses similar signal levels.

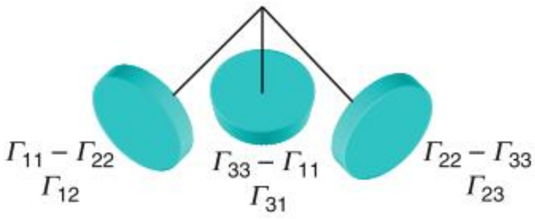

Figure 3-13: disposition of three discs of GGI in “umbrella” configuration to obtain a full-tensor gradiometer [6]

Each GGI provides the difference of two in-line components and a corresponding off-line component; hence the use of three orthogonally oriented disks (Figure 3-13) allows to retrieve three differences of in-line components and three off-line components (six gradients), i.e. all together constitute a full-tensor gradiometer. Moreover, the sum of all the in-line differences would ideally return a null value.
All the system is inertially stabilised by three gimbals controlled by two 2-degrees-of freedom gyroscopes and three orthogonal accelerometers [146]. Figure 3-15 shows off the complete gradiometer by Bell Aerospace.

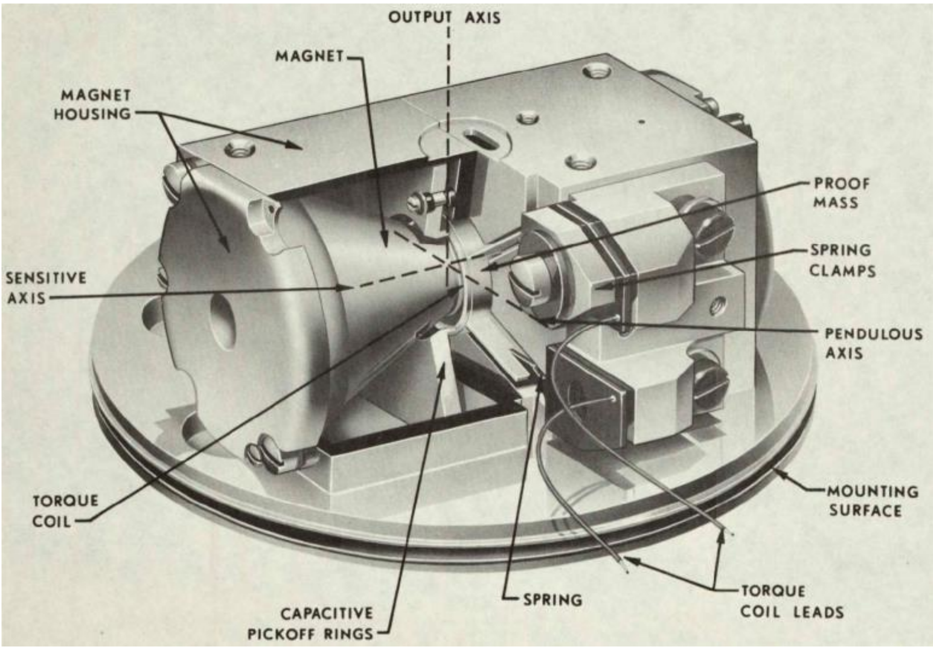

Figure 3-14: model VII of a single Bell accelerometer constituting the basic element of GGI [147]

The basic element of a single GGI is the Bell Model VII pendulous force rebalance accelerometer [146] (depicted in Figure 3-14). A cylindrical proof mass is hung through a flexural spring which allows a deflection of the proof mass when an acceleration acts along the sensing axis. Two ring-shaped capacitive pick-off located on either side of the proof

mass detect such a displacement as signal. It is amplified, converted to a current and applied to a torquer that forces the proof mass in its zero output. The current measured and applied to the torquer is related to the underwent acceleration. In the first version of the instrument, two accelerometers on a GGI were separated by a $10\ cm$ baseline; hence, the detection of a few Eötvös gradient required accelerometers with a sensitivity about $10^{-10}\ m/s^2$ [146].
The first FTG by Bell Aerospace was employed for aircraft, land vehicle and ship applications; it has been employed for military and commercial applications. The gradiometer was chosen by the US Navy for the gravity compensation requirements in its inertial navigation systems. Moreover, the Air Force Geophysics Laboratory used the same system to regional airborne gravity survey system [146]. A performance of about $6\ E/\sqrt{Hz}$ was achieved in the laboratory environment, whereas during the 1987 test flight, a level of about $30\ E/\sqrt{Hz}$ level [143]. After the first version, at the beginning of 1990s Bell Aerospace (later acquired by Lockheed Martin) proposed some improvements, such as increase in the baseline length (till to $30\ cm$) and doubling of the accelerometers (from 2 to 4 pairs, Figure 3-12) to reinforce the signal, grow of the rotation frequency and filter cut-off frequency to enhance sampling and spatial resolution.

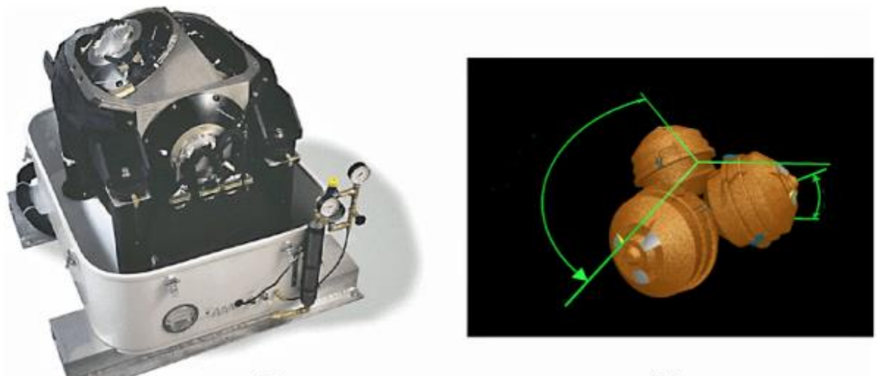

(a) (b)

Figure 3-15: the full tensor gradiometer by Bell Aerospace on an inertially stabilised platform (left, a)); the mounting in “umbrella configuration” (right, b)) [143]

At the end of 1990s, further improvements and simplifications of the Bell Aerospace and Lockheed Martin FTG version allowed to commercialise the product, trademarked as Falcon, to be used for airborne applications. Since 1994, Bell Geospace gained the commercial rights to manufacture the FTG for marine and airborne surveys [142]. The performance achieved are about $2-3\ E/\sqrt{Hz}$.

3.3.2.1.3 Draper Floated gradiometer

Another instrument belonging to the class of rotating gradiometer was developed in the 1970s and early 1980s by Milton Trageser of Charles Stark Draper Research Laboratory (Cambridge, USA), the Floated Gravity Gradiometer (FGG) [143][6]. The sensor employed the ‘floated gyro’ technology developed at the Massachusetts Institute of Technology (MIT) (Trageser 1984). Similarly to the RGG, the FGG sensed gravity gradient-induced differential torques on its dumbbell-like proof masses. The sensor had two masses at different heights, as in the Eötvös’ torsion balance. The gravity gradient measure was achieved by suspending the proof masses in a buoyant, viscous and magnetic fluid, in order to isolate them from vibrations [6].

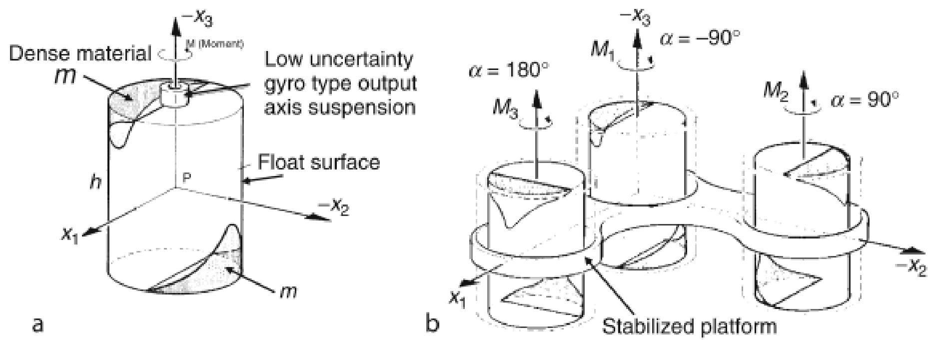

Figure 3-16: geometry of the floated gradiometer of Draper Research Laboratory: single unit (left, a)); group of three units on a stabilised platform (right, b)) [6]

The orientation of the floated proof masses was maintained by torque feedback loops supplied by external gyroscopes, which were integrated into the system.
Considering the equation (3-17), related to the Eötvös's torsion balance, if, for example, $\alpha = -90°$, is used (maintaining the north-east-down coordinate system and indicating that the first axis of the device points west, towards $-x_2$), then a deflection due to the gradients would be recovered by applying a moment M, with l radius of the device:

$$M = \tau(\theta_\alpha - \theta_0) = 2ml^2\Gamma_{12} - mlh\Gamma_{13} \tag{3-19}$$

Assuming the gradiometer on a stabilised platform with axes constrained to the local north-east-down system, three instruments (Figure 3-16) would measure the moments:

$$\begin{aligned} M_1 &= 2ml^2\Gamma_{12} - mlh\Gamma_{13} \\ M_2 &= 2ml^2\Gamma_{12} + mlh\Gamma_{13} \\ M_3 &= -2ml^2\Gamma_{12} + mlh\Gamma_{23} \end{aligned} \tag{3-20}$$

Some of the good performance offered by the floated gradiometer were the following:

- quick time response;
- low level of self-noise;
- relative insensitivity to angular vibration
- low level of fluid unbalance;
- reasonably low sensitivity to linear vibration, temperature and magnetic fields.

The Draper gradiometer was also intended for satellite and aircraft applications. The achieved performance, tested in laboratory, was about $1\ E/\sqrt{Hz}$. Like the Hughes RGG, the Draper Laboratory gradiometers did not reach the production stage but did demonstrate very good performance in the laboratory (1980s).

3.3.2.1.4 ARKeX Exploration gradiometer

ARKeX Ltd, a UK company (Cambridge), commissioned by the European Space Agency (ESA), has developed a vertical cryogenic Exploration Gravity Gradiometer (EGG),

operating at a temperature of 4 K. This gradiometer was specially designed to measure the vertical gradient [142][147] and it was used by the company for geophysical operations.
This gradiometer is based on the principle of superconductivity through the use of Meissner effect, that allows for contactless suspension of proof masses (levitation), and superconductivity itself, that allows for using a SQUID magnetometer to provide high-accuracy and stable measurements of proof mass displacements.
It is constituted by two vertically-spaced accelerometers, whose proof masses, with vertical sensing axes, have a H-shaped cross section (a hollow cylinder with a flange in the middle) and are suspended by levitation. Proof masses are made by Niobium (50 mm of diameter and length and 100 g in mass) and are separated by 15 cm. The gradiometer was installed inside a cryostat (4 K) and mounted on a gyrostabilised platform; the performance achieved were about 7 $E/\sqrt{Hz}$ [142].
After 2008, ARKeX established an agreement with Lockheed Martin to use the FTG technology. The result was an advanced eFTG (enhanced FTG) with higher accuracy and improved quality of shock absorption and thermal stabilisation, allowing to achieve noise levels of about 2 $E/\sqrt{Hz}$.

3.3.2.1.5 Gedex Airborne gradiometer

The Canadian company Gedex Inc. developed and patented a cryogenic High Definition Airborne Gravity Gradiometer (HD-AGG) composed by three orthogonally arranged pairs of angular accelerometers to measure the full tensor of gravity gradient [142][143][150]. The instrument used by Gedex has been developed at the University of Maryland (section 3.3.2.4 and [151]). It is a cross-component gradiometer type (torsion-balance) composed by pairs of angular accelerometers that share a common rotation axis, each of which is constituted by elongated test masses (Figure 3-17). The two test-masses in each pair have their long axes mutually orthogonal and are supported within housings connected to each other, via bolting, to a central metering cube structure; the assembled prototype is shown in Figure 3-17. When angular accelerations are sensed about the rotation axis of one of the test-mass pairs, each pair of accelerometers performs rotation in the same direction (“common-mode”) with respect to the body of the instrument, while accelerations induced by the local gravity gradient tensor impose to the two test-masses in each pair to rotate in opposite directions (differential-mode).

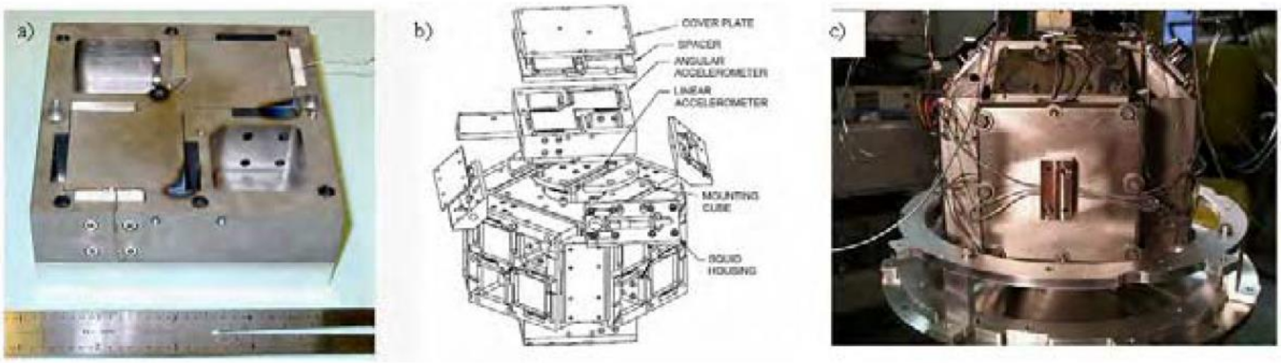

Figure 3-17: angular accelerometer by Gedex (10.2 x 10.2 x 2.5 cm, left, a), schematic diagram of the sensor (b) and assembled prototype (c) [150]

The angular accelerometers are carefully adjusted and calibrated to match as much as possible their characteristics. Any residual imbalance, misalignment of the sensitivity axes

and other technological imperfections are measured and taken into account in the gradiometer error model during the calculation of gravity gradients components [142].
The instrument is cooled down at cryogenic temperatures (< 5 K) with the aim of reducing the thermal noise and of making use of properties of superconducting materials. Indeed, proof mass, spring and housing are derived all from a single block of niobium (Nb).
Laboratory tests indicate that noise levels of $1\ E/\sqrt{Hz}$ (RMS) in the range $10^{-2} - 10^{-1}\ Hz$ can be achieved and $< 1\ E/\sqrt{Hz}$ between $10^{-1} - 1\ Hz$ [150]. Currently, it is going to be deployed at commercial level.

3.3.2.2 Electrostatically-suspended gradiometers

Gradiometry based on differential accelerometry, both in the linear and angular version, founds its principle on the accelerometers employed to accomplish the measure. A class of accelerometers largely employed in space missions relies on the electrostatically-suspended proof-mass concept: they are electrostatic accelerometers [151][152][153]. The operating principle of an accelerometer foresees the measure of the proof-mass motion relative to its frame to derive the underwent acceleration. In this case, the displacement is measured and the proof-mass is hung through an elastic element (spring-like) to restore the rest position. In the electrostatic accelerometers, the proof-mass is not connected to the frame, avoiding any mechanical contact, instead it is suspended by means of an electrostatic field. In this case, while the proof-mass follows its free-fall along the orbit, the relative displacement between proof-mass and spacecraft is monitored through a capacitive transducer; a closed-loop actuator exerts an electrostatic feedback force on the proof-mass in order to keep it motionless with respect to the spacecraft [151].
This type of accelerometers provide very high performance in terms of sensitivity due to the fact that the “spring” is provided through electrostatic suspension, guaranteeing an electrical stiffness very low and hence ensuring that also the frequency of the system is very low (section 3.3.2.3). The control loop ensures also that the displacements of the test mass with respect to its frame, rigidly connected to the spacecraft, is very small in the entire frequency band, determining the linearity of the system. Problems are connected to the on-ground calibrations where it is necessary to suspend the test mass against the Earth gravity.
Actually, this type of accelerometers, mainly produced by the ONERA French research centre (Office National d'Etudes et de Recherches Aérospatiales), has been employed in different space gravity missions, such as CHAMP, GRACE, GRACE-FO and GOCE. Each mission, in a sense, explores a different concept in measuring the gravitational field, CHAMP being the simplest, followed (also in mission complexity) by GRACE/GRACE-FO and then GOCE. However, the aim of accelerometers is different in those missions. In the first three missions the accelerometer provides the measurements of the satellite non-gravitational forces, in order to discriminate the position or velocity changes of the satellite due to the gravity field from those due to perturbations such as drag, solar radiation, albedo, etc. Instead, in GOCE, accelerometers constitute the core of the gradiometer and hence are the basic elements for the measurement of the gravity field through the gravity gradient.
Indeed, GOCE hosts on-board the first ever gravity gradiometer, whose operation, based on differential accelerometry, is founded on high-sensitivity electrostatic accelerometers. The gradiometer is constituted by six tri-axial closed-loop capacitive accelerometers, characterised by an outstanding resolution of $3 \cdot 10^{-12} m/s^2/\sqrt{Hz}$ arranged orthogonally in pairs at a distance of $50\ cm$ on a very stable carbon-carbon honeycomb structure [135][136][137][138]. The centre of the three gradiometer axes is chosen as close as

possible to the satellite centre of mass. Figure 3-18 shows the gradiometer core assembly and a single pair of accelerometers.
Each pair of accelerometers constitutes a gradiometer arm. As above anticipated, such accelerometers are based on the electrostatic principle of the proof mass suspension. The proof mass is floated in a small cage and is kept in the centre of the cage by electrostatic forces, generated by applying suitable voltages between the cage, equipped with eight pairs of electrodes, and the proof mass. Proof mass and cage constitute a capacitive system whose variation of capacitances depends on the variation of the gap between mass and electrodes.

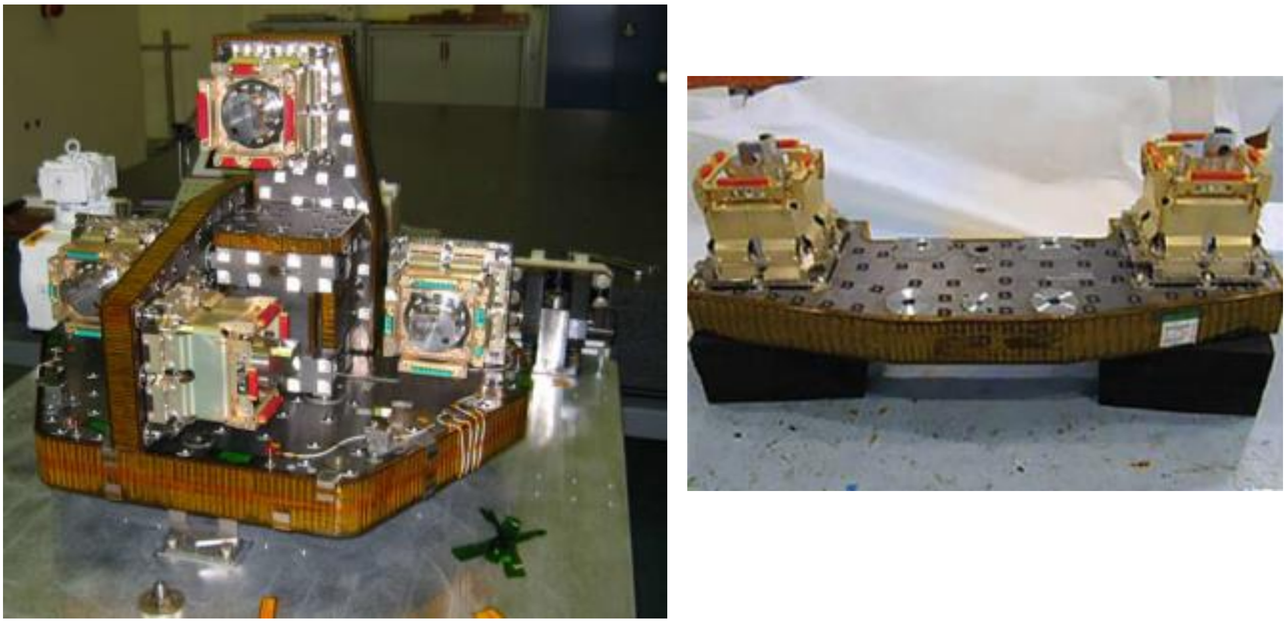

Figure 3-18: The GOCE gradiometer core (left): the six tri-axial accelerometers orthogonally mounted are shown along with the developed special carbon-carbon structure. On the right: single gradiometer arm with two accelerometers [135]

The accelerations effectively measured are derived from the voltages applied to maintain the proof mass levitated and centred in the cage. The gravity gradients, the observable to be measured, are recovered through the principle of the differential accelerometry. Measurements from two accelerometers belonging to the same arm and separated by $50\ cm$ are subtracted. This operation allows to remove noise and disturbing effects affecting both accelerometers, a process, named *common mode rejection*, which is fundamental to reach the sensitivity needed to detect the tiny gravity signals. The remaining signal is the difference in acceleration due to Earth's gravity detected at two points separated by a baseline of $50\ cm$, and it is an optimal approximation of the gravity gradient in this frame.
Beside the difference, the average of two measures on the same arm provides the external forces acting on the spacecraft such as atmospheric drag and solar radiation pressure. Such an information is sent as command input to the electric propulsion engine to balance the atmospheric drag and to make the spacecraft drag-free [138].
Geometrically, the proof masses have a parallelepiped shape with sizes of $4\ x\ 4\ x\ 1\ cm$, a $320\ g$ mass and are made by a platinum-rhodium alloy (Figure 3-19). Such a shape is chosen to allow the test of the accelerometers on-ground, levitating electrostatically against its weight the proof mass through the application of a high voltage on the electrodes on the larger side of the proof mass. However, this geometry implies that from one side it is not possible a complete verification on-ground of the accelerometers sensitivity. From the other

side, each accelerometer has two more sensitive axes (ultra-sensitive axes), whereas the third one is less sensitive (i.e. the axis orthogonal to the larger face).
Due to this asymmetry in the sensitivity, the arrangement of the accelerometers has been chosen conveniently so that the in-line direction, being more important because related to the in-line components of the gravity gradient, has been covered by ultra-sensitive axes.

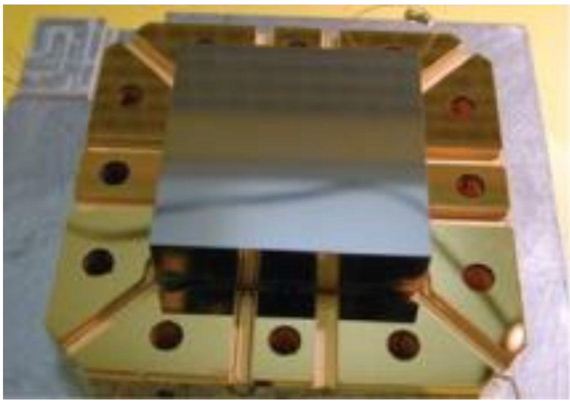

Figure 3-19: A single proof mass of the accelerometers employed in GOCE [135]

The other ultra-sensitive axes have been identified in order to guarantee higher precision in the measurement of the angular velocity and angular accelerations. Indeed, the three orthogonal one axis gradiometers are oriented roughly with the spacecraft axes: X-axis in flight direction, Y-axis orthogonal to the orbit plane and Z-axis radially downwards. The gradiometer spacecraft-fixed is nadir-pointed and rotates in space mainly around Y-axis. Hence, the remaining ultra-sensitive axes have been fixed to lie in the XZ plane in order to better record the main rotational motion of the gradiometer/spacecraft. Figure 3-20 depicts the arrangement of the six three-axis accelerometers according to this strategy.

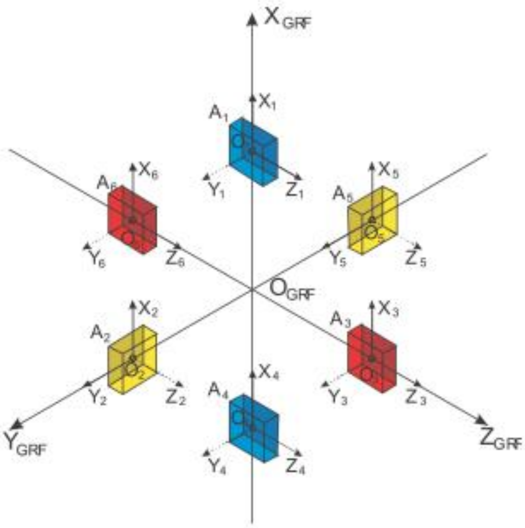

Figure 3-20: location of the GOCE six three-axis accelerometers in the gradiometer reference frame [137]. Solid and dashed arrows depict, respectively, ultra and less sensitive axes of proof masses

The three gradiometric arms are arranged at 90° to each other so that the gradients are obtained in all three dimensions. The result of a science measurement phase is a gravity gradient map evenly covering our planet except for small areas around the poles.

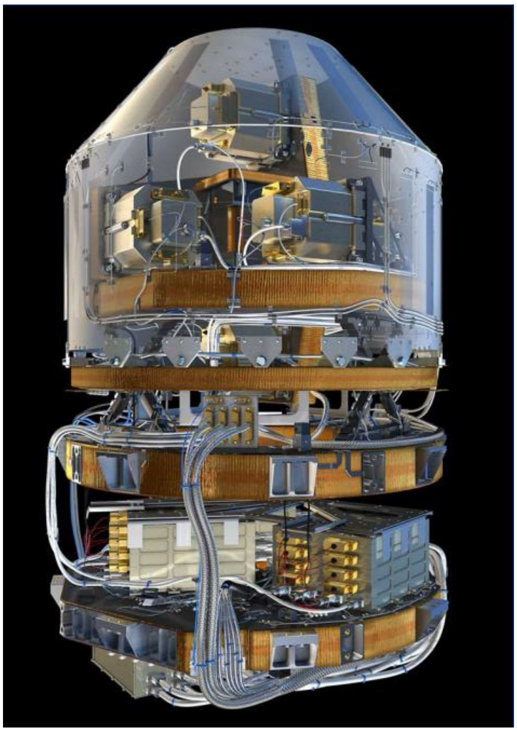

Gradiometer Characteristics	
Mass	$180\ kg$
Power	$100\ W$
Distance accelerometers	$0.5\ m$
Bandwidth as AOCS sensor	$DC\ to\ 5\ Hz$
Measurement bandwidth	$5\ \cdot 10^{-3} - \ 10^{-1}\ Hz$
Accelerometer sensitivity	$3\ \cdot 10^{-12}\ \ m/s^2/\sqrt{Hz}$
Structure stability	$0.2\ ppm/K$
Temperature stability	$0.01°C\ over\ 200\ s$

Figure 3-21: The whole assembly of the Electrostatic Gravity Gradiometer [135], along with its main characteristics

3.3.2.3 Mechanically-suspended gradiometers

No gravity space missions with mechanically-suspended gradiometers have been realised so far. However, terrestrial gradiometers with such a kind of accelerometers have been realised, as witnessed with RMGG by Hughes (section 3.3.2.1.1), partially with GGI by Bell (section 3.3.2.1.2) and with the first versions of Paik superconducting gradiometers (section 3.3.2.4) . Moreover, such a manufacturing technology for proof-masses is well employed in accelerometers for terrestrial and space use.
For space use, the electro-mechanically accelerometer ISA (Italian Spring Accelerometer) has been realised for the BepiColombo mission to Mercury jointly by IAPS/INAF and Thales Alenia Space Milan [154][155][156]. An advanced model, implementing an improved and better radiation hardening to the accelerometers as well, is going to be designed and manufactured by the same team for the JUICE mission to Jupiter moons [158][159]. The advancement with respect to ISA is related both to the sensor and to the electronics due to the different environment conditions the accelerometers would have to deal with and to the general objective of monitoring the non-gravitational perturbations underwent by the spacecraft (not mainly the solar radiation as employed in BepiColombo). Indeed, the Jovian system is characterised by very strong radiation belts which concentrate high energy particles making the radiation dose to be tolerated higher with respect to Mercury environment.
ISA accelerometer is part of the Radio-Science Experiments (RSE), a set of intertwined experiments aimed at determining the gravity field of Mercury, evaluating the rotation state of Mercury and carrying out some Einstein's General Relativity tests at Mercury. In this frame, ISA aims at measuring with very high accuracy all the non-gravitational accelerations perturbing the BepiColombo spacecraft trajectory and changing its orbit around Mercury

planet, such as the direct solar radiation pressure and the indirect radiation coming from the planet surface (planetary albedo and infrared emission).
The high sensitivity ISA accelerometer is a three-axis sensor able to work in space conditions on-board of a satellite in “free-fall” and therefore not subject to the Earth gravity. Apart from its high sensitivity and dynamics, one of its main features is the possibility to perform its calibration on ground, with Earth gravity, differently from other manufacturing technologies, such as the electrostatic one. Its fundamental peculiarity, which provides the name “ISA”, is that the proof mass of each individual sensing element is connected to its reference frame by means of a mechanical foil-shaped spring that allows its movement just along one direction (the so-called sensing axis), constraining it tightly in the other two directions. Every single axis of the accelerometer is constituted by three main parts:

- the mechanical oscillator
- the signal detector
- the actuation and control

The mechanical oscillator is constituted by a proof mass connected to the reference frame through a spring with low elastic constant. Accelerations, due to a change in the free-fall motion of the spacecraft, acting on its reference frame (fixed to the satellite) are seen as inertial accelerations acting on the proof mass. Relative displacements of the proof mass with respect to the frame need to be measured in order to recover the underwent accelerations. To this respect, two couples of plates face the central proof mass to form a capacitive transducer and a capacitive actuator. The coupling of these plates with the central proof mass realises four capacitors. The proof mass is electrically connected to the frame that is referred to the electrical ground. A $100\ \mu m$ gap between proof mass and plates is maintained by means of sixteen alumina washers (Al_2O_3), providing electrical insulation as well. Proof mass, plates and washers are assembled by screws and nuts, joining together both sensor sides, preventing the introduction of asymmetry effects. A couple of capacitors, named pick-up plates (the farthest from the spring) and used to gather the sensor response (capacitive transducer), detects any displacement of the proof-mass. These plates are included in a capacitance measurement bridge at equilibrium, whereas the other arms consist of known value fixed capacitors. The bridge is biased by a periodic signal coming from a generator and it is decoupled by an isolation transformer. Any sensing mass displacement causes a capacity variation of pick-up plates, hence an unbalancing of the bridge and a modulation of the output voltage. The remaining couple of capacitors forms the actuators, used to apply electrostatic forces to the proof mass. Their use is envisaged for different reasons: to calibrate the sensor on-flight applying a known acceleration, to set the rest position of the proof mass (operating point), to weaken the torsional spring constant k of the sensor [20]. In particular, the last action affects the quality factor Q of the sensor, decreasing its value: this allows for tuning the accelerometer sensitivity by using the actuators.
The system operates as a flexural harmonic oscillator, forced by an external acceleration and hence characterised by the following transfer function (Figure 3-22):

$$G(s) = \frac{1}{s^2 + \frac{\omega_0}{Q} + {\omega_0}^2} \tag{3-21}$$

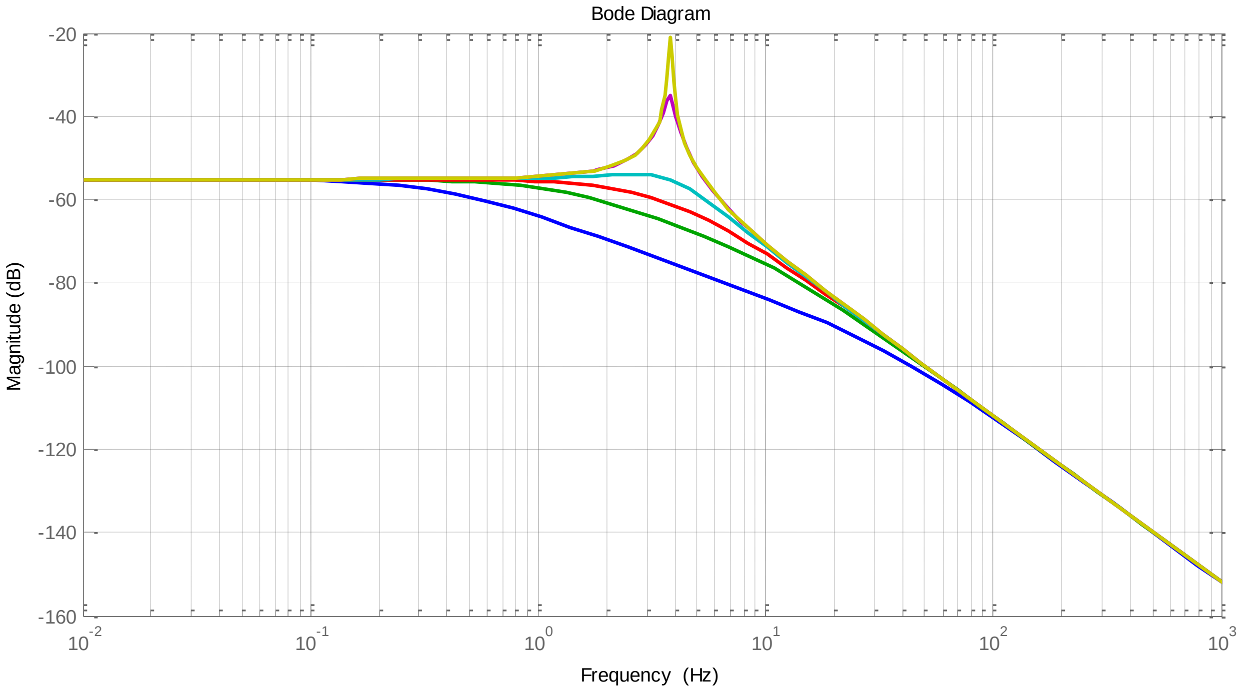

Figure 3-22: plot of an ideal transfer function for an accelerometer ISA-type: the amplitude at the resonance increases as Q increases; at frequencies higher than the resonance it attenuates at 40 dB per decade

where ω_0 is the natural angular frequency of the accelerometer ($\omega_0 = 2\pi\nu_0$) and Q its quality factor. The accelerometer returns a flat response for $\omega < \omega_0$, has a resonance peak at ω_0 and decreases fastly for $\omega > \omega_0$. ISA has a very low resonance frequency, $\nu_0 \cong 3.5\ Hz$ and is realised to work in the frequency range $3\,10^{-5} - 10^{-1} Hz$ with an accuracy till to $10^{-8}\, m/s^2$. In the operating frequency range, the transfer function between the sensed acceleration (a) and the proof mass displacement (x) is flat (within the accuracy required), hence frequency-independent: $x(\omega\ ) \approx a(\omega\ )/\omega_0^2$. Hence, the use of very low frequencies allows for increasing the sensor response (x) to detect the very small expected non-gravitational accelerations ($\sim\ 10^{-7} -\ 10^{-6}\ m/s^2$). Figure 3-23 shows some elements of a single EQM accelerometer (Engineering Qualification Model).

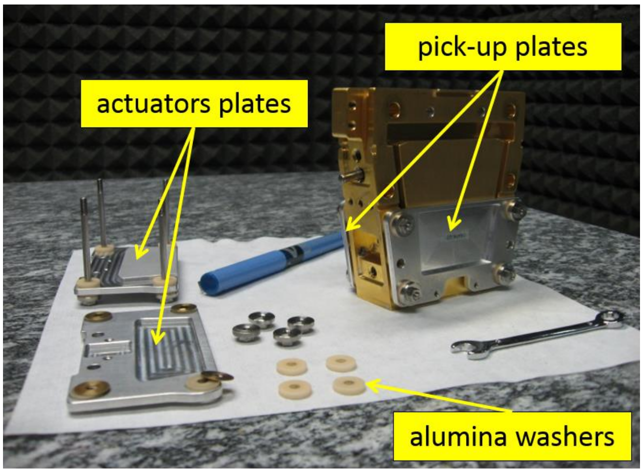

Figure 3-23: Details of a single ISA accelerometer used during tests at IAPS/INAF: pick-up plates (mounted), actuators, screws

Both the structure of the instrument and its intrinsic features are related to the requirements coming from the RSE. The main requirement is the capability of measuring accelerations as small as $10^{-8} m/s^2$ over a wide band (3×10^{-5} – $10^{-1}\,Hz$) including the expected perturbations frequency content. The measurement error budget includes the foreseen sources of error, such as intrinsic noise of the instrument, spurious signals due to inertial forces and gravity gradients, thermal effects, on-board micro-vibrations, various types of calibrations performed. The calibration procedures in particular are very important. It is worth to notice that, due to its working (three one-dimensional sensing elements arranged in order to measure the three components of the acceleration vector acting on a reference point, each of them basically an harmonic oscillator), the instrument is capable of an internal calibration; known acceleration signals can be given to the sensing elements, thereby enabling the calibration of the so-called transduction factors.

3.3.2.4 Superconducting gradiometers

Among the possible instruments, a very interesting type is constituted by the superconducting gravity gradiometers [163][164][165][143]. Such a kind of sensors capitalise on the property of superconductors to enhance the gradiometer performance in terms of sensitivity and stability.
The pioneering work on the development of Superconducting Gravity Gradiometers (SGG) was carried out by the group of H.J. Paik at the University of Maryland and by the group of F. van Kann at the University of Western Australia in the 1980s.
At the University of Maryland, several models of SGG were built with the support of NASA and other funding agencies [163][164][165][171]; this gradiometers were intended for space research in the field of geodesy and fundamental science [142]. These first versions were constituted by couples of accelerometers with mechanically suspended test masses to realise single and three-axis diagonal-component SGG.
The basic element of Paik gradiometer is constituted by a couple of accelerometers, each one including a superconducting proof mass held by a mechanical spring within a box [143][163]. The principle of operation for such a superconducting accelerometer is depicted in Figure 3-24. A circuit including a sensing coil is placed close to a superconducting proof mass. When the box undergoes to an acceleration, the proof-mass responds with a relative displacement with respect to the coil. Because of the Meissner effect, this motion induces a modulation of the coil inductance. Since the magnetic flux through any circuit with a superconducting coil needs to be constant, a variation of inductance of the sensing coil due to the displacement introduces a corresponding modulation of the current flow into the circuit. A SQUID amplifier (Superconducting Quantum Interference Device), connected to the superconducting loop, detects such a variation and is used as dc current-to-voltage power amplifier to produce an output signal [143][163][167].
In the first gradiometer, two superconducting accelerometers of this type, each with a proof mass, a suspension structure and sensing coils, are placed close to each other and the related circuits are linked together in such a way that the SQUID output provides the difference between the displacement of the two proof masses and hence the difference of gravitational acceleration at their position. A folded cantilever suspension constitutes the spring with a linear elastic constant, that is weak in the motion direction and relatively rigid in other directions [163]. The suspension is derived from a single piece of niobium (Nb) with the aim of obtaining mechanical precision and a high quality factor of resonance.
Two accelerometers of this type are mounted on the opposite sides of a high precision titanium-made cube (Ti) on a baseline of $16\ cm$ to realise a single-axis gravity gradiometer.

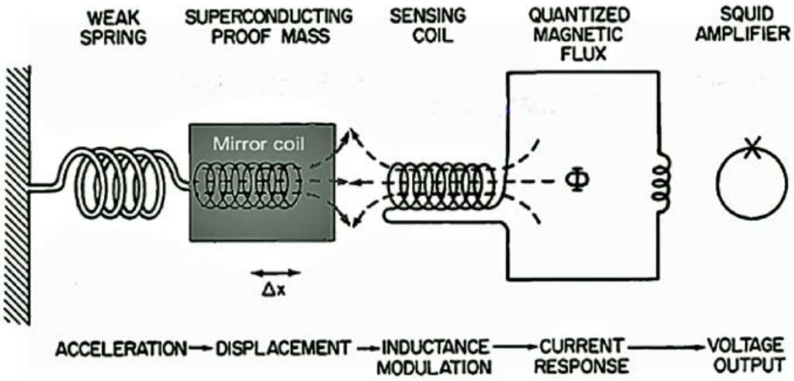

Figure 3-24: Scheme of the superconducting accelerometer principle developed at University of Maryland (from [143])

Figure 3-25 depicts a view of this configuration. The SGG is suspended in such a way to have a diagonal of the cube aligned to the vertical; with this approach, each gradiometer axis is equally biased with respect to the Earth's gravitational acceleration ("umbrella angle"). Moreover, this configuration also allows the interchange of the gradiometer axes by a $120°$ rotation about the vertical.
At last, the superconducting gradiometer is suspended by a Fiberglas rod inside a cryogenic vacuum space at 4 K. The instrument showed a performance level of about $1\ E/\sqrt{Hz}$ [163].
The intrinsic noise of the instrument derives from the Brownian noise of the proof masses, depending on the temperature, and from the intrinsic noise of the amplifier used to increase the signal level. By using cryogenic temperatures the thermal noise is maintained very low, whereas by using superconducting technology the signal coupling and amplification are made more efficient.
Such a SSG was used to carry out a preliminary test of the Newton's inverse-square law of gravitation [164]. Indeed, the sensing axis of the gradiometer was rotated into three orthogonal directions by rotating the whole experimental set-up by 120° around the vertical axis while the gradiometer was suspended in the umbrella angle; the projection of the three diagonal components of the gravity gradient were measured with this approach. At last the outputs were summed in order to obtain the trace of tensor, whose value, constrained by the Poisson equation, would vanish. Such a condition was verified within the experimental uncertainty [163].
An improved version of this SGG was developed combining three single-axis superconducting gravity gradiometers [166]. The three-axis gravity gradiometer was realised by mounting six accelerometers on the faces of a precision cube. The accelerometers on two opposite faces of the cube form one of three in-line gradiometers. The same configuration of previous SGG was adopted, maintaining each gradiometer tilted with respect to the vertical.
This experimental set-up was used to set the best limit of Newton's inverse-square law at $1\ m$, at the level of two parts in 10^4 [166][173].
A further improvement of this first SGG was developed [165] by combining a softer mechanical spring with magnetic levitation. Figure 3-26 shows the in-line SGG assembled at the University of Maryland, including three couples of accelerometers.
The instrument includes nine single-axis accelerometers. Three couples of linear accelerometers are mounted on the faces of a precisely machined titanium alloy (Ti) cube with the sensitive axes perpendicular to the faces of the cube. The proof masses of accelerometers on opposing faces are coupled together through superconducting circuits to

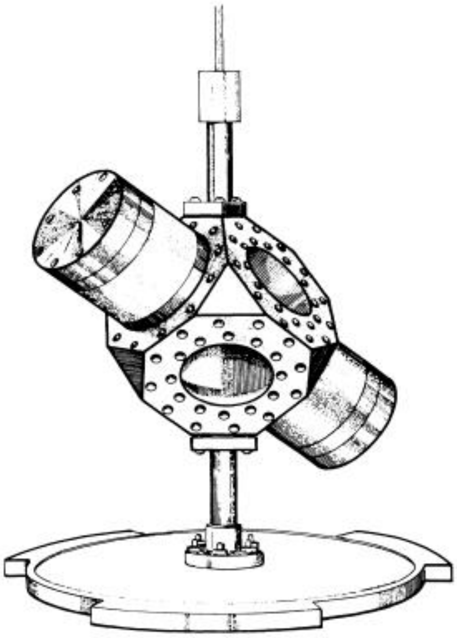

Figure 3-25: View of the single axis gravity gradiometer developed by the group of Paik at University of Maryland ([163])

realise three orthogonal gradiometers. A $19\,cm$ baseline divides each couple of accelerometers and the total mass of the SGG is $30\,kg$. Moreover, the SGG is cooled with liquid helium in a cryostat [165]. The operating principle is the same of the single-axis gradiometer previously described, however the spring is obtained combining mechanical flexures with magnetic levitation. In addition, in this SGG version, three superconducting angular accelerometers are mounted with their sensitive axes aligned with the three gradiometer axes.

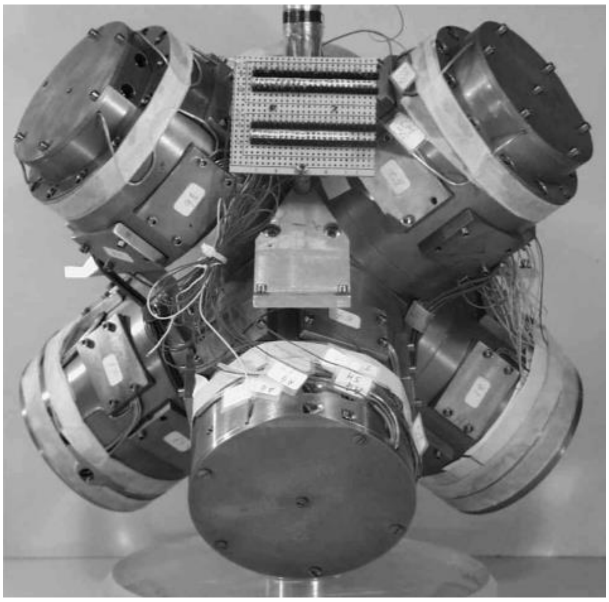

Figure 3-26: SGG assembled at University of Maryland, comprising six linear accelerometers (from [177])

With this three-axis configuration, the differential linear accelerations provide the three diagonal components of the gravity gradient tensor. Any platform linear acceleration is detected as common acceleration of the gradiometer proof masses. These signals, along

with the angular acceleration, allow correction of dynamic errors in all six degrees of freedom.
Such a three-axis diagonal component SGG demonstrated to reach a gradient sensitivity of $0.02\ E/\sqrt{Hz}$ over a baseline of $20\ cm$ [165].

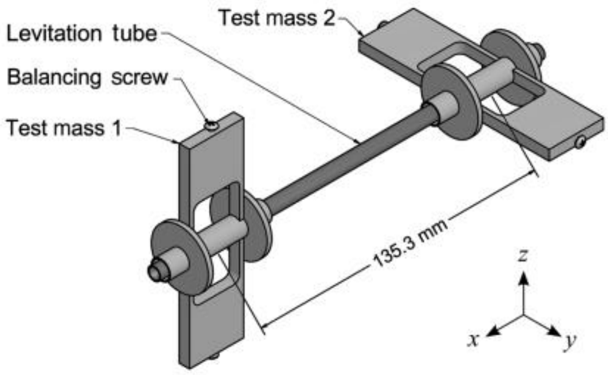

Figure 3-27: Perspective view of the SGG based on levitated test masses [173]

An improvement by 2 to 3 order of magnitudes in sensitivity of such a configuration could be achieved by replacing the relatively stiff mechanical spring of the proof mass with a contactless "magnetic" spring based just on magnetic levitation. Indeed, the group of Griggs and colleagues at the University of Maryland [173] started the development of a single-axis SGG based on levitated test masses since 2012 with the support of NASA's Earth Science Division. A prototype of SGG has been designed, built and tested to measure a diagonal and an off-diagonal component of gravity gradient (two components SGG) [173].
Figure 3-27 depicts a schematic view of the instrument. Two Niobium (Nb) proof masses are levitated by a current along a single horizontal Nb tube. Each proof mass has two wings 180° apart, which provide a moment arm about the tube axis (x). A balancing screw is provided at the end of each wing to adjust the center-of-mass position and bring it to the rotation axis. The current flowing along the tube provides stiff suspension in the radial directions (y and z) but leaves the test masses to translate freely along the x axis and rotate freely about the same axis.
The translational motion (diagonal component) is detected by using pancake-shaped Nb coils placed near the disk faces of the test masses, whereas the rotational motion (off-diagonal component) is detected by using pancake-shaped coils located near the rectangular surfaces of the test masses [173].

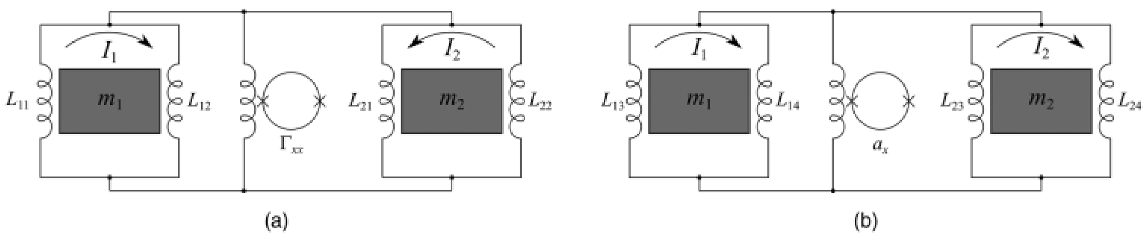

Figure 3-28: Sensing circuit of the SGG aimed at differencing (gravity gradient a)) and summing (linear acceleration b)) accelerometer signals [173]

Figure 3-28 depicts the sensing circuit of the diagonal component. Persistent currents I_1 and I_2 are generated into the superconducting circuits formed by the coils $L_{11}, L_{12}, L_{21}, L_{22}$. The acceleration signals sensed by the two test masses m_1 and m_2 are subtracted to obtain the gravity gradient Γ_{xx} by means of a SQUID, whereas with a change of direction for I_2 the acceleration signlas are added in the SQUID to obtain the common linear acceleration a_x. The ratio I_1/I_2, ideally one for perfect masses and coils, is calibrated to maximise the rejection ratio for the common mode output (CMRR).

This design gives a potential sensitivity of $1.4\ 10^{-4} E/\sqrt{Hz}$ in the frequency band $5\ 10^{-2}$ to $1\ Hz$ and better than $2\ 10^{-5} E/\sqrt{Hz}$ in the measurement band between $0.1\ Hz$ and $10^{-3} Hz$, over a baseline of $10\ cm$. Such sensitivities are achieved by a stable cooling at temperature lower than $6\ K$.

The objective of the group is to construct a full-tensor SGG through the assembly of six identical accelerometers with levitated test masses to be employed for Earth and planetary missions. Figure 3-29 depicts a partially exploded general view of the complete SGG assembly. Accelerometers will be mounted on a Titanium mounting cube for a total weight of the SGG assembly of $12\ kg$ and will fit within a sphere of $22\ cm$ in diameter [173].

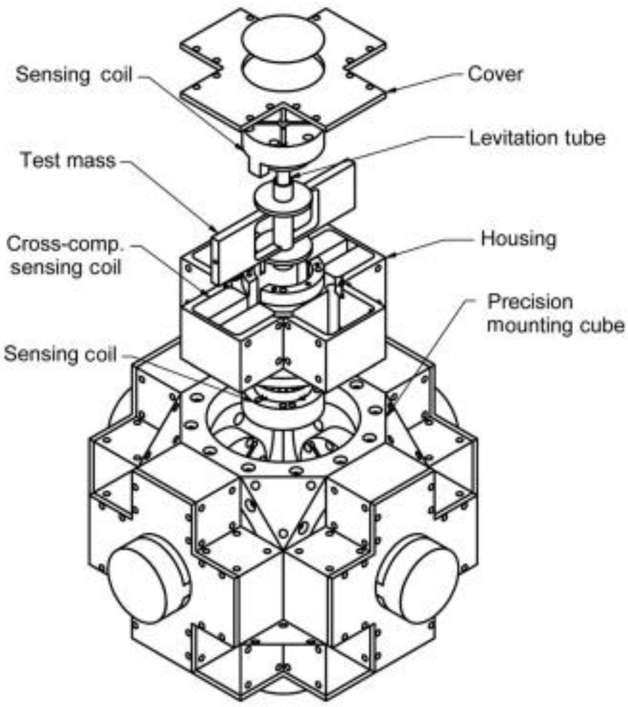

Figure 3-29: Partial exploded view of the planned full-tensor SGG showing main components ([173])

For the Earth and planetary science, it is envisaged by the group the development of a compact SGG with test masses of $100\ g$ each one and a baseline of $13.5\ cm$ that could achieve a noise level of $1.4\ 10^{-4} E/\sqrt{Hz}$ on the diagonal components and $3.5\ 10^{-4} E/\sqrt{Hz}$ for the off-diagonal, over the frequency range $10^{-3} - 5\ 10^{-2}\ Hz$. According to [174], a cryogenic superconducting gravity gradiometer of this kind could be employed in the investigation of Mars gravity field, allowing to reach a degree $l \sim 220$ from a single spacecraft in a 100 days mission. Moreover, it would enable the mapping of the time-variable gravity on a regional scale ($\sim 400\ km$).

3.3.2.5 Atom-interferometry-based gradiometers

Advancements in laser cooling and manipulation of atoms allowed the development of a new class of gravity sensors: quantum gravity gradiometers based on atom interferometry [175][177][143]. The technologic approach of this new gravity measurements is extremely different from the classical satellite tracking. Basically, in these instruments atoms are used as drag-free test masses. At the same time, the quantum wave-particle nature of atoms is capitalised on to carry out interferometric measurements of local accelerations. Therefore, it is possible to realise an interferometer based on atom-waves, similarly as happens with laser interferometers. Because of the finite mass of the atom, matter-wave interferometers are intrinsically sensitive to the gravity. The breakthrough in making affordable and easier the development of these atom-based interferometers has been the advancement in laser cooling of atoms, atom optics and manipulation of atoms [176][177].

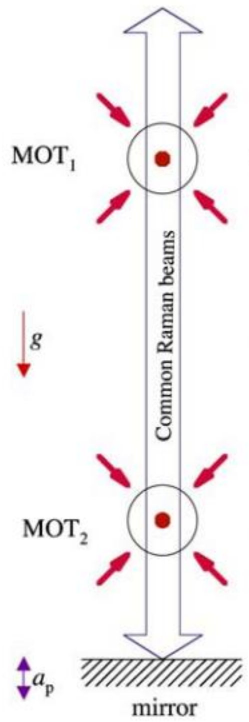

Figure 3-30: Two atom-interferometer accelerometers separated by a certain baseline, to illustrate the gravity gradiometry geometry. MOT_1 and MOT_2 are the magneto-optical traps which produce (red dots) trapped atom clouds ([177])

Caesium atoms are collected and cooled by lasers in a small cloud in a magneto-optic trap (MOT). The MOT is based on a three-couples of counter-propagating laser beams along three orthogonal axes centered on a non-uniform magnetic field. After collection, atoms are further cooled by lasers, to reduce their speed at few cm/s. Cold atoms are then vertically launched creating a so-called “atomic fountain” and atom interferometry is executed in the following free-fall of atoms.

The differential phase shift is related to the gravitational acceleration difference in the two locations.

A study by the Chinese academy of Sciences aims at the deployment of a Gravity Gradiometry mission at Venus in order to reconstruct its gravitational filed beyond the current knowledge by using an Atom-Interferometer Gravity Gradiometer (AIGG) [179].

The spacecraft would host a AIGG constituted by three couples of atom-interferometer accelerometers in an orthogonal arrangement. The principle of operation is as follows. An ensemble of Cesium atoms are cooled at cryogenic temperatures. For ultra-low temperatures, the speed of atoms is reduced to about 1 cm/s. The Cesium atoms with a slow movement are then placed in the gravitational field of Venus in free-fall motion. Through a laser system the gravitational acceleration is measured by observing the phase variation.

3.3.2.6 MEMS-based gradiometers

The technology of MEMS (Micro-machined Electro-Mechanical Systems) has been intensively studied since 1990s [143][181]. It is based on the trend in sensor technologies towards a progressive miniaturisation of components at micrometer and lower sizes (nano-technology is the term often used to describe this trend). MEMS is a process technology used to create integrated devices or systems making use of electrical and mechanical components. Such devices have the capability to sense, control and actuate on the micro-scale and to produce effects on the macro-scale [143]. This possibility is allowed because of manufacturing technology such as microelectronics, i.e. the production of electronic circuits on silicon chips, and micromachining, i.e. the techniques used to produce structures and moving parts of microdevices [182]. Actually, MEMS devices have an interdisciplinary nature since expertise in their design, engineering and manufacturing is derived from different areas, including integrated circuit fabrication technology, materials science, mechanical and electrical engineering, chemistry and chemical engineering, as well as fluid engineering, optics, instrumentation and packaging [181].
The potentiality of MEMS is evidenced by the several fields of application. Nowadays, their use is widespread in many types of applications, including automotive (e.g. pressure and temperature sensors, air bag systems), telecommunications (e.g. mobile applications, smartphone), medical and electronic devices (health monitoring sensors, vibration monitoring, microvalves, biosensors, inkjet printer heads, computer disk drive read/write heads), defence applications [143][181].

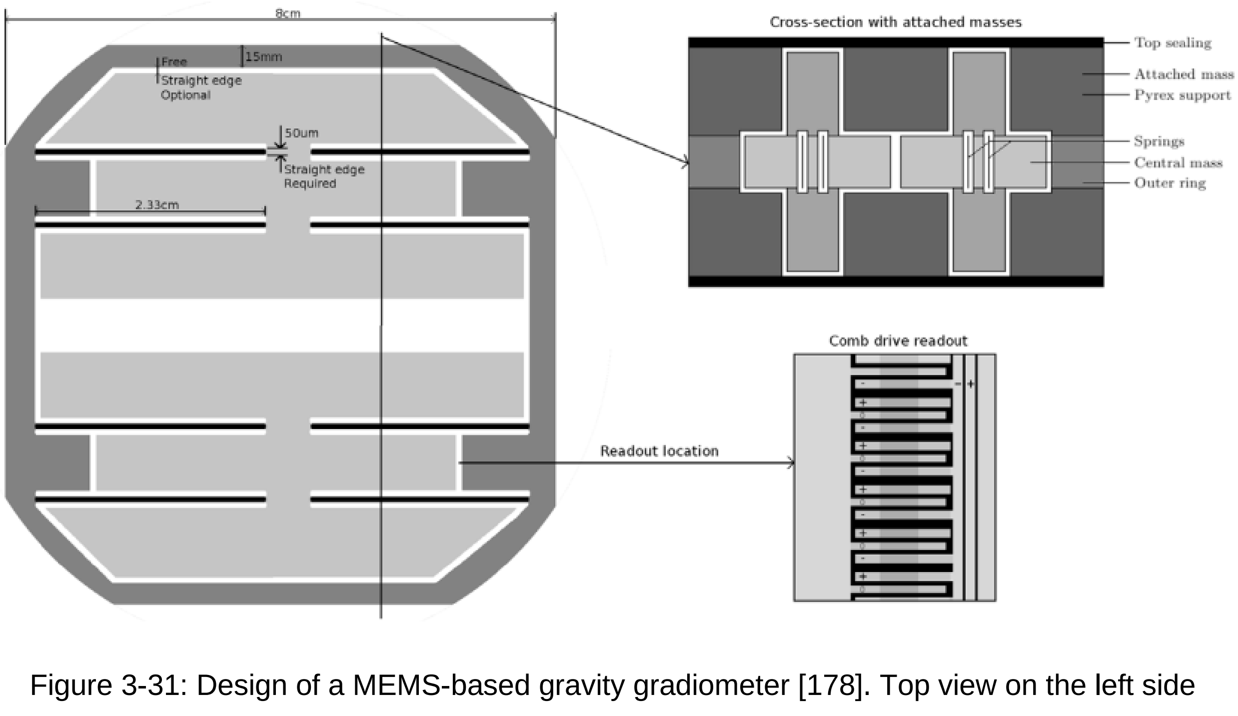

Figure 3-31: Design of a MEMS-based gravity gradiometer [178]. Top view on the left side

First researches to date on MEMS-based gravity gradiometers, potentially to be used in future space missions, began at the University of Twente in the Netherlands [180]. They studied a micro-gradiometer which would have in principle a level noise of $0.1 - 1\ E/\sqrt{Hz}$ and a weight below 1 kg. In particular, range into which design parameters of such a MEMS-based gradiometer should fall was investigated by the research group. Apart the natural constraint on the (limited) size and mass, analysis was focused on temperature, spring constant and quality factor. They found out that to have a bandwith within the range $10^{-3} - 1\ Hz$ for the measurements, a device with resonance frequency higher than $1\ Hz$ would be necessary and a low spring constant would needs, at least in the order of $1\ \ N/m$. However, this makes very difficult to manufacture and to test a weak constant spring. Simulations proved that such a spring would not be strong enough to tolerate gravity on-ground and hence additive masses (gold) should be added. Concerning the other parameters, a quality factor of 10^5 was assumed to reach a good sensitivity and a temperature of $77\ K$ was considered easily achievable in space. A conceptual design based on a whole wafer was developed and it is shown in Figure 3-32.
Concerning the read-out system, Flokstra group employs a capacitive design to sense the displacement of the sensing mass.
More recently, a group of the Optical and Semiconductor Devices from Imperial College of London carried out researches on a MEMS-based gravity gradiometer with a torsional spring [183], capable of operating over a range from 0 to 1 g, focusing its research on the proof-mass suspension system. Design, fabrication and characterisation of a seesaw-lever suspension for a silicon gravity-gradient sensor was carried out. Figure 3-33 shows off a schematic of the gradiometer suspension developed.

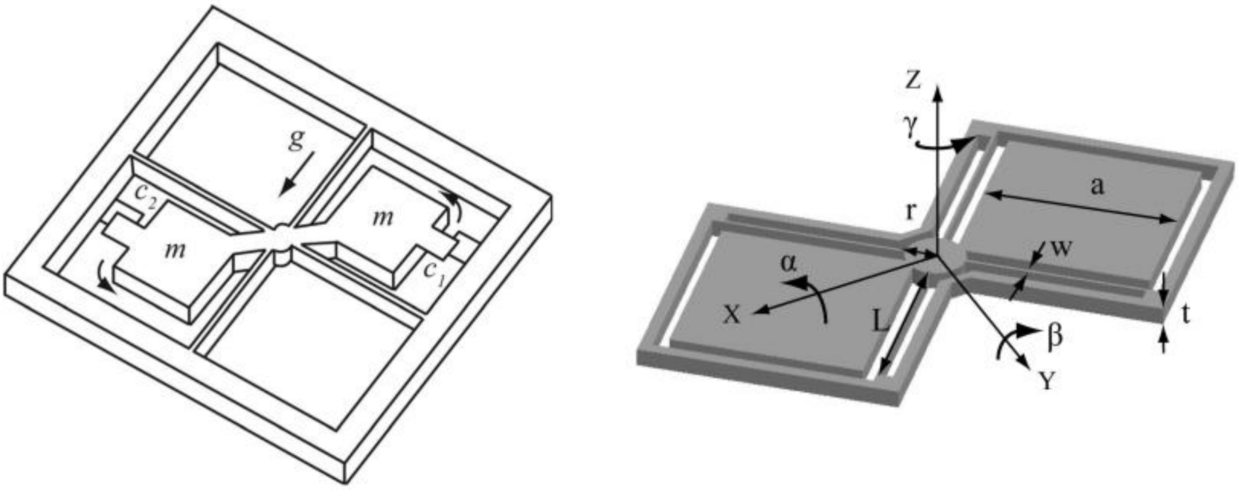

Figure 3-33: schematic of the gradiometer suspension described in the text (from [178])

Two square proof masses with a side length of *a* are linked to a central pivot with radius *r* and are surrounded by four flexural arms with length *L* and width *w,* creating a gap between frame and pivot. A gravity gradient between the proof masses induces a torque around the pivot aligned to Z axis balanced by the suspension force and the induced rotation can be sensed through a capacitive transducer. A gradiometer prototype with a proof-mass side-length of about 15 mm, 0.55 g in weight, connected to a 1 mm pivot radius and suspended by four 26 µm wide and 14 m long was built (shown in Figure 3-34). Such a system proved a fundamental frequency of 6.6 Hz for in-plane rotation and a good rejection of all cross-axis modes, offering a rejection factor spurious mode/fundamental frequency of about 14. The suspension was manufactured using through-wafer deep reactive-ion etching, a technique derived from silicon micromachining [183][184]. On the basis of analysis carried out, it was highlighted that the limit to the total noise of such a system, independently on the adopted configuration, is represented by the thermal noise. Actually, a MEMS-based gravity gradiometer based on this kind of suspension would reach a total noise floor around $10\ E/\sqrt{Hz}$, based on some assumptions on the Q achievable in vacuum (10^5) , on the negligible electronic noise assuming an electronics for the transducer inherited from NASA InSigh seismometer.

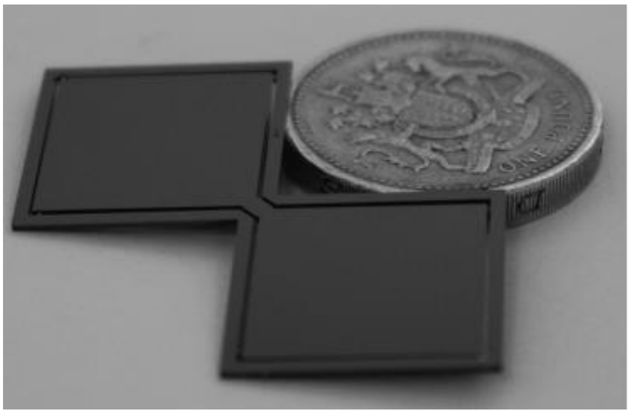

Figure 3-34: prototype of the MEMS gradiometer developed by Liu et al. A British pound coin is shown for size comparison.

At last, the MEMS technology seems very promising for gravity gradiometer theoretically, since it offers important advantages such as reduced masses and volumes. However, the current maturity is far from the needs of the expected scientific challenges.

3.3.3 Review results

Analysing the instruments review of section 3.3.2, some conclusions can be drawn. At first, just one space gradiometer, GRADIO, has been developed and flight-proved till now within the GOCE mission. Its outstanding performance were achieved because of the high-performance accelerometers, used as basic elements of the gradiometer, and of the state-of-the-art subsystems built around it. Indeed, such a mission is very peculiar since there is no neat division between spacecraft and payload: all the system works as one whole gravity instrument.
All the other systems, as reported in Table 3-1, have been developed just as prototypes, at test level or are simply under study. They employ different sensing technologies (mechanical superconducting, magnetically levitated, MEMS-type) to get the gravity gradient but the principle of measurement is led back to the two basic approaches: differential accelerometry and torsion balance.
Moreover, the achievable performance is often potential and have been tested in a limited approach, verifying just some elements. The most complete system is represented by the Paik group’s gradiometer, both in the superconducting mechanical and levitated version.

3.4 Scientific requirements vs Instruments state of the art

Analysis carried out in section 2.5 identified as output some targets potentially interesting to be studied. On the basis of the scientific community needs and on the gravity field knowledge state of the art, planetary bodies of interest have been identified in Mars, Venus, Ganymede, Europa and Titan.

As explained in section 3.3, gravity gradiometry is inherently more sensitive to the medium-high degrees of the gravity field. This is because the differentiation operation of the gravity acceleration, carried out to obtain the gravity gradient, allows to highlight the small features in the signal. Consequently, the small-scale elements in the gravity field, identified by the larger degrees l, are intrinsically enhanced when the observable is the gravity gradient. This characteristic is pointed out in the multiplicative factor $(l+1)(l+2)$ in front of the gravity gradient expression, that fosters and increases the power contents for higher degrees of the field, considering the same conditions of field strength and altitude. Moreover, this multiplier allows to counteract in part the attenuation factor $(R/r)^{l+3}$ due to the altitude as well. This is one of the reasons that makes satellite gradiometry attractive for the reconstruction of the gravity field with high accuracy and resolution with respect to other techniques.

Taking into account the inherent enhanced sensitivity of gravity gradiometry towards medium-high degrees and the result of gravity field survey for the Solar System bodies as per Table 2-8, it derives that the most interesting science objectives suitable for a gradiometry mission would be Mars and Venus planets.

A preliminary evaluation of the expected values of gravity gradients was performed for these bodies, including at this stage as comparison also the other targets. Table 3-3 shows off the results.

In general, the contribution [103] as expected average (RMS) signal σ_{lm} (root mean square of power per degree l), at a particular l, with for $l \gg 1$ generated by a body (terrestrial body) along the radial direction (rr), can be computed by the following equations (by using Kaula rule), for the gravitational acceleration and the gravitational gradient (the radial one), respectively (see also section 2.2.2 and equation (2-7) and (2-8), [17]):

$$\sigma_{lm}(\Delta g_{zz}) = \left(\frac{GM}{r^2}\right)\left(\frac{R}{r}\right)^l (l+1)\ \frac{k}{l^2}$$

$$\sigma_{lm}(\Gamma_{zz}) = \left(\frac{GM}{r^3}\right)\left(\frac{R}{r}\right)^l (l+1)(l+2)\ \frac{k}{l^2}$$

where $r = R + h$, with R body radius and h height of the spacecraft with respect to the planet surface, M mass of body and k is a constant depending on the considered body.

Moreover, by using the approximation suggested by [113] and [125], we can compute the power of the various gradients as the following:

$$\sigma_{lm}^2(\Gamma_{XY}) \approx \frac{1}{8}\sigma_{lm}^2(\Gamma_{ZZ})$$
$$\sigma_{lm}^2(\Gamma_{XX}) \approx \sigma_{lm}^2(\Gamma_{YY}) \approx \frac{3}{8}\sigma_{lm}^2(\Gamma_{ZZ})$$
$$\sigma_{lm}^2(\Gamma_{XZ}) \approx \sigma_{lm}^2(\Gamma_{YZ}) \approx \frac{1}{2}\sigma_{lm}^2(\Gamma_{ZZ})$$

where Γ_{ij} refers to the ij component amplitude of the gravity gradient for the degree l.

These estimates, assuming a spacecraft orbiting the chosen body at a certain altitude (h), a maximum field degree investigated (l) and a corresponding half-wavelength resolution (Δs, evaluated by $\Delta s = \pi R / l$ where R is the mean radius of the planet), allow to compute the radial gravitational acceleration $\boldsymbol{a_r}$ at h and the radial gravity gradient Γ_{rr} at the same altitude (in s^{-2} and Eotvos where $1\,E = 10^{-9}\ m/s^2$) through the Kaula's rule; the Kaula constant applied (k) is also specified. In Table 3-3 all these elements are reported.

As explained in section 2.2.2, the constant k in the Kaula's rule has a value depending upon the planet: $\mathrm{k} \cong 9\ 10^{-6}$ for Earth [53], $\mathrm{k} \cong 1.2\ 10^{-5}$ for Venus [64], $\mathrm{k} \cong\ 8.5\ 10^{-5}$ for Mars [80], $\mathrm{k} \cong 36\ 10^{-4}$ for the Moon [131], $k \cong 4\ 10^{-5}$ for Mercury [54].

Table 3-3 Estimates of gravity gradient (radial component) and radial acceleration for several planetary bodies. For each body, different altitudes h and degrees l are considered, with the corresponding spatial resolutions $\Delta \boldsymbol{s}$ (half-wavelength)

Venus	**h (km)**	**l_{max}**	**Δs (km)**	**a_r (m/s^2)**	**Γ_{rr} (m/s^2 over m)**	**Γ_{rr} (E = 10^{-9} m/s^2)**	**Notes**
	200	100	190	3.90e-8	6.36e-13	6.36e-4	k = 1.2e-5, [64]
	200	150	127	5.10e-9	1.24e-13	1.24e-4	-
	200	200	95	7.51e-10	2.43e-14	2.43e-5	-
	200	250	76	1.18e-10	4.76e-15	4.76e-6	-
	300	100	190	7.73e-9	1.24e-13	1.24e-4	-
	300	150	127	4.57e-10	1.10e-14	1.10e-5	-
	300	200	95	3.04e-11	9.68e-16	9.68e-7	-
	300	250	76	2.16e-12	8.59e-17	8.59e-8	-
	350	100	190	3.47e-9	5.53e-14	5.53e-5	
	350	150	127	1.39e-10	3.29e-15	3.29e-6	
	350	200	95	6.24e-12	1.97e-16	1.97e-7	-
	350	250	76	3.00e-13	1.18e-17	1.18e-8	-
Mars	200	100	107	9.24e-9	2.63e-13	2.63e-4	k = 8.5 10^{-5}, [80]
	200	150	71	3.50e-10	1.48e-14	1.48e-5	-
	200	200	53	1.49e-11	8.38e-16	8.38e-7	-
	200	250	43	6.78e-13	4.76e-17	4.76e-8	-
	200	300	36	3.21e-14	2.70e-18	2.70e-9	-
	300	100	107	5.61e-10	1.55e-14	1.55e-5	
	300	150	71	5.37e-12	2.21e-16	2.21e-7	-
	300	200	53	5.79e-14	3.17e-18	3.17e-9	-
	300	250	43	6.67e-16	4.56e-20	4.56e-11	-
	300	300	36	8.00e-18	6.55e-22	6.55e-13	-
Ganymede	200	30	276	1.98e-6	1.37e-11	1.37e-2	k = 4.2 10^{-4}
	200	50	165	2.71e-7	4.98e-12	4.98e-3	-
	200	100	83	3.44e-9	1.24e-13	1.24e-4	-
	300	30	276	6.52e-7	7.12e-12	7.12e-3	-
	300	50	165	4.46e-8	7.91e-13	7.91e-4	-
	300	100	83	9.98e-11	3.47e-15	3.47e-6	-
	400	30	276	2.23e-7	2.35e-12	2.35e-3	-
	400	50	165	7.00e-8	1.34e-13	1.34e-4	-
	400	100	83	3.26e-12	1.10e-16	1.10e-7	-
	500	30	276	7.90e-8	8.07e-13	8.07e-4	-
	500	50	165	1.44e-9	2.39e-14	2.39e-5	-
	500	100	83	1.19e-13	3.87e-18	3.87e-9	-
Titan	200	30	270	2.00e-6	2.31e-11	2.31e-2	k = 4.7 10^{-4}
	200	50	162	2.66e-7	4.98e-12	4.98e-3	-
	200	100	81	3.12e-9	1.15e-13	1.15e-4	-
	300	30	270	6.45e-7	7.18e-12	7.18e-3	-
	300	50	162	4.21e-8	7.62e-13	7.62e-4	-
	300	100	81	8.44e-11	3.00e-15	3.00e-6	-
	400	30	270	2.16e-7	2.32e-12	2.32e-3	-

	400	50	162	7.12e-9	1.24e-13	1.24e-4	-
	400	100	81	2.58e-12	8.85e-17	8.85e-8	-
Europa	200	30	163	4.78e-7	8.68e-12	8.68e-3	k = 5 10^{-4}
	200	50	98	2.54e-8	7.50e-13	7.50e-4	-
	200	100	49	3.00e-11	1.76e-15	1.76e-6	-
	300	30	163	8.16e-8	1.40e-12	1.40e-3	-
	300	50	98	1.44e-9	4.01e-14	4.01e-5	
	300	100	49	1.10e-13	5.94e-18	5.94e-9	
	400	30	163	1.53e-8	2.49e-13	2.49e-4	-
	400	50	98	9.45e-11	2.51e-15	2.51e-6	
	400	100	49	5.20e-16	2.71e-20	2.71e-11	

In literature, the change of Kaula's constant for a body follows a scaling law, depending on the relative gravity of each body in squared manner (or linear, sometimes [107][115]):

$$\frac{k_{planet}}{k_{Earth}} = \left(\frac{g_{Earth}}{g_{planet}}\right)^2 \tag{3-22}$$

where g are the gravitational accelerations of the bodies. The Kaula constant for bodies in Table 3-3 has been recovered from literature whenever available (list previous reported and for which references has been provided). Otherwise its value has been derived with the above reported approach.

Some assumptions have been carried out to fill in Table 3-3. The planetary bodies reported have been identified as being the most interesting from the point of view of the scientific community to improve their current understanding (section 2.5).

The chosen altitudes are derived from typical values used in past and future missions (if any) to the corresponding target. Hence, they constitute a trade-off between the mission needs (e.g. attitude control, drag compensation, radiation damage, etc.) and objectives (gravity field measure, surface imaging and spectrometry, topography, etc.) versus the planetary environment characteristics (atmosphere, radiation belts, magnetic field, solar irradiance and so on). For instance, all past Venus orbiter missions have been put on highly elliptical orbits, affected mainly by the large amount of fuel required to circularise the orbit [97]. However, improved gravity models and high-resolution global topography benefit greatly from circular orbits. Aerobraking techniques, where successive orbits in the planet's deep atmosphere are used to slow spacecrafts and make circular orbits, were applied in the past (Magellan, the first one). Spacecrafts devoted to Mars (especially) and Venus have been employed such a technique [97].

The maximum degree l_{max} has been chosen on the basis of the current gravity knowledge, as derived from section 2.4.

A more interesting evaluation of Table 3-3 is possible through Figure 3-35, Figure 3-36.

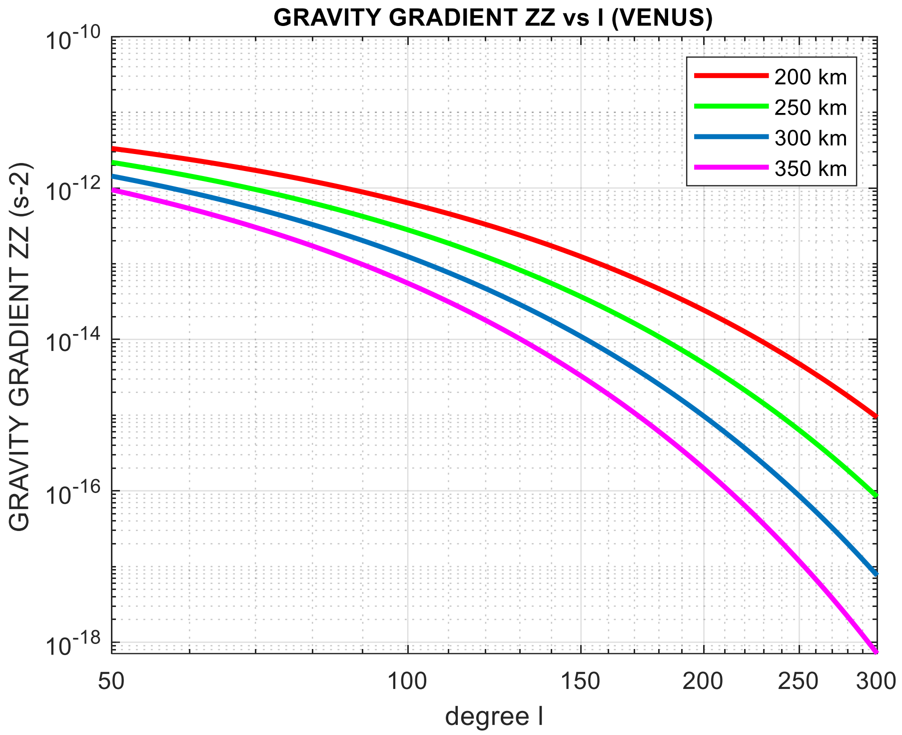

Figure 3-35: Estimate of Venus Γ_{zz} gravity gradient versus the degree l for different orbital altitudes

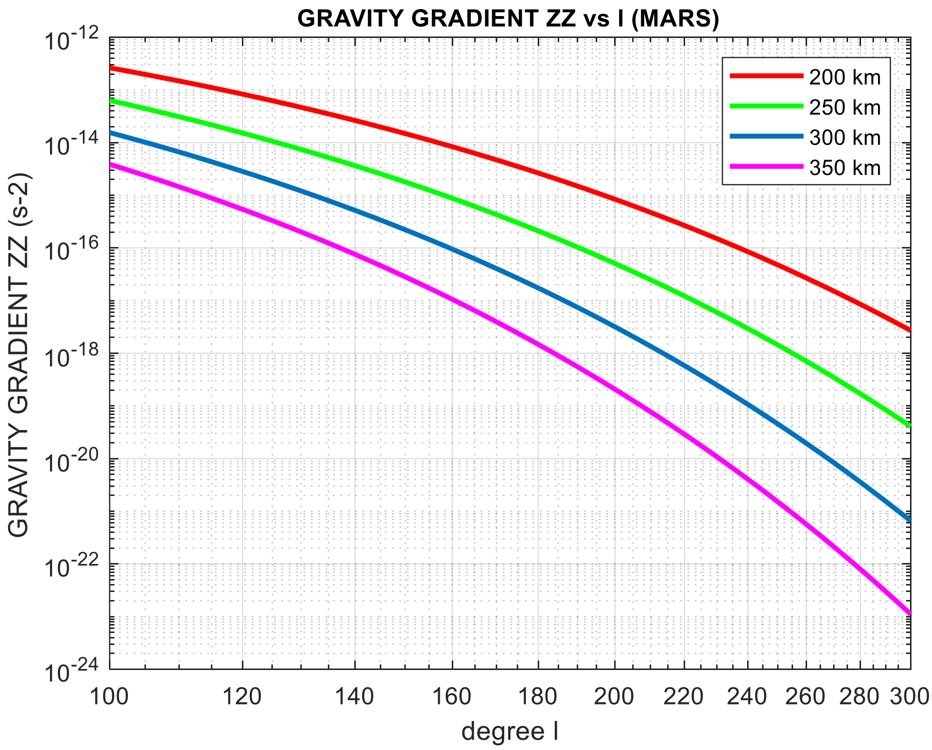

Figure 3-36: Estimate of Mars Γ_{zz} gravity gradient versus the degree l for different orbital altitudes

The rough estimates of the radial gravity gradient Γ_{rr} show off that the measure of the gravity gradients for planetary bodies is not an easy task. Indeed, the signal to be measured assumes at least a value around $10^{-4}\ E$. For instance, in case of a spacecraft around Venus,

at an altitude of $200\ km$, the minimum value to be measured by a gravity gradiometer would be around $10^{-4}\ E$ ($6.36\ 10^{-4}E$) in order to retrieve the radial gradient at a degree $l = 100$. Higher degrees, $l\ =\ 150 - 200$, require signal levels around $1\ 10^{-4}/2\ 10^{-5}E$.
In case of a spacecraft around Mars, the minimum value to be measured by a gravity gradiometer in order to improve the current gravity field knowledge ($l\ \geq\ 100$) would be around $10^{-4}\ E$ ($2.63\ 10^{-4}$), for an orbit at $200\ km$ of altitude and the retrieval of degrees till to $l\ =\ 100$. Higher degrees, till to $l\ =\ 150/250$, need signal levels at $10^{-5}/10^{-7}E$ ($1.48\ 10^{-5}/8.38\ 10^{-7}$)
In another example, for instance Europa, the hypothesis of a spacecraft orbiting directly Europa is not an easy accomplishment, because the radiation environment around it would make very hard the survival of any probe. Indeed, Europa Clipper, the NASA's probe currently being realised, aims at exploring the Jupiter's moon through an eccentric orbit around Jupiter, performing just repeated close flybys (~ 45) because of the strong radiations. However, in order to evaluate the performance to be achieved by a gravity gradiometer in such a hypothetic case a radiation-tolerant spacecraft with a limited lifetime could be envisaged.
Moreover, such considerations are optimistic considering that the computed values were carried out for the radial gradient (Γ_{zz}) that typically produces the stronger signal among the gravity gradient components.
However, these preliminary results need to be compared to the current state of the art of gradiometers, as carried out in section 3.3.2.
A comparison between the rough values estimated for different bodies in the Solar System (Table 3-3) and the performance achieved and theoretically achievable (Table 3-1) has been carried out. Signal estimates employed in the comparison table have been chosen among the more favourable cases. It is noticeable that the current and planned gradiometers do not achieve yet the needed accuracy to improve the current knowledge of the gravity field of these bodies. A comparison is shown in Table 3-4.
Indeed, the best achieved performance are obviously by the GOCE's gradiometer that reached $\sim 10^{-2}\ E$. Named GRADIO, this is the first space gradiometer have been developed and flight-proved till now. This was possible by using high-performance accelerometers and state-of-the-art subsystems from the thermal and mechanical point of view. Moreover, the spacecraft was built around the instrument in order to maximise its performance.
All the other gradiometers have been developed just as groundborne instruments and prototypes, at test level or are simply under study (TRL 2-5). The sensing technologies employed are widespread: *mechanical superconducting, superconducting magnetically levitated, atom-interferometry, MEMS-type.*
An important element to be highlighted is that here the state of the art in the gravity field knowledge has been assumed as the degree at which the signal-to-noise ratio is equals to the unit, corresponding to the maximum achievable resolution averaged over the planet. Considering the intrinsic fostering of small/medium wavelengths of the gravitational field by using gradiometry, this implies that lower degrees could be measured as well if the measure would improve that ratio. Indeed, gradiometry can improve the gravity field measurements over degrees higher than the current knowledge but also over lower degrees if it is increased the signal-to-noise ratio.

Table 3-4 Comparison of instruments performance versus signal estimates of planets gravity field

Instrument		Body				
		Venus	Mars	Ganymede	Titan	Europa
	Requirement (E)	$6\ 10^{-4}$	$3\ 10^{-4}$	$1\ 10^{-2}$	$2\ 10^{-2}$	$9\ 10^{-3}$
	Performance ($E/\sqrt{Hz}$)					
GRADIO/ GOCE	$2\ 10^{-2}$			X	X	
SGG/sc mech	$10^{-2} - 1$					
SGG/sc lev	$10^{-4} / 10^{-5}$ *(potential)*	X	X	X	X	X
Seesaw-suspension	10					
Absolute GG	1-4					
QGG/AIGG	30, 10^{-3} (potential)					
RGG	1-5					
GGI	2-30					
Draper	1					
ARKeX	2					
Gedex	1					

Another issue to be considered is which components of the gradient should be measured. Indeed, the gravity gradient tensor is constituted by five independent components and, ideally, the measure of all of them would be needed to reconstruct the overall gravity field. However, there is no neat correspondence between the measured components and the quality of the reconstructed field because several parameters intervene in the problem. GOCE for instance allows to measure 6 gravitational gradients and uses a full tensor gradiometer. GRACE, GRACE-FO and GRAIL, although deploy a sort of synthetic gradiometer (hence, not a physical instrument), measure just the Γ_{xx} component of the gradient, where x is the along track direction of the spacecraft. In general, a full tensor gradiometer offers the best results, whereas, when one or more components, in-line and/or off-line, are measured, the performance in terms of RMS error (error degree variance and error order-degree variance, section 2.2.2) of the recovered spherical harmonic coefficients need to be evaluated.

4. Gravity mission needs

4.1 Design variables

A satellite gravity mission, differently with respect to other remote sensing missions which observe a specific point at a specified location and time, provides information on the gravity signal integrated of the three-dimensional mass distribution seen from a specific location at a certain time. Objective of these missions is to measure gravity field observables such as gravity gradients, directly (GOCE) or indirectly (SST), or derive spherical harmonics of the gravity field through range and range-rate observables (radio-tracking) (section 3); the final scope is to derive the gravity field distribution. From those measurements other observables are derived such as gravity anomalies or geoid undulations with a given level of accuracy and a given spatial and temporal resolution.

When a satellite orbits a planetary body, the achievable spatial resolution for the observable depends on the requirement on the frequency bandwidth (as shown in 4.3), whereas the achievable accuracy becomes a requirement integrated over the specified bandwidth. The accuracy refers to the quality of data, whereas the frequency range identifies the timescale of the measured signals over which guaranteeing that quality.

At mission level, the parameters of interest are constituted at first by the accuracy, the spatial resolution and the time coverage; the time resolution and the spatial coverage are further elements to be considered. Those requirements are usually no independent on each other. Therefore, the definition of mission requirements implies a trade-off between them.

The accuracy refers to the achievable gravity signal level to be able to investigate the gravity-related processes of interest with a sufficient signal-to-noise ratio. The gravity signal depends on the altitude and on the investigated degree (section 2.2), hence low heights should be preferred for a gravity mission.

The spatial resolution is related to the spatial scale of the gravitational phenomenon to be investigated, i.e. to the spatial size of the masses involved into the processes to be studied (section 2.2.2). However, as shown in section 2, the signal amplitude decreases with the spatial resolution, i.e. small spatial scales provide small contributions to the general field with respect to the bigger ones. This parameter is related to the spatial wavelength λ, introduced by the spherical harmonic representation of the gravity field:

$$\lambda = \frac{2\pi R}{l}$$

Consequently, the contribution of the small wavelengths to the gravity field is embedded into the spherical harmonics of high degrees.

The time resolution reflects the time scale of processes that show themselves through the mass transport and movement. Indeed, a time variable gravity field is added to the basic static gravity field due to the several processes modifying a planet on the surface and in the interior. From this perspective, the time resolution requirement should be sufficient to cover partially or the most the spectrum of processes to be studied. The time scale covers different ranges depending on where they happen. For instance, referring to the Earth processes for whicha better knowledge is available [100], mass transport in the atmosphere happens on a time span from several hours to one year, whereas the same process on the solid-Earth is slower, from few to hundreds years; in the hydrosphere, times range from hours (ocean tides) to very hundreds/thousands years (melting of ice sheets).

However, apart the Earth, for which a systematic study of the time variable gravity field has started since the GRACE mission and is currently on-going with GRACE-FO, this aspect is in a very embryonic phase to be investigated for other planets, due to the lack of measures in terms of number and (time) continuity. Just for Mars some analyses tried to study the gravity over time by monitoring the mass variation of polar ice caps [99]. However, for medium-long term missions this is a design element to be taken into consideration for the future.

The time coverage refers to the whole mission lifetime. It depends on several factors often driven more by economic considerations rather than scientific objectives. However, this time is often driven by the need to study a periodic phenomenon which requires a specific revisitation period, i.e. the use of a repeat orbit, also known as repeat groundtrack. Repeat groundtrack orbits are characterised by the repeatition of groundtrack over a certain time interval and are employed usually in space missions that periodically revisit a certain point of a planet [5], such as a gravity mission. Its definition depends on the commensurability between the time interval it takes the satellite to make two consecutive equator crossings (nodal period, α) and the period of the Earth's rotation with respect to the ascending node. A satellite on a β/α repeat orbit fulfils β revolutions in α nodal days, where β and α are relative primes. Thus, the repeat period of such a satellite is $T_{rep} = \alpha$ (nodal days) with a revolution time of $T_{rev} = \alpha/\beta$ (nodal days) [128]. A trade-off on those parameters has to be found. Indeed, a short repeat period leads to sparse ground-track spacing, conversely, dense satellite coverage can only be attained at the cost of time resolution.
The spatial coverage is referred to the areas where the satellite can gather measures. For a gravity mission, a quasi-polar orbit is typically used. This means that some pole areas are not covered during the spacecraft revolutions.
At last, the achievable performance is the result of a trade-off among several factors, often mutually conflicting. The fundamental trade-off is on the temporal and spatial resolution, which depends on the altitude, on the sampling, on the mission lifetime.
The accuracy is related to the minimum gravity signal detectable from the instrument. However, the gravity signal decrease in magnitude as the altitude increases and such an attenuation is faster for shorter wavelengths than for longer wavelengths. Hence, for higher orbits a more accurate system is needed to observe with a defined spatial resolution and accuracy. At the same time, benefits come from these orbits for the spacecraft requirements and for the mission lifetime. The latter one is a much appealing characteristic for measurements that can monitor gravity-related processes on time as long as possible. On the other hand, lower orbits benefit from a higher gravity signal and hence relaxed requirements on the accuracy on the measurement instrument. However, decreasing the orbit altitude imposes more stringent requirements on the spacecraft.
Indeed, a low orbit requires some precautions. At first, the presence or less of atmosphere makes the mission more complicated. Lower orbits mean crossing through denser layers which offer significant drag and reduce progressively the altitude, as happens for Venus (especially) but Mars as well. Therefore, an orbit and attitude control system along track would be needed to counteract this effect. A potential approach is the use of a drag-free system, as per GOCE mission, i.e. to compensate for disturbances on the in-flight direction, detected as common mode accelerations on the gradiometer, by means of a dedicated thrusters firing. However, this means major propellant expenditure and consequently a major impact on the mission lifetime. Hence, at high level, the mission performance is limited by the flying altitude and the mission duration. For instance, GOCE employs electrical propulsion to counteract effects of atmospheric drag (along-track), whereas GRACE has no altitude control. This difference of approach is witnessed by the effective mission lifetime. GOCE was designed for a lifetime of 2 years, limited by the amount of propellant on board to keep the spacecraft at the nominal altitude ($\sim 250\ km$) (section 2.4.3.1.5). This can be

compared with the GRACE mission (section 2.4.3.1.3), which started its measurements at $\sim 500\,km$ and lasted for a 15 years activity (nominally 5 years). However, due to the extended solar minimum at the end of the past decade, GOCE performed 4 years and a half, beyond its mission lifetime.
As example of how science themes to be faced by future gravimetry missions map in the corresponding spatial and time resolutions, Figure 4-1 is reported, as derived from [33]. The main focus of the bubble plots, each one aimed at a theme, is on the Earth phenomena; however, planets gravity field is also reported. The bubble on the top, reported as unique "science theme" due to the still primitive knowledge of involved phenomena, recalls results previous obtained on the science needs for planets gravity knowledge (section 2.5). It shows that the time resolution is currently limited to static fields, while the spatial resolution covers the range $\psi \sim 20.000 - 100\ km$.

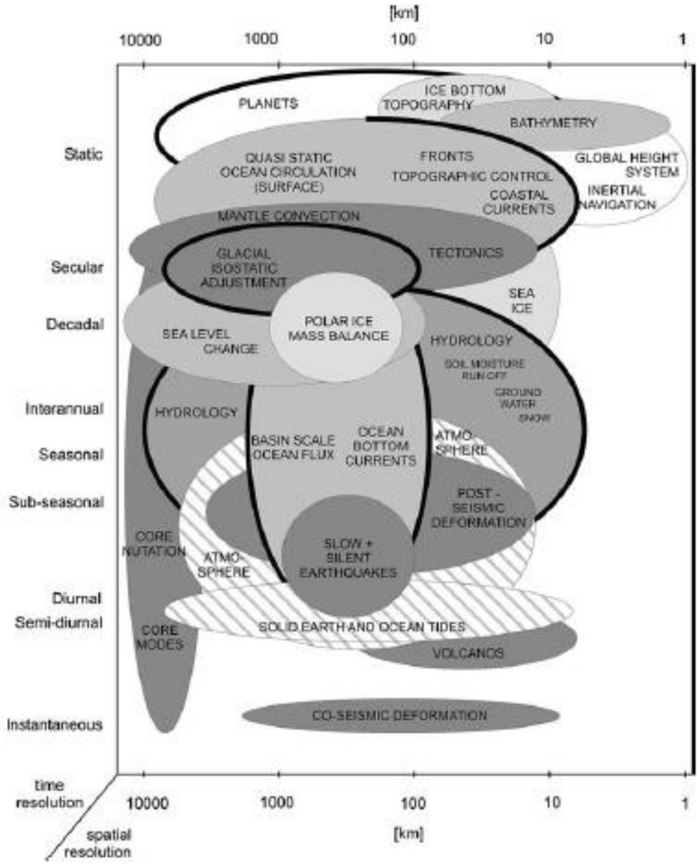

Figure 4-1: spatial and time scales of several geophysical processes on the Earth, as identified in [33]. Analogous and phenomena for planets, identified as unique bubble, are reported on the top (from [33])

On the basis of previous considerations, some elements can be identified in the design of a gravity mission. An overview is shown in Table 4-1. This table shows off some of the main elements to be considered in the design of a gravity mission. For general purpose, the SST technique is included as well, although it is not related to a real gradiometric instrument but rather to a synthetic one.

Table 4-1 Gravity mission design variables (modified from [127])

Variables	***Values***		
orbit altitude	high	low: drag measurement	very low: drag compensation
control	none	angular	angular + linear
proof masses	free-floating/SST	constrained/gradiometry	
Constrained/ gradiometry	differential accelerometry	rotating differential accelerometry	rotating torsional
Free-floating/ SST	SST-hl	SST-ll	Floating inside SC
arm length	SST-hl	SST-ll	spacecraft size constrained
gradiometric components	full	diagonal/off-diagonal	one component
temperature	ambient	low-temperature superconductivity	high-temperature superconductivity

The orbit altitude is an important design element to be considered. As often reported in previous sections, low altitudes for a gravity mission are preferred to increase the signal level, especially for high degrees l of the field. However, if the planetary body hosts an atmosphere, when the altitude is too low the drag effect become not negligible with respect to the spacecraft dynamics. In this case, measurement (accelerometer) or compensation (orbit control) of the drag is needed to take into account or to reduce its effects on the orbit. This condition can be set roughly at 250 km for orbits around Venus and at 200 km for orbits around Mars. For comparison, on the Earth, altitudes around 250-300 km, as those employed by GOCE, need to be provided with drag control system.
Proof masses, the sensing elements of the field, can be arranged according two approaches. They can be left free to move in the gravity field while the spacecraft case move in such a way to keep it into the centre (GRACE, GRACE-FO) or can be constrained mechanically or in other way (GOCE), as usually happens for a gradiometic instrument.
The distance between the proof masses over which to sense the gravity field can be more or less extended. For a pure gradiometer this distance is clearly constrained by the size of the spacecraft (1-2 metres), while for a SST approach it can range on 100-400 km, being just constrained by the microwave link established between the two spacecrafts (section 3.2.2); this length depends on the degree l of the field to be investigated.
The independent components of the gravity gradient are five. However, depending on the configuration employed, an instrument can measure one or more in-line and/or off-line components of the tidal tensor (i.e. the gravity gradient). In general, the measurement of all the five components is desired but implies an instrument more complex and demanding in terms of performance and controlled environment conditions.
At last, the operative temperature is another of the design variables for a gravity mission. Table 4.2 shows off the values of variable designs employed by the main gravity mission analysed in previous chapters.

Table 4-2 Design variables chosen for the main gravity missions analysed in previous chapters

	GOCE	GRACE	GRACE-FO	GRAIL	CHAMP
orbit altitude	≈250-280 km	≈500 km	≈500 km	≈50 km	≈450 km
control	Drag-free/ angular	angular + linear	angular + linear		angular + linear
proof masses	constrained	free-floating	free-floating	free-floating	free-floating
constrained: gradiometry	differential accelerometry	-	-	-	
free-floating: SST	-	SST-ll	SST-ll	SST-ll	SST-hl
arm length	0.5 m	≈200-300 km	≈200-300 km	≈200 km	-
gradiometric components	6 (5 + 1)	one component	one component	one component	-
temperature	ambient	ambient	ambient	ambient	ambient

The science requirements form the starting point from which deriving the mission requirements and the spacecraft/instrument requirements.

4.2 Science requirements

The science objectives have been identified in measuring the gravity gradient of two targets, Venus and Mars (section 3.4). A preliminary evaluation of the expected signal has been carried out in section 3.4. Starting from these results, a more precise evaluation of the gravity gradients was investigated, in order to have a simulation tool able to evaluate correctly the gravity gradient in terms of all the independent components. The tool was thought to be used for any planetary body and for any orbit around it. Hereafter, the focus is limited to circular orbits (zero eccentricity) because this type of orbits is used in gravity missions. Future work foresees to extend the formulation to elliptical orbits as well.

4.2.1 Gravity gradients in different coordinates

The starting point is the gravitational potential in terms of series of spherical harmonics and expressed in planetocentric spherical coordinates (r, λ, θ – radius, longitude and co-latitude (section 2.2.2):

$$V(r,\lambda,\theta) = \frac{GM}{R}\sum_{l=0}^{+\infty}\sum_{m=0}^{l}\left(\frac{R}{r}\right)^{l+1} P_{lm}(\cos\theta)(C_{lm}\cos m\lambda + S_{lm}\sin m\lambda) \qquad (4\text{-}1)$$

Such an expression relates the spatial and the spectral domain of the gravitational potential through the coefficients of the spherical harmonics, C_{lm} and S_{lm}.
We are interested in the second-derivatives of the gravitational potential, i.e. the gravitational gradient. Following the work of Koop in [125], it is possible to calculate the first and second-derivatives of the potential with respect to the chosen coordinate system.

Double diffrencing the previous equation, we get:

$$\Gamma_{zz} \equiv \Gamma_{rr} = \frac{\partial^2 V}{\partial r^2}$$

$$= \frac{GM}{R} \sum_{l=0}^{+\infty} \frac{(l+1)(l+2)}{R^2} \left(\frac{R}{r}\right)^{l+3} \sum_{m=0}^{l} P_{lm}(cos\,\theta)(C_{lm}\,cos\,m\lambda + S_{lm}\,sin\,m\lambda) \tag{4-2}$$

Different coordinate systems can be used depending on the application to which the computation can be applied.

The most common system is, of course, the cartesian coordinate system. Such a system is constituted by three mutual orthogonal axes X, Y, Z intersecting in a common origin and coincident with the body's centre: this is the planetocentric cartesian coordinate system.

However, the geometrical symmetry of the problem suggests using spherical coordinates. In this case, the gravitational potential is expressed in terms of the planetocentric spherical coordinates $r,\ \lambda,\ \theta$, respectively radius, i.e. radial distance from the origin, longitude and co-latitude, as in equation (4-1). Alternatively, the colatitude is substituted by the more common latitude φ (they are complementary angles). In this case, the Legendre polynomia are written in terms of $\sin\varphi$.

The equation (4-1) can be written down by interchanging the summation over l and m [125]:

$$V(r,\lambda,\theta) = \sum_{m=0}^{+\infty} \sum_{l=m}^{+\infty} \frac{GM}{R} \left(\frac{R}{r}\right)^{l+1} P_{lm}(\cos\theta)(C_{lm}\cos m\lambda + S_{lm}\sin m\lambda) \tag{4-3}$$

The previous equation can be arranged by using the following coefficients:

$$\begin{gathered} K_{lm}^{A}(r,\theta) = H_{lm}(r,\theta)\ C_{lm} \\ K_{lm}^{B}(r,\theta) = H_{lm}(r,\theta)\ S_{lm} \\ H_{lm}(r,\theta) = \frac{GM}{R}\left(\frac{R}{r}\right)^{l+1} P_{lm}(\cos\theta) \\ u_l = \frac{GM}{R}\left(\frac{R}{r}\right)^{l+1} \end{gathered} \tag{4-4}$$

i.e.:

$$V(r,\lambda,\theta) = \sum_{m=0}^{+\infty} \sum_{l=m}^{+\infty} (K_{lm}^{A}(r,\theta)\cos m\lambda + K_{lm}^{B}(r,\theta)\sin m\lambda) \tag{4-5}$$

By using the Koop approach reported in [125], the first- and second-derivatives of the gravitational potential in spherical coordinates with respect to $r,\ \lambda,\ \theta$ can be computed by using the expressions shown in Table 4-3.

Table 4-3 First- and second-derivatives of the gravitational potential with respect to the spherical coordinates (from [125])

Derivative wrt	$\boldsymbol{H_{lm}^{\cdot\cdot}}$	$\boldsymbol{K_{lm}^{A}}$	$\boldsymbol{K_{lm}^{B}}$
r	$\frac{-(l+1)}{r} u_l\, P_{lm}(\cos\theta)$	$H_{lm}^{r}\, C_{lm}$	$H_{lm}^{r}\, S_{lm}$
θ	$u_l \frac{\partial P_{lm}(\cos\theta)}{\partial\theta}$	$H_{lm}^{\theta}\, C_{lm}$	$H_{lm}^{\theta}\, S_{lm}$
λ	$m u_l P_{lm}(\cos\theta)$	$H_{lm}^{\lambda}\, S_{lm}$	$-H_{lm}^{\lambda}\, C_{lm}$
rr	$\frac{(l+1)(l+2)}{r^2} u_l\, P_{lm}(\cos\theta$	$H_{lm}^{rr}\, C_{lm}$	$H_{lm}^{rr}\, S_{lm}$
$r\theta$	$\frac{-(l+1)}{r} u_l \frac{\partial P_{lm}(\cos\theta)}{\partial\theta}$	$H_{lm}^{r\theta}\, C_{lm}$	$H_{lm}^{r\theta}\, S_{lm}$
$r\lambda$	$\frac{-m(l+1)}{r} u_l P_{lm}(\cos\theta)$	$H_{lm}^{r\lambda}\, S_{lm}$	$-H_{lm}^{r\lambda}\, C_{lm}$
$\theta\theta$	$u_l \frac{\partial^2 P_{lm}(\cos\theta)}{\partial\theta^2}$	$H_{lm}^{\theta\theta}\, C_{lm}$	$H_{lm}^{\theta\theta}\, S_{lm}$
$\theta\lambda$	$m u_l \frac{\partial P_{lm}(\cos\theta)}{\partial\theta}$	$H_{lm}^{\theta\lambda}\, S_{lm}$	$-H_{lm}^{\theta\lambda}\, C_{lm}$
$\lambda\lambda$	$-m^2 u_l\, P_{lm}(\cos\theta)$	$H_{lm}^{\lambda\lambda}\, C_{lm}$	$H_{lm}^{\lambda\lambda}\, S_{lm}$

Such an expression of the field is valid in a body-fixed reference frame, i.e. a reference co-rotating with the underlying body. However, for analysis of gradients along a specified orbit a different frame should be chosen. Such a reference system should hence be inertial and related to the satellite's track on a specific orbit. This is possible operating a transformation between the body-fixed reference frame (in general expressed in spherical coordinates r, λ, θ) and a reference system adapted to the Keplerian orbit, defined by the osculating orbital elements $(a, e, i, \Omega, \omega, M)$, respectively semimajor axis, eccentricity, inclination, right ascension of the ascending node, argument of pericentre and mean anomaly, as shown in Figure 4-2 for the Earth. The starting reference frame is the body-fixed frame with the x axis in the direction belonging to the plane defined by the reference meridian (Greenwhich in the case of Earth), the y axis rotated by 90 degrees on the planet's equatorial plane and the z axis pointing towards the north pole. Such a frame is at first rotated on the planet's equatorial plane by the angle Ω (RAAN, right ascension of the ascending node) so that the x axis is overlapped to that of the nodal line of the orbit, then is rotated around the line of nodes through the inclination i. At last it is followed by a counterclockwise rotation on the orbit plane from the node to the pericentre by the angle ω (pericentre argument).

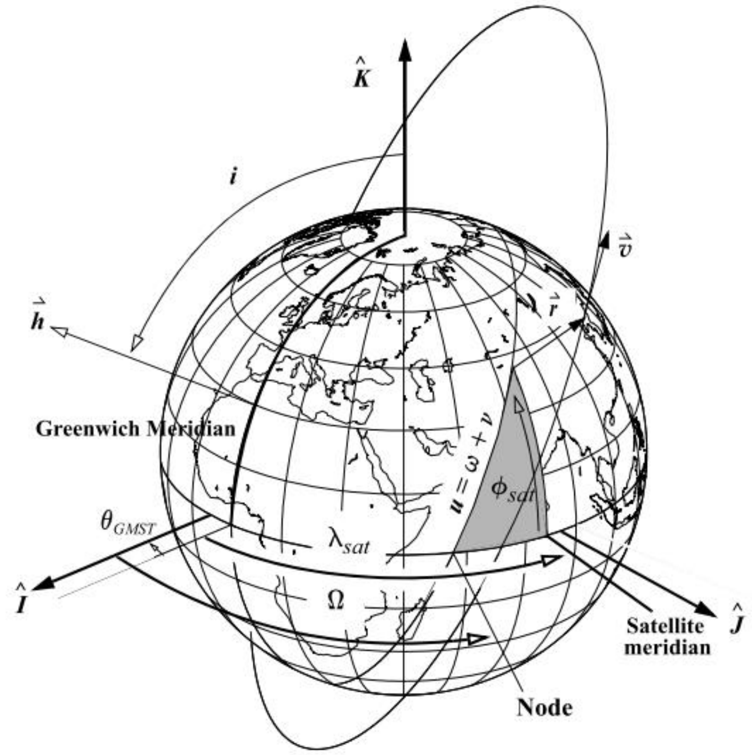

Figure 4-2: transformation between the body-fixed reference frame (in the figure the Earth is considered as fixed body) and the inertial reference frame adapted to the Keplerian orbit (from [5])

The application of such composite rotations transforms the gravitational potential $V(r,\lambda,\theta)$ into a corresponding function, $V'(a,e,i,\Omega,\omega,M)$, depending on the orbital parameters; this is again a harmonic function (i.e. solution of the Laplace equation), being the Laplace operator invariant under rotation [11], and hence can be expanded in spherical harmonics. The gravitational potential in such a new shape is known as Kaula expansion [13][11][125]:

$$V = \frac{GM}{R}\sum_{l=0}^{+\infty}\left(\frac{R}{r}\right)^{l+1}\sum_{m=0}^{l}\sum_{p=0}^{l}F_{lmp}(i)\left\{\begin{bmatrix} C_{lm} \\ -S_{lm}\end{bmatrix}_{l-m:\,odd}^{l-m:\,even}\cos\psi_{lmp} + \begin{bmatrix} S_{lm} \\ C_{lm}\end{bmatrix}_{l-m:\,odd}^{l-m:\,even}\sin\psi_{lmp}\right\} \tag{4-6}$$

where the new terms are represented by $F_{lmp}(i)$, the normalised inclination functions, and $\psi_{lmp} = (l-2p)\omega_0 + m\omega_e$, where $\omega_0 = \omega + M$ and $\omega_e = \Omega - \theta_g$, with θ_g as planet's argument of longitude. Considering that $k = l - 2p$, we have as well $\psi_{km} = k\omega_0 + m\omega_e$. The inclination functions are expressed as trigonometric polynomial in $\sin i$ and $\cos i$ following the formula:

$$F_{lmp}(i) = \sum_{t=0}^{\min(p,k)} \frac{(2l-2t)!}{t!\,(l-t)!\,(l-m-2t)!\,2^{2l-t}}\sin i^{l-m-2t} \cdot \sum_{s=0}^{\mathrm{m}}\binom{m}{s}\cos i^{s}\sum_{c}\binom{l-m-2t+s}{c}\binom{m-s}{p-t-c}(-1)^{c-k} \tag{4-7}$$

where k is the integer part of $(l-m)/2$ and c is summed over values making the binomial coefficients non-zero, that is with the lower index non-negative and not larger than the upper one [13][11].

Actually, the formula for the Kaula expansion in (4-6) is applicable just for an eccentricity $e = 0$, since the general formula as derived from Kaula [13][11] includes also the eccentricity functions $G_{lpq}(e)$:

$$V = \frac{GM}{R}\sum_{l=0}^{+\infty}\left(\frac{R}{r}\right)^{l+1}\sum_{m=0}^{l}\sum_{p=0}^{l}F_{lmp}(i)\sum_{q=-\infty}^{+\infty}G_{lpq}(e)\left\{\begin{bmatrix}C_{lm}\\-S_{lm}\end{bmatrix}_{l-m:\,odd}^{l-m:\,even}\cos\psi_{lmpq} + \begin{bmatrix}S_{lm}\\C_{lm}\end{bmatrix}_{l-m:\,odd}^{l-m:\,even}\sin\psi_{lmpq}\right\} \tag{4-8}$$

With $F_{lmp}(i)$, the normalised inclination functions, $\psi_{lmpq} = (l-2p)\omega_0 + (l-2p+q)l + m\omega_e$ and $G_{lpq}(e)$, the eccentricity functions (often named Hansen coefficients):

$$G_{lpq}(e) = \frac{1}{(1-e^2)^{l-1/2}}\sum_{d=0}^{p'}\binom{l-1}{2d+l-2p'}\binom{2d+l-2p'}{d}\left(\frac{e}{2}\right)^{2d+l-2p'} \tag{4-9}$$

where $q\ =\ 2p - l$, whereas $p' = p$ if $p \le l/2$ and $p' = l-p$ if $p \ge l/2$ [13][5].

Hereafter, the case with $e\ =\ 0$ has been considered and hence the equation (4-6), since typically the gradiometry missions exploit circular orbit for gravity field measurements. This is for a simpler post-processing of data and better sampling of the field. In the future, it is foreseen to extend the analysis to elliptical orbits, in order to have a more extended space of orbits.

By using the equation (4-6), the computation of the gravity field functionals can be carried out by evaluating the series expansion till to a maximum degree l, depending on the investigated spatial resolution, and by means of a set of spherical harmonic coefficients (C_{lm}, S_{lm}) till to the same degree.

Starting from the equation (4-6) and substituting:

$$\sum_{p=0}^{l} x \ \rightarrow \sum_{k=l[2]}^{l} x$$

$$F_{lmp}(i) \ \ \rightarrow F_{lm}^{k}(i)$$

$$\psi_{lmp} \ \rightarrow \ \psi_{km} = k\omega_0 + m\omega_e$$

In the case of interest, the gravity gradient expressions in terms of the Kaula expansion can be written as:

$$\Gamma_{zz} = \frac{GM}{R^3}\sum_{l=0}^{+\infty}\frac{(l+1)(l+2)}{R^2}\left(\frac{R}{r}\right)^{l+3}\sum_{m=0}^{l}\sum_{k=-l[2]}^{l}F_{lm}^{k}(i)\,(\,\alpha_{lm}\,cos\,\psi_{km} +\ \beta_{lm}\,sin\,\psi_{km}) \tag{4-10}$$

where the espression is referred to the ZZ component of the gravity gradient and:

$$\alpha_{lm} = \begin{bmatrix} C_{lm} \\ -S_{lm} \end{bmatrix}_{l-m:\,odd}^{l-m:\,even}$$

$$\beta_{lm} = \begin{bmatrix} S_{lm} \\ C_{lm} \end{bmatrix}_{l-m:\,odd}^{l-m:\,even}$$

Applying some changes of notation, it is possible to write:

$$\Gamma_{zz} = \sum_{l=0}^{L_{max}} \sum_{m=0}^{l} \sum_{k=-l[2]}^{l} \{A_{lmk}^{zz} \cos\psi_{km} + B_{lmk}^{zz} \sin\psi_{km}\} \tag{4-11}$$

where again the espression is referred to the ZZ component of the gravity gradient and where are valid the following relations:

$$\begin{aligned} A_{lmk}^{zz} &= H_{lmk}^{zz}\, \alpha_{lm} \\ B_{lmk}^{zz} &= H_{lmk}^{zz}\, \beta_{lm} \\ H_{lmk}^{zz} &= (l+1)(l+2)\, F_{lm}^{k}(i) \\ \gamma_l &= \frac{GM}{R^3}\left(\frac{R}{r}\right)^{l+3} \end{aligned} \tag{4-12}$$

The expression for the overall independent components are reported in Table 4-4 [125]. These components are referred to the local orbital coordinate system (see later the definition).

Table 4-4 Gravity gradient compoonents with respect to the local orbital coordinate system (from [125])

Derivative wrt	$\boldsymbol{H_{\ddot{l}mk}}$	$\boldsymbol{A_{lmk}}$	$\boldsymbol{B_{lmk}}$
xx	$-(l+1+k^2)\gamma_l F_{lm}^{k}$	$\alpha_{lm}\, H_{lmk}^{xx}$	$\beta_{lm}\, H_{lmk}^{xx}$
xy	$-\text{asin}\,(\omega_0)\gamma_l \dot{F}_{lm}^{k}$	$H_{lm}^{\theta}\, C_{lm}$	$H_{lm}^{\theta}\, S_{lm}$
xz	$-(l+2)k\, \gamma_l F_{lm}^{k}$	$\beta_{lm}\, H_{lmk}^{xz}$	$-\alpha_{lm}\, H_{lmk}^{xz}$
yy	$-((l+1)^2 - k^2)\gamma_l F_{lm}^{k}$	$\alpha_{lm}\, H_{lmk}^{yy}$	$\beta_{lm}\, H_{lmk}^{yy}$
yz	$-(l+2)\text{asin}\,(\omega_0)\gamma_l \dot{F}_{lm}^{k}$	$\alpha_{lm}\, H_{lmk}^{yz}$	$\beta_{lm}\, H_{lmk}^{yz}$
zz	$(l+1)(l+2)\gamma_l F_{lm}^{k}$	$\alpha_{lm}\, H_{lmk}^{zz}$	$\beta_{lm}\, H_{lmk}^{zz}$

In case of lack of such coefficients a fictious field can be generated by using the constraint of the Kaula rule for the behaviour of the field amplitudes. At the end a set of computed gravity potential values with respect to a local coordinate system is generated.
The temporal dependence of the equation (4-11) is introduced following the Koop's approach [125]. The series can be considered as a time series if we consider successive measurement points along the orbit. In particular, the argument ψ_{km} can be written down as following:

$$\psi_{km} = k\omega_0^0 + m\omega_e^0 + (k\dot{\omega}_0 + m\dot{\omega_e})(t - t_0)$$

where $\omega_0 = \omega_0^0 + \dot{\omega}_0(t - t_0)$ and $\omega_e = \omega_e^0 + \dot{\omega}_e(t - t_0)$, and $2\pi/\dot{\omega}_e$ is a nodal period whereas $2\pi/\dot{\omega}_0$ is one revolution. Assuming $t_0 = \omega_0^0 = \omega_e^0 = 0$ and considering a time $t = 0, 1, \dots, T_g$ where T_g is the mission duration, the argument can be written down as:

$$\psi_{km} = (k\dot{\omega}_0 + m\dot{\omega}_e)n\Delta t$$

with $n = 0, 1, \dots, N_p - 1$ and $N_p = T_g/\Delta t$ is the number of measurements along the orbit. If during the mission period T_g, there are N_r orbital revolutions and N_d nodal periods (i.e. the time interval it takes the satellite to make two consecutive equator crossing), then:

$$T_g = N_d \frac{2\pi}{\dot{\omega}_e} \quad \dot{\omega}_e = N_d \frac{2\pi}{T_g} = \frac{N_d}{\Delta t}\frac{2\pi}{N_p}$$

$$T_g = N_r \frac{2\pi}{\dot{\omega}_0} \quad \dot{\omega}_e = N_r \frac{2\pi}{T_g} = \frac{N_r}{\Delta t}\frac{2\pi}{N_p}$$

and the argument ψ_{km} is translated into:

$$\psi_{km} = \frac{2\pi n}{N_p} N_r (k + m\frac{N_d}{N_r})$$

If N_d and N_r are prime integers, the groundtrack repeats after $N_d$nodal periods and N_r orbital revolutions [125].

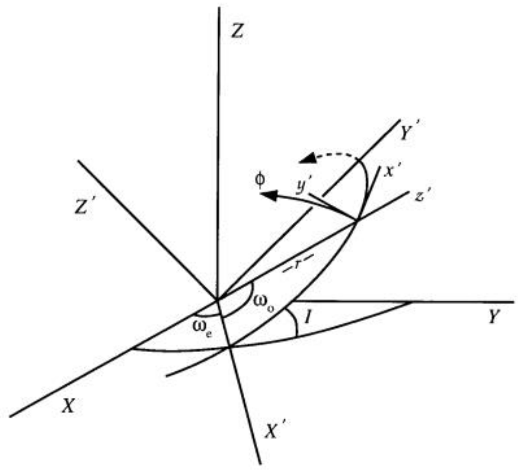

Figure 4-3: geocentric cartesian coordinate system, orbital coordinate system and local orbital coordinate system (from [125])

Three reference frames have been considered. The geocentric cartesian coordinate system (X, Y, Z) is defined with X-axis pointing at a reference meridian (Greenwich for the Earth), the Z-axis to the north-pole and Y to complete the right-handed system. A second reference system is obtained by rotating of ω_e around Z in order to obtain X' towards the ascending node and of i around the X' axis. This is named orbital Cartesian coordinate system. The third reference system is the local orbital coordinate system centred in a point on the spacecrat's orbit, the x-axis directed towards the along-track, the z axis directed radially towards the external and the y-axis directed across-track in order to have a right-handed system. This last frame is obtained form the first one, body-fixed, through successive rotations about ω_e, i, ω_0 and a translation of r. This is also the frame in which are evaluated the gravity gradient components.

4.2.2 Gravity gradient computation

Based on the previous formulas, a matlab code has been developed to compute six gravity gradient components, Γ_{zz}, Γ_{xx}, Γ_{xz}, Γ_{yz}, Γ_{xy} (5 independent) and Γ_{yy} (one diagonal), for any body and any circular orbit. The software receives as input the spherical harmonic coefficients for a planetary body till a l_{max} (C_{lm}, S_{lm}), the main body characteristics (G, M, R) and the orbit characteristics (a, e, i, Ω, ω, M). Moreover, orbit sampling and mission duration need to be defined. With respect to the last item, it is assumed to have an orbital period that matches the planet's rotational period. Such a condition guarantees to have a repeated ground track. Repeat groundtrack orbits are those which repeat their groundtrack over a certain time span [5]; they are typically employed by missions periodically revisiting a specific point on the planet, such as those devoted to study gravity. Moreover, it is considered that the mission duration equals one repeat period; in this way no ground-track repeat will happen during the mission. This condition is obtained when the number of orbit revolutions N_r around the planet, during the mission period, and the number of nodal days N_d in it, being one nodal day the time interval it takes the satellite to make two consecutive equator crossing, have to be relative prime integers.
The output provides the computation of the inclination functions $F_{lmp}(i)$ and of the six gravity gradients Γ_{zz}, Γ_{xx}, Γ_{xz}, Γ_{yz}, Γ_{xy} , Γ_{yy} for the chosen body and orbit. The inclination functions need to be early evaluated and then recalled from the main program. These functions have been initially computed by a dedicated routine. However, the need to reach very high degrees l implied very deep and heavy computations in terms of computer resources, with the result that effective values could be evaluated correctly till degree and order $l, m = 55$. Through researches in literature, the work of Gooding [124] has been found out as useful to accomplish the computations till very high degrees ($l \sim 1000$) by using an optimised routine. Routines developed have been reported in the appendix to the thesis with an explanation of the structure; moreover, comments are reported in the code as well.
On the basis of previous elements, it is possible to define a scenario for a gradiometry mission around a planetary body and on a defined orbit and to evaluate for that scenario the time series of a set of gravity gradients. Values of gravity gradients have been computed for the two targets derived as more interesting from the scientific point of view and more suitable in the hypothesis of a gradiometry mission: Venus and Mars.
Orbits have been chosen focusing on the mission objective, i.e. the retrieval of the gravitational field through the measure of the gravitational gradients. Specifically, circular orbits have been investigated.
Circular ($e = 0$) and quasi-polar ($i = 89°$) orbits were chosen as typically representative of orbits employed in gravity field missions. However, different case can be considered in successive developments of the thesis. Heights were chosen compatible with Magellan (Venus) and MRO (Mars) missions.
In the following results for the computed time series have been reported. Just the gradients of the main diagonal (Γ_{zz}, Γ_{xx}, Γ_{yy}) and one off-diagonal (Γ_{xz}) have been plotted.

For the Venus case, the plot is shown just for the first two orbits (about 3 hours). The gravitational field has been investigated till to the degree and order $l = 70$ for a circular quasi-polar orbit at an altitude $h = 300\ km$.
Concerning the diagonal values, Figure 4-4, Figure 4-5, Figure 4-6 show the time variation along the orbit of the Γ_{zz}, Γ_{yy}, Γ_{xx} gradients. Table 4-5 depicts the main characteristics used to produce the time series. The variations are of the order of few Eotvos with respect to the dominant monopole value with a value around $2536\,E$ and $-1268\,E$, respectively Γ_{zz} and Γ_{yy}, Γ_{xx}. Figure 4-7 shows the off-diagonal gradient Γ_{xz}; in this case no monopole value exists and the variations are lower, about tenth of Eotvos.
For clarity of the behaviour of time series, graphs are shown only for 3 and 3.5 hours, although the simulation spans over one day.
This approach, in which gravity gradients are computed in points of an equally-angular spaced grid located along the orbit, is named spherical harmonic synthesis [125]. In this case, it is required to have a set of known spherical harmonic coefficients. Alternatively, a fictious field can be computed. According to this approach, the gravity gradient synthesis allows to provide some information and understanding of the signals expected from a gradiometer mission.

Table 4-5 Main parameters used for the computation of gravity gradients for a spacecraft orbiting Venus

Planet	**Venus**	**Unit**
Height	300	km
Orbital period	1.550	h
Orbital velocity	7152	m/s
Inclination	89.00	degrees
Argument of pericentre	0.00	degrees
RAAN	67.80	degrees
Argument of longitude	10.00	degrees
Orbit sampling	4	s
Number of orbit revolutions	15	-
Maximum degree	70	-
Γ_{zz} *(monopole) - average*	2536.28	E
Γ_{xx} *(monopole) - average*	-1268.14	E
Γ_{yy} *(monopole) - average*	-1268.14	E

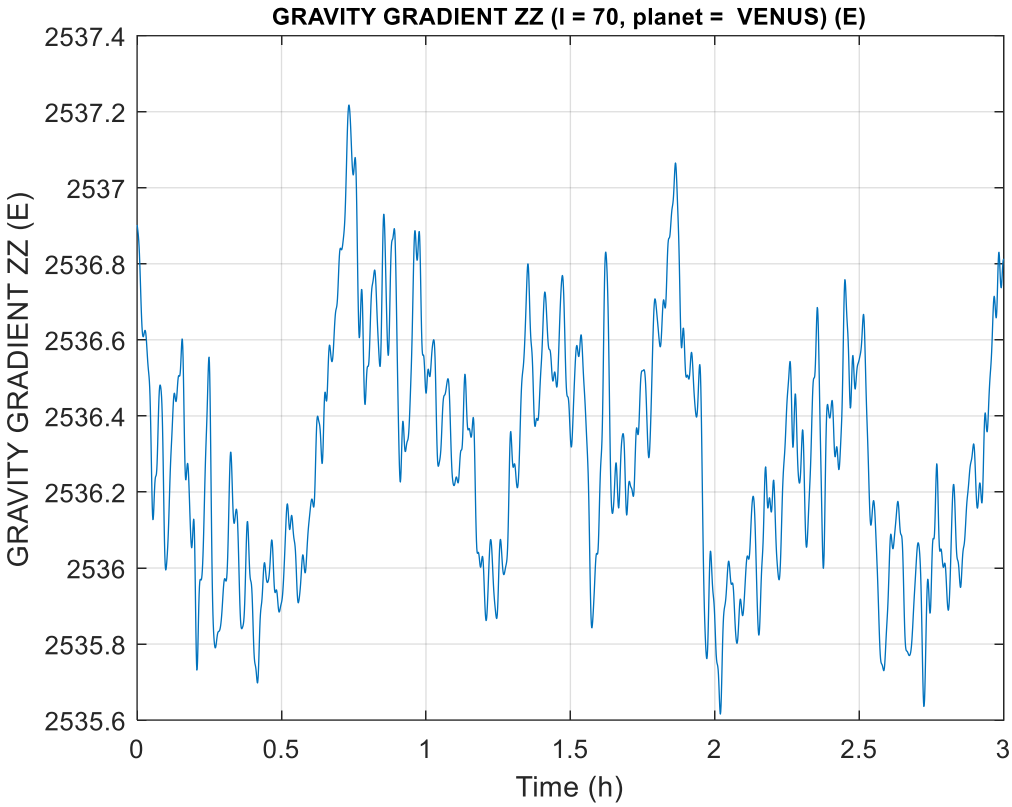

Figure 4-4: Gravitational gradient ZZ till degree l = 70 for an orbit around Venus at an altitude h = 300 km

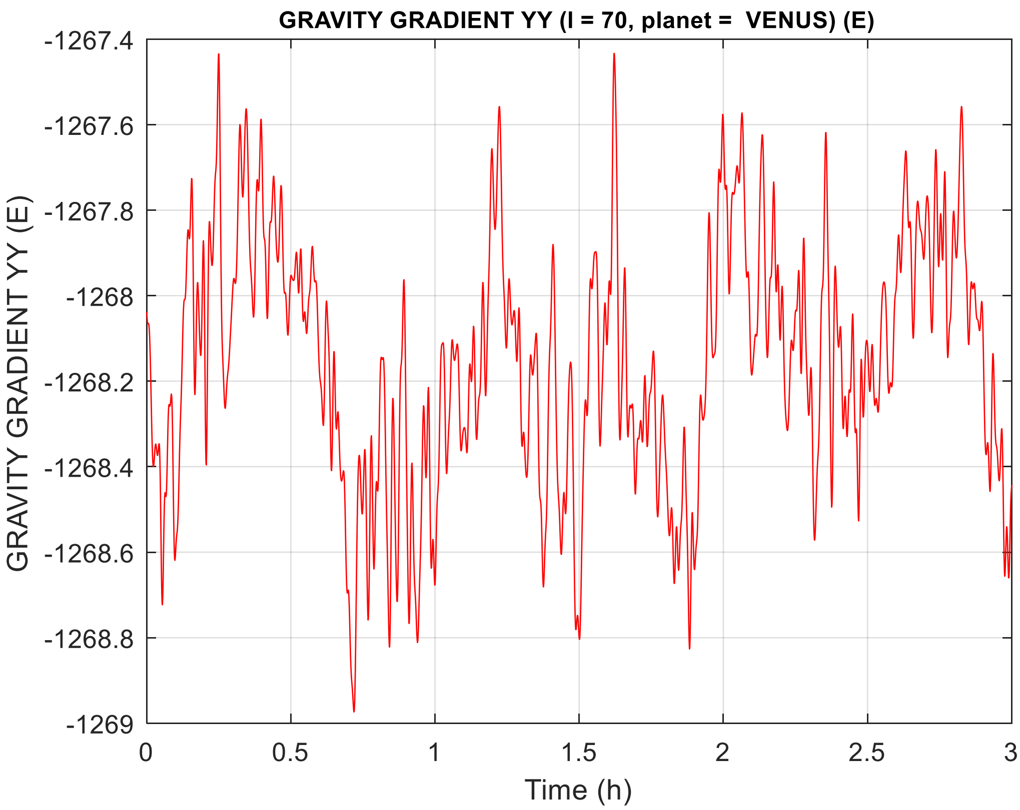

Figure 4-5: Gravitational gradient YY till degree l = 70 for an orbit around Venus at an altitude h = 300 km

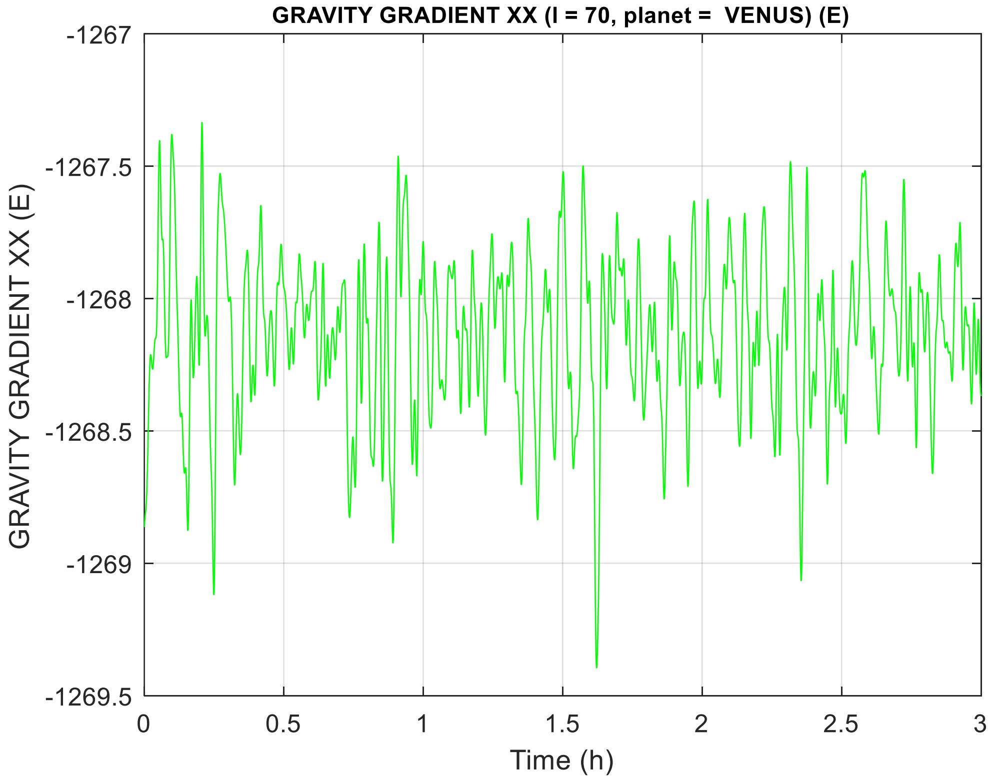

Figure 4-6: Gravitational gradient XX till degree l = 70 for an orbit around Venus at an altitude h = 300 km

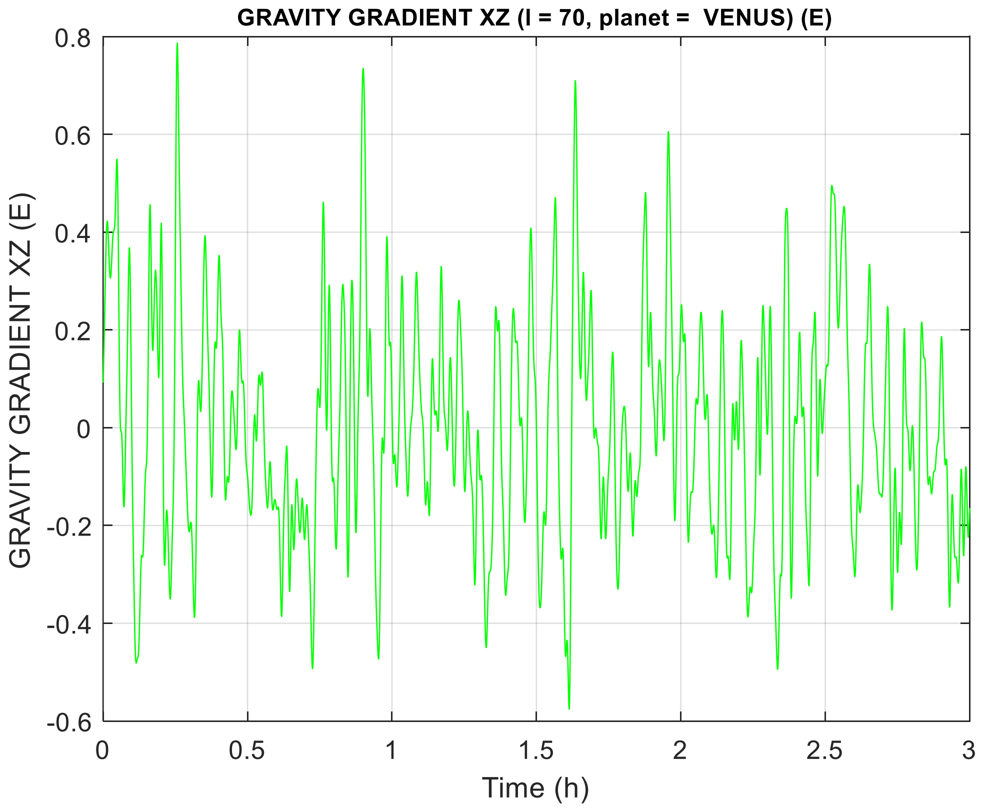

Figure 4-7: Gravitational gradient XZ till degree l = 70 for an orbit around Venus at an altitude h = 300 km

For the Mars case, the plot is shown for the first two orbits as well (about 3.5 hours). The gravitational field has been investigated till to the degree and order $l = 100$ for a circular quasi-polar orbit at an altitude $h = 300\ km$. The orbit characteristics are close to the MRO orbit.
Concerning the diagonal values, the Figure 4-8, Figure 4-9, Figure 4-10 show the time variation along the specified orbit of the Γ_{zz}, Γ_{yy}, Γ_{xx} gradients. Table 4-6 depicts the main characteristics used to produce the time series. In this case the variations are larger, of the order of $\sim 20\ E$ for the Γ_{zz} component with respect to a monopole value around $1705\ E$, $\sim 6\ E$ for the Γ_{yy} component with respect to a monopole value around $-850\ E$ and $\sim 15\ E$ for the Γ_{xx} component with respect to about $-850\ E$. Figure 4-7 shows the off-diagonal gradient Γ_{xz}; in this case no monopole value exists and the variations are in the order of $\sim 16\ E$.

Table 4-6 Main parameters used for the computation of gravity gradients for a spacecraft orbiting Mars

Planet	**Mars**	**Unit**
Height	255	km
Orbital period	1.890	h
Orbital velocity	3407	m/s
Inclination	89.00	degrees
Argument of pericentre	0.00	degrees
RAAN	67.80	degrees
Argument of longitude	10.00	degrees
Orbit sampling	4	s
Number of orbit revolutions	13	-
Maximum degree	100	-
Γ_{zz} *(monopole)*	1704.84	E
Γ_{xx} *(monopole)*	-852.42	E
Γ_{yy} *(monopole)*	-852.42	E

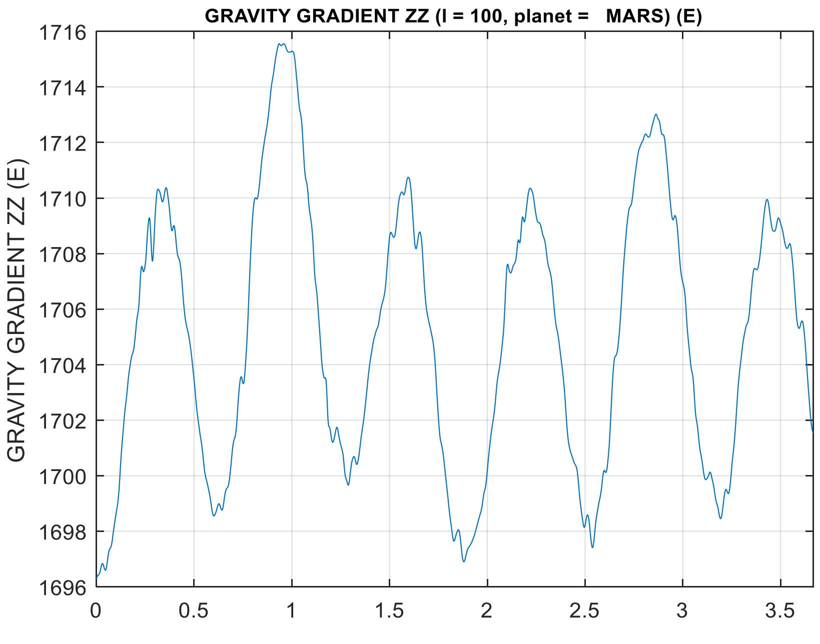

Figure 4-8: Gravitational gradient ZZ till degree $l = 100$ for an orbit around Mars at an altitude h = 255 km

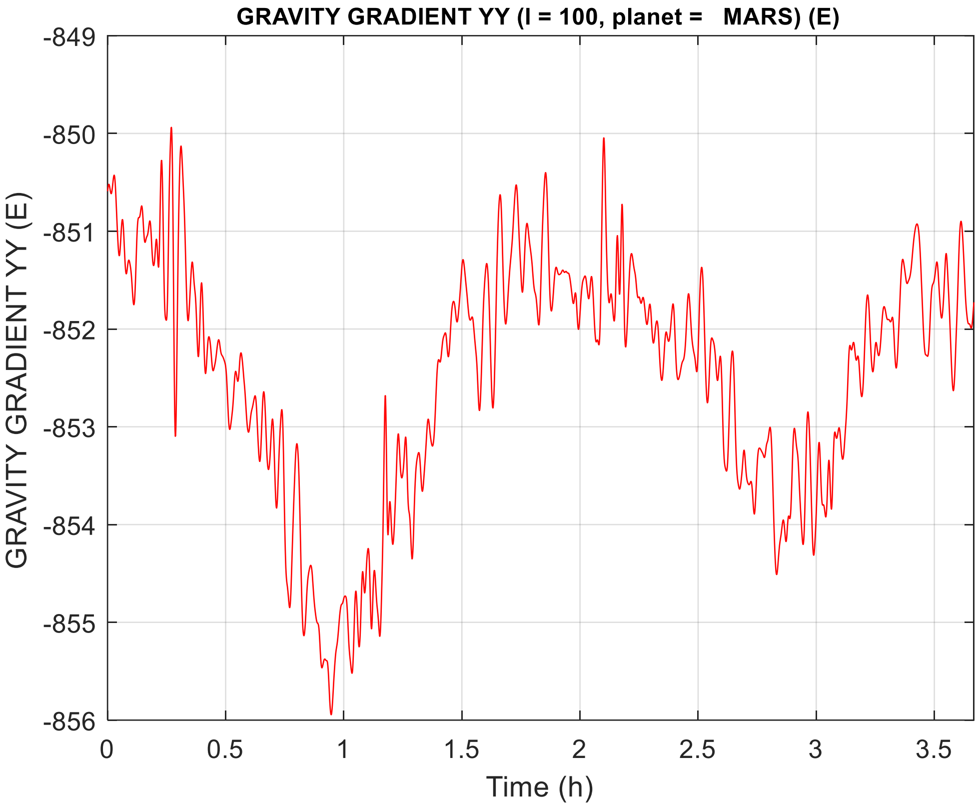

Figure 4-9: Gravitational gradient YY till degree $l = 100$ for an orbit around Mars at an altitude h = 255 km

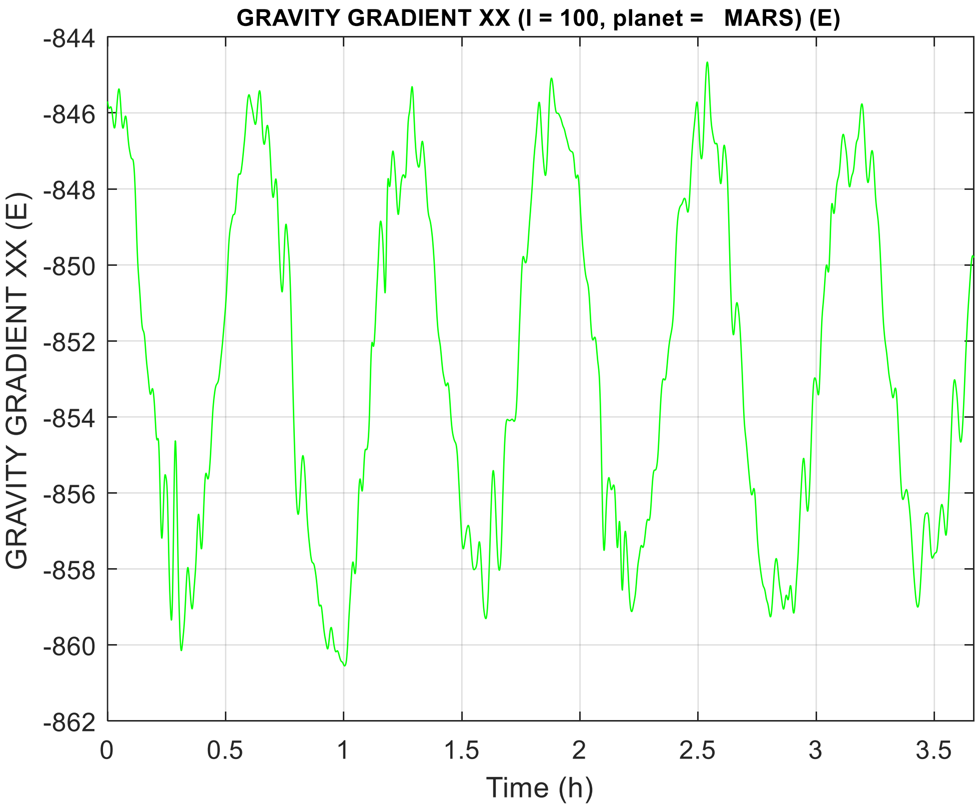

Figure 4-10: Gravitational gradient XX till degree $l = 100$ for an orbit around Mars at an altitude h = 255 km

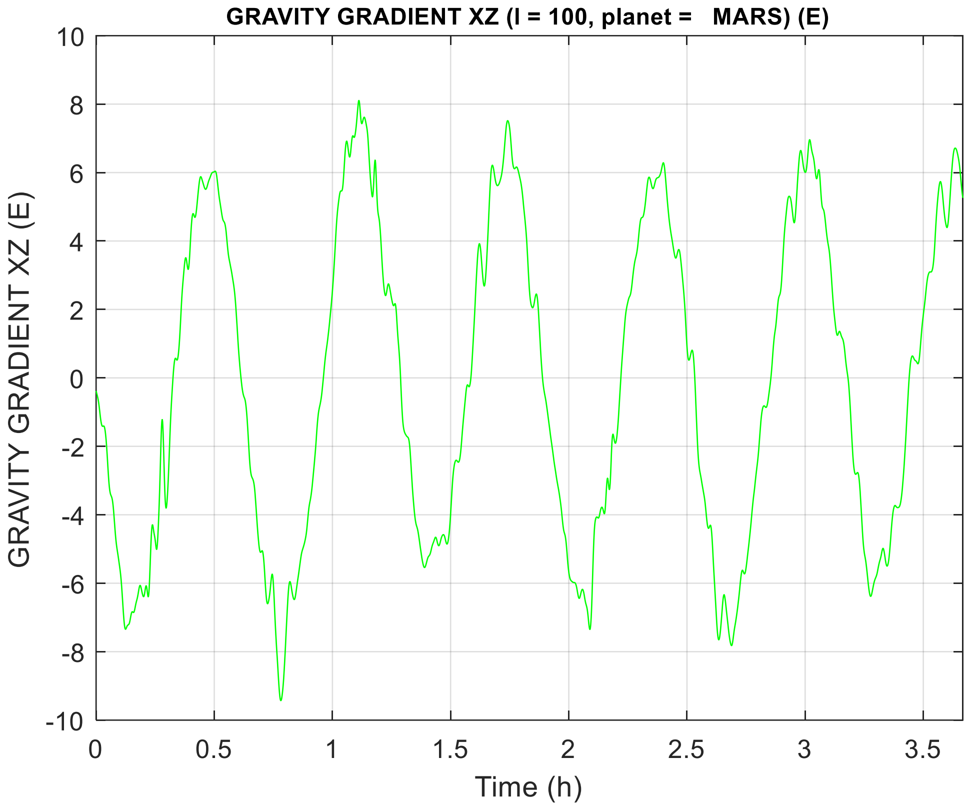

Figure 4-11: Gravitational gradient XZ till degree $l = 100$ for an orbit around Mars at an altitude h = 255 km

4.3 Mission requirements

From the science requirements (section 3.4 and section 4.2) hints for the definition of some mission requirements for a gravity mission at Mars or Venus are derived.
A potential mission to Mars should foresee a spacecraft orbiting in a range 200-300 km of height and able to measure a gravity gradient with signal levels around 10^{-13}-10^{-14} s^{-2} for corresponding maximum degrees $l = 100$ and around 10^{-18}-10^{-22} s^{-2} for corresponding maximum degrees $l = 300$. In the conditions specified in the previous section, the time series of the gradients for a 300 km of altitude and till $l = 100$, in an inertial frame body centred, would be represented by Figure 4-8, Figure 4-9, Figure 4-10 and Figure 4-11.
At the same time, a potential mission to Venus should foresee a spacecraft orbiting at an altitude in the range 200-350 km and should be able to sense signal levels of 10^{-13}-10^{-14} s^{-2} for degrees till to $l = 100$ and 10^{-15}-10^{-17} s^{-2} for degrees till to $l = 250$. In the conditions specified in the previous section, the time series of the gradients for a 300 km orbit altitude and till $l = 70$, in an inertial frame body centred, would be represented by Figure 4-4, Figure 4-5, Figure 4-6 and Figure 4-7.
Further science requirements impacting directly the mission can be derived with respect to the frequency band of the expected signal. Indeed, from the point of view of the typical frequencies of the gravity signal to be investigated during such a mission, the following considerations can be carried out. The gravity signal associated with harmonics of degree l has a wavelength [125]:

$$\Delta s = \frac{2\pi r}{l} \tag{4-13}$$

where $r = R + h$ is the altitude h of the spacecraft with respect to the body centre, with radius R.
According to the Nyquist theorem, at least a sampling frequency doubling the maximum frequency of the signal of interest is needed in order to prevent aliasing in the signal. This means that at least one data point along the orbit every $\Delta s/2$ is needed [125]; more data would be better as well. On the basis of such considerations, the typical timescale of the gravity signal would be:

$$\Delta\tau = \frac{\Delta s}{2v} = \frac{2\pi r}{2l\, v} = \frac{\pi r}{l\, v} = \frac{\pi r}{l}\sqrt{\frac{r}{\mu}} \qquad (4\text{-}14)$$

where $v = \sqrt{\mu/r}$ is the spacecraft orbital velocity, $\mu = GM$ is the gravitational parameter and l is the degree investigated. From the science needs the gravity field needs start from the current knowledge, as reported in Table 2-7 (section 2.5).
Different scenarios have been considered for each target by identifying a range of degrees l (l_{min} and l_{max}) and a range of orbit heights h.
The range of chosen degrees was derived from the science needs of the Table 2-7. In particular the maximum degree l_{max} is identified on the basis of this table, starting from the minimum value to be investigated in order to overcome the current knowledge to incremental values; on the other hand, l_{min} is referred to the quadrupole signal ($l = 2$).
The range of heights are the typical altitudes employed by past and present missions around those bodies (the same used for Table 3-3). For each scenario the corresponding frequency band of the expected gravity signal has been computed, following the previous considerations, and the minimum expected sampling frequency (twice the maximum signal frequency). Results are reported in Table 4-7.

Table 4-7 Typical frequency range of the expected gravity signal for the science targets previously identified; $l_{min}$is referred to the quadrupole signal whereas l_{max} is an incremental value starting from the current knowledge of the gravity field for that body

Venus	**h (km)**	**l_{ds} (known)**	**l_{min}**	**l_{max}**	**Δs (km)**	**$\Delta\nu$ (Hz)**	**Minimum sampling frequency (Hz)**
	200	70	2	100	190	$7.3\ 10^{-4}$-$3.7\ 10^{-2}$	$7.4\ 10^{-2}$
	200	70	2	150	127	$7.3\ 10^{-4}$-$5.5\ 10^{-2}$	$1.1\ 10^{-1}$
	200	70	2	200	95	$7.3\ 10^{-4}$-$7.3\ 10^{-2}$	$1.5\ 10^{-1}$
	200	70	2	250	76	$7.3\ 10^{-4}$-$9.2\ 10^{-2}$	$1.9\ 10^{-1}$
	300	70	2	100	190	$7.2\ 10^{-4}$-$3.6\ 10^{-2}$	$7.2\ 10^{-2}$
	300	70	2	150	127	$7.2\ 10^{-4}$-$5.4\ 10^{-2}$	$1.1\ 10^{-1}$
	300	70	2	200	95	$7.2\ 10^{-4}$-$7.2\ 10^{-2}$	$1.4\ 10^{-1}$
	300	70	2	250	76	$7.2\ 10^{-4}$-$8.9\ 10^{-2}$	$1.8\ 10^{-1}$
	350	70	2	100	190	$7.1\ 10^{-4}$-$3.5\ 10^{-2}$	$7.0\ 10^{-2}$
	350	70	2	150	127	$7.1\ 10^{-4}$-$5.3\ 10^{-2}$	$1.1\ 10^{-1}$
	350	70	2	200	95	$7.1\ 10^{-4}$-$7.1\ 10^{-2}$	$1.4\ 10^{-1}$
	350	70	2	250	76	$7.1\ 10^{-4}$-$8.9\ 10^{-2}$	$1.8\ 10^{-1}$
Mars	200	100	2	100	107	$6.1\ 10^{-4}$-$3.0\ 10^{-2}$	$6.0\ 10^{-2}$
	200	100	2	150	71	$6.1\ 10^{-4}$-$4.6\ 10^{-2}$	$9.2\ 10^{-2}$
	200	100	2	200	53	$6.1\ 10^{-4}$-$6.1\ 10^{-2}$	$1.2\ 10^{-1}$
	200	100	2	250	43	$6.1\ 10^{-4}$-$7.7\ 10^{-2}$	$1.5\ 10^{-1}$
	300	100	2	100	107	$5.9\ 10^{-4}$-$2.9\ 10^{-2}$	$5.8\ 10^{-2}$
	300	100	2	150	71	$5.9\ 10^{-4}$-$4.4\ 10^{-2}$	$8.8\ 10^{-2}$
	300	100	2	200	53	$5.9\ 10^{-4}$-$5.9\ 10^{-2}$	$1.2\ 10^{-1}$
	300	100	2	250	43	$5.9\ 10^{-4}$-$7.4\ 10^{-2}$	$1.5\ 10^{-1}$

As shown the previous equation, the frequency of the gravity signal decreases with the orbit height increase ($\Delta\tau$ increases), while it increases with the rise of the searched degree l.
For Mars the maximum frequency range of the gravity signal of interest spans within the range 2.9 10^{-2} – 7.4 10^{-2} Hz, depending on the chosen altitude and the gravity signal degree investigated (Table 4-7); this means that the sampling frequency of the measurement should be equals, at least, or higher than twice these frequencies. Therefore, the sampling frequency spans from about 0.06 Hz for a 200-300 km orbit height and a maximum degree l =100 till to 0.15 Hz for the same altitudes and a degree l = 250.
For Venus the maximum frequency of the signal would span in the range 3.5 10^{-2} – 9.2 10^{-2} Hz; in this case the sampling frequency of the measurements along the orbit should be from a minimum of 0.07 Hz for a 200-300 km orbit height and a maximum degree l =100 till to a maximum of 0.18-0.19 Hz for a 200-350 km height and a maximum degree l =250.
This means that the use of a gradiometer in the scenarios hypothesised requires a frequency band in those ranges. In particular, the upper limit is caused by the sampling rate used to collect the measurements along the spacecraft's orbit. The lower limit is computed with the same procedure as well. However, such a lower limit is typically nominal, since the effective achievable lower frequency is affected by instrumental and environmental effects. Typically, the thermal stability performance of the gradiometer affects the measured signal at lower frequency. Moreover, environmental effects due to non-gravitational perturbations affect, as well, the lower frequency. Therefore, these effects at lower frequencies can degrade the measured signal, although belonging to the frequency band.
A summary of requirements derived is reported in Table 4-8.

Table 4-8 Summary of mission requirements for a spacecraft with a gradiometer targeted at Mars and Venus

Planet	SC altitude (km)	Degree (max)	Signal level (m/s^2)	Frequency band (Hz)	Sampling frequency (Hz)
Mars	200	100-300	$2x10^{-13}$ – $3x10^{-18}$	$6x10^{-4}$-$8x10^{-2}$	6.0 10^{-2} - 1.5 10^{-1}
	300		$2x10^{-14}$ – $7x10^{-22}$	6.1 10^{-4}- 7.7 10^{-2}	5.8 10^{-2} - 1.5 10^{-1}
Venus	200	100-250	$6x10^{-13}$ – $5x10^{-15}$	$7x10^{-4}$-$1x10^{-1}$	7.4 10^{-2} –1.9 10^{-1}
	300		$1x10^{-13}$ – $9x10^{-17}$	7.2 10^{-4}- 8.9 10^{-2}	7.2 10^{-2} –1.8 10-
	350		$6x10^{-14}$ – $1x10^{-17}$	7.1 10^{-4}- 8.9 10^{-2}	7.0 10^{-2} –1.8 10^{-1}

An intrinsic issue is the reduction of gravity signal intensity as much as the distance from the source increases. Moreover, the signal magnitude is related to the mass source size, i.e. to the spatial scale. Therefore, at any given height the short-wavelengths (small features) are attenuated more than the long-wavelengths (large features). This means the altitude acts as a low-pass filter, fostering the large spatial scales and hence the low harmonics degrees (long-wavelengths).
Actually, considering the spherical harmonics expansion of the gravity gradient Γ_{rr} (radial component), which is a physical observable, this effect is well evidenced by the attenuation factor A figuring in front of it:

$$\Gamma_{rr}(r,\lambda,\varphi) = -\frac{GM}{R^3}\sum_{l=0}^{l_{max}}\sum_{m=0}^{l}(l+1)(l+2)\left(\frac{R}{r}\right)^{l+3} P_{lm}(\sin\varphi)\,(C_{lm}\cos m\lambda + C_{lm}\sin m\lambda)$$

$$A_{\Gamma_{rr}} = \frac{GM}{R^3}(l+1)(l+2)\left(\frac{R}{r}\right)^{l+3}$$

However, an important difference arises for the attenuation factor caused by the differentiation process with respect to the case of the gravitational potential (although not observable) or the gravity anomaly, respectively given by:

$$A = \frac{GM}{R}\left(\frac{R}{r}\right)^{l+1}$$

$$A_{\Delta g} = \frac{GM}{R^2}(l-1)\left(\frac{R}{r}\right)^{l+2}$$

Indeed, the gravity gradient introduces a multiplier factor $(l+1)(l+2)$ which allows in part to counteract the decrease of the field intensity due to the altitude and in part to amplify the components at high frequency, i.e. at high l and hence with high spatial resolution, as shown in Figure 4-12 and Figure 4-13. Indeed, satellite gradiometry, being derived as double derivative of the gravitational potential, allows to highlight the small-scale effects described by the higher degrees in the field. The factor $(l+1)(l+2)$ increases the power content for high degrees and at the same time counteracts partially the attenuation due to the altitude $((R/r)^{l+3})$.

The following Figure 4-12 and Figure 4-13 depict the behaviour of this factor (normalised with respect to the constant factor GM/R) versus the achieved spatial resolution, evaluated through $\Delta S = \pi R/l$, and versus the degree l of the field. Different orbit heights are considered ($100 - 500\ km$), with Mars as example of central body. The attenuation depends on the altitude and on the harmonic degree. For achieving any given spatial resolution, lower orbits should be preferred since they imply less attenuation and hence guarantee higher signal strength. For the same orbit, low degree harmonics (i.e. low resolutions) are fostered with respect to high degrees. Any gravity mission scenario aims at keeping the operative orbit as lower as possible to enhance the gravity signal. Moreover, such an approach is important as much as higher are the harmonics degrees to be investigated.

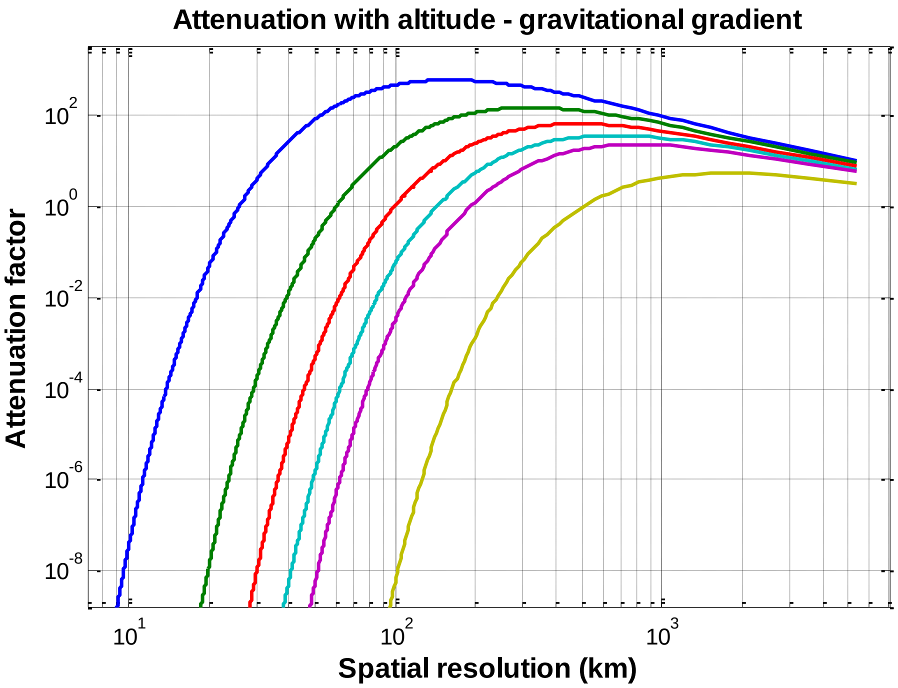

Figure 4-12: Attenuation factor of the gravity gradient versus the spatial resolution (planet Mars), for different orbital altitude. Different orbit heights are shown in colors: from left to right, 100 to 500 km (100 km step) and at last 1000 km

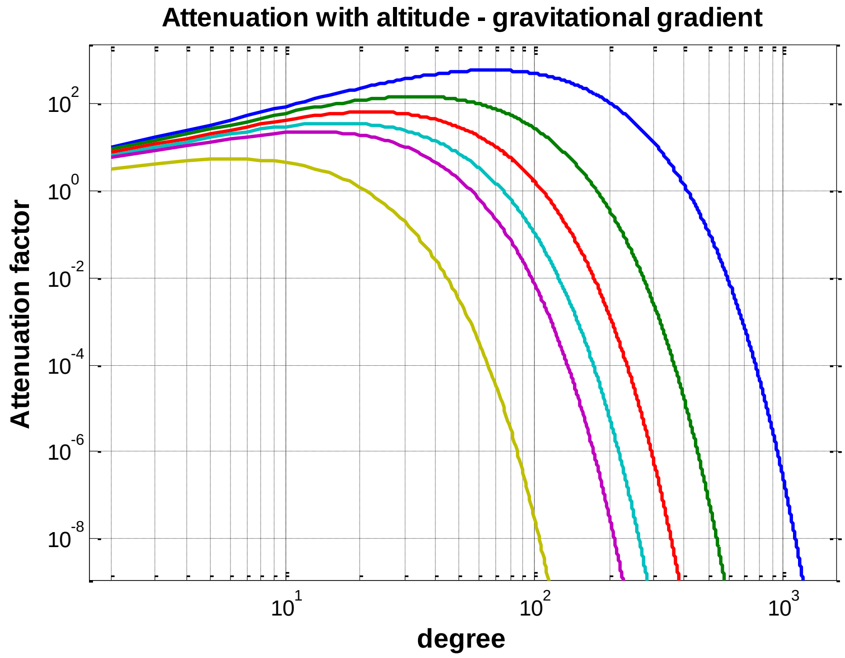

Figure 4-13: Attenuation factor versus the degree l for the gravity gradient. The same legend of previous figure is adopted.

4.4 Spacecraft requirements

In general, in the design of a gravity mission, errors related to gravity-sensing can be organised in three groups [185]: instruments-related, spacecraft-related and instrument/spacecraft coupling related. A list of main components is reported in Table 4-9. Instrument errors depend on the gravity sensing instrument. In case of a gradiometer, the most important is the instrument intrinsic noise. Basically, the intrinsic noise is generated by the combination of different sources such as thermal noise and electrical noise. Concerning intrinsic noise of the instrument, it is a combination of the Brownian noise of the test masses and intrinsic noise of the amplifier. To this respect, a proper low thermal sensitivity needs to be guaranteed by the gradiometer and a robust thermal control needs to be taken into account. However, other sources intervene in the overall budget. From the geometrical point of view, gradiometers based on accelerometers introduce errors in terms of misalignment of sensing axes and scale factor mismatch, i.e. the factor which translates the sensed acceleration into a voltage signal. Indeed, the differential approach allows to highlight the difference of sensed signals (differential mode), i.e. the gravitational gradient, and to (ideally) remove any disturbance with the same amplitude contemporary detected by the coupled accelerometers (common mode). Any geometrical asymmetry in terms of alignment and scale factor determines how well the common accelerations are rejected by carrying out the difference of outputs.
The coupling errors depend on the performance of the instrument and the spacecraft together: coupling of the satellite external perturbations with the misalignments of the instrument, coupling of satellite micro-vibrations and temperature variations with instrument characteristics. The GOCE experience proved that improvement of performance was achieved by optimising the spacecraft characteristics so to minimise their impact on the gradiometer. However, this is a special condition since typically a trade-off needs to be achieved.

The spacecraft errors include attitude recovery and pointing errors, errors in the determination of the external accelerations, on-board generated, such as motion of appendages, and external generated, such as the surface forces (drag, solar radiation, etc.).

Table 4-9 Some error sources in gradiometry [125]

Subsystem	***Type***	***Error***
instrument	geometrical	misalignment of accelerometers
		scale factor mismatch
		non-orthogonality of accelerometer sensing axes
		misalignment of accelerometers in gradiometer frame
	physical	accelerometers non-linearity
		scale factor stability
		calibration errors
		instrument noise
		finite baseline of the instrument
spacecraft	attitude	orientation
		unmodelled rotations
	non gravitational forces	surface forces (solar radiation, drag)
	environmental disturbances	micro-vibrations
		thermal variations
	self-gravitation	time varying components due sloshing and fuel consumption
		dynamic appendages (solar arrays, antennas, etc)
		reaction wheels noise

4.5 Instrument requirements

In order to derive some requirements for a gradiometric instrument needing to satisfy the mission requirements, the values adopted for ISA and JUICE accelerometer are the starting point.
Elements addressed in this section will be used to identify and design a gradiometer configuration able to perform the gravity gradient measures whose requirements have been derived in previous chapters. Heritage derived from know-how and expertise at IAPS on accelerometers and gradiometres is maximised.
The gradiometer is basically constituted by one or more couples of accelerometers. They can be linearly or angularly coupled, obtaining the configurations of linear gradiometer or angular gradiometer.
We consider hereafter a linear gradiometer with one or more coupled linear accelerometers. In this case the basic element of the gradiometer is a couple of linear accelerometers separated by a finite distance. Hoever, considerations hereinafter reported can be applied to an angular gradiometer as well.
The starting point for ISA or HAA-like accelerometers is their performance that can be summarised in the following Table 4-10.

Table 4-10 Main characteristics of ISA and HAA accelerometers on-board BepiColombo and JUICE missions, respectively

Instrument	ISA	HAA
Mission	BepiColombo	JUICE
Status	On flight (October 2018)	Development (launch 2022)
Measurement band (Hz)	$3 \cdot 10^{-5} - 10^{-1}$	$10^{-4} - 10^{-1}$
Accuracy $(m\ /\ s^2)$	10^{-8}	10^{-8}
Noise floor $(m\ /\ s^2/\sqrt{Hz})$	$3 \cdot 10^{-8} @\ 10^{-4}Hz,$ $7 \cdot 10^{-9} > 7 \cdot 10^{-4}Hz$	$3 \cdot 10^{-8} @\ 10^{-4}Hz,$ $8 \cdot 10^{-9} > 8 \cdot 10^{-4}Hz$
Active thermal control	1 mK	1 mK
Weight (kg)	≈9	≈14
Power consumption (W)	≈20	≈30

Taking into account such values, the following considerations can be carried out.
As derived in section 4.3, the frequency band of the expected gravity signal should belong to specific ranges. For a spacecraft orbiting Venus at an altitude between $200 - 350\ km$, the frequency range of the gravity signal covering $l = 2 - 200$ degrees belongs to the range $\sim 7\ 10^{-4} - 9\ 10^{-2}Hz$. In a similar approach, a spacecraft orbiting Mars at an altitude between $200 - 300\ km$, the frequency range for a gravity signal within the degrees $l = 2 - 250$ would cover the interval $\sim 6\ 10^{-4} - 9\ 10^{-2}Hz$.
From these considerations, it derives that the frequency requirement for the instrument should cover the range $\Delta\nu \sim 10^{-4} - 10^{-1}\ Hz$.
Concerning the signal level, a gradiometer with two coupled ISA- or HAA-like linear accelerometers placed at a distance of $1\ m$ would achieve roughly a sensitivity:

$$S = \frac{10^{-8}}{1} = 10^{-8}\ s^{-2} = 10\ E$$

This is a rough value assuming that the overall sensitivity of the gradiometer is equals to the sensitivity of its components, i.e. the accelerometers, here assumed ISA or HAA-like.
It is obvious that such a sensitivity is not enough to achieve the required performance measurements shown in the previous chapters. Moreover, it is not possible to extend the baseline between the sensors to enhance the sensitivity, because $1\ m$ or $2\ m$ is already a limit distance for a single spacecraft. Therefore, the instrument sensitivity needs to be increased significantly to achieve a value comparable with the signal level to be measured.
To increase the sensitivity of a gradiometer it needs to increase the sensitivity of the componing accelerometers. This can be achieved by acting on the factors limiting the sensitivity. These considerations can be applied both to linear and angular gradiometer.
A first preliminary choice needs to be aimed at the measurement approach. An open-loop scheme foresees a measure of the acceleration through an accurate measure of the displacement of a suspended sensing mass (suspended by spring, electrostatic force,

magnetic induction, or other system, see section 3.3.2.3); this is the ISA/BepiColombo and HAA/JUICE case. On the other hand, in a closed-loop scheme the sensing mass displacement is compensated by a feedback force, usually of electrostatic-type, and this force is proportional to the acceleration input.
On the basis of the ISA/HAA background the focus is herafter kept on the open-loop scheme. Indeed, the closed-loop scheme requires a different approach and especially a dedicated study on the feedback electronics and on the experimental operation and effectiveness of such a system. This is out of the scope of this work and could be dealt withas future activity in the group at IAPS.
Considering the open-loop approach, the sensor sensitivity can be increased by acting on specific elements, some of them being:

- transduction factor, depending on the transfer function (resonance frequency) and on the geometry of pick-up/actuator plates/sensor design
- thermal sensitivity, due to the combination of intrinsic thermal sensitivity of the sensor and to the performance of the thermal control
- sensor cooling

Transduction factor
Such a term is defined by the sensor output to the input acceleration ratio and it is directly related to the sensitivity. It depends on the transfer function of the sensor and its related resonance frequency, in addition to the geometry of pick-up plates and of the sensor in general.
Concerning the transfer function, referring to the section “3.3.2.3 Mechanically-suspended gradiometers”, the useful band of an accelerometer is identified by the flat part of the transfer function, characterised by a lower limit, typically constrained by thermal inputs, and an upper limit, fixed by the resonance frequency. These limits define the operative bandwidth and at the same time the achievable sensitivity.
Indeed, the resonance frequency is directly related to the sensitivity since in the flat region (section 3.3.2.3) the relation $x(\omega) \approx a(\omega)/\omega_0^2$ applies, where the sensed acceleration (a) and the proof mass displacement (x) are linked through the resonance frequency $\omega_0 = 2\pi\nu_0$. This relation highligths that reducing the resonance frequency provides an increase of the sensor response through a higher displacement of the sensing mass (x), with the same acceleration as input; hence, the sensitivity can be increased by reducing the resonance frequency. This is possible in different ways; for instance, by acting on the spring design and/or on the geometry of the sensor and /or by reducing the operating temperature of the system (point faced later).
Concerning the spring, it can be realised with different shapes and thickness (and materials for the whole sensor), depending on the type of gradiometer, i.e. linear or angular one, because different type of oscillations will be mainly solicited: typically, flexural modes for a linear gradiometer, while torsional modes for an angular gradiometer. The shape and the size affect the resonance frequency, while the material affects especially the thermal sensitivity and the endurance of the spring to the strong solicitations (this is of particular importance, for instance, to sustain stresses at launch). Taking into account the physical description of an accelerometer as a mechanical oscillator forced and damped (see section 3.3.2.3 and 5), the relation expressing the resonance frequency (ν_0) in terms of the system charateristics is:

$$\nu_0 = \frac{1}{2\pi}\sqrt{\frac{k_t}{I}}$$

where k_t is the spring constant while I is the moment of inertia. Applying this relation for coupled accelerometers, it shows off that, in general, a low frequency can be obtained by increasing the moment of inertia, i.e. increasing the mass and/or its distance from the rotation centre, for instance making thin and long arms to hold the sensing mass, and reducing the elastic constant of the spring, i.e. shape, size and eventually material. Although, indeed, it is difficult to realise mechanical oscillators with a frequency below 1 Hz. The increase in sensitivity (and hence the change in the transduction factor) can be evaluated taking into account the relation $x(\omega\ ) \approx a(\omega\ )/\omega_0^2$.
For two different frequencies, $\omega_1$and ω_2, and same input a, it holds:

$$x_2 = \frac{{\omega_1}^2}{{\omega_2}^2}\, x_1$$

i.e. the increase in sensitivity is related to the squared ratio between the resonance frequencies. This implies that a change in the frequency allows to change significantly its sensitivity.
As geometry of the sensor we mean the structure of the plates, their surfaces, the gap between plates. Indeed, the geometry of pick-up plates is another element on which to act. Tthe conversion of the sensing mass displacement into an electric signal can be carried out through different approaches. Referring to the ISA and HAA operations, as reported in section 3.3.2.3, a scheme based on a capacitive sensing can be adopted. A capacitive sensing translates a mechanical displacement of the sensing mass into a capacitance change between a couple of fixed plates and the sensing mass itself (mobile plate). Inserting this coupling within a capacitive bridge, including another couple of capacitances, allows to transform the capacitance change due to sensing mass displacement in a voltage change.
Referring to [157] and Figure 4-14, it is possible to prove that :

$$V_{out} \equiv V_{AB} = V_p \left(\frac{1}{1 + \frac{C_b}{C_a}} - \frac{1}{1 + \frac{C_2}{C_1}} \right)$$

where the V_p is the bias of the bridge, C_a and C_b fixed capacitances, whereas C_1 and C_2 are the variable capacitances between sensing mass and fixed plates, depending on the mass position.

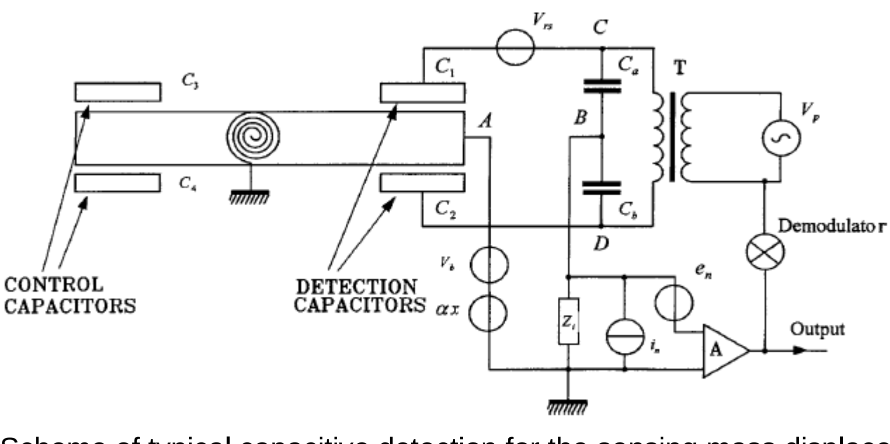

Figure 4-14: Scheme of typical capacitive detection for the sensing mass displacement (extract from [157])

Assuming $C_a = C_b = C$, the relation is simplified to:

$$V_{out} = \frac{V_p}{2}\left(\frac{C_2 - C_1}{C_1 + C_2}\right)$$

meaning that a voltage signal from the bridge is generated only when the sensing mass is not in central position with respect to the plates, i.e. when an external acceleration moves the sensing mass inducing a capacitance unbalance. Capacitances are related to the geometry of the sensor, according to the basic relation:

$$C = \varepsilon_0 \frac{S}{d_0}$$

where $\varepsilon_0 = 8.854\ 10^{-12}$ [F/m] is the vacuum dielectric constant (assuming vacuum between plates), d_0 is the nominal distance between the plates (or gap) and S the surface of each plate.
From those elements it derives that the sensitivity can be properly increased by reducing the plates gap and/or by raising the plates surface. Therefore, acting properly on these geometric parameters the sensitivity can be modified and improved.
Two other plates form another pairs of capacitors (C_3 and C_4) used to create an electrical field to force the position of the proof mass. They are used to allow the calibration of the system and to control some electromechanical parameters of the accelerometer (e.g. the mechanical Q factor).

Thermal sensitivity
One of the limiting factors of instrument accuracy is its sensitivity to temperature variations. For this reason, accelerometers are typically equipped with an active thermal control system that allows to stabilise the sensors temperature within fixed values; such a control is at less than 1 mK for ISA and HAA, a value at performance level for systems of this type. Although the use of such a control, a contribution from thermal variations comes into the overall budget error and hence to the final sensitivity. It is related to the intrinsic thermal sensitivity of the sensor, i.e. to the level of acceleration introduced per each change of temperature degree. The contribution of such a term to the overall budget can be reduced acting on the used materials and on the chosen geometries of the sensor (pick-up, actuators, spring-frame link). The basic driver is to reduce as much as possible internal temperature gradients and differential deformations.
Supposing a thermal stability of the instrument environment of 10^{-2} °C/day and taking into account that the signals to be detected are in the range 10^{-4}-10^{-1} Hz, we get that during the measure the temperature changes, as worst case, of:

$$\Delta T = \frac{10^{-2}}{86400} 10^4 = 1.2\ 10^{-3}\ °C$$

This implies that a gradiometer with a sensitivity of the order of 10^{-4} E (as derived before) needs to have an intrinsic stability of at least:

$$\Delta T_{stab\_grad} = \frac{10^{-4}}{1.2\ 10^{-3}} \approx 8 *\ 10^{-2} \frac{E}{°C} = 8 * 10^{-11} \frac{s^{-2}}{°C}$$

while the accelerometers components should have a stability of:

$$\Delta T_{stab\_acc} = \frac{10^{-14}}{1.2\ 10^{-3}} \approx 8 * 10^{-12}\ m/s^2/°C$$

Such a level of stability is very demanding for a single accelerometer. It can be achieved through a combination of low intrinsic thermal sensitivity and of well performing thermal control system.
The latter one can be tailored on the sensor by making a thermal control able to reduce thermal inputs by a suitable factor, for instance a factor 1000 (in case of ISA accelerometer) or better.
On the other hand, the intrinsic thermal sensitivity needs to be reduced as much as possible, in agree with the technology used for making the sensor, in order to achieve the expected overall thermal performance.
Different strategies can be pursued to improve the thermal behaviour of a sensor and hence its thermal sensitivity (i.e. variation of the pick-up and actuation capacitances as the thermal environment changes under operational measurement conditions), depending on the technology employed to make the sensor. Referring to the ISA and HAA technology (see section 3.3.2.3), some elements to be addressed in this perspective are the following:

- Reduce as much as possible, wherever present, the use of materials withdifferent coefficients of thermal expansion (CTE), in order to mitigate thermoelastic distortion and stress within the system and to reduce the thermal sensitivity.
  Indeed, in the ISA and HAA design, the mechanical sensor is basically constituted by two couples of plates facing the central proof mass (capacitive sensor), separated by a gap. The gap and the electrical isolation between them is maintained by using alumina washers. During thermal variations, the different CTE of aluminium, alumina and steel of fasteners (about 24 ppm/°C, 6 ppm/°C and 8 ppm/°C, respectively), can induce non-uniform thermoelastic distortions, changing the capacitance between plates and sensing mass and hence making the structure more sensitive to thermal variations.
- Mitigate the deformations induced on the plates by the temperature, affecting the flatness and hence the capacitance, by reviewing the mechanical design and the way in which plates and sensing mass are joined together.
- Another element to address in order to reduce the thermal sensitivity is the reduction of the proper frequency. This action is strictly related to the sensitivity and hence to the transduction factor. Indeed, the reduction of the resonance frequency allows to improve the sensitivity of a certain factor (depending on the squared ratio of frequencies) by increasing the displacement of the sensing mass with the same input acceleration. At the same time, this implies an increase of the same factor of the detected signal over the signal induced by the thermal sensitivity. The final effect is a reduction of the sensitivity to thermoelastic deformations on the sensor structure by the same factor.
- A more radical approach would be the change of the material used to make the sensor (Al7075 for ISA and HAA), aiming at looking for materials with a more robust thermal stability. This approach would be very interesting but would need to be deeply and carefully investigated because it would mean to identify the proper material not only in terms of thermal stability but also in terms of mechanical manufacturing, to review the whole design of the capacitive “sandwich” and its components (insulators, fasteners, etc.) and, especially, to test and to prove the improvement in the achievable performance.

At last, the fundamental sensitivity of any sensor is determined by the thermal noise limitation. In practice, this limit can never be reached, but many systems can approach it very closely.
Because this basic limit is dependent upon energy considerations, its computation depends only upon very general parameters of the sensor, such as its temperature, mass, effective length, and time of integration. The results can then be applied to all sensors, regardless of their detailed design. The basic formula states that the signal-to-noise ratio is given by the ratio of the signal energy stored in the sensor to the thermal energy (kT) present in the sensor. It is reported here the relation as provided by [176]. Such a relation yields the minimum gradient that can be measured for a thermally limited sensor:

$$\Gamma_{min} = \frac{(S/N)^{0.5}}{2\ d\ \tau}\left(\frac{2kT}{m_{tot}}\right)^{0.5}$$

where S/N is the desired signal-to-noise ratio, d is the distance between the sensing masses, τ is the time in which the measure needs to be integrated (integration time), k is the Boltzmann constant, T is the temperature of the instrument.

Sensor cooling
Since one of the limiting factors of the sensitivity is the temperature, the possibility of implementing a system to cool the sensor could be envisaged. Indeed, the use of a cryogenic system would allow to low the operating temperature. In these studies ([171][172][174]) such an approach is pursued. Although in these cases the main reason for the use of cryogenics temperatures is the use of superconducting materials to exploit their characteristics (see section 3.3.2.4), in general a gain in sensitivity is achieved because lowering the temperature allows to reduce the Brownian noise. Indeed, the Brownian motion of the sensor structure causes a thermal noise whose amplitude needs to be taken into account and reduced.
However, the drawback is to complicate significantly the instrument operation, increasing the mass of the instrument, including as well the cryogenic system and the related fluid. Moreover, being this cooling related to the availability of a cryogenics on-board, this affects deeply the mission lifetime, in addition to the overall mass budget.

At last, the overall considerations and analyses previous carried out allow to summarise some of the instrument requirements to perform the proposed measurements inTable 4-11.

Table 4-11 Summary of the main instrument requirements

<table>
<tr><th>Variables</th><th colspan="7">Values</th></tr>
<tr><td></td><td colspan="3">Venus</td><td colspan="4">Mars</td></tr>
<tr><td>orbit altitude (km)</td><td colspan="3">200-350</td><td colspan="4">200-300</td></tr>
<tr><td rowspan="2">Signal (s^{-2})</td><td>10^{-13}-10^{-14}</td><td rowspan="2">Spatial resolution</td><td>l = 100 (190 km)</td><td rowspan="2">Signal (s^{-2})</td><td>10^{-13}-10^{-14}</td><td rowspan="2">Spatial resolution</td><td>l = 100 (107 km)</td></tr>
<tr><td>10^{-15}-10^{-17}</td><td>l = 250 (76 km)</td><td>10^{-18}-10^{-22}</td><td>l = 300 (36 km)</td></tr>
<tr><td>Signal Frequency (Hz)</td><td colspan="3">$\sim 7\ 10^{-4}\ - 9\ 10^{-2}$</td><td colspan="4">$\sim 6\ 10^{-4}\ - 8\ 10^{-2}$</td></tr>
</table>

Minimum sample frequency (Hz)	$7.0\ 10^{-2}$ –$1.9\ 10^{-1}$	$6.0\ 10^{-2}$ - $1.5\ 10^{-1}$
Length (m)	< 2 m	< 2 m
Mass (kg)	< 50	< 50

5. Angular Gravity Gradiometer

In the following a preliminary model of a cross-component gradiometer is analysed and studied. The analysis starts from the use of IAPS technology heritage to envisage a sensor structure to be used as basic element of a torsion-balance gradiometer and aimed at the measurement of the gravity gradient cross-component.
On the basis of previous analyses, an instrument concept, able to satisfy the identified requirements to accomplish the gravity gradient measures, is proposed for a gravity gradiometer to be used in a space mission scenario. The mission scenario is realised on the basis of the science needs previously identified:

- On the basis of the simulation (matlab code), gravity gradient values were derived for Venus and Mars.
- On the basis of IAPS-technology heritage and the review of literature studies on gravity gradiometers, a sensor structure has been envisaged to be used as basic element of an angular accelerometer aimed at the measurement of the gravity gradient cross-component.
- The instrument has been designed taking into account the considerations on the increase of sensitivity carried out in section 4.5, in order to match the requirements.
- The instrument is based on a torsion-balance approach to the gravity gradiometer. It is constituted by two couples of test masses joined through two rods each one to a common centre by a torsional spring with constant k_t.
- The system looks like a dumbbell or precisely a barbell, i.e. a dumbbell with a long bar. The axis of the torsional spring constitutes the rotation axis of the system as well. Masses are constrained to rotate around it.
- Due to the intrinsic geometry, such a system is inherently sensitive to the ZY component of the gravity gradient, Γ_{zy}, and to the difference $\Gamma_{zz} - \Gamma_{yy}$.

5.1 Instrument concept

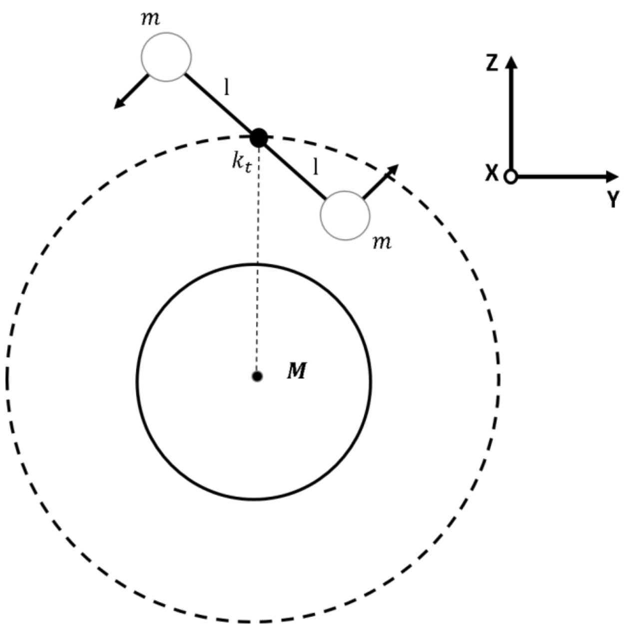

Figure 5-1: schematic view of the torsion-balance gradiometer around a planetary body; x axis is orthogonal to the orbital plane of the spacecraft hosting the instrument

Consider the system represented in Figure 5-1. The instrument is based on a torsion-balance approach. It is constituted by two proof-masses of mass m located at the ends of two rods of length l joined to a common centre by a torsional spring with constant k_t. The system looks like a dumbbell or precisely a barbell, i.e. a dumbbell with a long bar, where the axis of the torsional spring constitutes the rotation axis of the system. Moreover, in this frame the mass of the rod is assumed negligible. Later the continuous case will be addressed.
The gravity gradient of the central body acts on the masses at the ends of the joining arm and generates a torque on the system, inducing a rotation of the rod that is counteracted by the torsional force of the spring-mass system. Due to the intrinsic geometry and as proved later, such a system is inherently sensitive to the ZY component of the gravity gradient, Γ_{ZY}, and to the difference $\Gamma_{ZZ} - \Gamma_{YY}$.

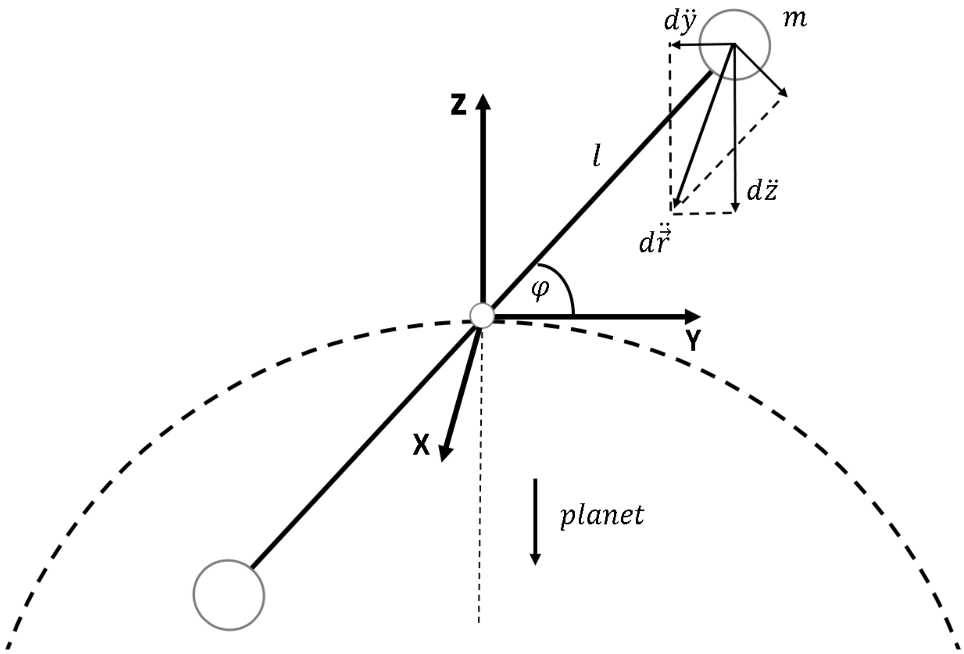

Figure 5-2: Geometric configuration in orbit for the single rod with two masses subjected to the torque of the gravity gradient

Define a local non-rotating orthogonal reference frame centred in the central point of the rod, where the spring is located and where the rotation axis goes through. Y and Z axis are assumed to be in the orbital plane, Z axis is aligned to the outward radial direction along the planet, and X axis is orthogonal outward the Z-Y plane.
The gravity gradient at the centre of the rod is expressed in this frame by the relation:

$$\Gamma_{ij} = \frac{d\ddot{r}_i}{dr_j} \tag{5-1}$$

where i and j are the directions over which to evaluate the gradient and hence $i = y, j = z,$ $k = x$. Referring to the Figure 5-2, the acceleration due to the gravity gradient, $d\ddot{r}_i = \Gamma_{ij}\, dr_j$, can be expressed as follows:

$$\begin{aligned} d\ddot{r}_y \equiv d\ddot{y} &= \Gamma_{yz} dz + \Gamma_{yy} dy \\ d\ddot{r}_z \equiv d\ddot{z} &= \Gamma_{zy} dy + \Gamma_{zz} dz \end{aligned} \tag{5-2}$$

Taken into account the relations in Figure 5-2, it holds:

$$\begin{gathered} dy = dl\ \cos\varphi \\ dz = dl\ \sin\varphi \\ dx = 0 \end{gathered} \tag{5-3}$$

The torque of the force f_{tg}moving the mass m is $M_f = l\, f_{tg}$, where the force is orthogonal to the rod and l is the half-length of the rod:

$$df_{tg} = m\, d\ddot{y}_{tg} \tag{5-4}$$

Moreover, taking into account the design in Figure 5-2, it holds as well:

$$d\ddot{y}_{tg} = d\ddot{z}\cos\varphi - d\ddot{y}\sin\varphi \tag{5-5}$$

Substituting and using the gravity gradient relation:

$$\begin{gathered} df_{tg} = m\,(d\ddot{z}\cos\varphi - d\ddot{y}\sin\varphi) = \\ = m[(\Gamma_{yz}dz + \Gamma_{yy}dy)\cos\varphi - (\Gamma_{zy}dy + \Gamma_{zz}dz)\sin\varphi] \end{gathered} \tag{5-6}$$

and substituting dy and dz:

$$df_{tg} = m\, dl\,(\Gamma_{yz}\cos\varphi^2 + \Gamma_{zz}\cos\varphi\sin\varphi - \Gamma_{yy}\cos\varphi\sin\varphi - \Gamma_{zy}\sin\varphi^2) \tag{5-7}$$

At last:

$$f_{tg} = ml\left[\frac{\Gamma_{zz} - \Gamma_{yy}}{2}\sin 2\varphi + \Gamma_{yz}\cos 2\varphi\right] \tag{5-8}$$

The same applies for the second mass, therefore at last we get for the total torque around the x axis:

$$M_x = M_A + M_B = 2ml^2\left[\frac{\Gamma_{zz}-\Gamma_{yy}}{2}\sin 2\varphi + \Gamma_{yz}\cos 2\varphi\right] \tag{5-9}$$

A gradiometer of this type is sensitive to the off-axis component Γ_{yz} of the gravity gradient and to the difference between two main in-axis components, $\Gamma_{zz} - \Gamma_{yy}$.
The dynamics equation for the system is the damped and forced mechanical oscillator as follows:

$$2ml^2\left(\ddot{\theta} + \frac{\beta}{2ml^2}\dot{\theta} + \frac{k_T}{2ml^2}\theta\right) = M_x \tag{5-10}$$

where θ is the angular displacement due to the torque, $I = 2ml^2$ is the moment of inertia of the body with respect to the rotation axis and ${\omega_0}^2 = k_T/2ml^2$ is the resonance angular frequency with $\omega_0 = 2\pi\nu_0$. Applying to the previous equation of motion for the two test masses system, we get:

$$2ml^2\left(\ddot{\theta} + \frac{\beta}{2ml^2}\dot{\theta} + \frac{k_T}{2ml^2}\theta\right) = 2ml^2\left[\frac{\Gamma_{zz} - \Gamma_{yy}}{2}\sin 2\varphi + \Gamma_{yz}\cos 2\varphi\right] \tag{5-11}$$

The transfer function of such a system (a second order system) is the following:

$$H(j\omega) = \frac{1}{2ml^2(-\omega^2 + j\omega\frac{\beta}{2ml^2} + {\omega_0}^2)} \tag{5-12}$$

Figure 5-3 depicts the behaviour of such a system. The plot is generated considering a system of two masses, 1 kg each one, with a distance of 0.5 m between them and assuming $I = 2md^2$.

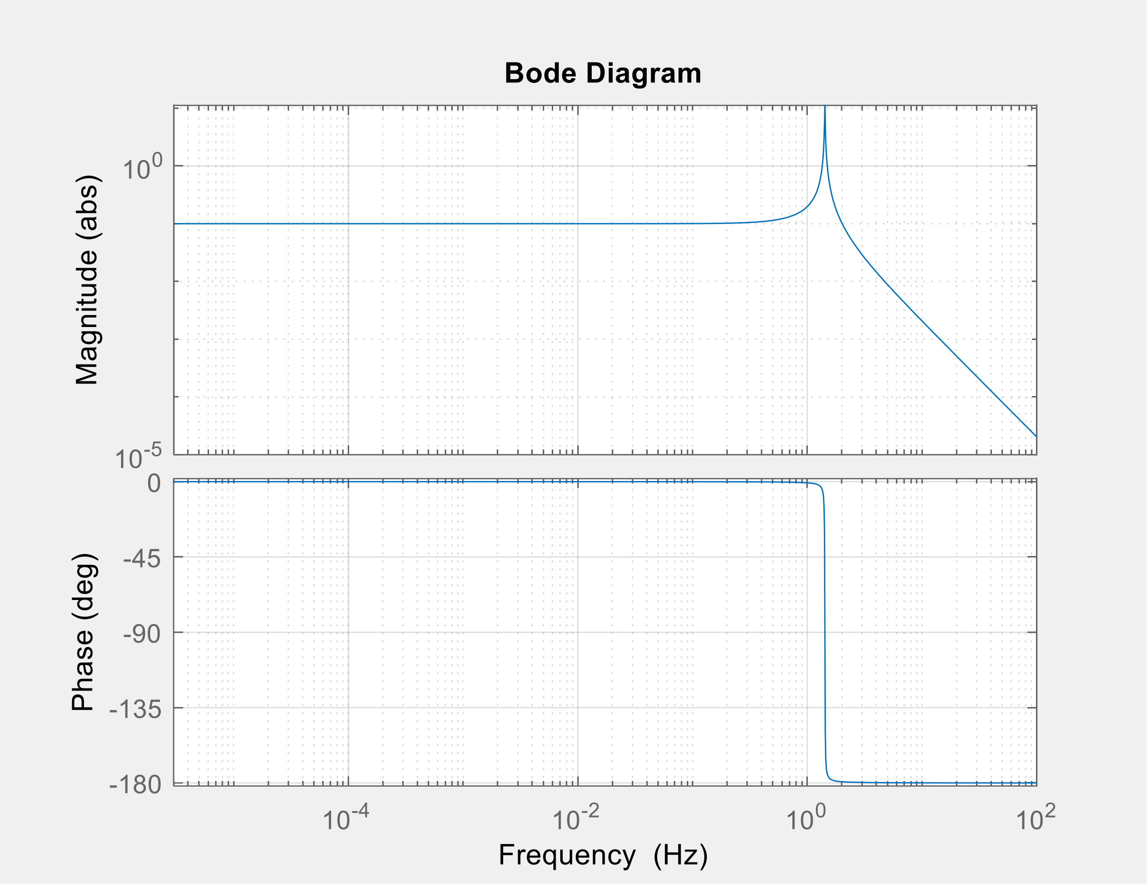

Figure 5-3: transfer function for the single bar - two masses

The transfer function is characterised by a flat region for $\omega \ll \omega_0$, a peak due to the resonance at $\omega = \omega_0$ and a fast decrease for $\omega \gg \omega_0$.
An improvement of such a system can be achieved by adding a second barbell with two proof masses placed in in the x-y plane at angle of 90° with respect to the first one. Figure 5-4 depicts the envisaged system.

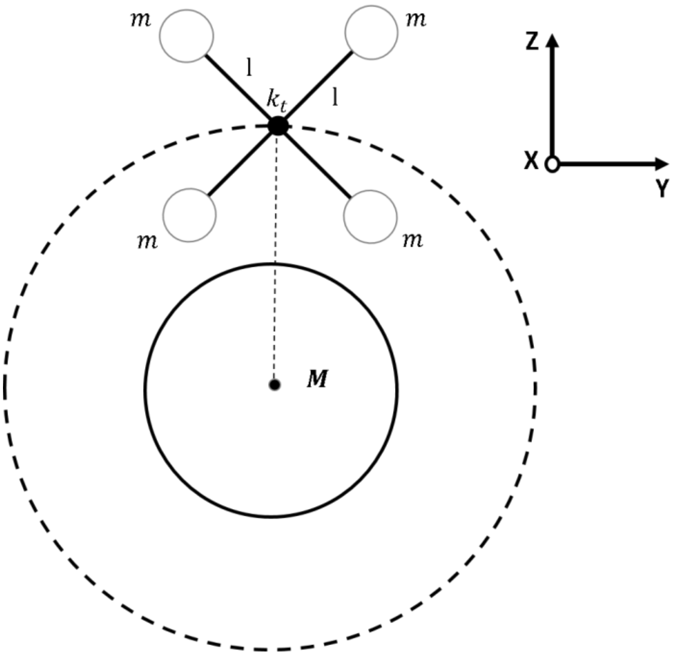

Figure 5-4: improvement of the initial system by adding a second bar orthogonal to the first one

In this case, a further gravity gradient torque M_{CD}, equals to the first one and acting on the second bar, is introduced; however this torque has an opposite sign due to an opposite rotation: $M_{CD} = -M_{AB}$. In this configuration, the effect is to produce a differential torque on the overall system doubled with respect to the previous case:

$$M_x = M_{AB} - M_{CD} = 2M_{AB} = 4ml^2\left[\frac{\Gamma_{zz}-\Gamma_{yy}}{2}\sin 2\varphi + \Gamma_{yz}\cos 2\varphi\right] \quad (5\text{-}13)$$

Consequently, the response to this torque is increased by doubling the induced rotation of the system. The dynamic equation and the related transfer function translates into, respectively:

$$4ml^2\left(\ddot{\theta} + \frac{\beta}{4ml^2}\dot{\theta} + \frac{k_T}{4ml^2}\theta\right) = 2ml^2\left[(\Gamma_{zz} - \Gamma_{yy})\sin 2\varphi + 2\,\Gamma_{yz}\cos 2\varphi\right] \quad (5\text{-}14)$$

and:

$$H(j\omega) = \frac{1}{4ml^2(-\omega^2 + j\omega\frac{\beta}{4ml^2} + {\omega_0}^2)} \quad (5\text{-}15)$$

Figure 5-5 depicts the behaviour of the transfer function in magnitude and phase versus the frequency. The plot is generated considering a system of four masses, 1 kg each one, with a distance of 0.5 m between them and assuming $I = 4ml^2$.

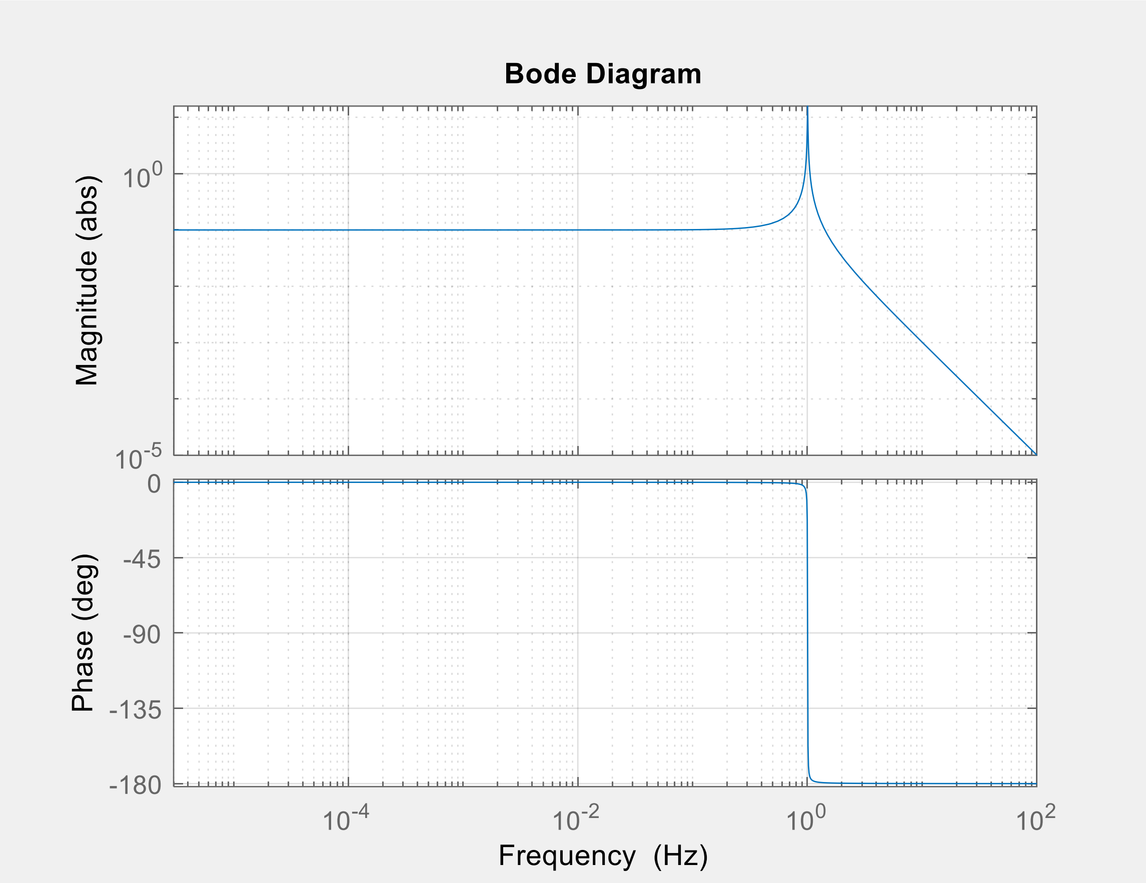

Figure 5-5: improvement in the transfer function for the two orthogonal bars with a couple of masses per each one, subjected to the torque of the gravity gradient

The transfer function is the same type of the previous one, characterised by a flat area for $\omega \ll \omega_0$, a peak due to the resonance at $\omega = \omega_0$ and a fast decrease for $\omega \gg \omega_0$. However, in this case, the change in the configuration modifies the resonance frequency, which decreases, due to the change in the moment of inertia.
In both cases (single and double bar) the typical operating condition is in the flat region, where the expression of the transfer function can be simplified to the following, assuming the condition $\omega \ll \omega_0$:

$$\frac{\theta}{M_x} = \frac{1}{\omega_0{}^2 I} \tag{5-16}$$

By using the expression previously found for the torque of the gravity gradient M_x and for the moment of inertia I, it is possible to get the relation that establishes how the rotation angle θ changes as function of the sensed gravity gradient for the case with two bars (θ_{2r}) (the same happens for the one bar case but adding a factor ½ in front of the expression):

$$\theta_{2r} = \frac{(\Gamma_{zz} - \Gamma_{yy}) \sin 2\varphi + 2\Gamma_{yz} \cos 2\varphi}{I\ \omega_0{}^2} \tag{5-17}$$

The working principle in both cases, single and two bars, is to measure the rotation angle θ due to the gravity gradient corresponding at different positions φ in order to derive the components $(\Gamma_{zz} - \Gamma_{yy})$ and Γ_{yz}. The output of the gradiometer includes two sinusoidal signals in quadrature: the first one is a measurement of the difference between two of the diagonal components $(\Gamma_{zz} - \Gamma_{yy})$ while the second one measures the corresponding off-diagonal component of the tensor Γ_{yz} in the coordinate frame of the sensor.
A way to enhance the weak output signals could be to modulate the output by rotating the crossed bars around the x axis with a constant angular velocity ω. With this approach, the signals to be measured would show off at a doubled frequency (2ω) with respect to the modulation frequency (ω). This condition allows to disentangle in frequency the gradients to be measured from other disturbances, that typically occur at the modulation frequency.
The behaviour of the rotation angle as function of the gravity gradient sensed is depicted in Figure 5-6, while the angle φ is modulated with an angular velocity ω: $\varphi = \omega t$:

$$\theta_{2r} = \frac{(\Gamma_{zz} - \Gamma_{yy}) \sin 2\omega t + 2\Gamma_{yz} \cos 2\omega t}{I\ \omega_0{}^2} \tag{5-18}$$

The plot is produced for a case with $\Gamma_{zz} = 2\ 10^{-13}\ s^{-2}$, $\Gamma_{yy} = 1\ 10^{-13} s^{-2}$, $\Gamma_{zy} = 0.5\ 10^{-13} s^{-2}, \omega = \ 1\ 10^{-3}\ rad/s$, i.e. $\nu = \ 1.6\ 10^{-4}\ \mathrm{Hz}$, a moment of inertia $I = 2.5\ 10^{-1}\ \mathrm{kg}\ m^2$; the system is composed of four masses, 1 kg each one, with a distance of 0.5 m between them.

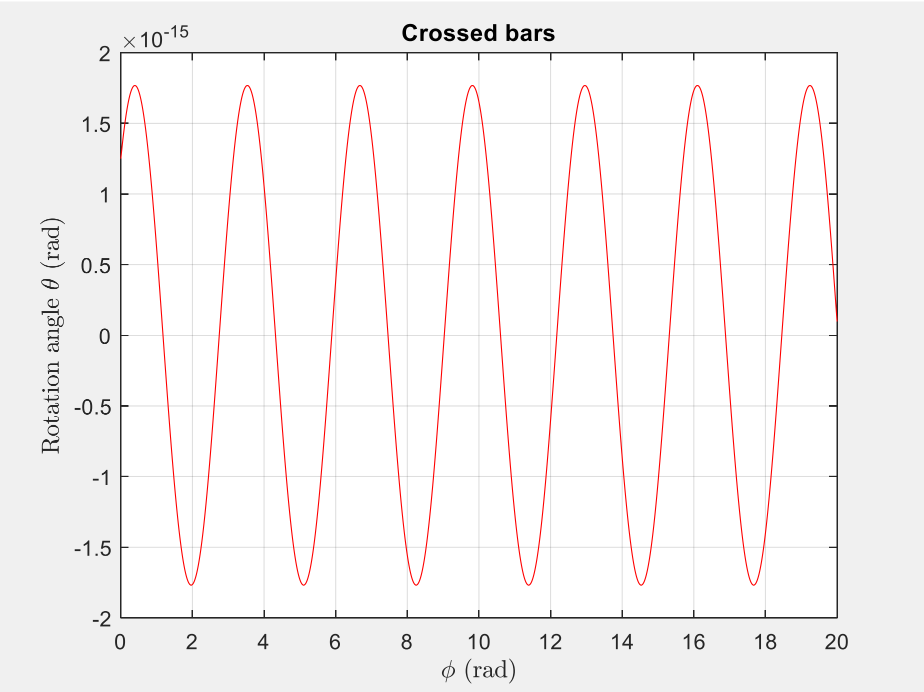

Figure 5-6: Modulation of the rotation angle θ induced by the gravity gradient torque when the crossed bars are rotated by the angular velocity ω

In this case, the gravity gradient induces a rotation of the system of an angle θ while the system is rotated around x axis by the angular velocity ω. The value of the angle is found at a doubled frequency (2ω) with respect to the modulation frequency, as depicted in Figure 5-7.

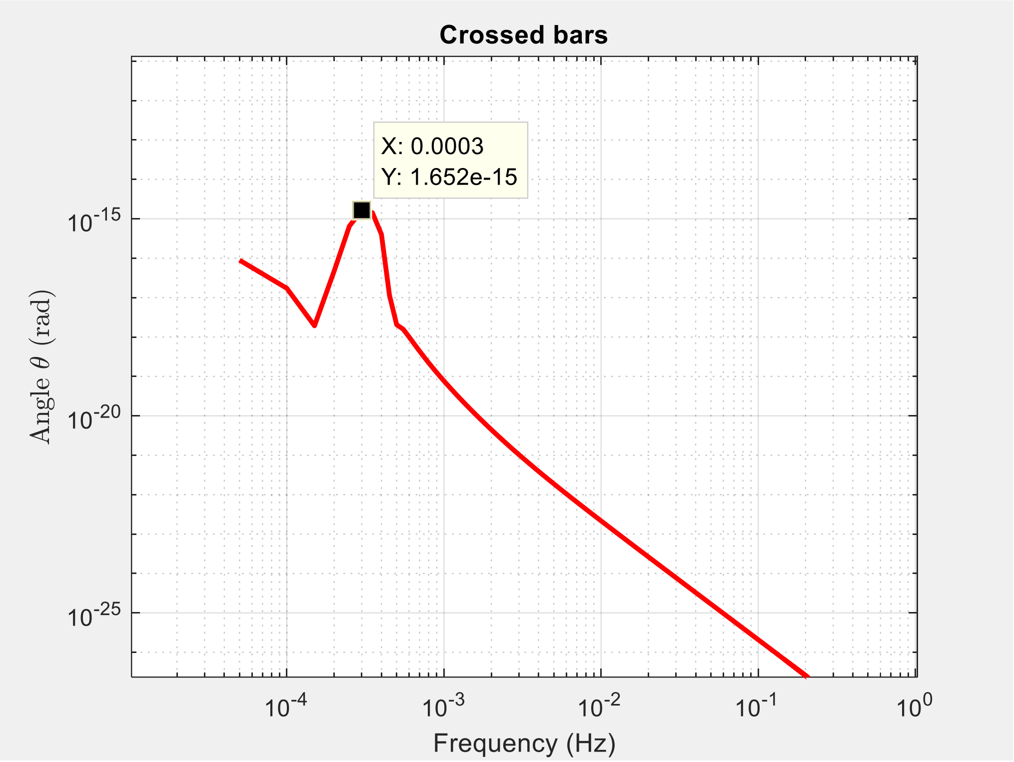

Figure 5-7: PSD of the modulated signal of previous figure. The peak is $\sim 1.6\ 10^{-15}\ rad$ at $\sim 3.2\ 10^{-4} Hz$, double of the modulation frequency

A gravity gradient of the order of $10^{-13} s^{-2}$induces between the arms a relative rotation $\theta \sim 1.6\ 10^{-15}\ rad$, corresponding to a linear displacement $\Delta x = \ \theta \cdot l\ {\sim}4\ 10^{-16} m.$.

The same equations above derived can be extended for the continuous case [126]. The torque for each element dm is:

$$\vec{M} = \vec{r}\ x\ \vec{F}$$

or in terms of components:

$$M_i = \sum_{jk} \varepsilon_{ijk} x_j F_k$$

where ε_{ijk} is the Levi-civita symbol, in which $\varepsilon_{ijk} = 0$ if two or more indices are equal, while $\varepsilon_{ijk} = \pm 1$, depending on the permution Π according to $(-1)^{\Pi} = \pm$. Introducing the force due to the acceleration by the gravity gradient derived from $d\ddot{x}_k = \Gamma_{kj}\ dx_j$ (Einstein sum) on the dm mass:

$$F_k = \Gamma_{kj}\ dx_j\ dm$$

The torque components integrated on the overall mass will be:

$$M_i = \int \varepsilon_{ijk} dx_j\ \Gamma_{kl}\ dx_l\ dm$$

The derivation of the continuous case is available in [126]. At last the torque is expressed for a continouos system with two orthogonal arms as follows:

$$M_x = \left(I_{yy} - I_{zz}\right)\left[\frac{\Gamma_{zz}-\Gamma_{yy}}{2}\sin 2\varphi + \Gamma_{yz}\cos 2\varphi\right]$$

In this case the dynamics equation of the system translates into:

$$I_{xx}\,(\ddot{\theta} + \frac{\beta}{I_{xx}}\dot{\theta} + \frac{k_T}{I_{xx}}\theta) = \left(I_{yy} - I_{zz}\right)\left[\frac{\Gamma_{zz}-\Gamma_{yy}}{2}\sin 2\varphi + \Gamma_{yz}\cos 2\varphi\right]$$

The corresponding transfer function is formulated as follows:

$$H(j\omega) = \frac{1}{I_{xx}(-\omega^2 + j\omega\frac{\beta}{I_{xx}} + {\omega_0}^2)} \tag{5-19}$$

Proceeding as previous for the discrete case, the corresponding relation establishing how the rotation angle θ changes as function of the sensed gravity gradient, for the case with two bars (θ_{2rc}) and in the flat region of the spectrum ($\omega \ll \omega_0$), is as follows:

$$\theta_{2rc} = \frac{\left(I_{yy} - I_{zz}\right)\left[\frac{\Gamma_{zz}-\Gamma_{yy}}{2}\sin 2\varphi + \Gamma_{yz}\cos 2\varphi\right]}{I_{xx}{\omega_0}^2} \tag{5-20}$$

In this case, the expression modifies to take into account of the principal moment of inertia of the continuous body.

5.2 Instrument feasibility and characteristics

Based on this approach, on the analysis of studies found in literature on gradiometric sensors and on the basis of the expertise at IAPS on accelerometric sensors, a possible concept of angular gradiometer compatible with the requirements previously defined has been identified as in Figure 5-8.
The gradiometer is constituted by four sensing masses arranged as couples at the end of two arms. The mass core is concentrated at the end of the arms, carving the interior part of each arm so that only a fork-shaped structure joins the sensing mass to the central torsional spring. This structure has been modified and worked with the aim of increasing the moment of inertia around the rotation axis and hence to reduce the resonance frequency; as described in section 4.5, this is one of the approaches to foster the instrument sensitivity to the gravity gradient to be measured. Indeed, the resonance frequency for such a system type, expressed by $\nu_o = 1/2\pi\sqrt{k_t/I}$, shows off that a low frequency can be obtained by making thin and long arms and a test mass with a large moment of inertia.

Figure 5-8 depicts the envisaged instrument. Arms are joined at the centre by means of a spring with a cruciform-shape which allows to separate the flexural from the torsional vibration modes (those of interest). Indeed, as established through know.how developed a t IAPS, such a shape allows to decouple the frequencies of torsion from those of flexion and traction; in this case the cruciform-shape allows to make large displacements when solicited with a torsional force while keeping low displacements when solicited with a flexural force. Figure 5-9 shows the detail of the spring, characterised by a diameter of 23 mm, a width of each cross arm of 3 mm, a curvature radius at the centre of 2.5 mm and a total length of 200 mm.

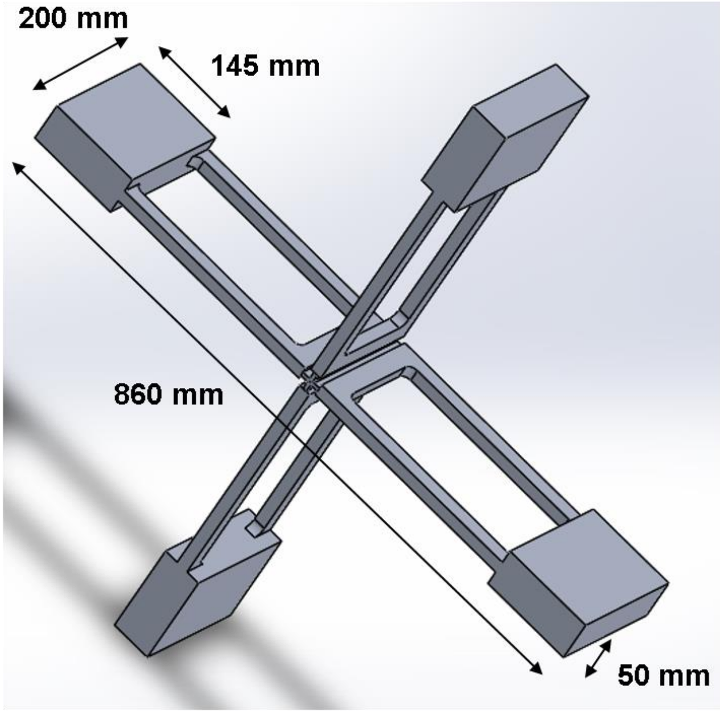

Figure 5-8: Possible concept for the angular gradiometer envisaged for the gravity gradient measurement

The last structure found is the result of several configurations that have been modified and worked, taking into account the need of reducing the resonance frequency as one of the mean to foster the sensitivity to the gravity gradient to be measured (section 4.5).

The sensor is assumed to be realised in Aluminium Al7075, the same material used for ISA and HAA accelerometers. This material, also known as Ergal, constituted by an alloy of Aluminium (Al), Zinc especially (Zn, 5-6 %, which affects the overall hardness), Magnesium (Mg, 2-3 %) and Copper (Cu, 1-2 %), is typically used in aerospace and aeronautical applications to realise structures needed to support important static and dynamical loads and maintaining at the same time lightness characteristics. The choice of this material derives from the heritage of sensors developed at IAPS, being a material with good thermal conductivity characteristics (in order to reduce thermal gradients inside the material), good durability, good hardness and a-magnetic properties, making it not sensitive to magnetic field action, and at last easiness of being manufactured and worked by milling machine.

The overall mass of the naked sensor is around 19 kg (18.9 kg), with each single proof mass of about 4 kg. The separation distance among ends of opposite masses is about 86 cm. The surface of the sensing mass is 2.9 10^{-2} m^2 (2.9 10^4 mm^2). The moment of inertia of each sensing mass with respect to the rotation axis (y) is 6.2 10^{-2} kg m^2. With respect to the two other axes, 1.9 10^{-2} kg m^2 (x) and 4.5 10^{-2} kg m^2 (z).

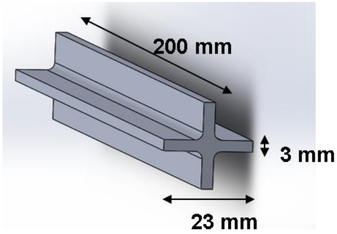

Figure 5-9: Detail of the cross-shaped spring used to realise the angular gradiometer described in the text

A modal analysis, carried out by means of the Solidworks CAD (Computer Aided Design), a software for the 3D parametric drawing and design by Dassault Systèmes [186], allowed to identify the oscillation modes of the overall system. In particular, the frequency of oscillation of the mode of interest, the fork mode (second and third mode, 11.21 and 11.28 Hz), is the mode of interest being solicited by a gravity gradient torque; it corresponds to a resonance frequency of about 11.2 Hz. The main mode is 10.2 Hz, while the following modes have resonances at 73 Hz and higher. The quality factor Q of the system, i.e. a quantity related to the Brownian noise and to the dissipation of the oscillations (see later on the noise on the detection chain), is about $1.5*10^3$. The result of the analysis is shown in Figure 5-10.

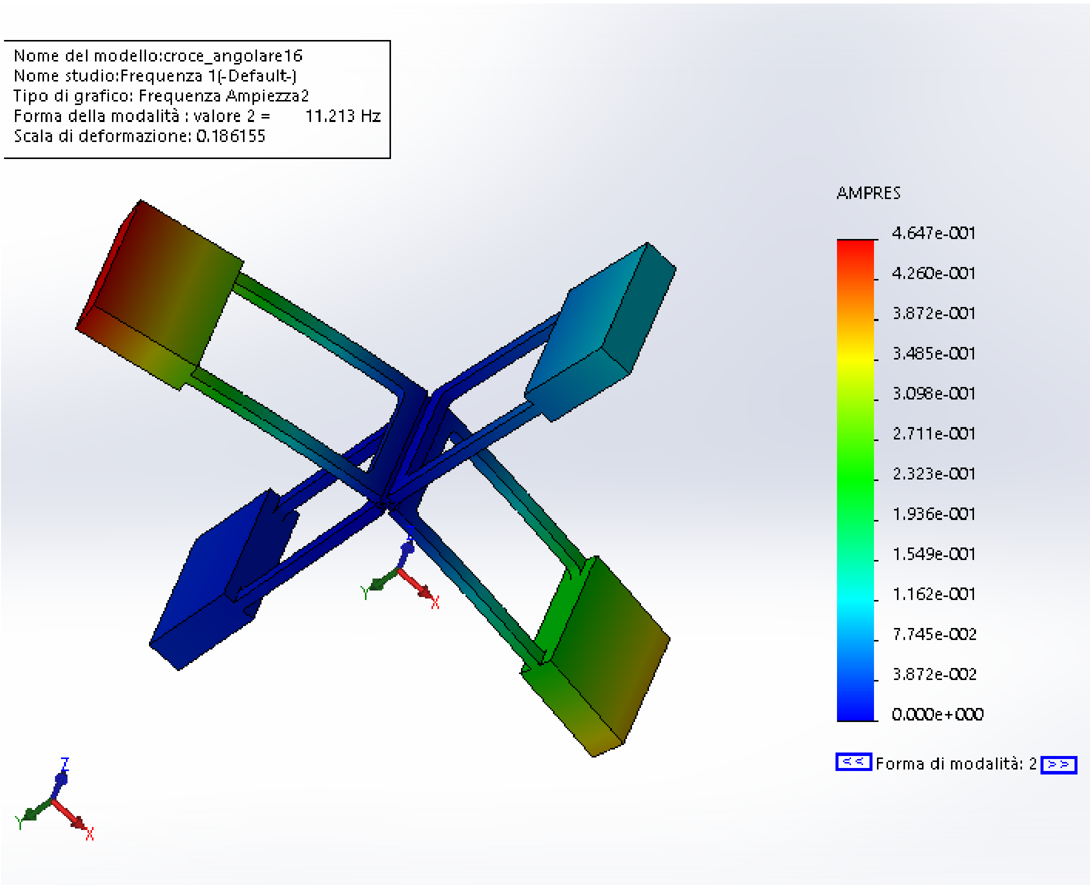

Figure 5-10: Modal frequency (2th) for the envisaged configuration

Due to the relatively closeness of fork and main mode frequency, an alternative configuration, with similar mechanical characteristics, has been envisaged to foster the decoupling . In this approach, the two arms are arranged on two separated springs, rather than a single one. Figure 5-11 shows off the different configuration identified.

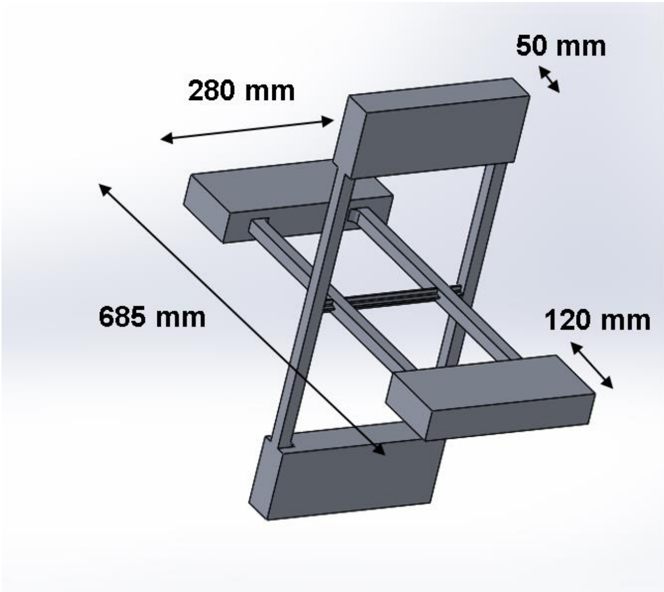

Figure 5-11: Alternative configuration for the angular gradiometer

A further modal analysis has been carried out with Solidworks for this configuration as well. In this case the frequency of oscillation of the fork mode (second mode) is around 17 Hz, while the main mode is at around 12 Hz (12.4 Hz), well far from the 36 Hz and 91 Hz of the following resonances. The quality factor Q of the system is about 700. The result of the analysis is shown in Figure 5-12.

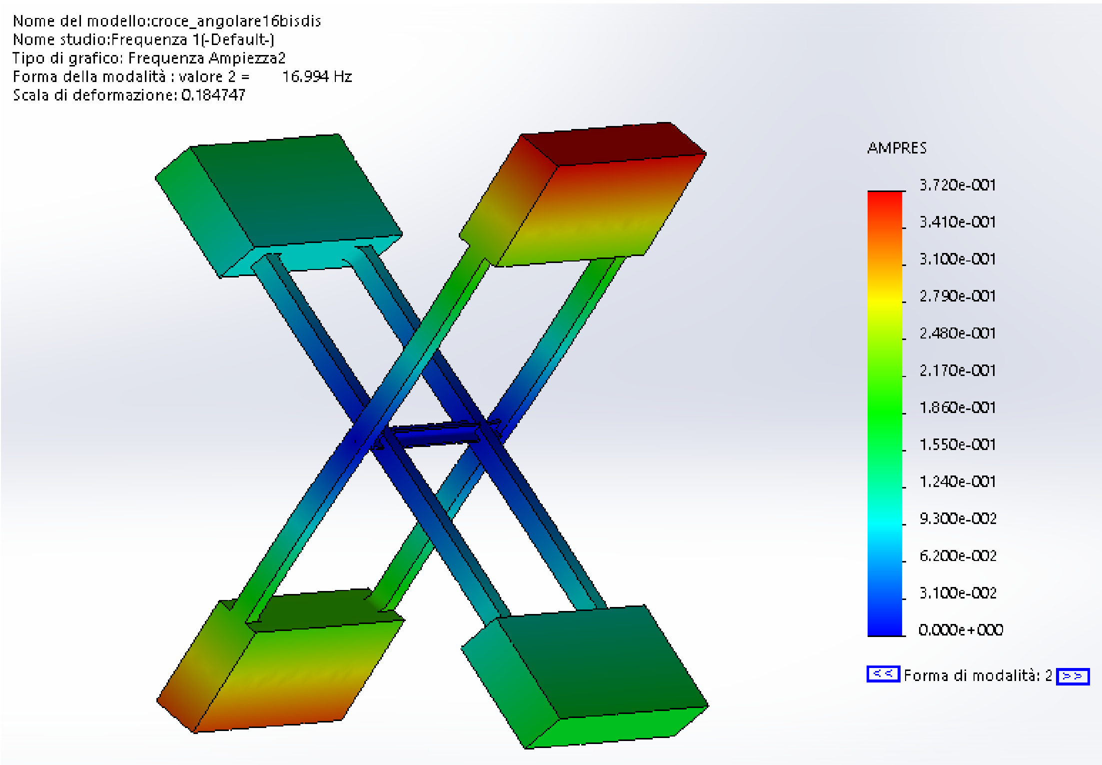

Figure 5-12: Alternative configuration for the angular gradiometer

In this configuration the overall mass of the sensor is around 21 kg, with each single proof mass of about 4.5 kg. The separation distance among ends of opposite masses is about 68 cm. The surface of each single mass is about 3.36×10^{-2} m^2. The moment of inertia of each sensing mass with respect to the rotation axis (y) is 8.6*10^{-1} kg m^2. With respect to the two other axes, 7.83*10^{-1} kg m^2 (z) and 8.51*10^{-1} kg m^2.

5.3 Signal detection and noise

For a continous system as previously defined, the equations relating the torque to the corresponding rotation angle allows to obtain the Figure 5-13 and Figure 5-14, in case of the first configuration identified; values relatively higher are achieved with the second configuration. These values are obtained assuming reference values of the gravity gradient (as derived from previous chapters, section 4.3/Table 4-8, section 3.3.3/Table 3-3 and figures at end of section 4.2.2), $\Gamma_{yy} = 1\ 10^{-13}s^{-2}, \Gamma_{zz} = 2\ 10^{-13}s^{-2}, \Gamma_{zy} = 0.5\ 10^{-13}s^{-2}$ (i.e. $10^{-4}\ E, 2\ 10^{-4}E, 0.5\ 10^{-4}E$).

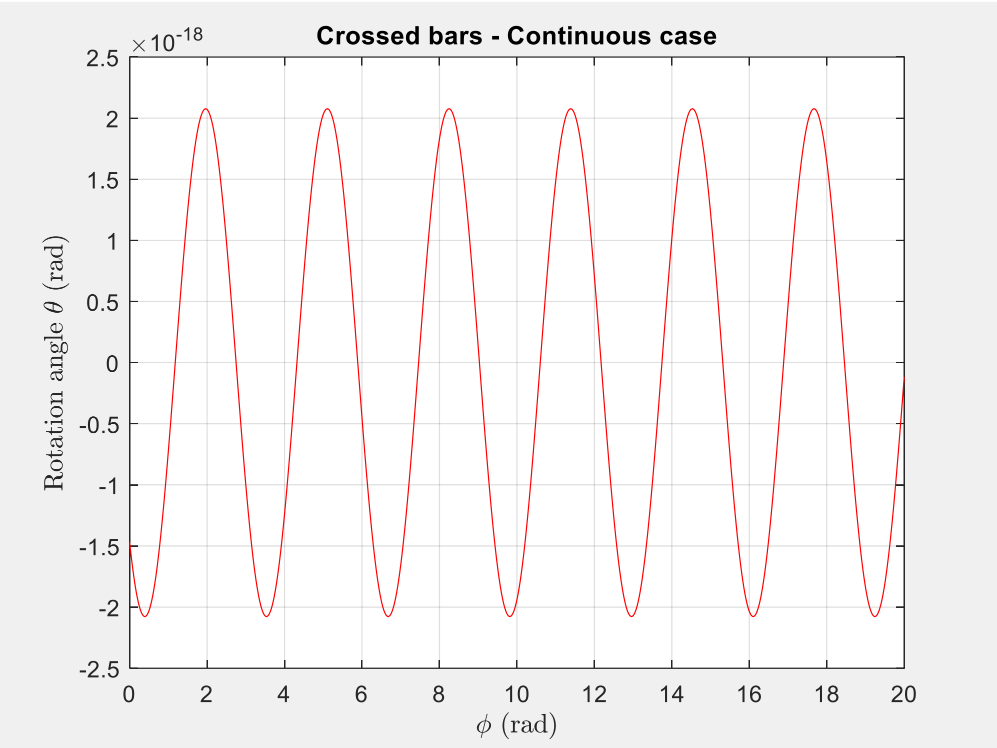

Figure 5-13: Modulation of the relative angle between the two arms of the gradiometer when subjected to a gravity gradient (10^{-13} s^{-2}), by rotating the overall system

Such an angle, result of the relative rotation between the two arms of the gradiometer when undergoes to a gravity gradient (10^{-13} s^{-2}), needs to be detected by a proper electronic read-out and properly amplified. This can be faced by using a capacitive system, the same approach implemented in ISA and HAA accelerometer. Moreover, this approach has been also applied for single axis gradiometers previously developed at IAPS [157].

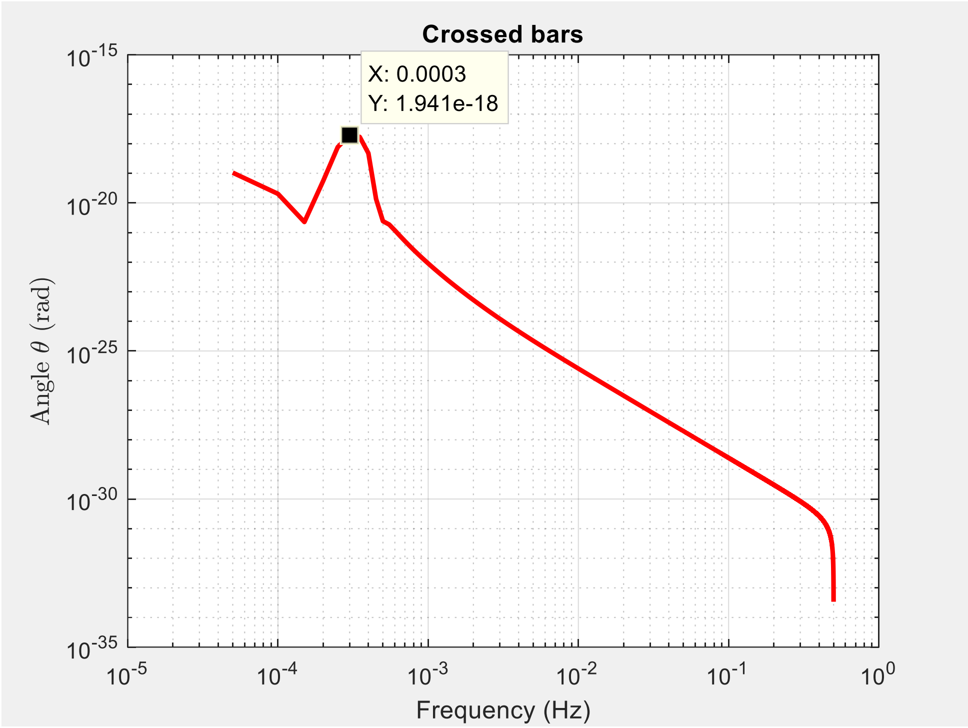

Figure 5-14: PSD of the previous modulated signal

The corresponding values of the torque modulated and its PSD values are shown in Figure 5-15 and Figure 5-16.

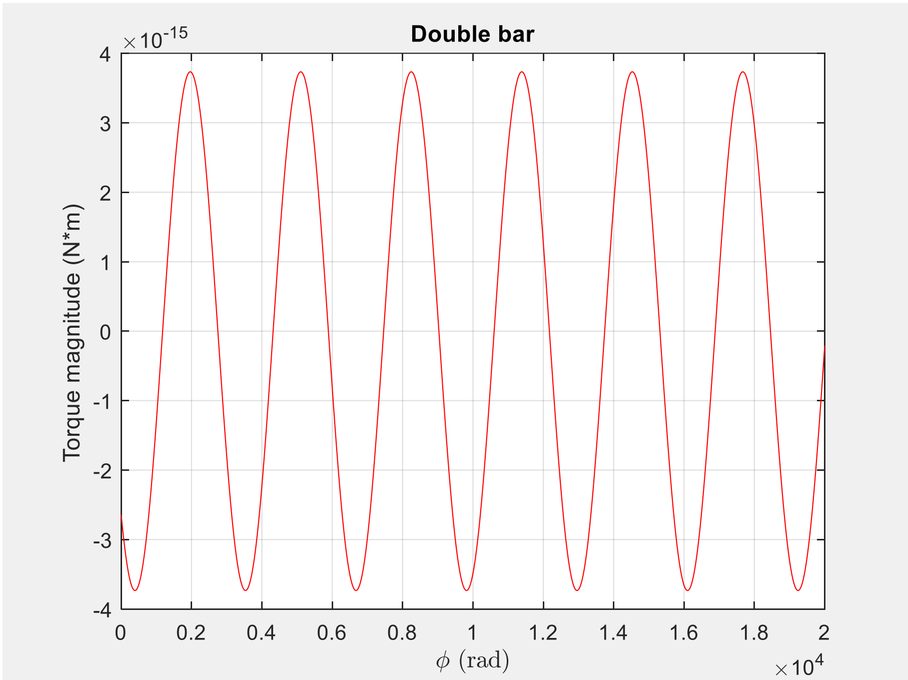

Figure 5-15: Modulation of the torque between the two arms of the gradiometer when subjected to a gravity gradient (10^{-13} s^{-2}), by rotating the overall system

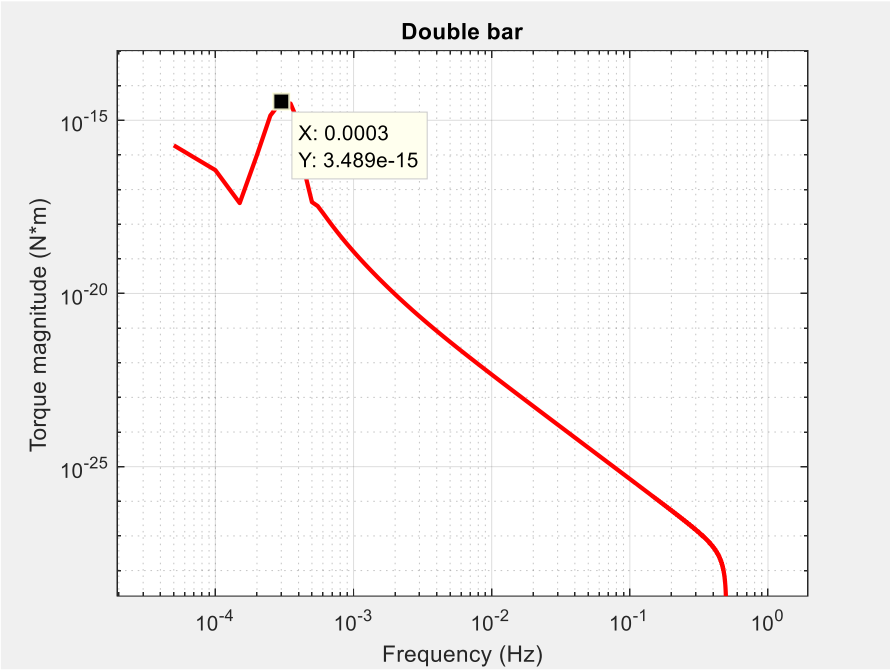

Figure 5-16: PSD of the previous modulated signal

Although the detection system is not part of the analysis to be carried out in this work, it needs to do some assumptions to prove the capability of detection.
The gravity gradient forces the torsional oscillator to move, inducing a relative movement between the two arms. Such a displacement can be detected by means of a capacitive bridge transducer, a possible scheme of which is shown in Figure 5-17 [155][157].

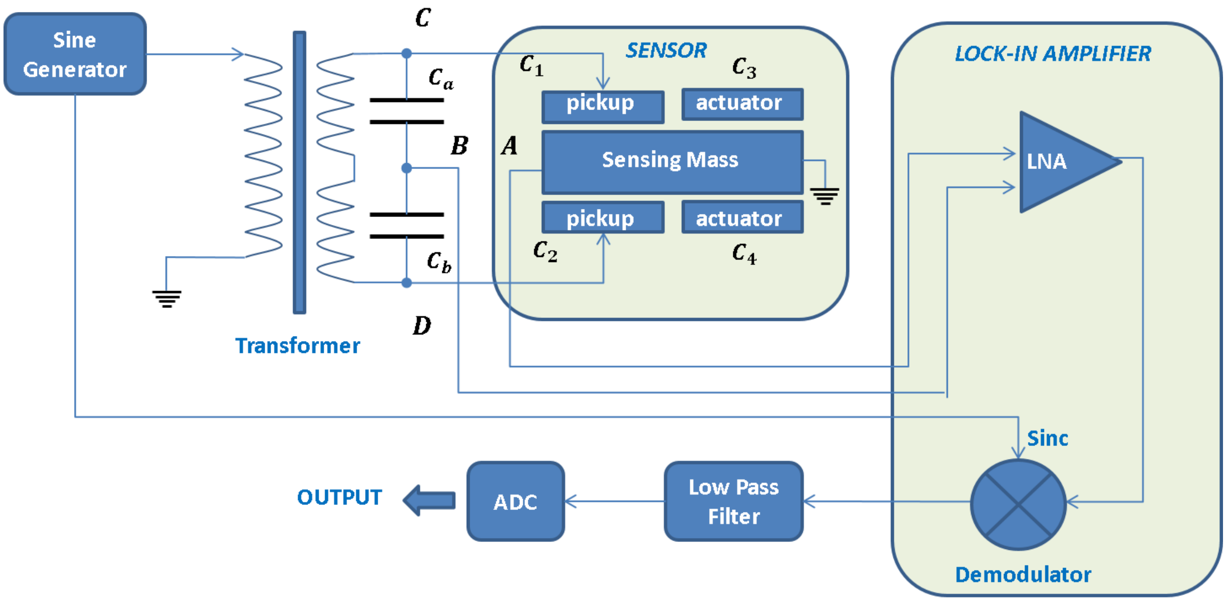

Figure 5-17: Scheme of the possible signal detection system employed to detect the sensing masses displacement

The bridge, constituted by two detection capacitors (pick-up/sensing mass) and two external fixed capacitors, C_a, C_b, is driven by a bias voltage V_p with a frequency f_p, trough a transformer. A displacement of the proof mass produces an unbalancing of the bridge and

an output signal at frequency $f_s \ll f_p$, detected as a modulation of the bias voltage. A high transducer factor α, referring to the displacement of the sensing mass to the voltage at the bridge output, is obtained by means of high values of the bias voltage V_p. The bridge attenuation prevents this high voltage from being transferred to the input of the amplifier. The output signal of the capacitive bridge is sent to a low noise amplifier, working at 10 kHz, where its noise is low. The remaining two capacitors, C_3, C_4, are used to control the system: a constant voltage applied across them induces a torque able to change the equilibrium position of the sensing mass and hence with a change of the bridge balance condition. A suitable voltage brings the bridge to equilibrium. High bridge attenuation is essential to avoid that the drive voltage appears at the amplifier and also reduces the noise introduced by the drive voltage generator.
After the amplifier, the signal is demodulated by using a reference frequency derived from the same generator, converted into a digital signal and acquired by the data acquisition system.
Taking into account results on the angle to be detected ($10^{-19} rad$, Figure 5-13 and Figure 5-14) and dimensioning the detection system to assume reasonable and realistic values, the angle change can be transformed in a voltage signal of few nV (1-5 nV) at the output of the bridge, signal that can be amplified with a proper low noise amplifier and taking into account a general low noise of the acquisition chain.
Referring to the detection systems developed at IAPS in the past [157][155], the voltage at the output of the capacitive bridge can be proven it is given by the formula:

$$V_{OUT} \equiv V_{AB} = V_{CD}\left(\frac{C_1(\theta)}{C_1(\theta) + C_2(\theta)} - \frac{C_a}{C_a + C_b}\right)$$

Taking into account that:

$$C_1(\theta) \approx C_0 + \frac{C_0}{d_1}\, b\, \theta$$
$$C_2(\theta) \approx C_0 + \frac{C_0}{d_2}\, b\, \theta$$

where C_0 is the nominal gap between faces and b represents the distance between the rotation axis and the middle point of the detector capacitors. Assuming that the gap between the faces of the capacitors is $d_1 \approx d_2 = d$, we obtain as signal:

$$V_{signal} = \alpha\, b\, \theta_{signal}$$

where the transducer factor α between the output voltage and the linear displacement is:

$$\alpha = \frac{n\, Q_e V_p}{2d}\, b$$

where n is the transformer factor, Qe is the quality factor of the electric circuit (equals to the inductance of the transformer multiplied the impedance of the capacitive bridge), d is the gap between proof mass and plates and V_p is the bias voltage of the bridge. Assuming $n = 1, Q_e = 30, V_p = 250\ V, d = 15\ \mu m$, a signal output of few nV is generated as output, signal that can be amplified for further processing.
Figure 5-18 depicts a possible layout for the first configuration with detection plates mounted (pick-up plates).

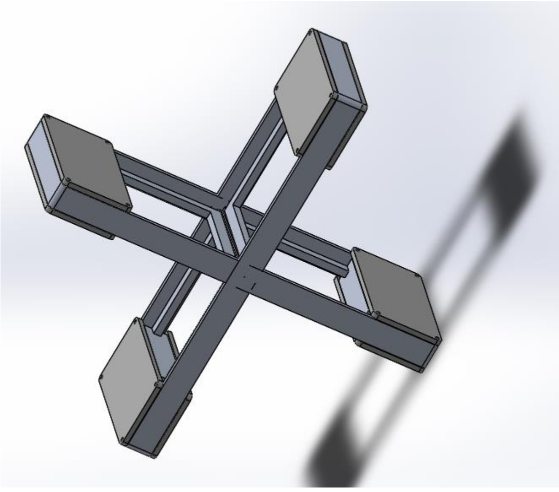

Figure 5-18: Layout of the possible signal detection system employed to detect the sensing masses displacement, where the sensing masses are coupled to counterposed plates (details in the text)

At last, such an instrument concept, with reasonable assumptions on the detection system, and with the two possible configurations, is theoretically able to detect the gravity gradient as per the requirements previous defined.

Component	Γ_{zz}	Γ_{yy}	Γ_{yz}	Unit
Signal level	$\sim 2 \cdot 10^{-13}$	$\sim 1 \cdot 10^{-13}$	$\sim 0.5 \cdot 10^{-13}$	s^{-2}

Body	h (km)	l_{max}	Δs (km)	$\Delta\nu$ (Hz)
Venus	300	100	190	10^{-4} - 10^{-2}
Mars	250	100	107	10^{-4} - 10^{-2}

Cross-component instrument		Value	Unit
Total mass	M	19	kg
Sensing mass	m	4	kg
distance	$2l$	0.8	m
frequency	ν	11	Hz

Cross-component instrument		Value	Unit
Total mass	M	21	kg
Sensing mass	m	4.5	kg
distance	$2l$	0.7	m
frequency	ν	17	Hz

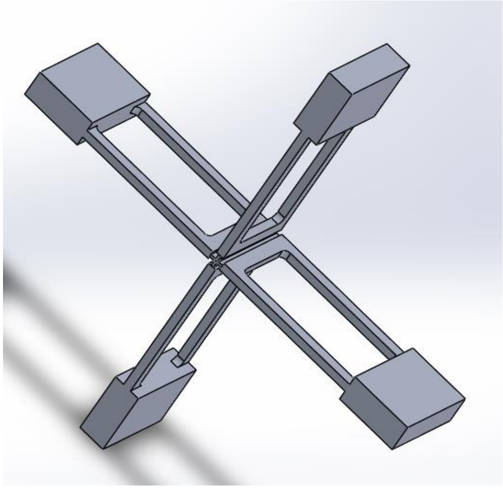

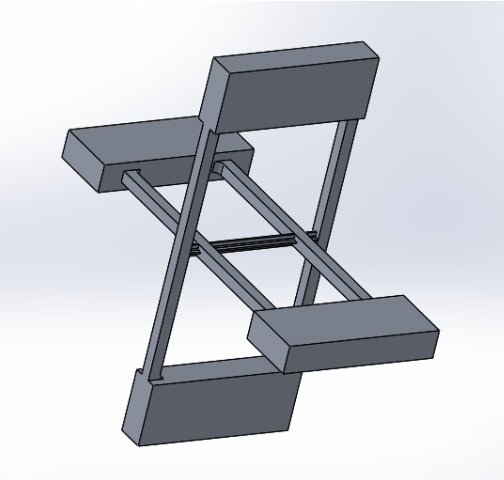

Figure 5-19: Summary of the main characteristics of the two configurations for the angular gradiometer

Figure 5-19 reports a summary of the main characteristics for the two configurations and the gravity gradient values used for the evaluation of performance. Such values were derived for a mission around Venus at 300 km till to $l = 100$ and for a mission around Mars at 250/300 km till to $l = 100$ (Table 4-8 in section 4.3).

An analysis of the noise expected along the detection chain can be carried out. Different contributions can be identified referring to the study in [157][155].
One of the main components is the Brownian noise, i.e. the Brownian motion associated to the mechanical oscillator which introduces a thermal noise (section 4.5), that is able to produce a torque per unit band equals to:

$$M_{BWN} = \sqrt{\frac{2k_B\, T\omega_0 I}{Q}}$$

where k_B is the Boltzmann constant, T the thermodynamical temperature of the oscillator, ω_0 the angular frequency, Q the quality factor and I the inertial moment of the test mass. From this expression it is clear that in order to obtain a low level of this noise it is necessary to have a mechanical oscillator with a high quality factor. Other possible approaches are the reduction of the temperature of the oscillator and/or the resonance frequency of it.
A second source of noise is the noise generated by the preamplifier (LNA, Low Noise Amplifer in Figure 5-17). This is characterised by the voltage and current noise according to the following expressions:

$$V_n = \sqrt{}(2k_B\, T_n\, Z_n)$$

$$i_n = \sqrt{2k_B T_n / Z_n}$$

with T_n equivalent noise temperature of the amplifier and Z_n noise impedance:

$$T_n = \frac{V_n\, i_n}{2k_B}$$

$$Z_n = \frac{V_n}{i_n}$$

These generators introduce in the chain a direct voltage to the input of the ideal preamplifier, and a charge fluctuation across the detections capacitors with consequent torque acting on the torsional oscillator.
Further noise is introduced by the losses associated with the four bridge capacitors. They can be expressed by a series resistances R_s and its associated noise voltage generator V_{rs} [177]. From the point of view of the mechanical oscillator, V_{rs} produces an output voltage equals to that of an equivalent torque expressed by:

$$M_{RD} = \sqrt{\frac{4\,k_B\,T\omega_0 I}{Q_{DE}}}$$

with the factor Q_{DE}, expressed by:

$$\frac{1}{Q_{DE}} = 4\frac{\omega_0}{\Omega_p}\frac{\tan\delta}{\beta}$$

where

$$\tan\delta \cong R_s\Omega_p C$$

If the amplifier has a high input impedance, on the loss resistance associated with the detection capacitors, there is no dissipation of the energy coming from the mechanical oscillator, i.e. the mechanical Q is not directly decreased by the transducer dissipations.
The total quality factor of the system, Q_{total}, which takes into account the dissipation in the oscillator and the thermal noise associated with the transducer losses, would be expressed by [157]:

$$\frac{1}{Q} = \frac{1}{Q} + \frac{1}{Q_e}$$

At last, the total torque noise per unit band can be expressed by the following formula [157]:

$$M_t = \sqrt{\frac{4k_B\omega_0}{m_r}\left[\frac{T}{Q_t} + T_n\frac{2Z_nC\omega_0}{\beta}\right]\frac{I^2}{b^2}}$$

Table 5-1 Summary of values used in the detection chain

Quantity	Symbol	Value	Unit
Boltzmann constant	k_B	1.38064852*10^{-23}	J/K
Total mass	mr	19	kg
System temperature	T	293	K
Angular pulsation	ω_0	≈120	rad/s
Quality factor	Qt	1500	
Noise temperature amplifier	Tn	0.2	K
Input impedance amplifier	Zn	10k	Ohm
Plate capacitance	C	≈17	nF
Dissipation coefficient	β	0.01	N/m/s

Moment of inertia	I	1.25 * 10^{-1}	kg m^2
Distance CM-rotation centre	b	0.4	m

By using values previously introduced and by doing some reasonable assumptions (see Table 5-1), the total torque noise for unit of band in the previous formula reaches the value:

$$M_t \approx 1.2\ 10^{-21}\ N\, m/\sqrt{Hz}$$

and a total quality factor of:

$$Q_t \approx 1500$$

The total torque noise is lower than the value expected as shown in Figure 5-15 and Figure 5-16 ($< 3.5\ 10^{-15}\ N\, m/\sqrt{Hz}$).
As stressed in section 4.5, an important element to be considered is the thermal stability. Indeed, any mechanical structure is sensitive to the thermal oscillations that induce changes in the distances and generate spurious signals. The way to solve this issue is double.
At first for the gradiometer manufacturing it needs to choose a mechanical material stable as much as possible to the temperature variations. However, in this case the material needs to have also other characterics useful at its feasibility, such as to be worked by milling machine, to have good thermal conductivity properties, good resistance and durability, and amagnetic properties. It is not easy to find a material covering all those characteristics. Being an element of wide discussion and analysis, this topic is not faced in this thesis but it will be dealt with through the future activities at IAPS group. Moroever, the change in the material would require a review of the overall assembly to evaluate the mechanical and thermal performance, theoretically and, especially, experimentally.
The second way to approach the thermal variations is to increase the thermal stability. This means that the signal changes induced by the temperature variations during the measure have to be lower than the instrument sensitivity. This is achieved by realising an instrument as much as possible stable with the temperature and able to work in thermally controlled environment.
Referring to the considerations reported at the end of section 4.5, the minimum gravity gradient measurable can be computed, by using the relation here reported again for convenience:

$$\Gamma_{min} = \frac{(S/N)^{0.5}}{2\, d\, \tau}\left(\frac{2k_B T}{m_{tot}}\right)^{0.5}$$

where S/N is the desired signal-to-noise ratio, d is the distance between the sensing masses, τ is the time in which the measure needs to be integrated (integration time), k_B is the Boltzmann constant, T is the temperature of the instrument. Assuming the values $S/N = 5$, $\tau = 250\ s$, $m_{tot} = 19\ kg,\ T = 293\ K, d = 0.43\ m$, we get as measurable minimum gravity gradient the value $\Gamma_{min} = \sim 2\ 10^{-13} s^{-2} = \sim 10^{-4}\ E$, i.e. a value corresponding at the value to be measured. For longer times of integration, longer than 250 s, the S/N can be increased and /or the minimum value achievable can be furtherly reduced.

Table 5-2 reports a comparison between the instrument requirements (section 4.5) and the expected performance of the proposed instrument, highlighting their fulfilment.

Table 5-2 Comparison between instrument requirements and expected performance of the proposed instrument concept

Variables	*Values*		
	Requirement	***Performance***	***Notes***
orbit altitude (km)	200-350 (Venus)	300	assumed circular orbit
	200-300 (Mars)	~250/300	assumed circular orbit
Sensitivity (s^{-2})	10^{-13}-10^{-14}	~10^{-13}	-
L_{max}	*100*	*100*	maximum degree
Frequency (Hz)	$10^{-4} - 10^{-1}$	$12\ Hz\ or\ 17\ Hz$ (Resonance frequency)	-
Mass (kg)	< 50	20	referred to the mechanical part
Length (m)	< 2	< 1	-

The solutions above depicted for a single axis gradiometer are envisaged to be improved and furtherly detailed in future activities carried out at IAPS after the present work. Indeed, further possibilities to increase the performance theoretically achievable with the above configurations can be faced in the future by addressing some items.
A first element is the possibility to further reduce the resonance frequency with respect to the values of two configurations proposed (i.e. 11 and 17 Hz), towards values closer to 1 Hz (or lower), although it is not an easy task to accomplish for the mechanical design. Indeed, a driver of the gradiometer performance (and hence of the acceleormeter components) is based onthe lowering of the resonance frequency. As shown in section 4.5, a reduction of the frequency reflects in an increase of the sensitivity (signal-to-noise ratio), and such an increase depends on the amount of reduction introduced. For instance, an increase of sensitivity (and transduction factor) of a 120 factor could be achieved by reducing from 11 Hz to 1 Hz the resonance frequency.
Moreover, this action (frequency reduction) affects positively as well the thermal behaviour of the sensor, allowing a reduction of all effects due to thermoelastic denformations of the sensor structure. Indeed, a frequency reduction implies an increased displacement of the sensing mass when the same input acceleration is provided, allowing to have a signal to peak more with respect to spurious background signal induced by the thermal sensitivity.
As highlighted in section 4.5, a particular element to be investigated is the thermal sensitivity. Preliminary experimental activity at IAPS on increasing performance of accelerometers has shown that using materials with CTE closer possible to that of the sensor material, both for insulators and fasteners, allows to reduce the thermal sensitivity of the capacitance among the electrodes and the sensing mass. Moreover, the use of thinner isolators allows a simpler electrodes geometry and hence better tolerances, resulting in a better mechanical coupling of the elements. This turns out in reduced thermoelastic stress, as well.
At last, investigation on a linear gradiometer could be also faced as alternative configuration with respect to the proposed angular gradiometer or as complementary instrument to allow the measure of in-line and off-line components at the same time.

6. Conclusions

This thesis is framed in the context of the measurement of the gravitational field of planetary bodies. In the last twenty years such a topic has become central to study interior and surface of planets and the related results have been widespreadly used in understanding the Solar System formation and evolution. Indeed, many planetary processes at large scale are ruled by the body internal structure, where surface and tectonic features are mainly the result of heat exchanges from the interior to the surface.

There are different approaches through which the study of the surface and the interior of a planet can be tackled: seismology, magnetic field studies, investigation of planetary rotation, gravity analysis. The gravity field measurement is one of the observational methods to investigate those processes and to place constraints on the structure of the planetary interiors, their formation and geologic evolution.

Within this framework, the thesis was centred on evaluating the gravitational gradiometry as a means to measure the gravitational field of planetary bodies in the Solar System. Satellite gravitational gradiometry, based on measuring the second derivatives of the gravitational potential $V(|\vec{x}|)$ along the 3-dimensions, i.e. the measure of the gravitational acceleration gradient, is a new window on space gravity missions recently opened through the GOCE mission around the Earth (2009-2013). Capitalise on the differentiation process of gravity accelerations allows to highlight small-scale surface and sub-surface features, making such a technique inherently sensitive to the medium and large degrees of the field structures (i.e. to high resolutions). In this context, the gravitational gradiometry puts itself as a complementary technique with respect to the traditional radio-tracking in the measurement of the gravitational field.

This thesis presented an assessment of the most up-to-date gravity fields of planetary bodies, highlighting strong issues and shortages; at the same time, needed improvements were considered. A diversified scenario on the current knowledge was derived. As multiple fleet of spacecrafts have visited some planetary bodies for a deep exploration, such as Mars, Venus and obviously the Earth and the Moon, very few satellites or none have reached other bodies. In the latter case, just few satellites entered the orbit's body, whereas others carried out single or multiple fly-bys. Moreover, excluding the Earth and the Moon, the spatial resolution is limited to the major structures and features, achieving hundreds of kilometers, also for the most explored planets, Mars and Venus. The result is that the gravity field knowledge is good for some bodies, and very poor or lacking for others.

The link between the field knowledge and the measurement of the planetary interiors was faced and delved into, showing the relationship with moment of inertia and interior models used to deepen their formation and evolution. Open science themes and questions were identified and science needs were derived, establishing a list of interesting bodies (from a scientific point of view) to be addressed with the gravitational gradiometry technique. Primary interests are demonstrated for Venus, which was explored last from Venus Express (2006-2014), and in particular to the different thermal, geological and atmospheric evolution, with respect to th Earth. At the same time, Mars keeps alive the interest in it, being the planet most targeted in terms of dedicated missions till now and for the future as well. The first seismometer out of the Earth and Moon (Apollo missions) is currently operating on Mars with Mars Insight. However, several questions related to the interior structure are still open. Comparison of the planetary bodies gravity field state of the art with the scientific needs allows to infer that the most interesting objectives are represented by Venus and Mars, in addition to specific targets among the Galilean and Saturnian moons, such as Ganymede, Europa, Titan.

Following the science needs, measurement techniques of the gravitational field were reviewed, identifying advantages and drawbacks. Gradiometric technique in its different variations was investigated and analysed, pointing out its potential benefits. In this context, spaceborne, airborne and groundborne main gradiometric instruments have been identified and analysed to identify the current status and performance. At last the scientific needs were compared to the instruments state of the art. Results showed that just one space gradiometer has been developed and flight-proved till now within the GOCE mission. Its outstanding performance ($\sim 10^{-2}E$) were achieved because of the synergic coupling of high-performance accelerometers, used as basic elements of the gradiometer, with the state-of-the-art of spacecraft subsystems built around it: all the system works as one whole gravity instrument.

All the other systems discussed have been developed as prototypes, at the test level or are simply under study (TRL 2-5). They employ different sensing technologies (mechanical superconducting, magnetically levitated, MEMS-type) to get the gravity gradient, but the principle of measurement is led back to the two basic approaches: differential accelerometry and torsion balance. However, the declared performance is often potential and have been tested in a limited approach, verifying just some elements. The most complete system on-ground developed is represented by the Paik's gradiometer and colleagues, both in the superconducting mechanical and levitated version.

Following these results, some scenarios of a spacecraft orbiting a planetary body among the ones identified, placed on a circular and polar orbit have been envisaged. For each scenario expected signal and frequency band to be measured by a gradiometric mission were derived. Moreover, a more precise evaluation of the gravity gradients was investigated, in order to have a simulation tool able to evaluate correctly the gravity gradient in terms of all the independent components (5, plus one redundant). The tool was thought to be used for any planetary body and for any orbit around it. Currently, the focus was limited to circular orbits because this type of orbits is typically used in gravity missions. As future work it could be possible to extend the formulation to elliptical orbits as well.

Simulations have been developed in matlab code to allow an estimate of the time series of expected gradiometric signals for any body and any (circular) orbit. Simulations were carried out to compute the time series of gravity gradients along a specified orbit, basically quasi-polar and circular, followed by a hypothetical spacecraft around Venus and Mars.

Following this analysis, needs for the design of a gravity mission were investigated and discussed, identifying advantages and drawbacks. Moreover, requirements to be matched by a typical gradiometric instrument/mission in terms of sensitivity and spectral band were set for identified scientific targets (chapter 4). In this frame, approaches to increase the sensitivity of a gradiometric instrument were introduced and analysed.

At last, an instrument concept able to satisfy the measure requirements for the target bodies was introduced and analysed. A single axis torsion-balance gradiometer based on IAPS technology has been proposed and analysed and its performance have been compared to the expected gradiometric signal for a spacecraft orbiting Mars or Venus, evaluated on the basis of the developed matlab code. Analysis and performance of the instrument in two different configurations were investigated and discussed. The analysed instrument concept proved to fulfil the requirements identified in chapter 4, as detailed in chapter 5. This analysis of an instrument concept to be used in planetary missions is considered as a starting point to be further developed and prosecuted both theoretically (design and materials improvement, additional simulations) and experimentally (dedicated tests on mechanical and thermal improvements of the design) within the frame of the research group at IAPS.

References

1. https://www.hq.nasa.gov/alsj/HamishALSEP.html
2. P. Lognonné, W.B. Banerdt, D. Giardini, *et al.* SEIS: Insight's Seismic Experiment for Internal Structure of Mars. *Space Sci Rev* 215, 12 (2019). https://doi.org/10.1007/s11214-018-0574-6
3. R. S. Nerem, C. Jekeli, W. M. Kaula, "Gravity field determination and characteristics: Retrospective and prospective", Journal of Geophysical Research, vol. 100, no. b8, pages 15,053-15,074, August 10, 1995
4. J. Vetter, "The Evolution of Earth Gravitational Models used in Astrodynamics", Johns Hopkins APL Technical Digest, Volume 15, Number 4 (1994)
5. D.A. Vallado, "Fundamentals of Astrodynamics and Applications", 4th edition, Space Technology Library
6. H. K. Gupta (ed.), "Encyclopedia of Solid Earth Geophysics", Encyclopedia of Earth Science Series, Springer Netherlands, 2011
7. G. Galilei, Discorsi e Dimostrazioni Matematiche intorno a due nuove scienze. Leiden, Louis Elsevier, 1638.
8. F. Fuligni, V. Iafolla, "Galileo and the Principle of Equivalence", European Space Agency - Publications - ESA WPP, 115; 104-112, 1996.
9. D. Bramanti, G. Catastini, A.M. Nobili, E. Polacco, E. Rossi and R. Vergara Caffarelli, "Galileo and the Universality of Free Fall" (extended abstract), STEP Symposium, ESA WPP-115; 319, 1993.
10. W.A. Heiskanen and H. Moritz, "Physical Geodesy", W.H. Freeman and Co., San Francisco, 1967.
11. A. Milani, G. F. Gronchi, "Theory of Orbit Determination", Cambridge University Press, 2010
12. F. Barthelmes, "Definition of Functionals of the Geopotential and Their Calculation from Spherical Harmonic Models", Scientific Technical Report STR09/02, GFZ German Research Centre for Geosciences, January 2013
13. Kaula, W. M. (1966), Theory of Satellite Geodesy: Applications of Satellites to Geodesy, 124 pp., Blaisdell, Walham, Mass.
14. F. Barthelmes, "Global Models", in Grafarend E. (eds) Encyclopedia of Geodesy. Encyclopedia of Earth Sciences Series, 2018
15. Tsoulis, D., and K. Patlakis (2013), "A spectral assessment review of current satellite-only and combined Earth gravity models", Rev. Geophys., 51, 186 – 243, doi:10.1002/rog.20012.
16. R. Rummel et al., "Spherical Harmonic Analysis of Satellite Gradiometry", Netherlands Geodetic Commission Publications On Geodesy, Number 39, 1993
17. R. Rummel, "Gravity Field from Space", Lecture Notes at Alpbach Summerschool 2014 "Space mission for geophysics of the terrestrial planets"
18. R. Rummel, G. Balmino, J. Johannessen, P. Visser, P. Woodworth, "Dedicated gravity field missions—principles and aims", Journal of Geodynamics, Volume 33, Issues 1–2, January–March 2002, Pages 3-20.
19. K. H. Ilk *et al.*, "Mass Transport and Mass Distribution in the Earth System", Proposal for a German Priority Research Program, München: GOCE-Projektbüro Deutschland, Techn. Univ. München, GeoForschungsZentrum Potsdam, January 2005
20. International Centre for Global Earth Models (ICGEM), http://icgem.gfz-potsdam.de/
21. C. Jekeli, "Heights, the Geopotential, and Vertical Datums", Ohio State University. Geodetic Science and Surveying. Report. no. 459, 2000

22. B. D. Tapley, B. E. Schutz, G. H. Born, “Statistical Orbit Determination”, Elsevier Academic Press 2004
23. B. Bertotti, P. Farinella, D. Vokrouhlicky, “Physics of the Solar System”, Kluwer Academic Publishers, Astrophysics and Space Science Library, V. 293, 2003
24. G. Beutler, “Methods of Celestial Mechanics, Vol. 1: Physical, Mathematical and Numerical Principles”, Springer 2005
25. R. R. Bate, D. D. Mueller, J.E. White, “Fundamentals of Astrodynamics”, Dover 1971
26. K. A. Carroll, D. R. Faber, “Asteroid Orbital Gravity Gradiometry”, 49th Lunar and Planetary Science Conference 2018.
27. H. S. Liu and B. F. Chao, “The Earth’s equatorial principal axes and moments of inertia”, Geophys. J. Int. 106, 699-702, 1991
28. S. Cicalò and A. Milani, “Determination of the rotation of Mercury from satellite gravimetry”, Mon. Not. R. Astron. Soc. 427, 468–482 (2012)
29. G. Balmino, “New space mission for mapping the Earth’s gravity field”, C. R. Acad. Sci. Paris, t. 2, Série IV, p. 1353–1359, 2001
30. M. A. Wieczorek, “Gravity and Topography of the Terrestrial Planets”, from “Treatise on Geophysics”, 10, 153-193, 2015
31. T. Spohn, “Physics of Terrestrial Planets and Moons: An Introduction and Overview”, from “Treatise on Geophysics”, 10, 153-193, 2015
32. R. Rummel, “Gravity and Topography of Moon and Planets”, in “Future Satellite Gravimetry and Earth Dynamics” – Springer 2005
33. J. Flury, R. Rummel, “Future Satellite Gravimetry and Earth Dynamics”, Institute for Astronomical and Physical Geodesy, Muenchen, Germany – Springer 2005
34. T. Guillot, D. Gautier, “Giant Planets”, Eds. G. Schubert and T. Spohn, Treatise on Geophysics, 2nd edition, Elsevier, 2015.
35. J.I. Lunine, “The atmospheres of Uranus and Neptune”, Annual review of astronomy and astrophysics, Vol. 31, pp 217-263.
36. D. Turrini *et al.*, “The Comparative Exploration of the Ice Giant Planets with Twin Spacecraft: Unveiling the History of our Solar System”, Volume 104, Part A, December 2014, Pages 93-107.
37. C. S. Arridge, “Uranus Pathfinder: exploring the origins and evolution of Ice Giant planets”, Experimental Astronomy (2012) 33:753–791
38. B. Christophe *et al.*, “OSS (Outer Solar System): a fundamental and planetary physics mission to Neptune, Triton and the Kuiper Belt”, Experimental Astronomy (2012) 34:203–242.
39. D. Charbonneau and S. Gaudi, “Exoplanet Science Strategy”, Committee on Exoplanet Science Strategy, Space Studies Board, Board on Physics and Astronomy - Division on Engineering and Physical Sciences, The National Academies Press, 2018
40. F. Sohl, G. Schubert, “Interior Structure, Composition, and Mineralogy of the Terrestrial Planets”, from “Treatise on Geophysics”, G. Schubert Editor, 2015
41. G. Schubert, K. M. Soderlund, “Planetary magnetic fields: observations and models”, Physics of the Earth and Planetary Interiors 187 (2011) 92-108.
42. M.R.R. de Oliveira, P.J.S. Gil, R. Ghail, “A novel orbiter mission concept for Venus with the EnVision proposal”, Acta Astonautica 148 (2018) 260-267.
43. “Venera-D: Expanding Our Horizon of Terrestrial Planet Climate and Geology Through the Comprehensive Exploration of Venus”, Report of The Venera-D Joint Science Definition Team, January 31, 2019
44. O. Baur, “Gravity Field of Planetary Bodies”, Space Research Institute (Austria), from encyclopedia of Geodesy, 2014.
45. E. F. Milone and W. J.F. Wilson, “Solar System Astrophysics”, Springer 2008

46. PDS Geosciences Node, http://pds-geosciences.wustl.edu/
47. ICGEM – International Center for Global Earth Models, http://icgem.gfz-potsdam.de/tom_celestial
48. “Satellite Gravity and the Geosphere: Contributions to the Study of the Solid Earth and Its Fluid Envelopes”, Committee on Earth Gravity from Space, National Research Council, 1997
49. Siddiqi, A. A., “Beyond Earth: A Chronicle of Deep Space Exploration, 1958-2016”, NASA History Program Office, 2018
50. J.L. Margot, S. J. Peale, S. C. Solomon, S. A. Hauck II, F. D. Ghigo, R. F. Jurgens, M. Yseboodt, J.D. Giorgini, S. Padovan, and D. B. Campbell, “Mercury ’ s moment of inertia from spin and gravity data”, Journal Of Geophysical Research, Vol. 117, 2012
51. Giberson, W.E. and Cunningham, N.W., “Mariner 10 mission to Venus and Mercury”, Acta Astronautica, Vol. 2, pp. 715-743, Pergmaomon Press, 1975
52. T. Spohn, F. Sohl, K. Wieczerkowski, V. Conzelmann, “The interior structure of Mercury: what we know, what we expect from BepiColombo”, Planetary and Space Science 49 (2001) 1561–1570
53. A. Milani, A. Rossi, D. Vokrouhlicky, D. Villani, C. Bonanno, “Gravity field and rotation state of Mercury from the BepiColombo Radio Science Experiments”, Planetary and Space Science 49 (2001) 1579–1596
54. E. Mazarico, A. Genova, S. Goossens, F.G. Lemoine, G. A. Neumann, M. T. Zuber, D. E. Smith, and S. C. Solomon, “The gravity field, orientation, and ephemeris of Mercury from MESSENGER observations after three years in orbit”, Journal of Geophysical Research 2014
55. Genova, A., Goossens, S., Mazarico, E., Lemoine, F. G., Neumann, G. A., Kuang, W., Sabaka, T.J., Hauck, S.A. II, Smith, D. E., Solomon, S.C., & Zuber, M. T., “Geodetic evidence that Mercury has a solid inner core”, Geophysical Research Letters, 2019
56. David E. Smith, Maria T. Zuber, Roger J. Phillips, Sean C. Solomon, Steven A. Hauck II, Frank G. Lemoine, Erwan Mazarico, Gregory A. Neumann, Stanton J. Peale, Jean-Luc Margot, Catherine L. Johnson, Mark H. Torrence, Mark E. Perry, David D. Rowlands, Sander Goossens, James W. Head, Anthony H. Taylor, “Gravity Field and Internal Structure of Mercury from MESSENGER”, Science, Mar 2012
57. Schulz R. and Benkhoff J., "BepiColombo: Payload and mission updates" Advances in Space Research 38, 572-577, 2006
58. R. Grard, A. Balogh, “Returns to Mercury: science and mission objectives”, Planetary and Space Science 49 (2001) 1395–1407
59. Benkhoff J., Casteren J. V., Hayakawa H., Fujimoto M., Laakso H., Novara M., Ferri P., Middleton H. R. and Ziethe R., "BepiColombo - Comprehensive exploration of Mercury: Mission overview and science goals" Planetary and Space Science 58 2-20
60. Genova A., Marabucci M. and Iess L., 2012 "Mercury radio science experiment of the mission BepiColombo", Mem. S.A.It. 20, 127
61. Milani A, Rossi A, Vokrouhlicky D, Villani D and Bonanno C, 2001 "Gravity field and rotation state of Mercury from the BepiColombo Radio Science Experiments" Planetary and Space Science 49 1579-1596
62. S. Cicalò, G. Schettino, S. Di Ruzza, E. M. Alessi, G. Tommei and A. Milani, “The BepiColombo MORE gravimetry and rotation experimentswith theORBIT14 software”, MNRAS457,1507–1521 (2016)
63. B.G. Williams, N.A. Mottinger, N.D. Panagiotacopulos, “Venus Gravity Field: Pioneer Venus Orbiter Navigation Results”, Icarus 56, 578-589 (1983)
64. S. Konopliv, W. B. Banerdt, and W. L. Sjogren, “Venus Gravity: 180th Degree and Order Model”, Icarus 139, 3-18 (1999)

65. Dumoulin, C., G. Tobie, O. Verhoeven, P. Rosenblatt, and N. Rambaux (2017), “Tidal constraints on the interior of Venus”, J. Geophys. Res. Planets, 122, 1338–1352
66. B. G. Bills, A. J. Ferrari, “A Harmonic Analysis of Lunar Gravity”, Journal Of Geophysical Research, Vol. 85, No. B2, Pages 1013-1025, February 10, 1980
67. A. S. Konopliv, R. S. Park, D.N. Yuan, S. W. Asmar, M. M. Watkins, J. G. Williams, E. Fahnestock, G. Kruizinga, M. Paik, D. Strekalov, N. Harvey, D. E. Smith, and M. T. Zuber, “The JPL lunar gravity field to spherical harmonic degree 660 from the GRAIL Primary Mission”, Journal Of Geophysical Research: Planets, Vol. 118, 1–20, doi:10.1002/jgre.20097, 2013
68. A. S. Konopliv, W. L. Sjogren, R. N. Wimberly, R. A. Cook, V. Alwar, “A High Resolution Lunar Gravity Field and Predicted Orbit Behavior”, JPL Technical Report 1993
69. S. C. Cohen and D. E. Smith, “LAGEOS Scientific Results: Introduction”, Journal of Geophysical Research, Vol. 90, No. B11, Pages 9217-9220, September 30, 1985
70. C. Reigber *et al.*, “CHAMP Mission 5 Years in Orbit”, In: Flury J., Rummel R., Reigber C., Rothacher M., Boedecker G., Schreiber U. (eds) Observation of the Earth System from Space. Springer, Berlin, Heidelberg, 2006
71. W. Keller, M.A. Sharifi, “Satellite gradiometry using a satellite pair”, Journal of Geodesy (2005) 78: 544–557
72. B. D. Tapley and S. Bettadpur, “The gravity recovery and climate experiment: Mission overview and early results”, Geophysical Research Letters, Vol. 31, L09607, 2004
73. M. Kato, S. Sasaki, Y. Takizawa, “The Kaguya Mission Overview”, Space Sci Rev (2010) 154: 3–19
74. N. Namiki *et al.*, “Farside Gravity Field of the Moon from Four-Way Doppler Measurements of SELENE (Kaguya)”, Science 323 5916 (2009): 900-5
75. F. G. Lemoine, S. Goossens , T. J. Sabaka, J. B. Nicholas, E. Mazarico, D. D. Rowlands, B.D. Loomis, D. S. Chinn, G. A. Neumann, D. E. Smith, and M. T. Zuber, “GRGM900C: A degree 900 lunar gravity model from GRAIL primary and extended mission data”, http://dx.doi.org/10.1002/2014GL060027
76. Konopliv, A. S., et al. (2014), “High-resolution lunar gravity fields from the GRAIL Primary and Extended Missions”, Geophys. Res. Lett., 41, 1452 – 1458
77. Liang, Wei (2018): SGG-UGM-1: the high resolution gravity field model based on the EGM2008 derived gravity anomalies and the SGG and SST data of GOCE satellite. GFZ Data Services. http://doi.org/10.5880/icgem.2018.001
78. Pavlis, N. K., S. A. Holmes, S. C. Kenyon, and J. K. Factor (2012), The development and evaluation of the Earth Gravitational Model 2008 (EGM2008), J. Geophys. Res.,117, B04406, doi:10.1029/2011JB008916.
79. Tapley, B. D., F. Flechtner, S. V. Bettadpur, M. M. Watkins, The status and future prospect for GRACE after the first decade, Eos Trans., Fall Meet. Suppl., Abstract G22A-01, 2013.
80. S. Konopliv, R. S. Park, W. M. Folkner, “An improved JPL Mars gravity field and orientation from Mars orbiter and lander tracking data”, Icarus 274 (2016) 253-260
81. A. S. Konopliv, W. L. Sjogren, “The JPL Mars gravity field, Mars50c, based upon Viking and Mariner 9 Doppler tracking data”, JPL Publication 95-5, February 1995
82. D. E. Smith, F. J. Lerch, R. S. Nerem, M. T. Zuber, G. B. Patel, S. K. Fricke, and F. G. Lemoine, “An Improved Gravity Model for Mars' Goddard Mars Model 1”, Journal Of Geophysical Research, Vol. 98, No. Ell, Pages 20,871-20,889, November 25, 1993
83. NASA – Mars exploration, https://mars.nasa.gov/programmissions/missions/log/
84. A. S. Konopliv, S. W. Asmar, W. M. Folkner, O. Karatekin, D. C. Nunes, S. E. Smrekar, C. F. Yoder, M. T. Zuber, “Mars high resolution gravity fields from MRO, Mars seasonal gravity, and other dynamical parameters”, Icarus 211 (2011) 401-428

85. NASA’s Planetary Data System - PDS Geosciences Node archives: http://pds-geosciences.wustl.edu/
86. NASA’s Planetary Geology, Geophysics and Geochemistry Laboratory, https://pgda.gsfc.nasa.gov/products/71
87. http://icgem.gfz-potsdam.de/tom_longtime
88. L. Iess, N. J. Rappaport, R. A. Jacobson, P. Racioppa, D. J. Stevenson, P. Tortora, J. W. Armstrong, S.W. Asmar, “Gravity Field, Shape, and Moment of Inertia of Titan”, Science. 2010 Mar 12;327(5971):1367-9
89. W. M. Folkner, L. Iess, J. D. Anderson, S. W. Asmar, D. R. Buccino, D. Durante, M. Feldman, L. Gomez Casajus, M. Gregnanin, A. Milani, M. Parisi, R. S. Park, D. Serra, G. Tommei, P. Tortora, M. Zannoni, S. J. Bolton, J. E. P. Connerney, and S. M. Levin, “Jupiter gravity field estimated from the first two Juno orbits”, Geophys. Res. Lett., 44, 4694 – 4700, 2017
90. L. Iess, W. M. Folkner, D. Durante, M. Parisi, Y. Kaspi, E. Galanti, T. Guillot, W. B. Hubbard, D. J. Stevenson, J. D. Anderson, D. R. Buccino, L. Gomez Casajus, A. Milani, R. Park, P. Racioppa, D. Serra, P. Tortora, M. Zannoni, H. Cao, R. Helled, J. I. Lunine, Y. Miguel, B. Militzer, S. Wahl, J. E. P. Connerney, S. M. Levin & S. J. Bolton, “Measurement of Jupiter’s asymmetric gravity field”, NATURE | VOL 555 | 8 march 2018
91. L. Iess, B. Militzer, Y. Kaspi, P. Nicholson, D. Durante, P. Racioppa, A. Anabtawi, E. Galanti, W. Hubbard, M. J. Mariani, P. Tortora, S. Wahl, M. Zannoni, “Measurement and implications of Saturn’s gravity field and ring mass”, *Science* 14 Jun 2019: Vol. 364, Issue 6445
92. D. Durante, D.J. Hemingway, P. Racioppa, L. Iess, D.J. Stevenson, “Titan's gravity field and interior structure after Cassini”, Icarus 326 (2019) 123–132
93. G. Schubert, J. D. Anderson, T. Spohn, W. B. McKinnon, “Interior Composition, Structure and Dynamics of the Galilean Satellites”, in “Jupiter: The Planet, Satellites and Magnetosphere”, Edited by Fran Bagenal, Timothy Dowling, William McKinnon, Cambridge University Press 2004
94. J. D. Anderson, R. A. Jacobson, and T. P. McElrath, “Shape, Mean Radius, Gravity Field, and Interior Structure of Callisto”, Icarus 153, 157–161 (2001)
95. A. K. Verma, J.L. Margot, “Expected precision of Europa Clipper gravity measurements”, Icarus 314 (2018) 35–49
96. S. Squyres, Vision and Voyages for Planetary Science in the Decade 2013–2022 (National Academy of Sciences, Washington, DC, 2011)
97. L. S. Glaze, C. F. Wilson, L. V. Zasova, M. Nakamura, S. Limaye, “Future of Venus Research and Exploration”, Space Sci Rev (2018) 214:89
98. A. Genova, “ORACLE: A Mission Concept to Study Mars’ Climate, Surface and Interior”,
99. A. Genova, S. Goossens, F. G. Lemoine, E. Mazarico, G. A. Neumann, D. E. Smith & M. T. Zuber (2016), “Seasonal and static gravity field of Mars from MGS, Mars Odyssey and MRO radio science”, Icarus, 272, 228-245.
100. A. Anselmi et al., “Assessment of a Next GenerationMission for Monitoring the Variations of Earth’s Gravity”, Final Report of Next Generation Gravity Mission (NGGM) study, by a team led byThales Alenia Space for ESA (2010).
101. Zuber, M.T., Smith, D.E., Lehman, D.H. et al. “Gravity Recovery and Interior Laboratory (GRAIL): Mapping the Lunar Interior from Crust to Core”, Space Sci Rev (2013) Vol. 178, Issue 1, pp 3-24, 2013
102. M. Küppers, P. Michel, I. Carnelli, S. Ulamec, P. A. Abell and the Hera team, “Hera – The European Contribution To The First Asteroid Deflection Demonstration”, 50th Lunar and Planetary Science Conference 2019 (LPI Contrib. No. 2132).

103. J. W. McMahon, D. Farnocchia, D. Scheeres, and S. Chesley, “Understanding Kaula’s Rule for Small Bodies”,47th Lunar and Planetary Science Conference (2016).
104. J. K. Miller, A. S. Konopliva, P. G. Antreasian, J. J. Bordia, S. Chesley, C. E. Helfrich, W. M. Owen, T. C. Wang, B. G. Williams, D. K. Yeomans, D. J. Scheeres, “Determination of Shape, Gravity, and Rotational State of Asteroid 433 Eros”, Icarus Volume 155, Issue 1, January 2002, Pages 3-17.
105. A. S. Konopliv, S. W. Asmar, R. S. Park, B. G. Bills, F. Centinello, A. B. Chamberlin, A. Ermakov, R. W. Gaskell, N. Rambaux, C. A. Raymond, C. T. Russell, D. E. Smith, P. Tricarico, M.T. Zuber, “The Vesta gravity field, spin pole and rotation period, landmark positions, and ephemeris from the Dawn tracking and optical data”, Icarus Volume 240, 15 September 2014, Pages 103-117.
106. M. Pätzold , T. Andert, M. Hahn, S. W. Asmar, J. P. Barriot, M. K. Bird, B. Häusler, K. Peter, S. Tellmann, E. Grün, P.R. Weissman, H. Sierks, L. Jorda, R. Gaskell, F. Preusker, F. Scholten, “A homogeneous nucleus for comet 67P/Churyumov-Gerasimenko from its gravity field”, Nature, 2016 Feb 4; 530(7588):63-5.
107. A.S. Konopliv, S.W. Asmar, R.S. Park, B.G. Bills, F. Centinello, A.B. Chamberlin, A. Ermakov, R.W. Gaskell, N. Rambaux, C.A. Raymond, C.T. Russell, D.E. Smith, P. Tricarico, M.T. Zuber, “The Vesta gravity field, spin pole and rotation period, landmark positions, and ephemeris from the Dawn tracking and optical data”, pages 103-117
108. A. S. Konopliv, R. S. Park, A. T. Vaughan, B. G. Bills, S. W. Asmar, A.I. Ermaakov, N . Rambaux, C.A.Raymond, J.C. Castillo-Rogez, C.T. Russell, D.E. Smith, M. T. Zuber, “The Ceres gravity field, spin pole, rotation period and orbit from the Dawn radiometric tracking and optical data”, Icarus 299 (2018) 411-429.
109. H. F. Levison and the Lucy Science team, “Lucy: Surveying The Diversity of the Trojan Asteroids: The Fossils Of Planet Formation”, 47th Lunar and Planetary Conference 2016
110. D. Y. Oh, S. Collins, D. Goebel, B. Hart, G. Lantoine, S. Snyder, G. Whiffen, L. Elkins-Tanton, P. Lord, Z. Pirkl and L. Rotlisburger, “Development of the Psyche Mission for NASA’s Discovery Program”, The 35th International Electric Propulsion Conference, Georgia Institute of Technology, USA, October 8 –12, 2017
111. M. R.R.de Oliveira, P. J. S. Gil, R. Ghail, “A novel orbiter mission concept for venus with the EnVision proposal”, Acta Astronautica, Volume 148, July 2018, Pages 260-267
112. A. Freeman, S. E. Smrekar, S. Hensley, M. Wallace, C. Sotin, M. Darrach, P. Xaypraseuth, J. Helbert, E. Mazarico, “VERITAS – a Discovery-class Venus surface geology and geophysics mission”, IEEE Aerospace Conference 2016, Big Sky, MT, US
113. R. Rummel, “Spherical Spectral Properties of the Earth's Gravitational Potential and its First and Second Derivatives”, Part III: From The GBVP Towards A 1 cm Geoid Geodetic Boundary Value Problems in View of the One Centimeter Geoid, Volume 65 of the series Lecture Notes in Earth Sciences pp 359-404, 2005 Springer
114. A. Milani, A. Rossi, D. Vokrouhlicky, D. Villani, C. Bonanno, “Gravity field and rotation state of Mercury from the BepiColombo Radio Science Experiments”, Planetary and Space Science 49 (2001) pp. 1579–1596.
115. J. W. McMahon, D. Farnocchia, D. Scheeres, and S. Chesley, “Understanding Kaula’s Rule for Small Bodies”,47th Lunar and Planetary Science Conference (2016).
116. D. Dirkx, I. Prochazka, S. Bauer, P. Visser, R. Noomen, L. I. Gurvits, B. Vermeersen, “Laser and radio tracking for planetary science missions—a comparison”, Journal of Geodesy https://doi.org/10.1007/s00190-018-1171-x

117. S. W. Asmar and J. W. Armstrong, L. Iess, P. Tortora, "Spacecraft Doppler tracking: Noise budget and accuracy achievable in precision radio science observations", RADIO SCIENCE, Vol.40, RS20001, 2005
118. S. W. Asmar and N. A. Renzetti, "The Deep Space Network as an instrument for radio science research", JPL Publication 80-93, 1993.
119. P. W. Kinman, "Doppler Tracking of Planetary Spacecraft", IEEE Transactions On Microwave Theory And Techniques, Vol 40, N. 6, June 1992.
120. B. Bertotti, G. Comoretto, L. Iess, "Doppler tracking of spacecraft with multi-frequency links", Astronomy&Astrophysics 269, 608-616 (1993).
121. G. Mariotti, P. Tortora, "Experimental validation of a dual uplink multifrequency dispersive noise calibration scheme for Deep Space tracking", Radio Science, Vol. 48, 111–117, 2013.
122. B. Bertotti, L. Iess, P. Tortora, "A test of general relativity using radio links with the Cassini spacecraft", Nature, vol. 425, pages 374–376 (2003).
123. L. Iess, G. Boscagli, "Advanced radio science instrumentation for the mission BepiColombo to Mercury", Planetary and Space Science 49 (2001) 1597–1608.
124. R. H. Gooding, C. A. Wagner, "On the inclination functions and a rapid stable procedure for their evaluation together with derivatives", Celest Mech Dyn Astr (2008) 101:247–272
125. R. Koop, "Global gravity field modelling using satellite gravity gradiometry", Netherlands Geodetic Commission, Publications on Geodesy, New Series, N. 38, 1993
126. R. Rummel, "Satellite Gradiometry", Lecture Notes in Earth Sciences, Vol. 7, Mathematical and Numerical Techniques in Physical Geodesy, edited by H. S0nkei, Springer-Verlag Berlin Heidelberg (1986).
127. R. Haagmans, P. Silvestrin, R. Floberghagen, C. Siemes, L. Massotti and O. Carraz, "Observing Mass Distribution and Transport in the Earth System from an ESA Perspective", 5th International GOCE User Workshop, ESA 2014
128. T. Reubelt, N. Sneeuw, M. A. Sharifi, "Future mission design options for spatio-temporal geopotential recovery", Gravity, Geoid and Earth Observation, 2010, Volume 135
129. M. M. Watkins, S. V. Bettadpur, "The Grace Mission: the challenges of using micron-level satellite-to-satellite ranging to measure the Earth's Gravity Field", International Symposium on Space Flight Dynamics, Biarritz-France, 2000
130. ESA eoPortal Directory, https://earth.esa.int/web/eoportal/satellite-missions/g/grace
131. F. G. Lemoine, S. Goossens, T. J. Sabaka, J. B. Nicholas, E. Mazarico, D. D. Rowlands, B. D. Loomis, D. S. Chinn, D. S. Caprette, G. A. Neumann, D. E. Smith and M. T. Zuber, "High-degree gravity models from GRAIL primary mission data", Journal of Geophysical Research: Planets, Vol. 118, 1676–1699, doi:10.1002/jgre.20118, 2013
132. Daniel Schütze on behalf of the LRI team, "Measuring Earth: Current status of the GRACE Follow-On Laser Ranging Interferometer", Journal of Physics: Conference Series 716 (2016)
133. R. Floberghagen, M. Fehringer, D. Lamarre, D. Muzi, B. Frommknecht, C. Steiger, J. Pineiro, A. da Costa, "Mission design, operation and exploitation of the gravity field and steady-state ocean circulation explorer mission", Journal of Geodesy (2011) 85:749–758

134. A. Allasio, A. Anselmi, G. Catastini, S. Cesare, M. Dumontel, M. Saponara, G. Sechi, A. Tramutola, B. Vinai, G, Andrè, M. Fehringer, D. Muzi, “Goce Mission: Design Phases and In-Flight Experiences”, Advances in the Astronautical Sciences, February 2010
135. M. Fehringer, G. Andre, D. Lamarre & D. Maeusli, “A Jewel in ESA’s crowne”, in ESA Bulletin n.133, February 2008
136. M. R. Drinkwater, R. Haagmans, D. Muzi, A. Popescu, R. Floberghagen, M. Kern and M. Fehringer, “The Goce Gravity Mission: Esa’s First Core Earth Explorer”, Proceedings of the 3rd International GOCE User Workshop, 6-8 November, 2006, Frascati, Italy, ESA Special Publication, SP-627, ISBN 92-9092-938-3, pp.1-8, 2007.
137. R. Rummel, W. Yi, C. Stummer, “GOCE gravitational gradiometry”, J Geod (2011)
138. M.v d Meijde, R. Pail, R. Bingham, R. Floberghagen, “GOCE data, models, and applications: a review”, International Journal of Applied Earth Observation and Geoinformation 35 (2015) 4–15
139. GOCE System Critical Design Review (CDR), Executive summary, May 2005
140. G. Sechi, M. Buonocore, F. Cometto, M. Saponara, A. Tramutola, B. Vinai, G. Andrè, M. Fehringer, “In-Flight Results from the Drag-Free and Attitude Control of GOCE Satellite”, Proceedings of the 18th World Congress, The International Federation of Automatic Control - Milano (Italy) August 28 - September 2, 2011
141. C. Siemes, “GOCE gradiometer calibration and Level 1b data processing”, ESA Working Paper EWP-2384, 2011
142. M. I. Evstifeev, “The State of the Art in the Development of Onboard Gravity Gradiometers”, Gyroscopy and Navigation, 2017, Vol. 8, No. 1, pp. 68–79.
143. A. V. Veryaskin, “Gravity, Magnetic and Electromagnetic Gradiometry - Strategic technologies in the 21st century”, chapter 1: “Gravity Gradiometry”, Morgan & Claypool Publishers, Feb 2018.
144. R. L. Forward, “Review of Artificial Satellite Gravity Gradiometer Techniques for Geodesy”, Research Report, Hughes, 1973
145. R. L. Forward et al., “Research on Gravitational Mass Sensors”, Final Report, Hughes Research Laboratories, 1964
146. C. Jekeli, “The Gravity Gradiometer Survey System”, Eos, vol. 69, N.8, February 23, 1988, pp. 105-116/117
147. J. M. Lumley, J. P. White and G. Barnes, D. Huang, H. J. Paik, “A superconducting gravity gradiometer tool for exploration”, Airborne Gravity 2004 Workshop, 2004, Geoscience Australia
148. E. H. Metzger, A. Jircitano, C. Affleck, “Final Report satellite Borne Gravity Gradiometer Study”, NASA Goddard Space Flight Center, March 1976
149. D. Di Francesco, A. Grierson, D. Kaputa and T. Meyer, “Gravity gradiometer systems – advances and challenges”, Geophysical Prospecting, 2009, 57, 615-623
150. K. A. Carroll, D, Hatch and B, Main, “Performance of the Gedex High-Definition Airborne”, Airborne Gravity 2010 Workshop, Geoscience Australia 2010
151. P. Touboul, B. Foulon, E. Willemenot, “Electrostatic space accelerometers for present and future missions”, Acta Astronautica Vol. 45 (10), 605–617, 1999
152. B. Christophe, D. Boulanger, B. Foulon, P.-A. Huynh, V. Lebat, F. Liorzou, E. Perrot, “A new generation of ultra-sensitive electrostatic accelerometers for GRACE Follow-on and towards the next generation gravity missions”, Acta Astronautica, Volume 117, December 2015, Pages 1-7.

153. S. Kenyon et al. (eds.), “Geodesy for Planet Earth”, International Association of Geodesy Symposia 136, Springer-Verlag Berlin Heidelberg, 2012, pp. 215-221
154. V. Iafolla, E. Fiorenza, C. Lefevre, D. M. Lucchesi, M. Lucente, C. Magnafico, R. Peron, F. Santoli, “The BepiColombo ISA accelerometer: ready for launch”, 3rd IEEE Metrology for Aerospace (MetroAeroSpace), Florence, Italy, June 22-23, 2016
155. E. Fiorenza, M. Lucente, C. Lefevre, F. Santoli, V. Iafolla, “Zero-g positioning for the BepiColombo ISA Accelerometer”, Sensors & Actuators A: Physical, Vol. 240, 1 April 2016, pages 31-40
156. V. A. Iafolla, E. Fiorenza, C. Lefevre, D. M. Lucchesi, M. Lucente, C. Magnafico, S. Nozzoli, R. Peron, F. Santoli, “The role of the ISA accelerometer in the Radio Science Experiments of the BepiColombo mission to Mercury”, Thirtheen Marcel Grossman Meeting- MG13, Stockholm, 1-7 July 2012.
157. V. A. Iafolla, S. Nozzoli, E. Fiorenza, “One axis gravity gradiometer for the measurement of Newton’s gravitational constant G”, Physics Letters A 318 (2003) 223–233.
158. P. Cappuccio, M. Di Benedetto, G. Cascioli and L. Iess, “Report on JUICE 3GM gravity experiment performance”, Vol. 12, EPSC2018-1066, 2018 European Planetary Science Congress 2018
159. ESA – JUICE website, http://sci.esa.int/juice/61110-juice-instruments/
160. M. V. Moody and H. J. Paik, “A Superconducting Gravity Gradiometer for Inertial Navigation”, PLANS 2004. Position Location and Navigation Symposium
161. Gravity Gradiometer
162. “Swarm Flyby Gravimetry”, NIAC PHASE I Final Report, The Johns Hopkins University Applied Physics Laboratory, April 1, 2015
163. H. A. Chan, H. J. Paik, “Superconducting gravity gradiometer for sensitive gravity measurements – I. Theory”, Physical Review D, V 35, N 12, 1987
164. H. A. Chan, M. V. Moody, and H. J. Paik, “Superconducting gravity gradiometer for sensitive gravity measurements – II. Experiment”, Physical Review D, V 35, N 12, 1987
165. M. V. Moody, H.J. Paik, E. R. Canavan, “Three-axis superconducting gravity gradiometer for sensitive gravity experiments”, Review of scientific instruments, Vol. 73, n .11, Nov 2002
166. M. V. Moody and H. J. Paik, “Gauss's Law Test of Gravity at Short Range”, Physical Review Letters, Vol. 70, n.9, 1993
167. H. C. Ohanian, R. Ruffini, “Gravitation and Spacetime”, Cambridge University Press, 2013
168. C. M. Will, “The Confrontation between General Relativity and Experiment”, Living Rev. Relativity,17, (2014), 4, http://www.livingreviews.org/lrr-2014-4
169. H. J. Paik, J-P. Richard, “Development of a Sensitive Superconducting Gravity Gradiometer for Geological and Navigational Applications”, NASA Contract Report 4011, 1986
170. M. V. Moody and h. J. Paik, “A Superconducting Gravity Gradiometer for Inertial Navigation”, PLANS 2004. Position Location and Navigation Symposium, IEEE 2004
171. C.E. Griggs, H.J. Paik, M. V. Moody, S.C. Han, D.D. Rowlands. F. G Lomoine, P.J. Shirron, “Levitated Superconducting Gravity Gradiometer for Planetary Missions”, International Workshop on Instrumentation for Planetary Missions (IPM-2014), Greenbelt, Maryland (near Washington DC) - November 4-7, 2014.

172. X. Li, F.G. Lemoine, H.J. Paik, M. Zagarola, P.J. Shirron, C.E. Griggs, M.V. Moody, S.C. Han, “Design of Superconducting Gravity Gradiometer Cryogenic System for Mars Mission”, 19th International Cryocooler Conference (ICC 19); 20-23 Jun. 2016; San Diego, CA; United States
173. C. E. Griggs, M. V. Moody, R. S. Norton, H. J. Paik, and K. Venkateswara, “Sensitive Superconducting Gravity Gradiometer Constructed with Levitated Test Masses”, Physical Review Applied 8, 064024 (2017).
174. C. E. Griggs et al., “Tunable Superconducting Gravity Gradiometer for Mars Climate, Atmosphere, and Gravity Field Investigation”, 46th Lunar and Planetary Science Conference, 2015.
175. M. Kasevich and S. Chu, “Measurement of the Gravitational Acceleration of an Atom with a Light Pulse Atom-Interferometer”, Appl. Phys. B 54, 321-332 (1992).
176. N. Yu, J. M. Kohel, L. Romans, and L. Maleki, “Quantum Gravity Gradiometer Sensor for Earth Science Applications”, Earth Sci. Tech. Conf. 2002 (Pasadena).
177. N. Yu, J. M. Kohel, J. R. Kellogg, L. Maleki, “Development of an atom-interferometer gravity gradiometer for gravity measurement from space”, Appl. Phys. B 84, 647-652 (2006).
178. R. J. Cesarone, D. S. Abraham and L. J. Deutsch, “Prospects for a Next-Generation Deep-Space Network”, Proceedings of the IEEE, Vo. 95, No. 10, October 2007
179. W. Zheng, H. Hsu, M. Zhong, M. Yun, “Future dedicated Venus-SGG flight mission: accuracy assessment and performance analysis”, Advances in Space Research 57 (2016), pp. 459-476
180. J. Flokstra, R. Cuperus, R. Wiegerink, J. Sesé, H. Hemmes, C. Sotin, “Gravity Gradient Sensor Technology for future planetary missions”, Executive Summary, Del 5, ESA ITT AO/1-3829/01/NL/ND, July 2005
181. “An Introduction to MEMS (Micro-Electromechanical Systems)”, PRIME Faraday Partnership, 2002
182. J. Fraden, “Handbook of Modern Sensors – Physics, Designs and Applications”, Springer, 2004.
183. H. Liu, W.T. Pyke, and G. Dou, “A seesaw-lever force-balancing suspension design for space and terrestrial gravity-gradient sensing”, Journal of Applied Physics 119, 12
184. H. Liu, W.T. Pyke and G. Dou, “Design, Fabrication and Characterization of a Micro-Machined Gravity Gradiometer suspension”, SENSORS, 2014 IEEE.
185. Aguirre-Martinez, M. & Sneeuw, N. “Needs and Tolls for future Gravity Measuring Missions”, Space Science Reviews (2003) 108: 409
186. https://www.solidworks.com/

APPENDIX

Gravity gradient computation

A more precise evaluation of the gravity gradients was investigated, in order to have a simulation tool able to evaluate correctly the gravity gradient in terms of all the independent components (5), in addition to the third in-axis component, as explained in section 4.2.1 and 4.2.2.
The tool was thought to be used for any planetary body and for any orbit. Hereafter, the focus is limited to circular orbits ($\boldsymbol{e}=\mathbf{0}$). Future work foresees to extend the formulation to elliptical orbits as well.
The software is made of the following routines:

- Routines to compute the inclination functions $F_{lmp}(i)$ and the cross-track inclination functions (introduced by Koop [125]) till degree and order $l, m = 55$ and to produce an output in tabular format (2 routines, “f_inc_norm” and “f_inc_cross_norm”, called by the main routine “computa_f_inc”);
- Routine derived from Gooding [124] to compute the inclination functions $F_{lmp}(i)$ till very high degrees ($l \sim 1000$) and to produce an output in tabular format (not reported hereinafter);
- General routine for the computation of the six gravity gradients based on the Kaula expansion in terms of orbital elements; the computation is carried out along a defined orbit and with inclination functions loaded by the computation of previous routines.

The general routine receives as input the spherical harmonic coefficients for a planetary body till a l_{max} (C_{lm}, S_{lm}), the main body characteristics (G, M, R) and the orbit characteristics (a, e, i, Ω, ω, M). The output provides the computation of the inclination functions $F_{lmp}(i)$ and of the six gravity gradients Γ_{zz}, Γ_{xx}, Γ_{xz}, Γ_{yz}, Γ_{xy} , Γ_{yy} for the chosen body and orbit. The inclination functions are early evaluated and then recalled from the main program. These functions have been initially computed by a dedicated routine till degree and order $l, m = 55$. For very high degrees l, a more computational efficient routine from Gooding [124] was used.

1. “computa_f_inc”

```
%%%%%%%%%%%%%%%%%%%%%%%%%%%%%%%%%%%%%%%%%%%%%%%%%%%
%%%%% COMPUTATION KAULA INCLINATION FUNCTIONS %%%%%
%%%%% AND CREATION OF RELATED LOOKUP TABLE %%%%%%%%

clear
clc

format long

%
tic
in_d = 89;               % inclination (degrees)
lmax = 55;               % degree max

jjj = 1;  %%% index for l variation
l = (1:lmax);
```

```
%%% write inclination function data on a file
fid = fopen('f_inc_norm_i89_l55.txt','w');
fid2 = fopen('f_inc_cross_norm_i89_l55.txt','w');
for jjj = 1 : length(l)

    l(jjj);

    % corresponding values of m, i.e. l + 1
    m = (0:l(jjj));

    %%% index for m variation
    for j = 1 : length(m)

        %%%% p = 0:l, corresponding to k = -l : 2 : l
        jj = 1;    %%% index for k variation, i.e. p
        p = (0:l(jjj));

        for  jj = 1 : length(p)

             p(jj);
             k = l(jjj) - 2*p(jj);

        %%% normalisation factor for inclination functions
        [Fn(jjj, j, jj)] = f_inc_norm(l(jjj), m(j), p(jj), in_d);

        fprintf(fid,'%3i %3i %3i %4.10e\n', l(jjj), m(j), p(jj), Fn(jjj, j,
jj));

        end

        %%%% p = 0:l-1, i.e. l - 2p -1, corresponding to k = -(l - 1) : 2 :
        %%%% l - 1

        kkk = 1;    %%% index for k1 variation
        p1 = (0:l(jjj)-1);

        for  kkk = 1 : length(p1)

             l;
             m;
             p1(kkk);
             k1 = l(jjj) - 2*p1(kkk) - 1;

             %%% compute the cross-track inclination function (from Koop thesis,
pag. 220)
             [Fcn(jjj, j, kkk)] = f_inc_cross_norm(l(jjj), m(j), p1(kkk), in_d);

             fprintf(fid2,'%3d %3d %3d %16.10f\n', l(jjj), m(j), p1(kkk),
Fcn(jjj, j, kkk));

        end

    end

end

fclose(fid);
```

```
fclose(fid2);
toc

data1 =
load('C:\Users\Maverick\Marco\Dottorato\matlab\error\finali\f_inc_norm_i89_l55.t
xt');
ll1 = data1(1:end,1);
mm1 = data1(1:end,2);
pp1 = data1(1:end,3);
Fn = data1(1:end,4);

Finc = [ll1 mm1 pp1 Fn];

data2 =
load('C:\Users\Maverick\Marco\Dottorato\matlab\error\finali\f_inc_cross_norm_i89
_l55.txt');
ll2 = data2(1:end,1);
mm2 = data2(1:end,2);
pp2 = data2(1:end,3);
Fcn = data2(1:end,4);

Finc_c = [ll2 mm2 pp2 Fcn];
```

2. “f_inc_norm”

```
%%%%%%%%%%%%%%%%%%%%%%%%%%%%%%%%%%%%%%%%%%%%%%%%%%%%%%%
%%%%%%% NORMALISED KAULA INCLINATION FUNCTIONS %%%%%%%%%%
%%%%%%%%%%%%%%%%%%%%%%%%%%%%%%%%%%%%%%%%%%%%%%%%%%%%%%%
%%%% Atot = output of normalised inclination function
%%%% ll = harmonics degree
%%%% mm = harmonics order
%%%% kk = l - 2*pp, variable change
%%%% in_dd = orbit inclination in degrees

function [Atot]  = f_inc_norm(ll, mm, pp, in_dd)

    %%%%% INPUT PARAMETERS %%%%%%%%
    in = deg2rad(in_dd);      % conversion to radians
%     pp = (ll - kk)/2;        % link between classical p variable and the new k
variable
    kk = ll - 2 * pp;
    q = floor((ll - mm)/2);  % compute the integer of
    t = 0 : min(pp, q);      % t values
    s = 0 : mm;              % s values

    %%%% normalisation factor for inclination functions
    if mm == 0
           deltam = 1;
        else
           deltam = 0;
    end

    Nlm = sqrt((2 - deltam)*((2*ll + 1)*factorial(ll - mm))/factorial(ll + mm));

    %%% index for t variation
    for w = 1 : length(t)
```

```
        gi = 2*ll - 2*t(w);
        AA(w) = (factorial(gi)/(factorial(t(w))*factorial(gi/2)*factorial(ll -
mm - 2*t(w))*2^(gi)))*sin(in)^(ll - mm - 2*t(w));

        %%% index for s variation
        for y = 1 : length(s)

            c = 0 : ll - mm - 2*t(w) + s(y);  % c values

            %%% index for c variation
            for i = 1 : length(c)

                %%%% verify conditions for the sum over c
                if (mm - s(y)) - (pp - t(w) - c(i)) < 0 ||  pp - t(w) - c(i) < 0
                    B(i) = 0;
                else
                    B(i) = nchoosek(mm - s(y), pp - t(w) - c(i)) * (-1)^(c(i) -
q);
                end

                if ll - mm - 2*t(w) + s(y) - c(i) < 0 || c(i) < 0
                    C(i) = 0;
                else
                    C(i) = nchoosek(ll - mm - 2*t(w) + s(y), c(i));
                end

               D(i) = nchoosek(mm, s(y))*cos(in)^s(y) * C(i) * B(i);

            end

            % sum over c (i.e. C and B), at s fixed
            Asd(y) = AA(w)*sum(D);

            % reinitialise A and D
            A = [];
            D = [];
        end

        % sum over s
        Ast(w) = sum(Asd);

    end

    Atot = Nlm*sum(Ast);

end
```

3. “f_inc_cross_norm”

```
%%%%%%%%%%%%%%%%%%%%%%%%%%%%%%%%%%%%%%%%%%%%%
%%%%%%% CROSS-TRACK INCLINATION FUNCTIONS %%%
%%%%%%%%%%%%%%%%%%%%%%%%%%%%%%%%%%%%%%%%%%%%%
Formulas from pag. 220 of Koop thesis "global gravity field modelling using
satellite gravity gradiometry"
%%%% Atot = output of inclination function
```

```
%%%% ll = harmonics degree
%%%% mm = harmonics order
%%%% kk = l - 2*pp, variable change
%%%% in_dd = orbit inclination in degrees

function [Astot]  = f_inc_cross(ll, mm, pp, in_dd)

    %%%%% INPUT PARAMETERS %%%%%%%%
    in = deg2rad(in_dd);       % conversion to radians
%     pp = (ll - kk)/2;         % link between classical p variable and the new k
variable
    kk = ll - 2*pp - 1;
    q = floor((ll - mm)/2);  % compute the integer of
    t = 0 : min(q, pp);      % t values
    s = 0 : mm;              % s values

     %%%% normalisation factor for inclination fucntions
    if mm == 0
           deltam = 1;
        else
           deltam = 0;
    end

    Nlm = sqrt((2 - deltam)*((2*ll + 1)*factorial(ll - mm))/factorial(ll + mm));

    %%% t variation
    for w = 1 : length(t)

        gi = 2*ll - 2*t(w);
        AA(w) = (((-
1)^(t(w))*factorial(gi))/(2^ll*factorial(t(w))*factorial(gi/2)*factorial(ll - mm
- 2*t(w))));

        %%% s variation
        for y = 1 : length(s)

            f(y) = sin(in)^(ll - mm - 2*t(w) - 1)*cos(in)^(s(y) - 1)*((ll - mm -
2*t(w))*cos(in)^2 - s(y)*sin(in)^2);

            %%% c variation
            cmin = max(0, pp - t(w));
            cmax = min(ll - mm  - 2*t(w)+ s(y) - 1, mm - s(y));
            c = cmin : cmax;

            if cmin > cmax
                c = 0;
            end

            %%%%
            for i = 1 : length(c)

                %%% verify condition for the sum over c
                if (mm - s(y)) - (pp - t(w) - c(i)) < 0 ||  pp - t(w) - c(i) < 0
                    B(i) = 0;
                else
                    B(i) = nchoosek(mm - s(y), pp - t(w) - c(i));
                end

                if (ll - mm - 2*t(w) + s(y) - 1 - c(i)) < 0 || c(i) < 0
```

```
                C(i) = 0;
            else
                C(i) = nchoosek(ll - mm - 2*t(w) + s(y) - 1, c(i));
            end

            %%% intermediate computations
            A(i) = AA(w)* nchoosek(mm, s(y))* 2^(2*t(w) - ll + 1)*(-1)^(q +
t(w)) * f(y) * C(i) * B(i) * (-1)^(c(i));

            D(i) = nchoosek(mm, s(y))* 2^(2*t(w) - ll + 1)*(-1)^(q + t(w)) *
f(y) * C(i) * B(i);

            end

            As(y) = sum(A);          % sum over C(i) and B(i), with s and t
fixed, and AA included
            Asd(y) = AA(w)*sum(D);   % sum over C(i) and B(i), with s and t
fixed, and AA not included

            A = [];
            D = [];

        end

        Astd(w) = sum(As);    % sum over s, with t fixed
        Ast(w) = sum(Asd);    % sum over s, with t fixed

    end

    Astot = Nlm*sum(Ast);

end
```

4. “gradient_grid_read_table_time”

```
%%%%%%%%%%%%%%%%%%%%%%%%%%%%%%%%%%%%%%%%%%%%%%%%%%%%%%
%%%% GRAVITATIONAL FUNCTIONALS - GRAVITY GRADIENT %%%%
%%%%%%%%%%%%%%%%%%%%%%%%%%%%%%%%%%%%%%%%%%%%%%%%%%%%%%%%%%%%%%%%%%%%%%%%%%%%%%%%
%%%% SPHERICAL HARMONICS SYNTHESIS WITH KAULA EXPANSION IN TERMS OF ORBITAL
ELEMENTS %%%%%
%%%% COMPUTED ALONG A DEFINED ORBIT AND WITH INCLINATION FUNCTIONS LOADED
%%%% BY A LOOKUP TABLE

clear
clc
clf
format long

%%%%%%%%%%
% EARTH
%%%%%%%%%
%planet = 'Earth';
%G = 6.672e-11;       % m^3/(kg*s^2)
%mu = 0.3986004415e6*1e9; %%% m^3/s^2
%M = 5.972e24;        % kg Terra
%R = 6378*1e3;      % radius Earth in m
%%%%%%%%%%%%%%%%%%%%%%%%%%%%%%%%%%%%%%%%%%
```

```
%%%% EARTH DATA %%%%%%%%%%%%%%%%%%%%%%%%%%
%%%%%%%%%%%%%%%%%%%%%%%%%%%%%%%%%%%%%%%%%
%%% GOCE data
%%data =
%importdata('C:\Users\Maverick\Marco\Dottorato\tesi\modelli_gravità\TERRA\GGM05S
%.gcf');

% l = data(50:end,1);
% m = data(50:end,2);
% C_lmi = data(37:end,4);
% S_lmi = data(37:end,5);
% E_Clm = data(37:end,6);
% E_Slm = data(37:end,7);

% A = [l m C_lmi S_lmi E_Clm E_Slm];

%%%%%%%%%%%%%%%%%%%%%%%%%%%%%%%%%%%%%%%%%%
%%%% MARS %%%%%%%%%%%%%%%%%%%%%%%%%%%%
%%%%%%%%%%%%%%%%%%%%%%%%%%%%%%%%%%%%%%%%%%
planet = 'Mars';
mu = 0.4282837581575610e+05*1e9; %%% GM in m^3/s^2
G = 6.672e-11;       % m^3/(kg*s^2)
M = 6.419e23;        % kg Mars mass
R = 3390*1e3;       % radius Mars in m
% % c = 8.5e-5;       % Kaula constant for Mars (from konopliv MRO120D)
%%%%%%%%%%%%%%%%%%%%%%%%%%%%%%%%%%%%%%%%%
%%%% MARS DATA %%%%%%%%%%%%%%%%%%%%%%%%%%
%%%%%%%%%%%%%%%%%%%%%%%%%%%%%%%%%%%%%%%%%
data =
importdata('C:\Users\Maverick\Marco\Dottorato\tesi\modelli_gravità\MARTE\MRO120D
\jgmro_120d_sha.tab.txt');
% data =
importdata('C:\Users\Maverick\Marco\Dottorato\matlab\error\finali\jgmro_120d_sha
.tab.txt');

% %%%%%%%%%%%%%%%%%%%%%%%%%%%%%%%%%%%%%%%%%
% %%%% VENUS %%%%%%%%%%%%%%%%%%%%%%%%%%%%%%
% %%%%%%%%%%%%%%%%%%%%%%%%%%%%%%%%%%%%%%%%%
% planet = 'Venus';
% mu = 0.3248585920790000E+06*1e9;  % GM in m^3/s^2
% M = 4.869e24;         % kg Venus mass
% R = 6051*1e3;         % radius Venus in m
% % c = 1.2e-5;           % Kaula constant for Venus (from Konopliv)
% %%%%%%%%%%%%%%%%%%%%%%%%%%%%%%%%%%%%%%%%
% %%%% VENUS DATA %%%%%%%%%%%%%%%%%%%%%%%%%%
% %%%%%%%%%%%%%%%%%%%%%%%%%%%%%%%%%%%%%%%%
% data =
importdata('C:\Users\Maverick\Marco\Dottorato\matlab\error\finali\shgj180u.txt')
;
% %%%%%%%%%%%%%%%%%%%%%%%%%%%%%%%%%%%%%%%%%%%%%%%%%%%%%%%%%%%%
% %   Table 10-1.  The Magellan mapping orbit
% % -------------------------------------------------
% %     Parameter                        Value
% % -------------------------------------------------
% % Periapsis altitude, km (miles)      257 (172)
% % Apoapsis altitude, km (miles)     8,000 (5,000)
% % Periapsis latitude                 10 degrees N
% % Orbit peroid, hours                  3.15
% % Inclincation (relative to            85.3
% % Venus's equator), degrees
```

```
% %%%%%%%%%%%%%%%%%%%%%%%%%%%%%%%%%%%%%%%%%
% %%%% MOON %%%%%%%%%%%%%%%%%%%%%%%%%%%%
% %%%%%%%%%%%%%%%%%%%%%%%%%%%%%%%%%%%%%%%%%
% planet = 'Moon';
% M = 7.348e22;           % kg Moon mass
% R = 1738*1e3;           % Moon radius in m
% mu = 0.4902800305555400E+04*1e9; %%% m^3/s^2
% c = 3.6e-4;       % Kaula constant for Moon (from Lemoine 2013)
% %%%%%%%%%%%%%%%%%%%%%%%%%%%%%%%%%%%%%%%%
% %%%% LOAD DATA %%%%%%%%%%%%%%%%%%%%%%%%
% %%%%%%%%%%%%%%%%%%%%%%%%%%%%%%%%%%%%%%%%
% data =
importdata('C:\Users\Maverick\Marco\Dottorato\matlab\error\finali\gggrx_0660pm_s
ha.tab');
% % data = importdata('jggrx_1500e_sha.tab');

% %%%%%%%%%%%%%%%%%%%%%%%%%%%%%%%%%%%%%%%%%
% %%%% MERCURY %%%%%%%%%%%%%%%%%%%%%%%%%%%%
% %%%%%%%%%%%%%%%%%%%%%%%%%%%%%%%%%%%%%%%%%
% planet = 'Mercury';
% M = 3.302e23;        % kg Mercury mass
% R = 2440*1e3;       % Mercury radius in m
% mu = 2.2031870798779644e4*1e9;   % GM in m^3/s^2;
% % c = 4e-5;           % Kaula constant for Mercury (from Mazarico 2014)
% %%%%%%%%%%%%%%%%%%%%%%%%%%%%%%%%%%%%%%%
% %%%% MERCURY DATA %%%%%%%%%%%%%%%%%%%%%%%%%%
% %%%%%%%%%%%%%%%%%%%%%%%%%%%%%%%%%%%%%%%%
% data =
importdata('C:\Users\Maverick\Marco\Dottorato\matlab\error\finali\ggmes_50v06_sh
a.tab');

l = data(2:end,1);
m = data(2:end,2);
C_lmi = data(2:end,3);
S_lmi = data(2:end,4);
E_Clm = data(2:end,5);
E_Slm = data(2:end,6);

A = [l m C_lmi S_lmi E_Clm E_Slm];

%%%%%%%%%%%%%%%%%%%%%%%%%%%%%%%%%%%%%%%%%%%%%%%%%%%%%%%%%%%%%%%%
%%%%% ORBITAL PARAMETERS r, omega0 (i.e. omega and M), i %%%
%%%%%%%%%%%%%%%%%%%%%%%%%%%%%%%%%%%%%%%%%%%%%%%%%%%%%%%%%%%%%%%%
% h = 0;
%%% MARS
%%%% MRO --> 255-kilometer x 320-kilometer near-polar orbit around Mars.
h = 255*1e3;              % orbit heigth wrt the surface in m
%%% VENUS
%%%% Magellan --> Periapsis altitude, km 257, Apoapsis altitude, km 8,000
% Periapsis latitude, 10 degrees N, Orbit peroid, hours 3.15, Inclincation
%%%(relative to Venus's equator  85.3 degrees
% h = 300*1e3;              % orbit heigth wrt the surface in m
r = R + h;                % orbit heigth wrt the centre in m
Per = 2*pi*sqrt(r^3/(mu));  % orbital period

%%%%%%%%%%%%%%%%%%%%%%%%%%%%
%%% ORBITAL DATA %%%%%%%%%%%
%%%%%%%%%%%%%%%%%%%%%%%%%%%%
omega_p = deg2rad(0);   % perigee argument
```

```
n = sqrt(mu/r^3);          % mean motion
omega = deg2rad(67.8);     % RAAN
tetag = deg2rad(10);       % Planet's argument of longitude
M = deg2rad(0);
in_d = 89;               % inclination (degrees)

%%% time dependence
sample = 4;             % orbit sampling in time (s)
points = round(Per/sample);     % points along the orbit
step = 360/points;
len = step*r;     % minimum orbit length corresponding to step
Tr = (86400);     % mission duration
Np = Tr/sample;  %%% number of measures during the mission Tr
time = 0:sample:(Np);
Nr = round(Tr/Per);      %%% number of orbit revolutions in Tr
Nd = 1;                  %%% nodal days number in Tr
omega0_dot = 2*pi/Per;     %%% rad/s
% omegae_dot = 2*pi/;      %%% rad/s
% Tday = 2*pi/omegae_dot;    % period of one nodal day
% Tnodal = 2*pi/omega0_dot; % period of one revolution

%%%% planet-pointing
%%%% angular rate due to planet-pointing
ang_rate = 2*pi/Per

%%%%%%%%%%%%%%%%%%%%%%%%%%%%%%%%%%%%%%%%%%%
%%% LOAD TABLE INCLINATION FUNCTIONS %%%%%
%%%%%%%%%%%%%%%%%%%%%%%%%%%%%%%%%%%%%%%%%%%
% data1 =
importdata('C:\Users\Maverick\Marco\Dottorato\matlab\error\finali\f_inc_norm_pro
va.txt');
% data1 =
load('C:\Users\Maverick\Marco\Dottorato\matlab\error\finali\f_inc_norm_i89_l55.t
xt');
data1 =
load('C:\Users\Maverick\Marco\Dottorato\matlab\error\finali\f_inc_norm_i89_l200.
txt');
% data1 =
importdata('C:\Users\Maverick\Marco\Dottorato\matlab\error\finali\f_inc_norm_i14
4_l20.txt');

lll = data1(1:end,1);
mmm = data1(1:end,2);
ppp = data1(1:end,3);
Fnnn = data1(1:end,4);

Finc = [lll mmm ppp Fnnn];

% % data2 =
load('C:\Users\Maverick\Marco\Dottorato\matlab\error\finali\f_inc_cross_norm_pro
va.txt');
% data2 =
load('C:\Users\Maverick\Marco\Dottorato\matlab\error\finali\f_inc_cross_norm_i89
_l55.txt');
%
% % data2 =
importdata('C:\Users\Maverick\Marco\Dottorato\matlab\error\finali\f_inc_cross_no
rm_i144_l20.txt');
%
% ll2 = data2(1:end,1);
```

```
% mm2 = data2(1:end,2);
% pp2 = data2(1:end,3);
% Fcn = data2(1:end,4);
%
% Finc_c = [ll2 mm2 pp2 Fcn];

ii = 1;  %%% index for row of Finc table
iii = 1; %%% index for row of Finc_c table
%%%%%%%%%%%%%%%%%%%%%%%%%%%%%%%%%%%%%%%%%

tic
%%% max degree l
% lmax = 70; %%% VENUS
lmax = 100;  %%% MARS
%%% find index ki = lmax
% ki = find(l == lmax, 1, 'first');

%%%%%%%%%%%%%%%%%%%%%%%%%%
%%%% PRINT ORBIT DATA
fprintf('Planet = %8s\n', planet);
fprintf('Orbit height (km) = %2.3f\n', h/1e3);
fprintf('Orbital period (hours) = %2.3f\n', Per/3600);
fprintf('Orbital velocity (m/s) = %2.3f\n', sqrt(mu/r));
fprintf('Orbital angular rate (rad/s and degree/s) = %2.6f %2.6f\n', ang_rate,
rad2deg(ang_rate));
fprintf('Inclination (degrees) = %2.2f\n', in_d);
fprintf('Argument of pericentre (degrees) = %2.2f\n', rad2deg(omega_p));
fprintf('RAAN (degrees) = %2.2f\n', rad2deg(omega));
fprintf('Argument of longitude (degrees) = %2.2f\n', rad2deg(tetag));
fprintf('Orbit sampling in time (s) = %2.2f\n', sample);
fprintf('Orbit sampling in frequency (Hz) = %2.2f\n', 1/sample);
fprintf('Number of points considered along the orbit = %2.2f\n', points + 1);
fprintf('Spacing between points (m) = %2.2f\n', len);
fprintf('Mission duration (s and day) = %5.2f %5.2f\n', Tr, Tr/86400);
fprintf('Number of measures during the mission = %2.2f\n', Np);
fprintf('Number of orbit revolutions = %2.2f\n', Nr);
fprintf('Maximum degree = %2.2f\n', lmax);

%%%%%%%%%%%%%%%%%%%%%%%%%%%%%%%%%%%%%%%%%%%%%%%%%%%%%%%%%%%%%%%%

%%% time
jai = (0 : Np - 1);
%%% index for l change
i = 1;
% jjj = 1;  %%% index for l variation
ll = 1:lmax;

for jjj = 1 : length(ll)
% for jjj = 1 : l(ki)

  ll(jjj);

    %%% local gravity gradient formulas are retrieved from table 4.1 pag. 54 of
    %%% Koop thesis, in terms of variables (r, omega0, in_d). For gradient
    %%% yz and xy, formulas are taken from table 4.2 at pag. 56

    %%% multiplicative factor for gravity gradient
%     gamma_l = (mu/R^3)*(R/r)^(l(jjj) + 3);
    gamma_l = (mu/R^3)*(R/r)^(ll(jjj) + 3);
```

```
    %%% select the right spherical harmonics coefficients
    if A(i,1) == ll(jjj)

    %%% corresponding values of m, i.e. l + 1 values for each m
    Clm = C_lmi(i:i+ll(jjj));
    Slm = S_lmi(i:i+ll(jjj));
    eClm = E_Clm(i:i+ll(jjj));
    eSlm = E_Slm(i:i+ll(jjj));

    i = i + ll(jjj) + 1;

    end

    % corresponding values of m, i.e. l + 1
    m = (0:ll(jjj));

    %%% index for m variation
    for j = 1 : length(m)

        m(j);
        %%% choose the harmonic coefficient wrt l - m
        if  mod(ll(jjj) - m(j), 2) == 0      %%% l - m pari
            alfa_lm = Clm(j, :);
            beta_lm = Slm(j, :);
        else
            alfa_lm = -Slm(j, :);   %%% l - m dispari
            beta_lm =  Clm(j, :);
        end

        %%%% p = 0:l, corresponding to k = -l : 2 : l
        jj = 1;    %%% index for k variation, i.e. p
        p = (0:ll(jjj));
        for  jj = 1 : length(p)

            k = l(jjj) - 2*p(jj);

        %%% normalisation factor for inclination functions (from table)
        if Finc(ii, 1) == ll(jjj) && Finc(ii, 2) == m(j) && Finc(ii, 3) == p(jj)

           Fn = -Finc(ii,4);

        end

        ii = ii + 1;

        %%% argument of trigonometric functions
%          psi_km = k * omega0_0 + m(j)  * omegae_0;
%          psi_km = k * omega0_0 + m(j)  * omegae_0 *m(j) + (k * omega0_dot + m(j)
* omegae_dot)*(t - t0);
        psi_km = (2*pi*jai/Np)*Nr*(k + m(j)  * Nd/Nr); %% t0 = 0 e omega0_0 =
omegae_0 = 0

        %%% compute gravity gradient zz, yy, xz, xx;
        %%% local gravity gradient formulas are retrieved from table 4.1 pag. 54
of
        %%% Koop thesis, in terms of variables (r, omega0, in_d).
        %%% jj =  index for k variation. i.e. of p
```

```
        kappa_zz = Fn * (alfa_lm * cos(psi_km) + beta_lm * sin(psi_km));
        kappa_yy = -((ll(jjj) + 1)^2 - k^2) * kappa_zz;
        kappa_xz = -(ll(jjj) + 2) * k * Fn * (beta_lm * cos(psi_km) - alfa_lm *
sin(psi_km));
        kappa_xx = -(ll(jjj) + 1 + k^2) * kappa_zz;

        Tzz(:, jj) = (ll(jjj) + 1) * (ll(jjj) + 2) * gamma_l * kappa_zz;
        Tyy(:, jj) = gamma_l * kappa_yy;
        Txz(:, jj) = gamma_l * kappa_xz;
        Txx(:, jj) = gamma_l * kappa_xx;

        end

%         %%% compute gravity gradient xy, yz
%         %%% For gradient yz and xy, formulas are taken from tabel 4.2 at pag.
56
%         %%%% p = 0:l-1, i.e. l - 2p -1, corresponding to k = -(l - 1) : 2 :
%         %%%% l - 1
%
%         kkk = 1;    %%% index for k1 variation
%         p1 = (0:ll(jjj)-1);
%
%         for  kkk = 1 : length(p1)
%
%              ll;
%              m;
%              p1(kkk);
%              k1 = ll(jjj) - 2*p1(kkk) - 1;
%
%              %%% argument of trigonometric functions
% %              psi_km1 = k1 * omega0_0 + m(j) * omegae_0;
%              psi_km1 = (2*pi*jai/Np)*Nr*(k1 + m(j) * Nd/Nr); %% t0 = 0 e
omega0_0 = omegae_0 = 0
%
%              %%% compute the cross-track inclination function (from Koop
thesis, pag. 220)
%              %%% normalisation factor for inclination functions (from table)
%              if Finc_c(iii, 1) == ll(jjj) && Finc_c(iii, 2) == m(j) &&
Finc_c(iii, 3) == p1(kkk)
%
%                  Fcn = Finc_c(iii,4);
%
%              end
%
%              iii = iii + 1;
%
%              %%% kkk = index for k1 variation
%              kappa_xy = Fcn*(alfa_lm * cos(psi_km1) + beta_lm * sin(psi_km1));
%              kappa_yz = Fcn*(beta_lm * cos(psi_km1) - alfa_lm * sin(psi_km1));
%
%              Txy(:, kkk) = -k1 * gamma_l * kappa_xy;            %%%
alternative version
%              Tyz(:, kkk) = -(ll(jjj) + 2) * gamma_l * kappa_yz;  %%%
alternative version
%
%         end

        %%% sum over k and k1 values,i.e. over p, at l and m fixed, and save in
variable S
```

```
        Szz(:, j) = sum(Tzz, 2);
%          Sxy(:, j) = sum(Txy, 2);   %%% alternative version with cross-track
inclination function (from Koop thesis, pag. 220)
%          Syz(:, j) = sum(Tyz, 2);   %%% alternative version with cross-track
inclination function (from Koop thesis, pag. 220)
        Syy(:, j) = sum(Tyy, 2);
        Sxz(:, j) = sum(Txz, 2);
        Sxx(:, j) = sum(Txx, 2);

        if ll(jjj) == 1

            SSzz(:, j) = sum(Tzz, 2);
%              SSxy(:, j) = sum(Txy, 2);   %%% alternative version with cross-
track inclination function (from Koop thesis, pag. 220)
%              SSyz(:, j) = sum(Tyz, 2);   %%% alternative version with cross-
track inclination function (from Koop thesis, pag. 220)
            SSyy(:, j) = sum(Tyy, 2);
            SSxz(:, j) = sum(Txz, 2);
            SSxx(:, j) = sum(Txx, 2);

        end

        %%% initialise
        Tzz = [];
%          Txy = [];
%          Tyz = [];
        Tyy = [];
        Txz = [];
        Txx = [];

    end

    %%% save in variable U and sum over m values, at l fixed
    Uzz(:, jjj) = sum(Szz, 2);   % not k dependent
%      Uxy(:, jjj) = sum(Sxy, 2);   % alternative version
%      Uyz(:, jjj) = sum(Syz, 2);   % alternative version
    Uyy(:, jjj) = sum(Syy, 2);
    Uxz(:, jjj) = sum(Sxz, 2);
    Uxx(:, jjj) = sum(Sxx, 2);

    %%%% value of the gradient at l fixed and at m values
    sSzz(:, 1:jjj+1) = Szz;
%      sSxy(:, 1:jjj+1) = Sxy;
%      sSyz(:, 1:jjj+1) = Syz;
    sSyy(:, 1:jjj+1) = Syy;
    sSxz(:, 1:jjj+1) = Sxz;
    sSxx(:, 1:jjj+1) = Sxx;

    %%% initialise
    Szz = [];
%      Sxy = [];
%      Syz = [];
    Syy = [];
    Sxz = [];
    Sxx = [];

end

toc
```

```
%%% sum over l, at a certain point of the orbit
Gzz = sum(Uzz, 2) + 2*mu/r^3;     % aggiunta del termine per l=0, ossia il
monopolo che è Gzz = +2*mu/r^3
% Gxy = sum(Uxy, 2);               % Gyy = -mu/r^3; Gxx = -mu/r^3
% Gyz = sum(Uyz, 2);
Gyy = sum(Uyy, 2) - mu/r^3;
Gxz = sum(Uxz, 2);
Gxx = sum(Uxx, 2) - mu/r^3;

% output = [Gzz; Gxx; Gyy; Gxy; Gyz; Gxz];
% fid = fopen('GG.txt','w');
% fprintf(fid,'%s %16s %16s %16s %16s %16s\n', 'Gzz', 'Gxx', 'Gyy', 'Gxy',
'Gyz', 'Gxz');
% fprintf(fid,'%1.10e %16.10e %16.10e %16.10e %16.10e %16.10e\n', Gzz, Gxx, Gyy,
Gxy, Gyz, Gxz);
% % fprintf(fid,'%5.10e\n', Gzz,);
% fprintf(fid,'%5.10e\n', Gxx);

% fclose(fid);

traccia = Gxx + Gyy + Gzz;

%%%%% PSD %%%%%

[pzz,szz] = psdblack(Gzz, length(Gzz), 1/sample);
[pxx,sxx] = psdblack(Gxx, length(Gxx), 1/sample);
[pyy,syy] = psdblack(Gyy, length(Gyy), 1/sample);

figure(9)
clf
loglog(szz, pzz.^.5,'LineWidth', 1.5)
hold on
loglog(sxx, pxx.^.5, 'r', 'LineWidth', 1.5)
loglog(syy, pyy.^.5, 'g', 'LineWidth', 1.5)
grid on
title('GG PSDBlack')

fprintf('Monopole value Gzz (s-2 and E) = %5.10e %5.4f\n', 2*mu/r^3,
2*mu/r^3/1e-9);
fprintf('Monopole value Gxx (s-2 and E) = %5.10e %5.4f\n', -mu/r^3,  -mu/r^3/1e-
9);
fprintf('Monopole value Gyy (s-2 and E) = %5.10e %5.4f\n', -mu/r^3,  -mu/r^3/1e-
9);

time = Tr;
time_h = linspace(1, Tr, Tr/sample)/3600;

figure(1)
clf
% plot((Gzz-2*mu/r^3)/1e-9)
% plot((Gzz-2*mu/r^3))
plot(time_h, Gzz/1e-9)
% plot(time_h, (Gzz-2*mu/r^3)/1e-9)
grid on
% xlim([0 time_h(2701)]) % Venus
xlim([0 time_h(3301)])
xlabel('Time (h)')
ylabel('GRAVITY GRADIENT ZZ (E)')
```

```
% ylabel('GRADIENTE DI GRAVITA ZZ (s^-2)')
title('GRAVITY GRADIENT ZZ (l = 100) (E)')
% title('GRAVITY GRADIENT ZZ (l = 70) (E)')

figure(2)
clf
% plot((Gyy + mu/r^3)/1e-9,'r')
% plot((Gyy + mu/r^3),'r')
plot(time_h,(Gyy)/1e-9,'r')
% plot(time_h, (Gyy + mu/r^3)/1e-9, 'r')
grid on
% xlim([0 time_h(2701)])
xlim([0 time_h(3301)]) %Mars
xlabel('Time (h)')
ylabel('GRAVITY GRADIENT YY (E)')
% ylabel('GRADIENTE DI GRAVITA YY (s^-2)')
title('GRAVITY GRADIENT YY (l = 100) (E)')
% title('GRAVITY GRADIENT YY (l = 70) (E)')

figure(3)
clf
% plot((Gxx + mu/r^3)/1e-9,'g')
% plot((Gxx + mu/r^3),'g')
plot(time_h,(Gxx)/1e-9,'g')
% plot(time_h,(Gxx + mu/r^3)/1e-9,'g')
grid on
% xlim([0 time_h(2701)])
xlim([0 time_h(3301)]) % Mars
xlabel('Time (h)')
ylabel('GRAVITY GRADIENT XX (E)')
% ylabel('GRADIENTE DI GRAVITA XX (s^-2)')
title('GRAVITY GRADIENT XX (l = 100) (E)')
% title('GRAVITY GRADIENT XX (l = 70) (E)')

% figure(4)
% clf
% plot(Gxy/1e-9)
% % plot(Gxy)
% grid on
% ylabel('GRADIENTE DI GRAVITA XY (E)')
% % ylabel('GRADIENTE DI GRAVITA XY (s^-2)')

% figure(5)
% clf
% plot(Gyz/1e-9,'r')
% % plot((Gyz),'r')
% grid on
% ylabel('GRADIENTE DI GRAVITA YZ (E)')
% % ylabel('GRADIENTE DI GRAVITA YZ (s^-2)')

figure(6)
clf
plot(time_h, (Gxz)/1e-9,'g')
grid on
% xlim([0 time_h(2701)])
xlim([0 time_h(3301)]) % Mars
xlabel('Time (h)')
ylabel('GRAVITY GRADIENT XZ (E)')
% ylabel('GRADIENTE DI GRAVITA XZ (s^-2)')
title('GRAVITY GRADIENT XZ (l = 100) (E)')
```

```
% title('GRAVITY GRADIENT XZ (l = 70) (E)')

%%%% PLOT AT L FIXED VS TIME
elle = lmax;

figure(71)
clf
plot(Uzz(:, elle)/1e-9)
% plot((Uzz(:, elle)- 2*mu/r^3)/1e-9)
grid on
xlabel('Time (s)')
ylabel('GRAVITY GRADIENT ZZ (E)')
title('GRAVITY GRADIENT ZZ AT l FIXED (100), SUM OVER m, VS TIME (E)',
'fontsize', 9)
% title('GRAVITY GRADIENT ZZ AT l FIXED (70), SUM OVER m, VS TIME (E)',
'fontsize', 9)

figure(72)
clf
plot(Uyy(:,elle)/1e-9, 'r')
% plot((Uyy(:,elle)+ mu/r^3)/1e-9, 'r')
grid on
xlabel('Time (s)')
ylabel('GRAVITY GRADIENT YY (E)')
title('GRAVITY GRADIENT YY AT l FIXED (100), SUM OVER m, VS TIME (E)',
'fontsize', 9)
% title('GRAVITY GRADIENT YY AT l FIXED (70), SUM OVER m, VS TIME (E)',
'fontsize', 9)

figure(73)
clf
plot(Uxx(:, elle)/1e-9,'g')
% plot((Uxx(:, elle) + mu/r^3)/1e-9,'g')
grid on
xlabel('Time (s)')
ylabel('GRAVITY GRADIENT XX (E)')
title('GRAVITY GRADIENT XX AT l FIXED (100), SUM OVER m, VS TIME (E)',
'fontsize', 9)
% title('GRAVITY GRADIENT XX AT l FIXED (70), SUM OVER m, VS TIME (E)',
'fontsize', 9)



% figure(74)
% clf
% % plot(ll(1:end),Uxy(500,1:end),'k')
% plot(Uxy(:, elle),'k')
% grid on
% xlabel('degree l')
% ylabel('GRADIENTE DI GRAVITA XY AT L FIXED VS TIME (s^-2)')

% figure(75)
% clf
% % plot(ll(1:end),Uyz(500,1:end),'y')
% plot(Uyz(:, elle),'y')
% grid on
% xlabel('degree l')
% ylabel('GRADIENTE DI GRAVITA YZ AT L FIXED VS TIME (s^-2)')

figure(76)
clf
```

```
plot(Uxz(:, elle)/1e-9,'m')
grid on
xlabel('Time (s)')
ylabel('GRAVITY GRADIENT XZ (E)')
title('GRAVITY GRADIENT XZ AT l FIXED (100), SUM OVER m, VS TIME (E)',
'fontsize', 9)
% title('GRAVITY GRADIENT XZ AT l FIXED (70), SUM OVER m, VS TIME (E)',
'fontsize', 9)

%%%% PLOT AT TIME FIXED, VS L
%%%% time chosen = 1801*4/3600 = dopo  ore di orbita
%%%% time chosen = 2701*4/3600 = dopo 3 ore di orbita
figure(81)
clf
% plot(ll(2:end),Uzz(500,2:end) + 2*mu/r^3)
% plot(Uzz(2701, :)/1e-9)
plot(Uzz(3301, :)/1e-9) % Mars
grid on
xlabel('Degree l')
ylabel('GRAVITY GRADIENT ZZ (E)')
title('GRAVITY GRADIENT ZZ AT TIME FIXED VS l, SUM OVER m (E)', 'fontsize', 9)

figure(82)
clf
% plot(Uyy(2701, :)/1e-9, 'r')
plot(Uyy(3301, :)/1e-9, 'r')% Mars
grid on
xlabel('Degree l')
ylabel('GRAVITY GRADIENT YY (E)')
title('GRAVITY GRADIENT YY AT TIME FIXED VS l, SUM OVER m (E)', 'fontsize', 9)

figure(83)
clf
% plot(Uxx(2701, :)/1e-9,'g')
plot(Uxx(3301, :)/1e-9,'g') % Mars
grid on
xlabel('Degree l')
ylabel('GRAVITY GRADIENT XX (E)')
title('GRAVITY GRADIENT XX AT TIME FIXED VS l, SUM OVER m (E)', 'fontsize', 9)


% figure(84)
% clf
% % plot(ll(1:end),Uxy(500,1:end),'k')
% plot(Uxy(:, 9000),'k')
% grid on
% xlabel('degree l')
% ylabel('GRADIENTE DI GRAVITA XY AT L FIXED VS TIME (s^-2)')

% figure(85)
% clf
% % plot(ll(1:end),Uyz(500,1:end),'y')
% plot(Uyz(:, 9000),'y')
% grid on
% xlabel('degree l')
% ylabel('GRADIENTE DI GRAVITA YZ AT L FIXED VS TIME (s^-2)')

figure(86)
clf
% plot(Uxz(2701, :)/1e-9,'m')
```

```
plot(Uxz(3301, :)/1e-9,'m')
grid on
xlabel('Degree l')
ylabel('GRAVITY GRADIENT XZ (E)')
title('GRAVITY GRADIENT XZ AT TIME FIXED VS l, SUM OVER m (E)', 'fontsize', 9)


%%%% PLOT AT L FIXED (the last computed, f.i. l = 70) VS M, at TIME FIXED
%%%  time chosen = 9000*4/3600 = dopo 10 ore di orbita

figure(91)
clf
% plot(sSzz(2701,1:end)/1e-9)
plot(sSzz(3301,1:end)/1e-9) %MArs
grid on
xlabel('order m')
ylabel('GRAVITY GRADIENT ZZ (E)')
title('GRAVITY GRADIENT ZZ VS m AT l = 100 AT FIXED TIME (E)', 'fontsize', 9)
% title('GRAVITY GRADIENT ZZ VS m AT l = 70 AT FIXED TIME (E)', 'fontsize', 9)

figure(92)
clf
% plot(sSxx(2701,1:end)/1e-9, 'g')
plot(sSxx(3301,1:end)/1e-9, 'g') % Mars
grid on
xlabel('order m')
ylabel('GRAVITY GRADIENT XX (E)')
title('GRAVITY GRADIENT XX VS m AT l = 100 AT FIXED TIME (E)', 'fontsize', 9)
% title('GRAVITY GRADIENT XX VS m AT l = 70 AT FIXED TIME (E)', 'fontsize', 9)

figure(93)
clf
% plot(sSyy(2701,1:end)/1e-9, 'r')
plot(sSyy(3301,1:end)/1e-9, 'r') % Mars
grid on
xlabel('order m')
ylabel('GRAVITY GRADIENT YY (E)')
title('GRAVITY GRADIENT YY VS m AT l = 100 AT FIXED TIME (E)', 'fontsize', 9)
% title('GRAVITY GRADIENT YY VS m AT l = 70 AT FIXED TIME (E)', 'fontsize', 9)

% figure(94)
% clf
% plot(sSxy(elle,1:end), 'm')
% grid on
% xlabel('order m')
% ylabel('GRADIENTE DI GRAVITA XY VS M AT L = 55 AT FIXED TIME (s^-2)')

% figure(95)
% clf
% plot(sSyz(elle,1:end), 'k')
% grid on
% xlabel('order m')
% ylabel('GRADIENTE DI GRAVITA YZ VS M AT L = 55 AT FIXED TIME (s^-2)')

figure(96)
clf
string86 = sprintf('GRAVITY GRADIENT XZ VS m AT l = %d AT FIXED TIME (E)',
elle);
% plot(sSxz(2701,1:end)/1e-9)
plot(sSxz(3301,1:end)/1e-9) %MArs
```

```
grid on
xlabel('order m')
ylabel('GRADIENTE DI GRAVITA XZ (E)')
title(string86,'fontsize',9)
```